
Noble-metal nanoparticles produced with colloidal lithography: fabrication, optical properties and applications

Dissertation

zur Erlangung des akademischen Grades des Dr. rer. nat.
im Fachbereich Chemie der Johannes Gutenberg-Universität Mainz

vorgelegt von

Noelia Laura Bocchio

geboren in Rosario, Argentinien

Mainz, August 2008

Diese Arbeit wurde in der Zeit von Mai 2005 bis August 2008 am Max-Planck-Institut fuer Polymerforschung in Mainz angefertigt.

The work for this dissertation was carried out between May 2005 and August 2008 at the Max-Planck-Institute for Polymer Research in Mainz (Germany).

Financial support: Max Planck Gesellschaft, Bundesministerium für Bildung und Forschung

*Zwei Dinge sind zu unserer Arbeit nötig:
Unermüdliche Ausdauer und die Bereitschaft, etwas, in das man viel Zeit und Arbeit
gesteckt hat, wieder weg zu werfen.*

Albert Einstein

Table of contents

1	Introduction.....	11
	Metallic nanoparticles and their applications	11
	Plasmons	11
	Plane interfaces.....	12
	Plasmon resonances in metallic nanoparticles	13
	Objective and main structure of this work.....	17
2	Fabrication	21
2.1	Single, isolated nanocrescents on a flat substrate.....	23
2.1.1	Sample preparation	23
2.1.2	Geometrical description.....	25
2.1.3	Standard crescent shaped nanoparticles.....	26
2.2	Close-packed arrangements of nanocrescents	27
2.2.1	Fabrication of a mask of evenly spaced colloids	28
2.2.2	Controlled particle size reduction	28
2.2.3	Fabrication of the crescent shaped structures.....	29
2.3	Surface tailoring I: Thin films on metal nanostructures.....	31
2.3.1	Preparation of thin films and surfaces	31
2.3.2	Surface functionalization	32
2.3.3	Polyelectrolyte attachment	33
2.4	Surface tailoring II: surface modification for the study of bio- recognition events	39
2.4.1	Biotinylation	39
2.4.2	Streptavidin (SAv) attachment.....	39
2.4.3	Bioconjugation of the SAv-modified Au nanoparticles (SAv- AuNPs)	39
2.5	Summary	40
3	Understanding resonances	41
3.1	Isolated particles.....	41
3.1.1	Varying ϕ structures	42
3.1.2	Metal thickness (t)	53
3.1.3	Colloidal size (d_{coll})	53

3.1.4	Metal deposition angle (θ_i).....	56
3.1.5	Etching angle (ϵ).....	58
3.1.6	Materials.....	58
3.2	Close-packed crescent shaped nanostructures.....	60
3.2.1	Experimental	60
3.2.2	Results and discussion.....	61
3.3	Summary and conclusions.....	64
4	- Sensing with crescent shaped nanoparticles	66
4.1	Introduction.....	66
4.2	Thin layer sensing with multipolar resonances	68
4.2.1	Sample preparation	68
4.2.2	Characterization	68
4.2.3	Results and discussion.....	69
4.3	Testing the sensing capabilities of the nanocrescents for bio- recognition events	81
4.3.1	Sample preparation	82
4.3.2	Characterization	82
4.3.3	Results and discussion.....	83
4.4	Conclusions	88
5	- Fluorophores close to crescent shaped nanoparticles	90
5.1	Two-photon excitation.....	91
5.2	Experimental.....	92
5.2.1	Sample preparation	92
5.2.2	Characterization	93
5.3	Results and discussion.....	95
5.4	Summary and conclusions.....	108
6	- Fabrication of discs and ellipsoid-like noble metal nanoparticles.....	111
6.1	Introduction and motivation.....	111
6.2	Fabrication.....	112
6.2.1	General methodology	112
6.2.2	Sample preparation	113
6.3	Characterization	114
6.3	Results and discussion.....	114

6.3.1	Nanodiscs ($\varepsilon = 0^\circ$)	114
6.3.2	Ellipsoids ($\varepsilon > 0$)	121
6.4	Conclusions	125
7	- Sensing with metallic nanodiscs	126
7.1	Thin film sensing with Au nanodiscs	127
7.1.1	Experimental	127
7.1.2	Characterization	128
7.1.3	Results and discussion.....	128
7.2	Sensing of bio-recognition events with nanodiscs	132
7.2.1	Experimental	132
7.2.2	Results and discussion.....	132
7.3	Conclusions	137
8	- Tailoring plasmon resonances – blue shifting.....	139
8.1	Introduction.....	139
8.2	Experimental.....	140
8.2.1	Sample preparation	140
8.2.2	Characterization	141
8.3	Results and discussion.....	142
8.4	Conclusions.....	144
9	Summary and outlook	146
9.1	Crescent shaped nanoparticles	146
9.2	Ellipsoid-like nanoparticles	148
	Appendix A.....	157
	Materials and Methods	157
	Data analysis.....	160
	Appendix B	161
	Au crescents.....	161
	Ag crescents.....	164
	Thin layer sensing experiments - Supporting information.....	165
	Two photon experiments - Supporting Data	169
	Ag-UPD experiments - Complementary experiment on 100 nm Au discs	171
	Appendix C.....	172

Fitting Lorentzian, Gaussian and Voigt curves	174
Crescents	174
Discs	175
References	179
Collaborations.....	191
Acknowledgements	193
Curriculum Vitae – Noelia Laura Bocchio.....	195
Publications	196

1 . Introduction

Metallic nanoparticles and their applications

Metallic structures with typical dimensions of the wavelength of light and below may support optical resonances [Novotny and Hecht 2006]. The resonances can be associated to i.e. colored materials when they appear in the visible range [Murray and Barnes 2007]. This effect was noticed more than a century ago [Faraday 1857; Zsigmondy 1905], though the unique optical properties of some metallic particles in the visible range had already been used long before to colour glasses and ceramics [LycurgusCup].

The optical properties of metallic nanoparticles, namely, their extinction spectra (absorption and scattering), are associated to an electron-resonance phenomenon, known as *plasmons*. Actually, the investigation of optical phenomena in connection to the electromagnetic response of metals has been termed *plasmonics*, or nanoplasmonics, and is a rapidly growing field [Novotny and Hecht 2006].

Plasmons

Free conduction electrons in a metal determine in great manner the optical response of the material; that is, the interaction of the metal with the electromagnetic radiation [Ashcroft and Mermin 1976; Novotny and Hecht 2006].

The dielectric function of the metals, a strongly frequency dependent quantity, is a key point to describe these phenomena [Ashcroft and Mermin 1976; Novotny and Hecht 2006], and can be estimated with simplified models, i.e., the Drude model.

The Drude model [Ashcroft and Mermin 1976] is an approximation that describes the response of the metal in terms of these free electrons when driven by an external oscillating field, and allows to calculate a dielectric function of the material. It represents the response of the metal very well up to certain frequencies (usually in the visible or UV part of the spectrum), where interband transitions set in and further corrections are necessary [Ashcroft and Mermin 1976; Novotny and Hecht 2006]. In this model, the dielectric functions have the following form:

$$\epsilon_{drude}(\omega) = 1 - \frac{\omega_p^2}{\omega^2 + i\omega\Gamma}$$

Where $\omega_p = \sqrt{ne^2 / m_e \epsilon_0}$ is the volume plasma frequency, e the charge of the electron, and m_e its effective mass; Γ represents the damping term. These simple approximations are very useful, since, as will be shown in the following, the dielectric constants of the materials involved play a fundamental role determining the occurrence of several phenomena.

Plane interfaces

Surface plasmon is a term used for naming the collective oscillations of the electrons at a metal-dielectric interface [Knoll 1998; Homola 2006; Novotny and Hecht 2006]. Surface plasmons propagate along this interface; there, the electromagnetic fields, energy and charges are highly localized to a scale of some hundred nanometers [Knoll 1998], which translates in a high sensitivity of these modes to the properties of the interface (both metal and dielectric). It is this property what makes them ideal as sensing platform in the nanoscale [Knoll 1998; Homola 2006]. By solving Maxwells equations with proper boundary conditions, a dispersion relation can be obtained:

$$k_{spp} = k_0 \sqrt{\frac{\epsilon_m \epsilon_d}{\epsilon_m + \epsilon_d}}$$

where k_{spp} and k_0 are the wavevectors of the plasmon mode and in free space; ϵ_m and ϵ_d the dielectric functions of the metal and medium.

The excitation of surface plasmons in a metal dielectric interface can be achieved by different approaches, i.e. via prism coupling or using gratings [Knoll 1998; Homola 2006]. The experimental approach for studying these modes consists of monitoring the changes in reflectivity at the metal-dielectric interface when changing the local dielectric environment, i.e., while studying biological binding reactions at the interface [Knoll 1998] or simply changing the dielectric medium. Comprehensive reviews on all the fundamental concepts and applications around the use surface plasmons resonances (SPR) can be found in [Knoll 1998; Homola 2006].

This technique has been widely explored and has been proven to be most adequate for building sensing platforms; reaching the point of existing various successful commercial applications around this.

Confined plasmon modes in particles, on the other hand, are not so widely spread as the propagating modes in plane interfaces, though they present several interesting potential applications. They can also be used as part of a sensing platform, or for enhanced spectroscopies, but with slightly different technical approaches.

It is the interest of this work to explore plasmon resonances in metallic nanoparticles, to understand their response, to quantify their environment sensitivity, and to use the confined near fields associated to them to trigger other phenomena, i.e. fluorescence processes.

In order to gain a general idea on basic phenomena associated to spectral response, material properties and local environment sensing with metallic nanoparticles, a simplified model introduced in the literature will be presented in the following.

Plasmon resonances in metallic nanoparticles

When the free electrons are confined in three dimensions, as for nanoparticles, specific particle-plasmon resonances can occur depending on the geometries and the materials involved (medium and metal). These resonances can lead to large charge accumulations, and highly localized, strongly enhanced near fields.

The simplest idealized geometry for a particle is a sphere. The response of a sphere to an exiting electric field can be calculated solving Maxwell's equations; the exact analytical treatment of this problem was applied by Mie in the early 20th century to study the scattering of light by these particles, and can be calculated for all wavelength vs. diameter ratios [Bohren and Huffman 1983].

For small spherical particles, though, some approximations can be made regarding the resonances, and their associated scattering and absorption.

Small spherical particles – quasi static approximation

Qualitative understanding of some phenomena related to plasmon resonances in nanoparticles can be gained if considering the case of very small spherical nanoparticles (smaller than the skin depth of the metal), with no retardation effects.

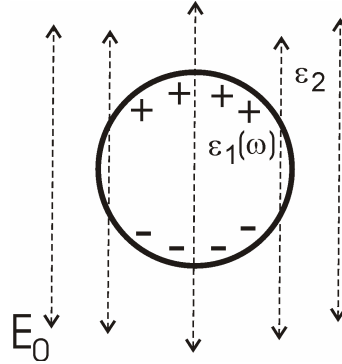


Figure 1-1: sketch of a sphere in a given electric field (E_0). The metal and the surrounding medium are represented through ϵ_1 and ϵ_2 .

If a small metallic sphere is placed in an electric field [Novotny and Hecht 2006], then a dipole μ can be induced by it. The dipole has the form $\mu = \epsilon_2 \alpha(\omega) \mathbf{E}_0$, where $\alpha(\omega)$ represents the polarizability, which has the form:

$$\alpha(\omega) = 4\pi\epsilon_0 a^3 \frac{\epsilon_1(\omega) - \epsilon_2}{\epsilon_1(\omega) + 2\epsilon_2}$$

where, a represents the radius of the sphere, $\epsilon_1(\omega)$ the dielectric function of the metal (which could be represented, i.e. via a corrected Drude model), and ϵ_2 that of the surrounding medium.

If the power radiated by the sphere's dipole (μ) is divided by the intensity of the exciting wave, a scattering cross section can be determined [Bohren and Huffman 1983; Novotny and Hecht 2006].

In that case, the scattering cross section has the following form:

$$\sigma_{scatt} = \frac{k^4}{6\pi\epsilon_0^2} |\alpha(\omega)|^2$$

with k being the wavevector in the surrounding medium.

There, it is already possible to recognize the role played by the dielectric functions of the metal and medium in the scattering, through the polarizability. This value is expected to increase drastically for a small denominator (when a resonance is met). It is also very important to point out that, as the dielectric function of the metal is a frequency-dependent quantity, the spectral occurrence of the resonance is directly linked to the surrounding medium, a fact that is used as a local sensing properties of the particles and has been applied in many contexts, from simple bulk experiments, to the recognition of binding events on the surface of these nanoparticles [Englebienne 1998; Frederix et al. 2003; Willets and Van Duyne 2007].

If a particle is irradiated with a wave, the power decrease is not only due to scattering, but absorption can also play a significant role [Bohren and Huffman 1983; Novotny and Hecht 2006]. The combination of both phenomena is usually referred to as extinction. By using Poynting's theorem [Bohren and Huffman 1983; Novotny and Hecht 2006], the power absorbed by the particle can be easily estimated, rendering an absorption cross section of the form:

$$\sigma_{abs} = \frac{k}{\epsilon_0} \text{Im}[\alpha(\omega)]$$

With k being the wavevector in the surrounding medium.

If the expression for α is replaced in the last two equations (scattering and absorption), it is possible to observe that the scattering scales with a^6 , while the absorption the a^3 , which explains that for large particles, extinction has mainly a scattering component, while for small particles, the contribution to the extinction is mostly dictated by absorption [Novotny and Hecht 2006].

This interplay of absorption and scattering is what determines the color of the noble metal nanoparticles' suspensions, or, i.e. the coloured glasses like that of the Lycurgus Cup.

The combination of material properties, size and shape of the particles, as well as their surrounding medium, determines the resonances in each particular case (for comprehensive reviews on the subjects refer to [Mulvaney 1996; Novotny and Hecht

2006; Murray and Barnes 2007; Willets and Van Duyne 2007]), and results in their characteristic extinction spectra.

The case presented here is just a simplified example that provides a good qualitative approach to more complex structures. For larger particles, or with complex shapes, in general, full numerical calculations are necessary to describe the interaction with light [Tavlove 1995]. The quality of these approximations relies not only on the capabilities of the methods of calculation, but the proper description of the geometry and the material parameters (namely, the dielectric functions of the metal and of the medium in the nanoscale) play a fundamental role. As an example of this, usually, the description of the materials is based on bulk measurements, and this does not necessarily holds for small particles; as it is for a local description of the dielectric media surrounding them.

Metal nanoparticles are particularly interesting for several reasons. Ranging from the noble metal colloids and their distinctive colours used in ancient times to fabricate glasses [LycurgusCup], through their environment-sensitivity and the corresponding impact in chemo- and bio- sensing platforms [Englebienne 1998; Frederix et al. 2003; Novotny and Hecht 2006; Novotny 2007; Willets and Van Duyne 2007], for enhanced spectroscopies [Farahani et al. 2005; Anger et al. 2006; Biteen et al. 2006; Novotny and Hecht 2006; Gerber et al. 2007; Ringler et al. 2008] , or even in the metamaterials field [Pendry 2000; Linden et al. 2004; Smith et al. 2004; Enkrich et al. 2005; Pakizeh et al. 2006], the metallic particles have proven efficient to have a broad spectrum of applications.

A key role in all the phenomena mentioned above is played by the near fields, particularly when meeting a plasmon resonance [Novotny and Hecht 2006]. It is the strength (or field enhancement factors) and the spatial confinement of the latter what influences the capabilities of the particles in all of these applications. As introduced, drastically enhanced optical near fields can result in i.e. both enhanced excitation of a local absorber and enhanced emission of a local source which is located in this region [Girard et al. 1995; Barnes 1998; Novotny and Hecht 2006], a property that has been widely exploited for applications in enhanced spectroscopies. Also, the high sensitivity of the spectral response to local changes in the dielectric environment in

the close surrounding makes them promising for chemical and biosensing applications [Englebienne 1998; Haes, Zou et al. 2004; Whitney et al. 2005].

Many approaches to produce nanoparticles have been explored in the last years; ranging from chemical methods based on colloid chemistry [Turkevich et al. 1951; Mulvaney 1996; Boleininger et al. 2006], or by means of (conventional and non-conventional) lithographic approaches, like electron-beam [Krenn, Schider, Rechberger, Lamprecht, Leitner and F.R. 2000; Linden et al. 2004], focused ion-beam [Farahani et al. 2005] and nanosphere (or “natural”) lithography [Fischer and Zingsheim 1981; Deckman and Dunsmuir 1982; Willets and Van Duyne 2007]. The latter is a particularly versatile technique, which has been used to produce, in a rather simple and parallel manner, several complex structures like discs [Hanarp, Käll et al. 2003], truncated prisms [Haes et al. 2005], rings [Aizpurua, Hanarp, Sutherland, Käll, Bryant and Garcia de Abajo 2003; Rochholz et al. 2007], metal-dielectric sandwiches [Pakizeh et al. 2006], crescents [Shumaker-Parry et al. 2005], among others.

Objective and main structure of this work

In this work, the fabrication, optical properties and applications (namely sensing) of nanometer-sized metal particles produced via colloidal lithography are explored experimentally. Two main geometrical configurations of metal nanoparticles are used for such a purpose: the crescent-shaped and the ellipsoid-like ones.

The motivation behind exploring common phenomena for differing architectures is associated to exploring the influence of shapes and materials in the resonances and, from an application point of view, for their sensitivity.

The present work is divided in two main sections, one devoted to each family of nanoparticle shapes. Each of these sections is structured in sub-sections presenting results on two main subjects, namely: (a.) fabrication, tailoring and basic understanding of the optical properties, and (b.), sensing capabilities of the nanoparticles. For the nanocrescents, first results on resonance-mediated enhanced-fluorescence are also included in the corresponding section.

Since both parts of the work share a common structure and are oriented to the investigation of the same fundamental problems, the general concepts behind each subject are introduced mostly in the first part of this document, while referencing and reviewing for each particular structure (crescents or discs/ellipsoids) is added in each chapter.

The experimental techniques used for the sample fabrication and characterization were based on standard procedures (i.e. scanning electron microscopy, transmission spectroscopy, atomic force measurements); their description can be found in an Appendix devoted to “Materials and Methods” included at the end of this work. Extra (complementary/supporting) information related to each particular set of experiments can also be found in this document, distributed in the different Appendices.

Part I

Model System: Crescent-shaped nanoparticles

2 . Fabrication

Crescent shaped noble metal nanoparticles were introduced in 2005 [Rochholz 2005; Shumaker-Parry et al. 2005; Rochholz et al. 2007] as a novel model nanoparticle system. These particles were fabricated using an approach combining colloidal masks, oblique metal deposition and ion etching. This method, of simple conception, great ease and reproducibility, gives rise to nanostructures that present multiple plasmonic resonances in the near infrared part of the spectrum and can be easily studied using conventional spectroscopic techniques [Rochholz et al. 2007].

The interesting geometry and optical properties of these particles have likely driven many other groups to produce structures with comparable geometries, but making use of somewhat more sophisticated techniques, i.e. e-beam lithography, obtaining comparable results [Linden et al. 2004; Lu et al. 2005; Clark et al. 2007; Sheridan et al. 2007; Li et al. 2008]. Compared to the latter, the nano crescents produced with colloidal masks require minimum equipment and effort to be produced; resulting in very reproducible large area ($\sim \text{cm}^2$) samples, which makes them ideal for potential large scale production.

Fabrication

The general procedure to make crescent shaped nanoparticles using colloidal masks is based on a simplified lithographic approach introduced early in the 80's by Fischer et. al. and, subsequently, by Deckman et al. [Fischer and Zingsheim 1981; Deckman and Dunsmuir 1982]. The concept involving the use of colloids as masks was further developed by other authors to produce, i.e. square micrometer sized arrangements of triangular shaped particles. An interesting review on this subject is given by Zhang. et. al. [Zhang et al. 2006]. Different names ranging from, i.e. "natural lithography" in the early work of Deckman, "Fischer-patterns"- referring to the work of Fischer et. al., to "nanosphere lithography" (NSL) - as introduced by the Van Duyne group - have been assigned to the different versions of this technique, being this last one the most commonly used nowadays.

In this chapter, the general fabrication procedures and new approaches are introduced for the crescent shaped nanoparticles. Section 2.1 introduces the fabrication of single, isolated particles on flat substrates and new developments around it. Section 2.2 deals with a novel approach to produce large (several mm^2) areas covered with close-packed arrangements of nanocrescents.

Since all fabrication procedures give rise to bare structures, it is of interest for further surface tailoring and sensing purposes to introduce specific chemical functionalities on the surface of the particles, and on the substrates. These procedures are of fundamental importance for further studies on the environment-sensing capabilities of these particles.

In this context, section 2.3 deals with the chemical treatment of the samples, adding silanes / thiols and studying the attachment of, i.e., thin polyelectrolyte layers as a further fabrication/tailoring approach to control the morphology and optical properties of the nanocrescents.

Section 2.4 presents a second approach for the surface tailoring procedures, that is, the surface modification for the study of bio-recognition events. All chemical treatments introduced in these sections have a general character and can be extended directly to other noble metal nanoparticles attached to a surface.

2.1 Single, isolated nanocrescents on a flat substrate

2.1.1 Sample preparation

Polystyrene “PS” nanospheres (*Polystyrene Nanobead: NIST, Polysciences, Warrington, USA*), were randomly dispersed on a piranha ($\text{H}_2\text{SO}_4:\text{H}_2\text{O}_2$, 2.5:1) cleaned glass (or, when preferred silicon) substrate (*Objektträger Glas, Menzel Glaeser, Germany*). The colloid concentrations were tailored to obtain single, isolated structures ($1 - 2 \text{ particles}/\mu\text{m}^2$) [Rochholz 2005]. Typically, a 1:100 (v/v) dilution was used for this purpose. A 20 – 40 nm thick gold film was evaporated (*Auto 306, Edwards, Sussex UK*) on the colloid-covered substrates (t : thickness), the samples being tilted by an angle θ_i relative to the metal source. The maximum possible thickness of the film is a function of the size of the colloids [Rochholz 2005], and can be varied as desired, with a lower limit set by the quality of the films produced by the deposition machine; in this case approximately 20 nm. Following the metal deposition, the coated samples are exposed to an argon ion beam (*RR-I SQ76, Roth & Rau, Wüstenbrand, Germany*) incident on the substrate with a given angle ε (usually perpendicularly, that is, $\varepsilon = 0$), and etched. After the etching process, the colloidal mask is removed mechanically by means of an adhesive tape (*Scotch Magic Tape 810: 19mm \times 33m, 3M France*) and a second ion-beam etching step is applied in order to ensure the removal of any extra sputtered material from the surface. By doing multiple metal depositions (which can be done at different θ_i), and rotating the sample a given angle (φ_j) in between deposition steps, it is possible to deliberately close the gap between the tips of the resulting metal particles in a controlled manner. Figure 2-1 a. through d. show schematically the steps of this process, from the colloid dispersion on the surface to the removal of the mask, with all its main variables. By doing multiple depositions, it is also possible to produce structures that look highly symmetrical; i.e. rings. Figure 2-1 e. through h. present scanning electron micrographs of structures produced using one (e.), two (f., g.) and three (h.) metal deposition steps.

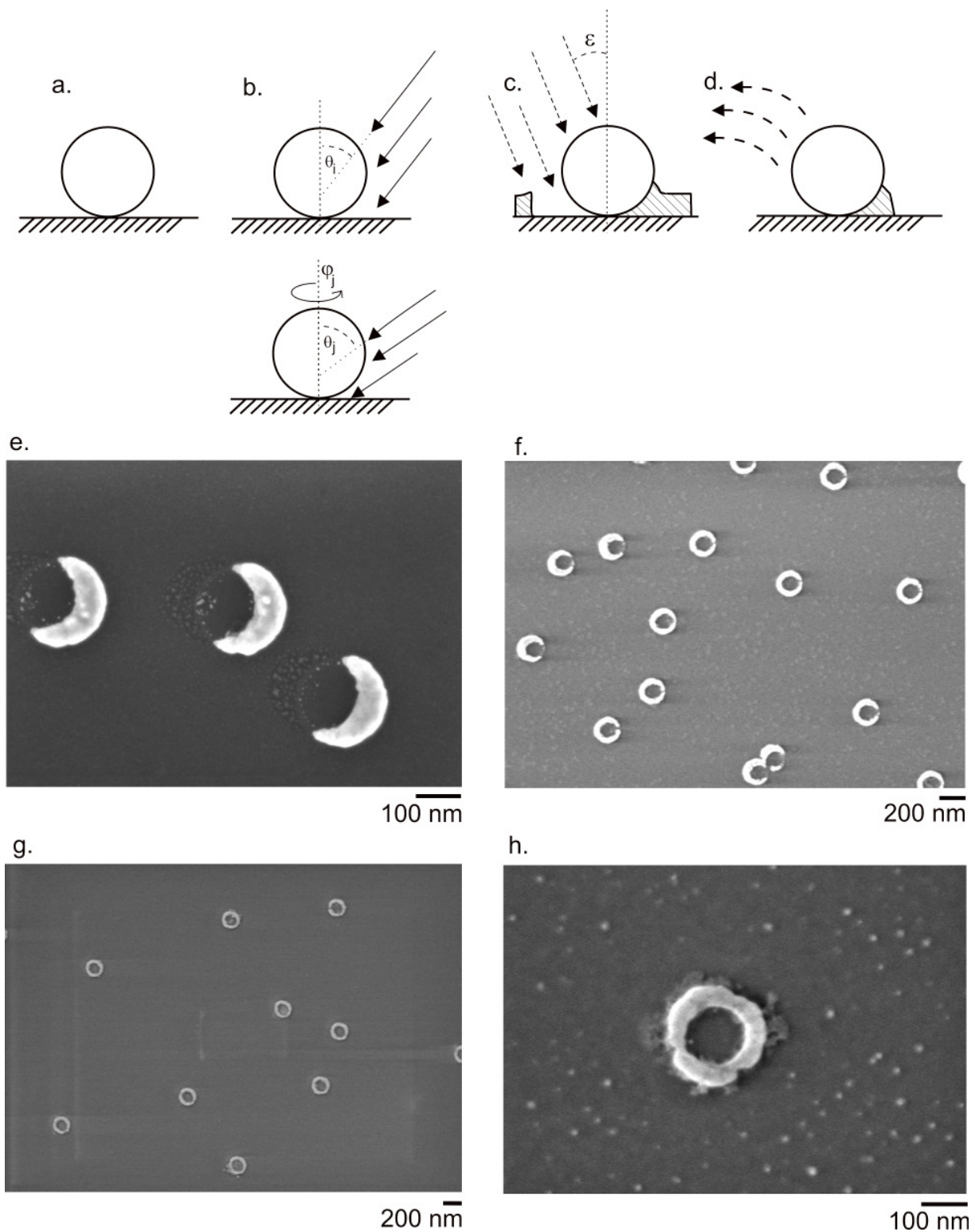


Figure 2-1: a. colloids' deposition on a clean, flat (Si or glass) surface, b. oblique (θ_i) metal deposition – this step can be done multiple times, combining different deposition angles (i.e. θ_i , θ_j), rotation of the sample between depositions (ϕ) and different metal thicknesses (t); c. ion etching of the surface (at a given angle, ϵ), d. mechanical removal of the colloids. Structures produced using 150 nm PS colloids. 1 deposition ($\phi = 0$), 2 depositions (f. $\phi = 140$, g. $\phi = 180$) and 3 metal depositions ($\phi = 0, 120, 240$). All four samples were etched perpendicularly to the substrate ($\epsilon = 0$).

As the colloids are scattered on the surface, usually well separated (some hundred nanometers) from another, the particles produced by this method appear also generally well separated and randomly scattered on the surface. Another very important characteristic is that all particles are oriented in the same direction on the substrate. Since the metal is deposited in an equal manner for all colloids at the same time, this can only result in all of them having the same final orientation (see, i.e. Figure 2-1 e. and f.), which allows for simple ensemble spectroscopic measurements.

2.1.2 Geometrical description

The general geometrical characteristics of the nanocrescents can be described by means of the main process parameters, namely, colloid size (d_{coll}), deposition angles (θ_j), thickness (t) of the metal film deposited on the substrate, number of metal depositions and rotation angle between them (φ_j), and etching angle (ε). This last one has been set to 0 for the examples analyzed throughout this work, meaning all samples were etched perpendicularly to the substrate.

Figure 2-2 depicts an idealized geometry of a crescent structure as obtained by double evaporation. In a single evaporation step, the crescent covers a circle segment corresponding to an angle α . This angle can be described with a simple equation (see below). The maximum width (w) of the structure can also be described using geometrical considerations [Rochholz 2005; Rochholz et al. 2007]. Both sketches of the resulting (theoretical) structures and the description of the parameters is presented below.

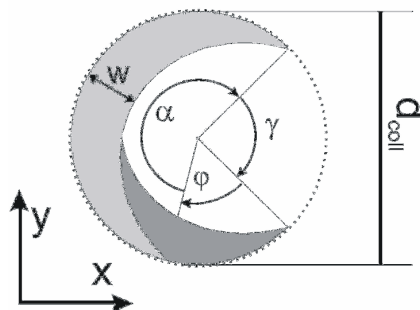


Figure 2-2: Sketch of the particle geometry indicating the rotation angle φ for double evaporation, the diameter d_{coll} of the masking colloid and a coordinate system to be referred to. The angle α defines the circular segment ideally covered by the gold film in a single evaporation step.

$$\cos\left(180 - \frac{\alpha}{2}\right) = \frac{\tan(\theta)}{1 + \cos(\theta) + \sin(\theta)\tan(\theta)}$$

$$w = \frac{d_{coll}}{2} \left[1 - \frac{(1 - \sin(\theta))}{\cos(\theta)} \right]$$

For the $\theta = 30^\circ$ case, these considerations yield a $\alpha = 211^\circ$. By double evaporation, the circular segment covered by the structure is increased by the rotation angle α . The resulting opening angle β is then obtained as ($\beta = 360^\circ - \alpha$). One examples for these structures can be observed in Figure 2-1 f.

Deviations from the idealized geometry occur: real samples lack perfectly sharp tips, or smooth surfaces. Particularly, for structures with almost closed gaps between tips, i.e. Figure 2-1 f., certain dispersion in geometry can be observed with structures with greater openings as predicted. Such effects can in principle be associated to, i.e. slight displacements of the colloids during the metal depositions. Also granularity, as it is commonly known for thermally evaporated metal films, is seen in the scanning electron images, which translates into a not perfectly defined contour. Slight thickness variations are also to be expected, since the metal evaporator does not necessarily produce perfect, homogeneous metal films.

2.1.3. Standard crescent shaped nanoparticles

Unless otherwise specified, one typical geometry was used throughout this work, for sensing and enhanced spectroscopy studies. This configuration corresponds to that obtained using 150 nm colloids¹, one metal deposition of a 40 nm thick gold film at a relative angle θ of 30° . Following the metal deposition, the gold-coated samples were etched using an argon ion beam inciding perpendicularly to the substrate ($\epsilon = 0$). This configuration will be referred to throughout this work as *standard crescent shaped nanoparticles*.

¹ 150 nm colloids, nominal diameter, were bought from *NIST, Polysciences* but scanning electron micrographs revealed a size of 200 nm.

2.2 Close-packed arrangements of nanocrescents

When the colloidal masks are no longer isolated particles but colloidal monolayers, a wealth of complex structures can be produced using nanosphere lithography, i.e. truncated pyramids [Haynes and Van Duyne 2001], arrangements of discs [Zheng et al. 2008], rods [Kosiorsek et al. 2005], dumbbells or intricate nets of nanowires [Zhang et al. 2007; Zhang et al. 2007].

In this work, an easy and versatile nanofabrication approach for large area arrays of crescent shaped metal nanoparticles is demonstrated. Crescent shaped metal nanoparticles are a particularly interesting system for their geometry and optical properties [Shumaker-Parry et al. 2005; Rochholz et al. 2007].

These structures are very similar to split ring resonators [Pendry et al. 1999], which makes them very promising candidates for the design of metamaterials [Linden et al. 2004; Smith et al. 2004], reason for which it is most interesting to produce large scale arrangements of these particles.

The approach presented in this section to produce arrangements of nanocrescents relies on the combination of nanosphere lithography [Deckman and Dunsmuir 1982], the fabrication of large size, high quality colloidal monolayers [Retsch et al. 2008] and their size reduction by means of plasma etching [Haginoya et al. 1997].

A general scheme describing the conceptual approach is presented in Figure 2-3.

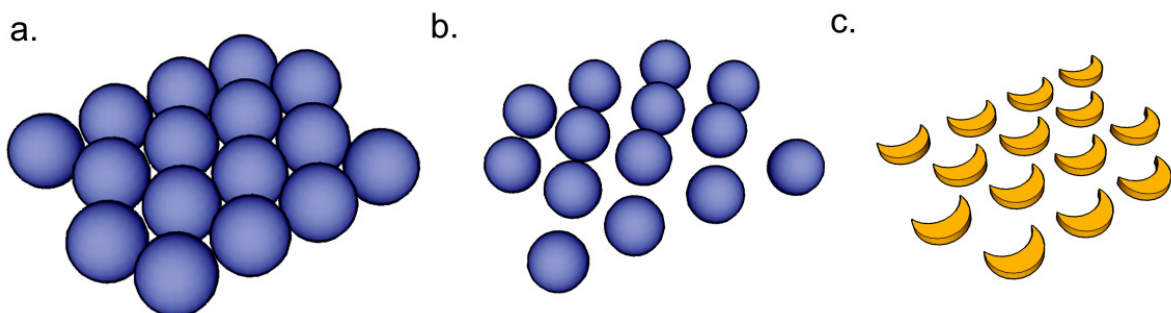


Figure 2-3: sketch of a colloidal monolayer (a.) before and after (b.) the plasma etching. The etched monolayer is the basic template for the crescent fabrication (c.), following the conventional metal deposition and Ar ion etching of the surface.

In the following, each of the preparation steps schematised Figure 2-3 will be described in detail.

2.2.1 Fabrication of a mask of evenly spaced colloids

The PS colloid monolayers were produced by depositing a drop of a colloidal dispersion on a clean substrate and floating the particles onto an air-water interface, by slow immersion of the substrate in water, under a shallow angle. The PS particles detach from the substrate at the substrate-water-air three-phase contact line and remain afloat at the air-water interface. Subsequently, the floating layer of colloidal particles is picked up by a second glass substrate [Retsch et al. 2008]. The quality and size of these monolayers (which can be up to several square millimeters) determines in great manner the final quality of the samples to be prepared.

The particles used for the monolayer fabrication step were prepared by an emulsifier-free emulsion polymerization, and purified by several cycles of centrifugation and redispersion in ultrapure (Milli-Q) water. All glass substrates were sonicated twice with a 2 % aqueous solution of a commercial detergent (*Hellmanex, Hellma GmbH, Mühlheim, Germany*) for 15 minutes, and extensively rinsed with ultrapure water and ethanol. Plasma cleaning (10 % O₂, 90 % Ar, 300 watt, 5 minutes) was used to hydrophilize the substrates. Finally the substrates were silanized with N-trimethoxysilylpropyl-N,N,N-trimethylammonium chloride according to a process reported in the literature [Jonas 2002].

2.2.2 Controlled particle size reduction

After the close-packed monolayer was deposited on the glass substrate, the mean colloid size was reduced via plasma etching. This process was done in a plasma reactor. The reactor is composed of a 30 cm long, 10 cm wide glass cylinder, 2 annular electrodes, a high frequency Generator (*Eni*) and a vacuum pump (*Trivac 16BCS, Leybold*). The pressure in the chamber reached 10⁻⁴ mbar. The etching gas flow was controlled via a multigas controller (*MKS, 647B*). The samples were etched with 5 SCCM Ar and 1 SCCM O₂ for 30 seconds, at 130 watts [Tamm 2008].

Figure 2-4 (a.) presents a scanning electron micrograph of a template before the ion etching process. The resulting template after the etching process can be seen in (b.) from a top view, and in (c.), from a lateral one. Different domains form the monolayers, with a slight mismatch in their orientations, which can be seen in Figure 2-3 (c.). It is evident from this last image that the etching process does not reduce the colloids homogeneously, but rather strongly from the top, giving rise to ovoidal (or microlens-like [Tan et al. 2004]) structures that are partially interconnected. This factor can in principle affect the final shape of the metal nanostructures, as well as the shadow produced by the neighbouring structures.

2.2.3 Fabrication of the crescent shaped structures

The fabrication of the crescent shaped nanoparticles, starting from this colloidal mask, follows exactly the same procedure as for the isolated structures introduced in the previous sections.

Figure 2-5 (a.) and (b.) present pictures (a. optical image, b. SEM image) of a sample produced by this method. It is important to note that, depending on the quality of the monolayers, it is possible to produce samples covering an area of several square millimeters. This method represents clear advantages when compared to conventional electron or focused ion beam lithography approaches, given its simplicity and high throughput, and presents a way to produce high quality, easy to handle macroscopic substrates for plasmonic applications.

The arrangement of the particles, though not completely perfect, extends over several micrometers. In this scale, the particles are arranged in domains, resembling grains in polycrystalline materials.

The ease of fabrication and the quality achieved by this method opens a way for producing high quality substrates for plasmonic application, i.e. arrangements of split-ring resonators for applications as metamaterials [Pendry et al. 1999; Linden et al. 2004].

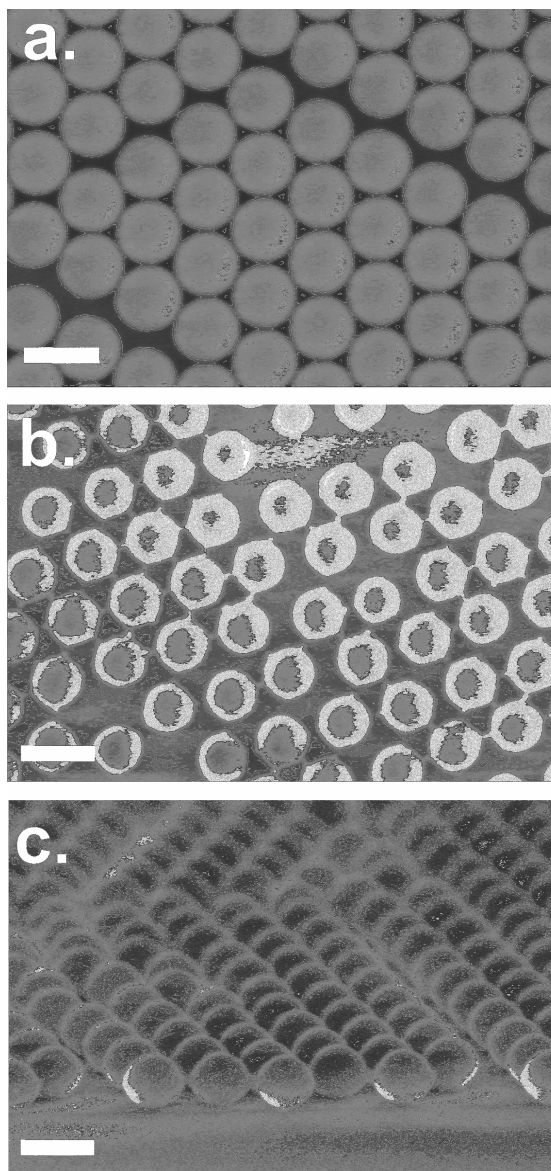


Figure 2-4: 180 nm PS nanoparticle monolayer before (a.) and after (b., c.) plasma etching. The scale bars represent 200 nm.

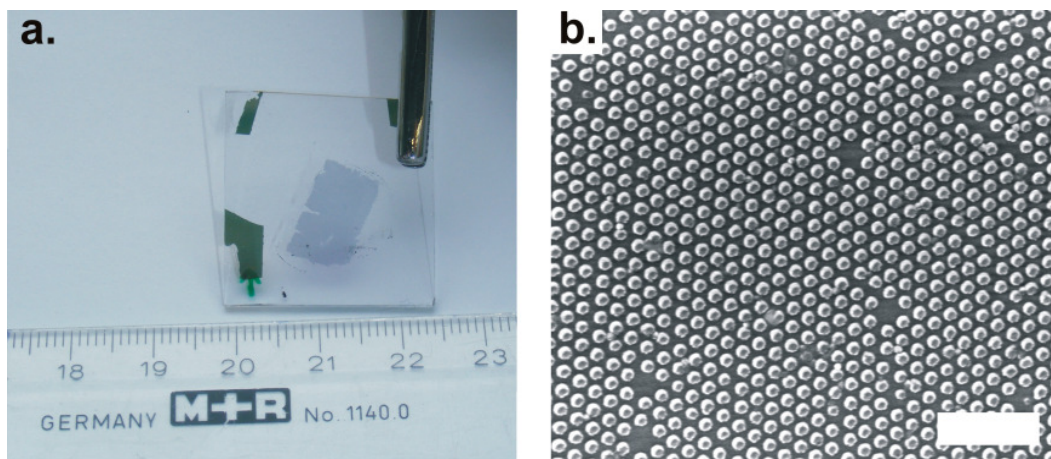


Figure 2-5: a. photo and b. scanning electron micrographs of one sample prepared by this method. The scale bar in (b.) represents 1 μm.

2.3 Surface tailoring I: Thin films on metal nanostructures

The methodology introduced so far deals with the fabrication of bare metal nanoparticles on flat substrates. The use of compounds like silanes or thiols allows for the chemical tailoring of both metal and glass surfaces adding functionalities to the structure/substrate, and allowing for the further attachment of i.e. polymer brushes, polyelectrolytes, fluorophores, or proteins.

In the following a series of simple surface tailoring procedures are introduced.

Firstly, two simple surface functionalization approaches are presented, combined with the deposition of polyelectrolyte layers. The results of these procedures are tested in terms of topology of the samples (via atomic force microscopy measurements) and optical properties (via transmission spectroscopy).

Secondly, conventional thiol functionalization and streptavidin attachment procedures are introduced. These procedures are finally aimed to study, in the subsequent chapters, the sensing capabilities of these particles to a few recognition events.

All of the methods presented in this section will be used throughout this work and can be applied not only to the crescent shaped nanoparticles, but also in principle to any other noble metal nanoparticle bound to a glass substrate. The procedures described here will be applied throughout this work and referred to when necessary.

2.3.1 Preparation of thin films and surfaces

The Layer-by-layer assembly of charged polymers is a standard method for growing films with controlled thickness on the nanometer scale. This robust approach was introduced by Decher et. al. in the early 90's [Decher et al. 1992; Decher 1997; Bertrand et al. 2000; Klitzing et al. 2004]. The method is based on the electrostatic attraction between oppositely charged polyelectrolytes (PE) and is particularly attractive because of its simplicity and versatility.

In order to attach the PE to the structures/surfaces in a controlled manner, two main surface functionalization approaches were tested. Thiols or silanes with chains of two different functionalities were used to selectively functionalize the metal nanoparticles or the glass substrate. The layer-by-layer deposition of thin polyelectrolyte bilayers was carried out in the same manner for both approaches; the resulting surface morphology was investigated by means of atomic force measurements.

To this purpose, *standard* gold crescent-shaped nanoparticles were prepared on glass substrates. The samples were exposed to different surface functionalization agents and subsequently immersed alternating in cationic and anionic polyelectrolyte solutions in order to build up nanometric layers on top of the nanostructures.

2.3.2 Surface functionalization

The samples were modified with either a thiol or a silane, which attach preferentially to the gold or to the glass surface, respectively (Figure 2-6). After this, they were immersed in the polyelectrolyte solutions as many times as required. In the following, the surface functionalization procedures are described in detail.

2.3.2.1 Silanization with APTES

The samples were introduced in a clean glass container together with some drops of 3-aminopropyltriethoxysilane (3-APTES) (Aldrich). The system was heated to 135 °C and the substrates were exposed to the vapor of the silane for 3 hours. After this treatment, the samples were removed from the container and thoroughly rinsed with ethanol, ultrapure (*Milli-Q*) water and dried with nitrogen.

2.3.2.2 Thiol functionalization with 3-MPA

The samples were immersed for 1 hour in a 3 mM aqueous solution of 3-mercaptopropionic acid (3-MPA) (Sigma), rinsed thoroughly with ultrapure (*Milli-Q*) water, and dried with nitrogen.

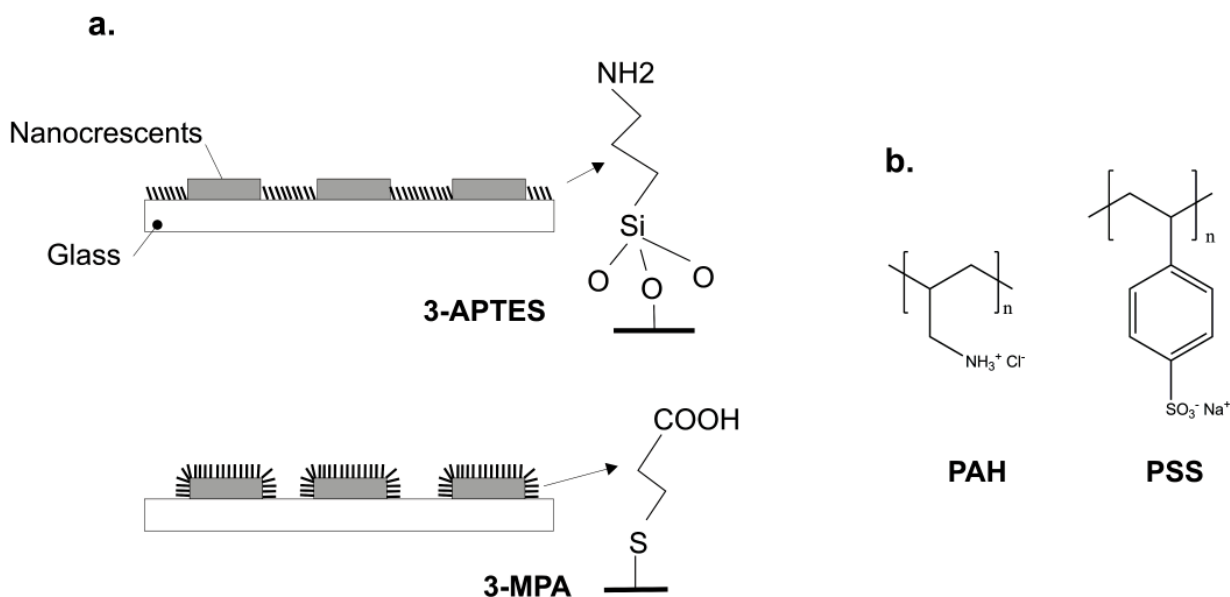


Figure 2-6 (a.) Schematic drawing showing the attachment of silane and thiol monolayers on the glass and gold surfaces (b) structures of PAH and PSS

2.3.3 Polyelectrolyte attachment

Polyelectrolyte layers were built on the samples using polyallylamine (PAH) and polystyrene sulfonate (PSS) as polycation and polyanion. Polyallylamine hydrochloride (PAH) (Aldrich, $M_w = 15000$) and polystyrene sulfonate (PSS) (Aldrich, $M_w = 70000$) aqueous solutions were prepared for this purpose, and brought to pH ~ 3 via addition of HCl. Salts were added to adjust the ionic strength of the solutions, following the general characteristics of a procedure described in the literature [Vasilev 2004]. The concentration of the polyelectrolytes was 0.02 M (in monomer units), 0.5 M for the $MnCl_2$ (PSS solution) and 2 M for NaBr (in the PAH solution). After the silane and/or thiol treatments, the samples were immersed alternatingly in the PSS and PAH solutions, building up the bilayers. For each bilayer cycle the samples were immersed for 20 min in the polycation solution (PAH) and then rinsed several times with ultrapure (Milli-Q) water. After this, they were dipped in the polyanion (PSS) solution for another 20 min and rinsed again with ultrapure water. Once the desired number of bilayers was reached, the samples were dried using a stream of nitrogen.

Characterization

Topography

The topography and phase of the surfaces upon the addition of functionalizing agents and polyelectrolyte bilayers were investigated using atomic force microscopy (AFM). The images of the samples were taken in air at room temperature with a commercial AFM (*Nanoscope IIIa, Veeco*) in tapping mode. Silicon cantilevers (*Olympus*) 160 μm long, 50 μm wide and 4.6 μm thick, with an integrated tip of a nominal spring constant of 42 N/m and a resonance frequency of 300 kHz were used. The tip was scanned at rates around 0.4 Hz for scan sizes \sim 2 microns, and minimal applied forces were used when imaging.

UV-Vis/NIR transmission spectroscopy

Non-polarized light transmission spectra were recorded in an UV-Vis/NIR spectrometer (*Perkin Elmer, Lambda 900*), both before and after the treatment with the different materials, for each sample.

Results

Figure 2-7 presents topography and phase images of a typical sample, where the crescent-shaped particles are easily recognized: a profile of these structures shows their thickness, corresponding to the values expected from the metal deposition conditions during the sample making process (\sim 35 nm). The random distribution of the particles on the surface and the fact of having the same orientation is typical for their fabrication process.

3-MPA Thiol – functionalized samples

Figure 2-8 documents the evolution of the topography and in phase for samples functionalized with 3-MPA (thiol with negative charge, used to attach positively charged polyelectrolytes to the gold structures) and the addition of a different number of polyelectrolyte (PE) bilayers (between 0 and 9). Both sets of images show that the amount of material on the glass and nanoparticles increases with the number of immersions of the samples in the polyelectrolyte solutions; these measurements

show also the progressive loss of sharpness of the structures upon the addition of the polymer.

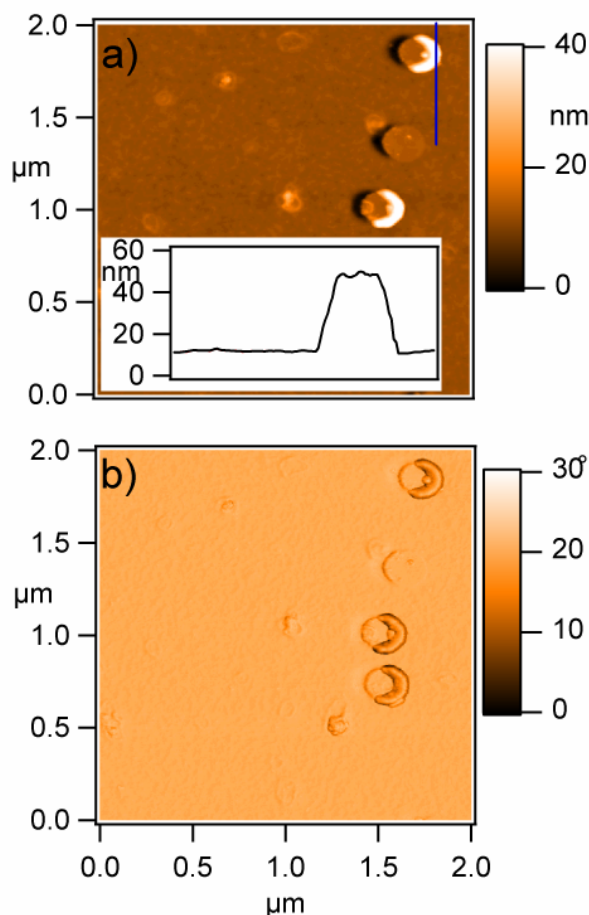


Figure 2-7 Tapping mode AFM topography (a) and phase (b) images of gold crescent shaped nanoparticles on glass. A height profile of the nanoparticle and substrate (along the indicated vertical line) is presented in the inset.

The topographic images reveal that the height of the polyelectrolytes goes up for the nanoparticles and for the kind of circular islands the polyelectrolytes form on the glass substrate upon the immersion in the PE solutions. These facts allow to estimate the increase of thickness per bilayer, which is about 4 nm per PAH/PSS cycle, up to 3 bilayers. The adhesion of material on sites not corresponding to the particles themselves might be due to electrostatic interactions between a negatively charged glass surface and the positively charged PAH, leading to the formation of the growing polymer islands. For seven and more deposition cycles (Figure 2-8 d. and Figure 2-8 e.), the phase images reveal that the whole sample is fully covered by the same material (polyelectrolytes), so that the localization of the nanoparticles is only possible by means of height measurements with the AFM.

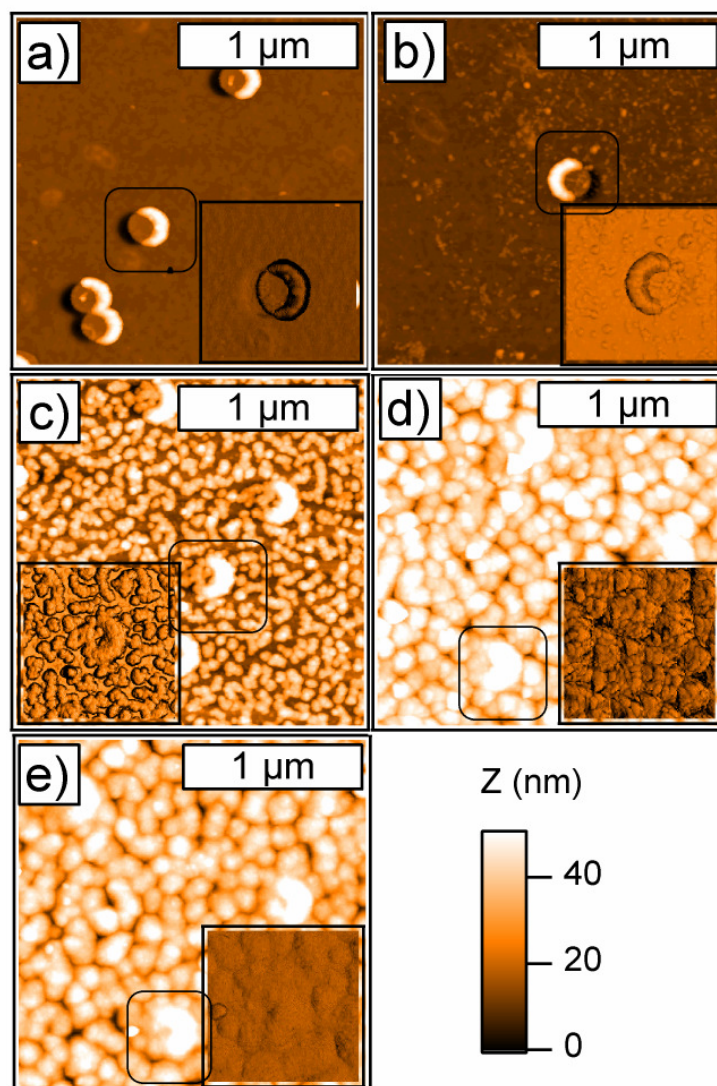


Figure 2-8 AFM topography and phase of samples with nanocrescent structures treated with 3-MPA, as a function of the number of times dipped in polyelectrolyte solutions (PAH+PSS): a) 0 bilayer; b) 1 bilayer; c) 3 bilayers; d) 7 bilayers; e) 9 bilayers. The vertical scale is 50 nm in all cases. The insets present the phase image of the selected area from the topographic image.

3-APTES silanized samples

After the silanization process of the samples, the APTES is covalently bonded to the glass forming a rather smooth monolayer on the substrate (RMS = 0.5 nm in the areas without crescents). The APTES carries a positively charged amino function, on which the negatively charged PSS can electrostatically attach, and subsequently multiple bilayers, grown. When adding the bilayers, the height profile images (Figure 2-9) shows that the relative height of the nanostructures with respect to the surface is not changed (always 35 nm approx.). By looking at the phase image of a sample only treated with the silane (Figure 2-9a) and to other silanized samples with 2 and 4 polyelectrolyte bilayers (Figure 2-9 b and c, respectively), a change in the phase on

the different components can be clearly noticed, which indicates that the PSS and PAH system is attaching to the silanised glass as well as to the gold crescents.

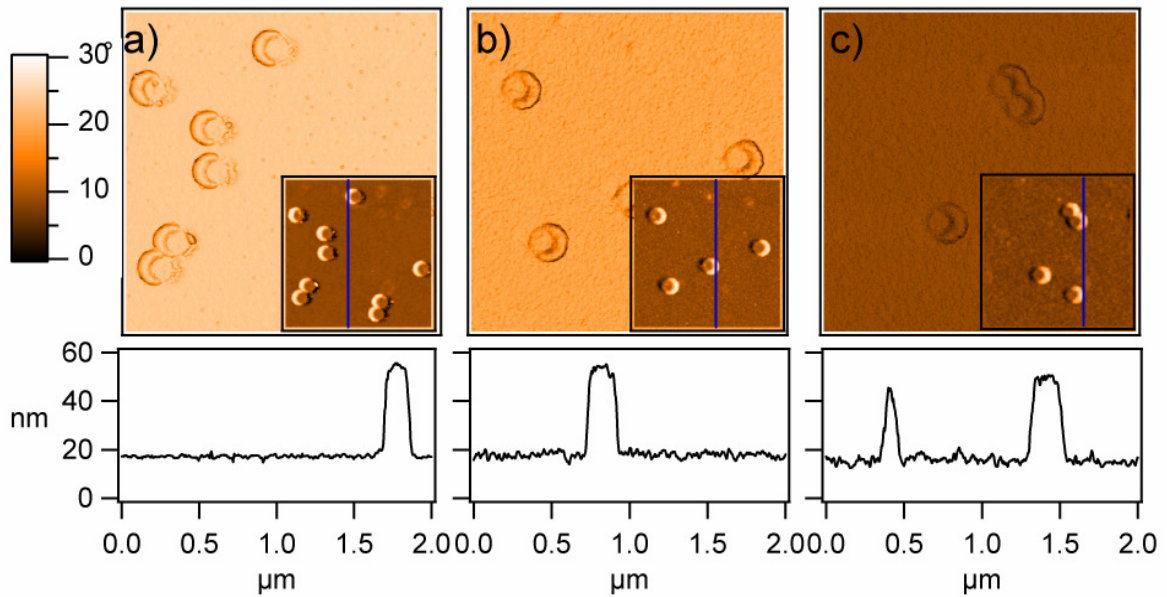


Figure 2-9 Tapping mode AFM phase images (top) and section profiles (bottom) for samples treated with APTE and with 0 (a), 2 (b) and 4 (c) bilayers of polyelectrolytes. All the images have the same z-scale. Their corresponding topographic images are presented in the insets.

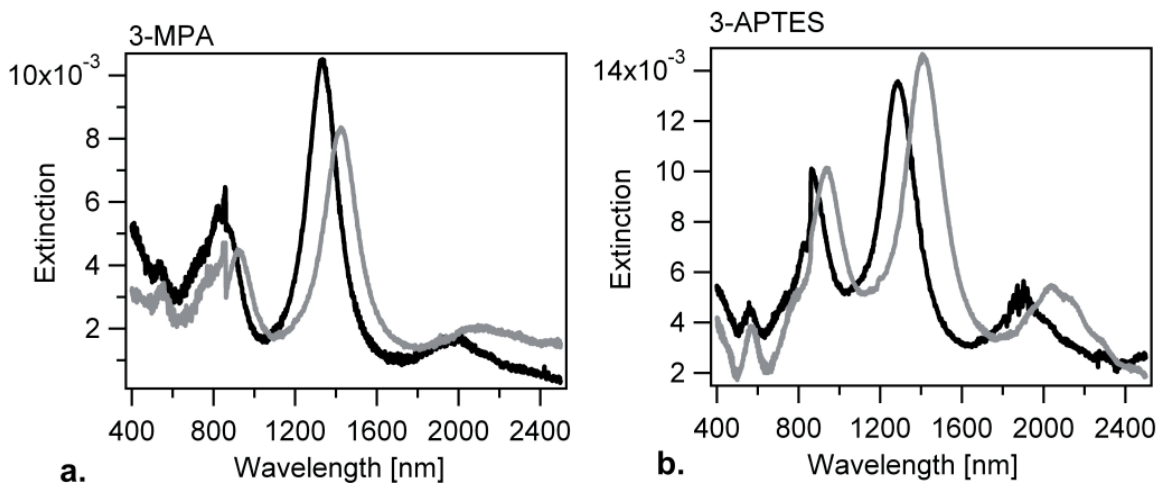


Figure 2-10: extinction spectra before (black) and after (grey) the attachment of 3-MPA (a.) and of 3-APTES (b.) and 3 polyelectrolyte bilayers.

Figure 2-10 (a.) and (b.) present the extinction spectra of crescent shaped nanoparticles before and after the surface functionalization and polyelectrolyte attachment. The displacements of the resonances are comparable in both cases, showing as indication that the attachment of the polyelectrolytes on the structures is in both cases comparable. The topographies are, on the contrary, quite different. The silanization procedure gives rise to a thorough, smooth coverage of the samples,

while the thiol functionalization results in a coverage of the gold structures, but rather appears to form agglomerations on the rest of the sample.

Since the optical response of the crescents is comparable in both cases, the use of one or another functionalization approach will be determined by the application; i.e. where a full coverage on the whole surface is needed, APTE will be the choice.

The thiol approach, faster and simpler than the silane one, will be the common approach for following experiments involving PE attachment to the metallic nanoparticles, unless otherwise specified.

2.4 Surface tailoring II: surface modification for the study of bio-recognition events

A second approach to add chemical functionality to the samples was explored, in this case, a conventional biotinylation procedure and further binding of streptavidin. These procedures are of fundamental importance for further studies on the sensitivity of the metal nanoparticles to bio-recognition events.

In this section, the materials and procedures used for further bio-recognition test that will be presented and used throughout this work are introduced.

2.4.1 Biotinylation

The Au and Ag nanocrescents supported on a glass slide were incubated during 8-10 hours in an ethanolic solution containing a binary mixture of a biotin-terminated thiol (12-mercaptododecanoic-(8-biotinoylamido-3,6-dioxaoctyl)amide) (Aldrich) and a hydroxy-terminated thiol (11-mercaptoundecanol) (Aldrich) in a 1:9 ratio. This particular composition provides the optimum coverage of biotin centers for obtaining maximum streptavidin (SAv) binding, as reported by Spinke et al [Spinke et al. 1993] and López and-coworkers [Pérez-Luna 1999]².

2.4.2 Streptavidin (SAv) attachment

The bioconjugation of SAv (Aldrich) was accomplished by placing the biotinylated substrates in 1 μ M SAv (in 0.1 M phosphate buffered saline “PBS”) during 2 hours followed by extensive rinsing with ultrapure (Milli-Q) water.

2.4.3 Bioconjugation of the SAv-modified Au nanoparticles (SAv-AuNPs)

The glass-supported biotinylated Au and Ag nanocrescents were immersed during 2 hours in a SAv-NP suspension (0,01 M phosphate buffered saline

² This procedure was optimized originally for gold surfaces, but will be applied here both for Au and Ag nanoparticles

(PBS), pH 7.2, 1% bovine serum albumin (BSA), 20 % glycerol, 15 nM sodium azide; $\sim 2.5 A_{520}$ units/m³) commercially available from Sigma Aldrich. The size of the Au NP was 10 ± 2 nm. After the incubation in the SAV-NP solution the samples were carefully rinsed with ultrapure (Milli-Q) water.

2.5 Summary

In the last two sections several simple and versatile surface treatments were introduced, first, to build up thin polyelectrolyte layers on the metallic nanostructures and the substrate, and second, to bind SAV-terminated species to the nanoparticles.

The different surface chemical functionalization to build the polyelectrolyte layers gave comparable results in terms of optical properties; a further selection of a method in particular will be based in the surface morphology desired for each experiment.

The biotinylation and bio recognition schemes were briefly introduced as an extension of the fabrication techniques / surface functionalization procedures.

All the methods presented here have a general character and can in principle be applied to other nanoparticles bound to a substrate.

³ A_{520} corresponds to the absorption at 520 nm for a calibrated solution (Aldrich). No further data is available on the product description available online to date.

3 . Understanding resonances

Crescent-shaped metal structures show interesting resonances in the near infrared part of the spectrum [Rochholz 2005]; which can be measured as strong extinction peaks in conventional UV-Vis/NIR transmission spectroscopy [Shumaker-Parry et al. 2005]. In order to understand and control these optical resonances, a thorough study on crescents with different geometrical characteristics was carried out [Rochholz et al. 2007]

In this chapter, a brief summary on previous [Rochholz 2005] and new results on the optical properties crescent shaped nanostructures is presented, along with a qualitative interpretation of the measurements.

Section 3.1 deals with the optical response of isolated particles prepared on glass substrates. Section 3.2 summarizes first results on close-packed arrangements of nanocrescents. Finally, the conclusions extracted from both approaches are presented.

3.1 *Isolated particles*

Crescent shaped nanoparticles can be described, in terms of geometry, via the mask size (d_{coll}), deposition angles (θ_i), rotation angles for multiple metal deposition processes (φ_j), metal thickness (t) and etching angle (ε).

Previous studies [Rochholz 2005] have shown that the crescents' contour length plays a fundamental role in the occurrence of the different resonant modes. The latter can be tailored by changing any of the geometrical parameters already introduced. In order to study systematically the influence of the contour length of the nanocrescents on their resonances, a simplified approach is presented. Structures produced with the same colloidal masks (equal size) and varying opening angles (φ_j) were produced, leaving all other parameters constant (t, ε, θ_i).

3.1.1 Varying ϕ structures

Sample preparation

The experiments presented in this first approach correspond to structures produced using 200 nm colloids, gold as a material, $\theta = 30^\circ$, $0^\circ < \phi_j < 160^\circ$ and 2 metal depositions, 20 nm thick each. All samples were etched using with an Ar ion-beam perpendicular to the substrate ($\varepsilon = 0$).

Table 3-1 displays a summary of the cases presented in this work

ϕ	Structure	
0 (1 metal deposition)	Crescents	Bocchio
40 (2 metal depositions)		Extracted from the PhD thesis by H. Rochholz [Rochholz 2005]
60 “		
80 “		
100 “		
120 “		
140 “		Bocchio
160 “		
180 “		
3 metal depositions at 0° , 120° and 240°	Symmetrical rings	

Table 3-1: geometrical configurations of crescent shaped nanoparticles

Characterization

Extinction spectra of the particles produced on glass substrates were recorded in an UV-Vis-NIR spectrometer equipped with polarization optics (*Perkin-Elmer, Lambda 900*) operating in transmission mode. Scanning electron micrographs were recorded on a Leo Gemini electron microscope, model 1530.

Figure 3-1 presents a sketch of the particles' geometry, and their orientation relative to the incident electric field component for polarized-light transmission measurements. In the following, these excitation conditions will be referred to as “**u**”,

when the light is polarized parallel to the symmetry plane of the particles, and “**c**” in the perpendicular case. The structures can be read as the letters “**u**” and “**c**” for these two combinations.

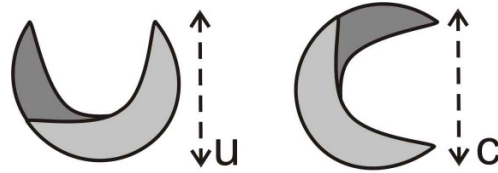


Figure 3-1: sketch of the “u” and “c” polarizations; the dashed arrow represents the electric field

Results and discussion

Figure 3-2 presents the extinction spectra of samples with prepared $\phi = 0^\circ, 40^\circ, 60^\circ, 80^\circ, 100^\circ, 120^\circ, 140^\circ, 160^\circ$ and 180° , for both **c** and **u** polarizations (a. and b.), and for non-polarized light (c.). For easier understanding and visualization, Figure 3-3 presents scanning electron micrographs of some representative structures with $\phi = 0^\circ, 120^\circ, 140^\circ$, and 180° .

A naming code for the strongest resonances is assigned based on the dataset corresponding to $\phi = 120^\circ$ (see Figure 3-2). It is composed namely by the polarization condition (**c** or **u**), and the order of occurrence of the peaks in the spectrum (lower numbers for lower energy resonances).

As it is evident from the measurements, the particles exhibit completely different extinction spectra upon illumination with light polarized parallel and perpendicular to the symmetry plane of the structures. The discussion and interpretation of the data will be focused on the strong, reproducible features like **c1**, **c2**, and **u1**. Further considerations on the weaker features (**w1**, **w0**, **pp**) will be done following the latter.

Structures with large gaps

Figure 3-2 presents polarized (a. and b.) and non-polarized (c.) extinction spectra of crescent shaped samples prepared with two metal evaporations, ϕ ranging from 0° to 180° . All samples measured with **u** polarization present one main peak that evolves

from approximately 800 nm on into the infrared, for increasing φ . This resonance is termed **u1**. A second resonance is present at roughly 550 nm, but it does not seem to shift significantly.

For the **c** polarization, 2 main peaks are detectable, which also red shift systematically upon closing the gap in the structure. These considerations hold up to $\varphi = 120^\circ$. These resonances are termed **c2** and **c1**. A third weak peak is also detectable at about 500 nm that, as in the case of the **u** resonance, does not seem to red shift significantly upon the gap closing of the nanostructures.

The non-polarized measurements (see Figure 3-2 c.) are a combination of the results for the two main polarizations. Within experimental accuracy, the extinction $E(\varphi)$ for an arbitrary angle δ of the polarization of the incident light relative to the long axis of the crescents follows:

$$E(\delta) = E_U \sin^2(\delta) + E_C \cos^2(\delta)$$

with the extinctions E_U and E_C as obtained for **u** and **c** polarizations [Rochholz 2005]. This shows that the microscopic symmetry of the sample directly translates in a macroscopic response and no further effects due to an imperfect sample preparation or experimental artifacts are observed.

Structures with small gaps

The spectra measured for “small-gap” structures ($\varphi > 120^\circ$) with **c** polarization changes qualitatively from the “large-gap” cases. A new double peak structure emerges around 1070 nm, and a peak appears around 1900 nm, which does not fit in the progression of the increasingly red-shifted **c** peaks. This behavior can be interpreted as being due to the two tips starting to interact optically at $\varphi = 140^\circ$ (see Figure 3-3).

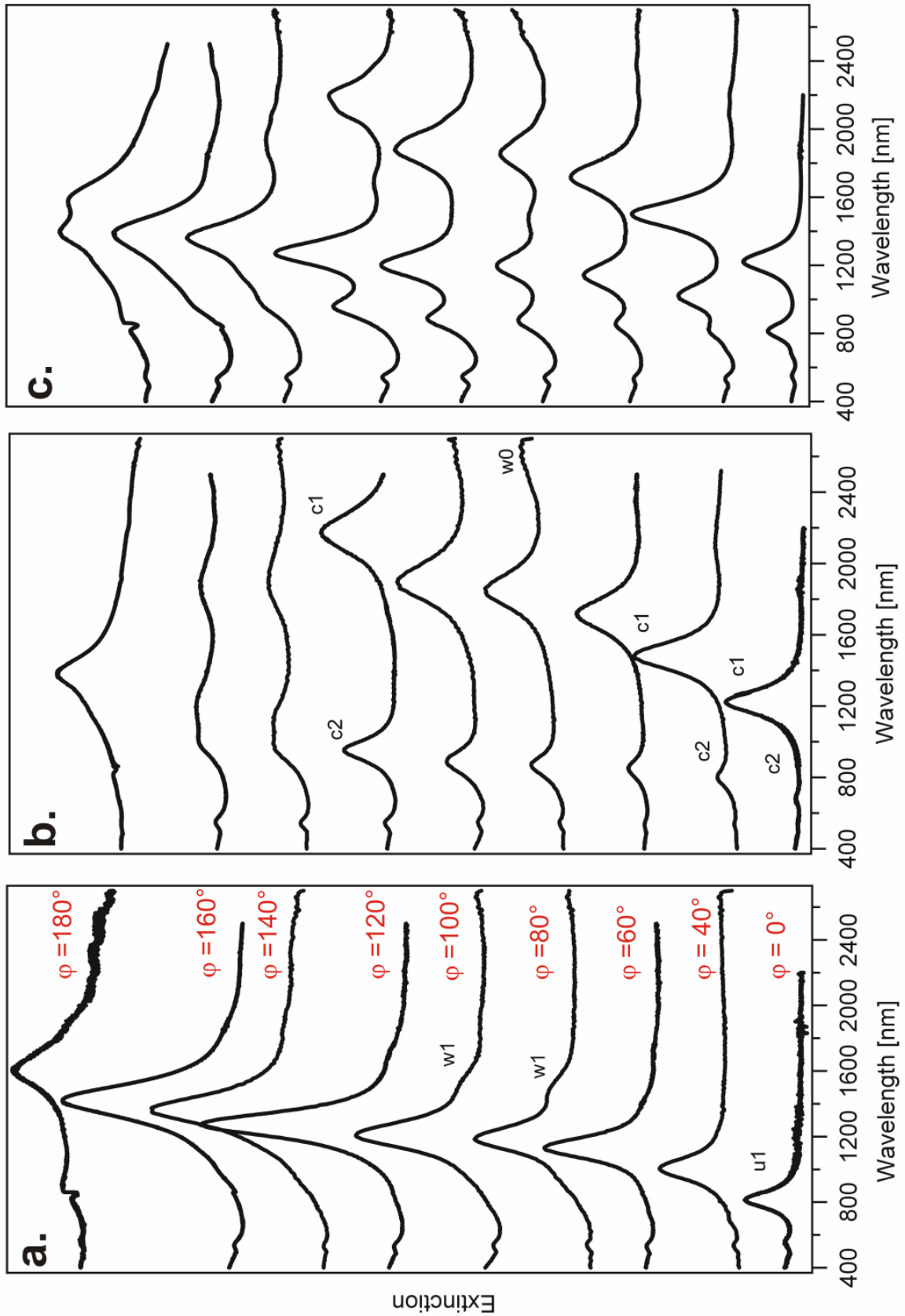


Figure 3-2: Extinction spectra for varying crescent opening, produced by double evaporation (φ) as indicated in Fig. 1. The diameter of the masking colloid and the film thickness were held constant at $d_{\text{coll}}=200$ nm and $d_{\text{Au}}=2 \times 20$ nm respectively. a), b) and c) show extinction spectra recorded with u-polarized, c-polarized and non-polarized light, respectively.

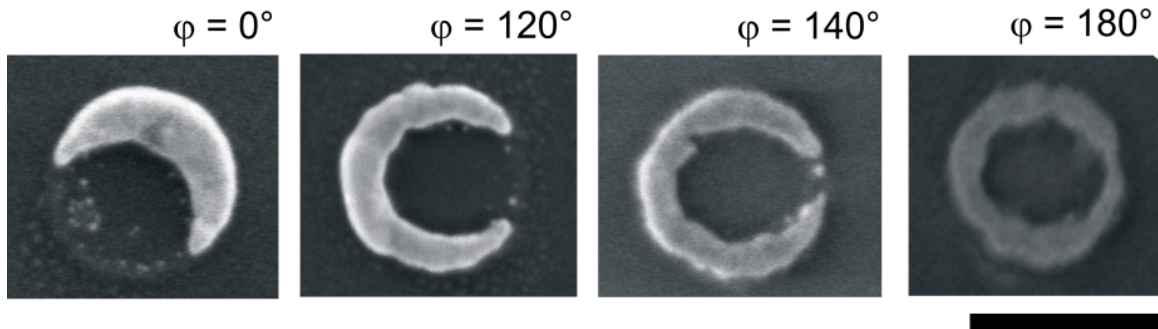


Figure 3-3: crescent shaped nanoparticles produced by multiple metal depositions, with different φ_j , with exception of the first ($\varphi = 0$, 1 deposition). The scale bar represents 200 nm.

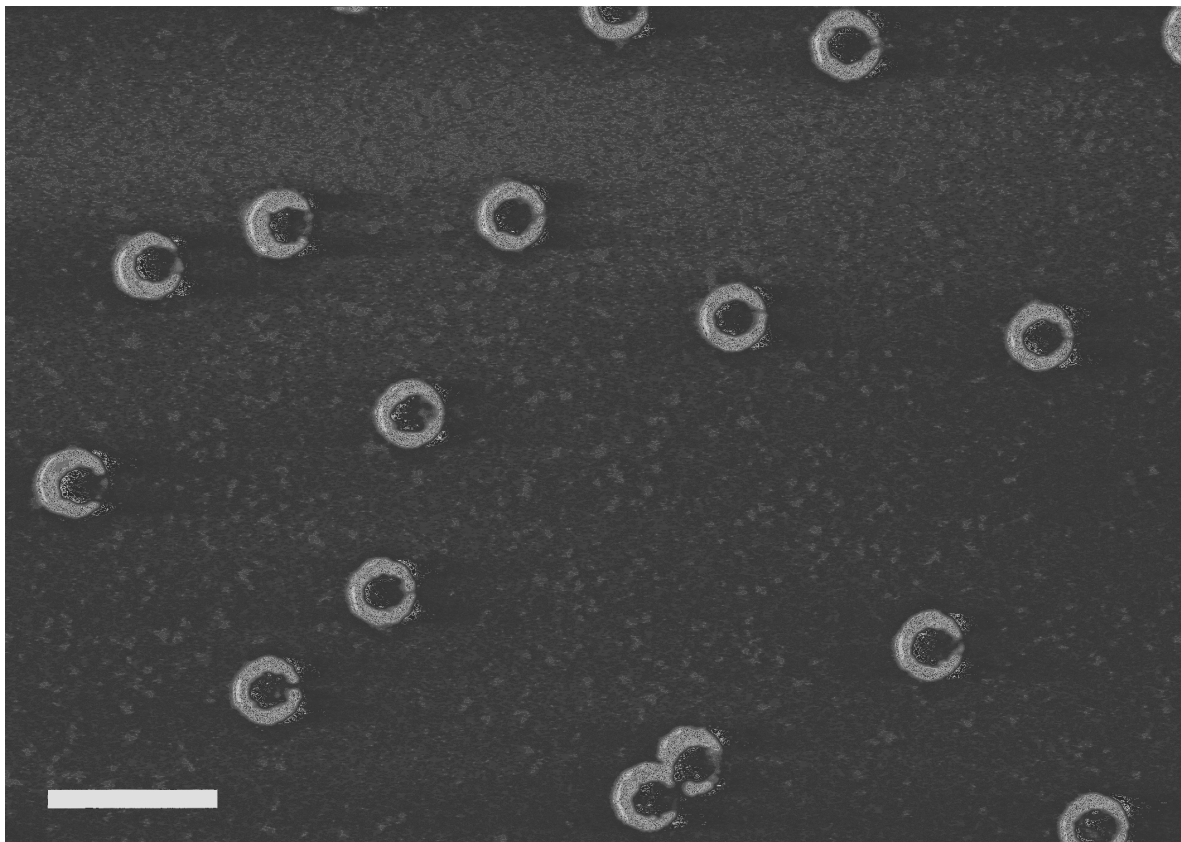


Figure 3-4: Representative scanning electron micrographs of crescents prepared with φ : 140° . (d_{coll} : 200 nm, t_{Au} : 20nm+20nm). The scale bar represents 500 nm.

The response obtained for $\varphi = 140^\circ$, where for perfect samples a very small gap is expected, and for $\varphi = 160^\circ$ (where the gap is expected be closed from geometrical considerations) are similar, but do not fit in the continuous evolution of the structures with large gap. For the symmetric structure obtained for $\varphi = 180^\circ$, again a qualitatively different behavior is observed, where for each polarization one strong peak is detected.

Figure 3-4 presents a scanning electron micrograph of a $\phi=140^\circ$ sample. The majority of the crescents still appear to have a small open gap but apparently sufficiently close tips already interact, dominating the optical response of the entire structure. No effect of gap closing is seen in the extinction spectra for **u**-illumination. This can be understood based on the symmetry of both illumination conditions and the crescents. Upon illumination with **u**-polarized light the tips of the structure are equally charged at any time and at the gap no current flows. As a result, no drastic effect on the resonances is observed and the spectra for $\phi = 160^\circ$ are very similar to the ones obtained for $\phi = 140^\circ$. Scanning electron micrographs of these two samples show in both cases a majority of ring-like structures that still exhibit a small gap.

For $\phi = 180^\circ$, closed structures with two symmetry planes are obtained. They exhibit an optical response which is again qualitatively different from the ‘almost connected’ ring structures obtained with $\phi = 160^\circ$ and $\phi = 140^\circ$. Only one characteristic resonance peak for each polarization is observed at 1419 nm for **u** and at 1377 nm for **c** polarizations, which resembles the response of ring-like structures [Aizpurua, Hanarp, Sutherland, Käll, Bryant and de Abajo 2003]. The fact that both resonances do not appear at the same wavelengths when excited in either the **c** or **u** conditions reflects the fact that by double evaporation still no rotational symmetry is obtained (see Figure 3-3). An extra shoulder is observed in the 800 nm range for the **u** polarization measurement performed on this sample, related most likely to the u_1 resonance of the single crescents.

Structures that almost exhibit rotational symmetry are obtained when three metal layers are deposited on top of the colloidal mask with equal angular spacing in between deposition steps ($\phi = 0^\circ, 120^\circ, 240^\circ$). Extinction spectra measured on such structures for the two main polarizations and for non-polarized light are shown in Figure 3-5. The higher symmetry of the particles gives rise to almost identical spectra. When considering this structure, it is possible to identify this resonance with the dipolar resonance on ring-shaped metal objects as discussed by Aizpurua et. al [Aizpurua, Hanarp, Sutherland, Käll, Bryant and de Abajo 2003] with a charge distribution as sketched in Figure 3-5 c). This resonance, the one with the lowest order possible, allows in turn for an ordering of the other strong features, once these are separated by means of polarization measurements.

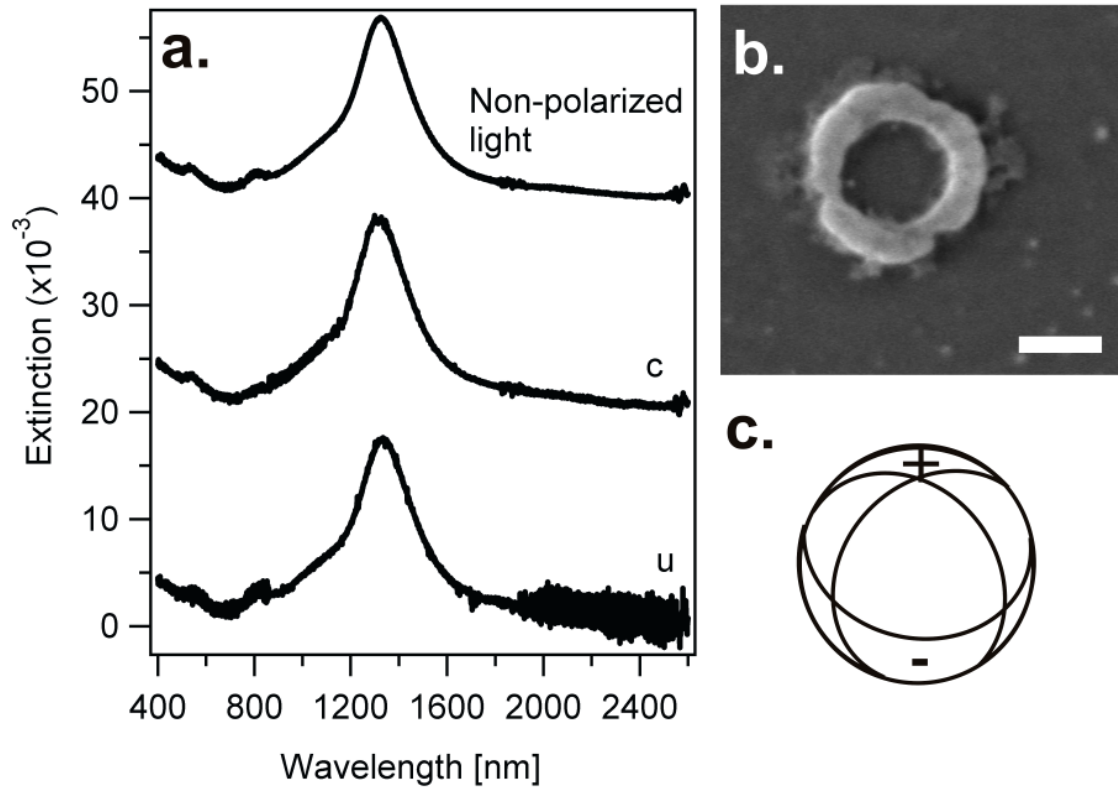


Figure 3-5: a) UV-Vis extinction for non-polarized, c polarized and u polarized light of a structure that was obtained by a triple evaporation routine with (φ : 0° , 120° , 240° , $t_{Au}=3 \times 20$ nm, $d_{coll}=150$ nm colloids); (b.) corresponding scanning electron micrograph (c) Sketch of the structure as produced and of the proposed oscillating charge distribution of the resonance

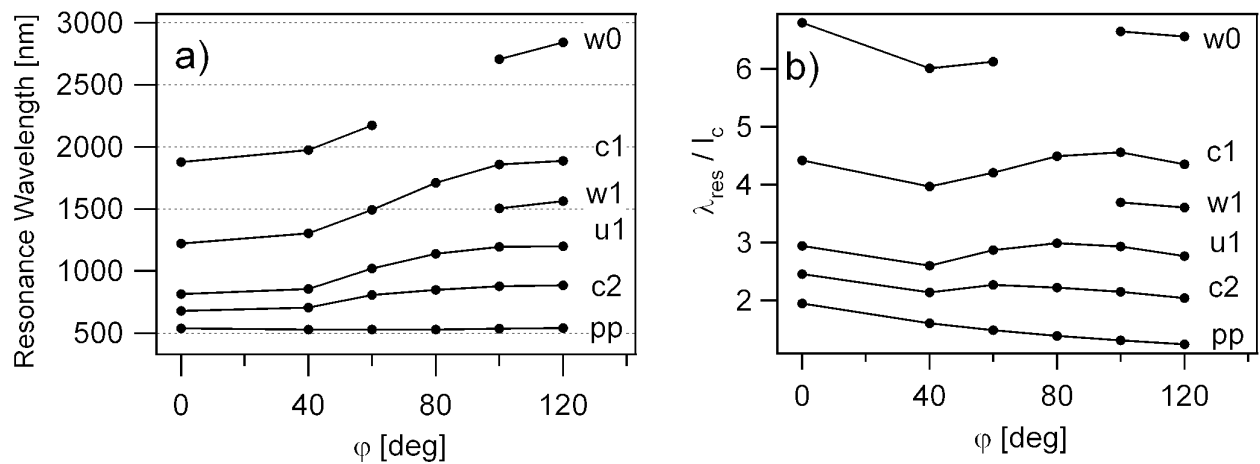


Figure 3-6: influence of crescent contour length on the optical resonances. a) Resonance wavelengths for a range of rotation angles φ as indicated in the graph. b) Resonance wavelengths (λ_{res}) normalized by the contour length (l_c) of the crescent; see text for details.

Data analysis

The peaks' positions and widths can be determined from fitting Lorentzian curves to the measured extinction spectra. This method has been proven the most suitable one in terms of minimal error (see details in Appendix C and [Rochholz et al. 2007]). This fact is particularly important because it implies that, in spite of investigating an ensemble of particles, the major contribution to the finite width of the measured maxima is due to the lifetime-limited line width of the resonances. These results imply that the line widths as obtained from the fits are a true physical property of the observed resonances.

Multiple resonances in nanocrescents – Interpretation

Peak positions as determined from fitting procedures for structures with large gaps ($\varphi \leq 120^\circ$) are displayed in Figure 3-6 (a.). Apart from the **pp** resonance, all maxima appear clearly red shifted with increasing rotation angles (φ) in between deposition steps.

The simplest geometrical approximation for a crescent is a rectangular slab, a case that has been thoroughly studied in the past [Krenn, Schider, Rechberger, Lamprecht, Leitner, Aussenegg et al. 2000; Schider et al. 2003] The resonances excited along the slab can be interpreted as standing waves along the structure, formed by a superposition of a forward and a backward propagating mode of an infinitely extended stripe. For narrow structures only one fundamental propagating mode, analogous to the zero-order mode in dielectric waveguides is supported for a specific wavelength. This phenomenon allows for the determination of the dispersion relation of this mode by assigning the proper integer number of nodes for the observed standing wave resonances [Puscasu et al. 2001; Schider et al. 2003].

In a simplified slab model, a resonance occurs whenever the resonance condition

$$n \frac{\lambda_s}{2} = L$$

is fulfilled, n being the order of the resonance, L the length of the supporting metal structure and λ_s the wavelength of the supported mode. Although the crescents under investigation are clearly different from a rectangular slab since they are both

bent and do not possess a constant width of the metal, comparison of these two cases provides first physical understanding of the resonances. First evidence that the description as slabs even provides quantitative information is rationalized by normalizing the experimentally observed resonance wavelengths by the contour length l_c of a crescent, approximated by

$$l_c = \frac{d_{coll}}{2}(\alpha + \varphi)$$

where d_{coll} represents the diameter of the mask, α and φ are geometrical parameters introduced in the previous sections. This quantity is identified with the length L of the model slab. If the dispersion relation $\omega(\mathbf{k})$ for the guided modes is linear in the frequency regime under consideration, the quantity λ_{res}/l_c is expected to be constant. A detailed plot of this quantity for the measured resonances is shown in Figure 3-6 (b.). An approximately constant value for λ_{res}/l_c is seen for the **u1** and **c1** resonances, while the short-wavelength resonance **c2** shows a slight deviation from this behaviour. The resonances at $\varphi=140^\circ$ and beyond are not considered since here gap closing, a clear topological change occurs. The **pp** resonance is included for comparison. Its resonance wavelength is fairly independent of φ ; as a consequence, the quantity λ_{res}/l_c exhibits a clear and regular decrease, according to the increase in the particles' contour length. A dispersion plot can be constructed calculating the wave vector \mathbf{k} and the angular frequency ω , as follows:

$$k = \frac{2\pi}{\lambda} = \frac{n\pi}{l_c} = \frac{n\pi}{\left[\frac{d_{coll}}{2}(\varphi + \alpha) \right]} = \frac{2n\pi}{d_{coll}(\varphi + \alpha)}$$

$$\omega = 2\pi\nu = 2\pi \frac{c}{\lambda_{res}}$$

The order n of the resonances can be deduced from the observation that **u1** is continuously transformed into the dipolar ring resonance upon gap closure. Thus, **u1** is identified with the charge distribution corresponding to $n = 2$ as sketched in Figure 3-7. Then, **c1** and **c2** can be assigned to $n = 1$ and $n = 3$, respectively. In order to

excite these resonances, the electrical field vector must be parallel to the net polarization of the crescents in perfect agreement with the experimental observation.

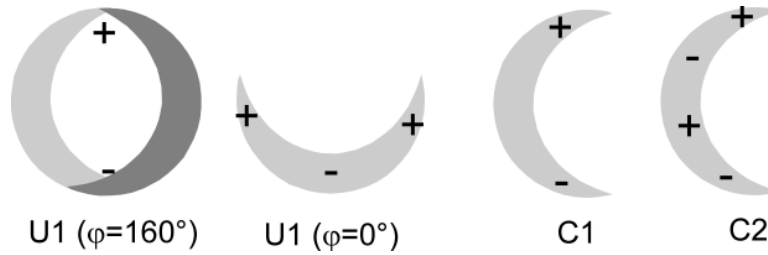


Figure 3-7: Sketch of charge distribution for the resonance on a closed ring and the three strongest resonances of open crescents.

Using these values for n , the dispersion curve shown in Figure 3-8 is constructed. The behaviour of **c1** ($n=1$), **u1** ($n=2$) and **c2** ($n=3$) is in good agreement with a dispersion curve as it was discussed for the rectangular slab [Schider et al. 2003], thus providing a very good description of the three strongest resonances.

While the slab model applied fails to describe the **pp** resonance, a simple interpretation will be given based on the experimental data discussed below. It must be noted that the description in terms of standing waves on a slab with two non-interacting ends is restricted to large-gap geometries ($0^\circ \leq \varphi \leq 120^\circ$), it is neither applicable for the ‘small gap’ ($140^\circ \leq \varphi \leq 160^\circ$) nor for the fully symmetric structures ($\varphi = 180^\circ$).

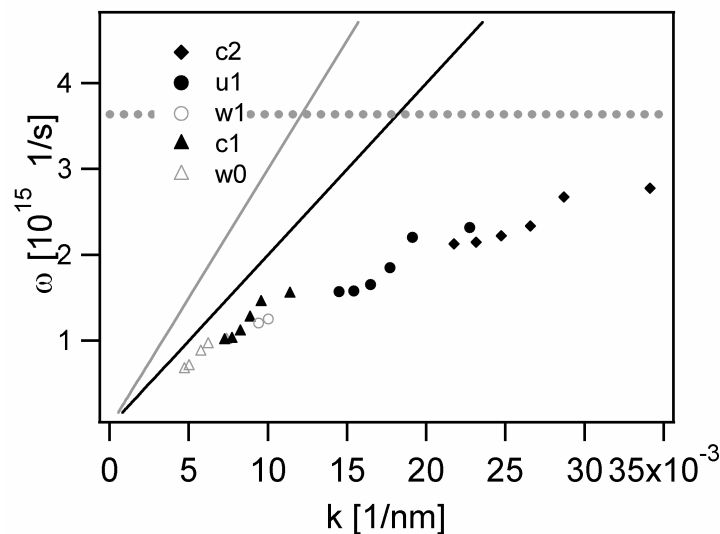


Figure 3-8 : dispersion plot $\omega(k)$ for five resonances. The dotted line indicates the limiting frequency for surface plasmons on plane substrates.

The weaker w_0 and w_1 resonances cannot be described in this simple picture. These resonances would follow the same dispersion curve if the non-integer orders n (w_0) = 0.65 and n (w_1) = 1.3 were assigned; remarkably these numbers differ by a factor of two.

The structures with $\varphi_i > 0$ were all prepared in two evaporation steps. The resulting strength of w_0 is quite variable as can be seen in Figure 3-9. It is possible to note furthermore that the strength of w_1 is correlated with the one of w_0 . This may suggest that w_0 and w_1 are based on a physical effect that is somewhat different from the effect leading to the other, stronger maxima, probably, colloid aggregation and the resulting optical interaction of crescents plays some role for these features.

The weaker (w_0 / c_0) resonance - a colloid aggregation problem?

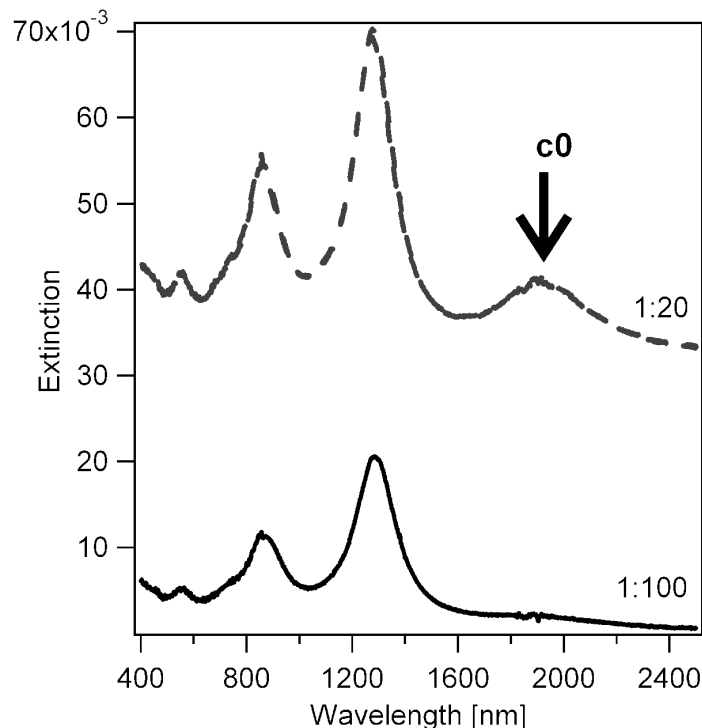


Figure 3-9: Extinction spectra of two independent samples, prepared on the same manner, but using two different concentrations of colloids for the mask

Figure 3-9 presents extinction spectra of *standard* gold crescent shaped nanoparticles, made with the same geometrical characteristics, but using 2 different colloidal masks concentrations (1:100 and 1:20, [v/v]), freshly prepared. The use of a suspension with higher concentration of colloids gives rise to a significative increase in the relative intensity of w_0 , which appears at roughly 2000 nm in the spectrum.

This phenomenon is also polarization dependent and can only be observed for the c condition (w_0 can also be termed as c_0 – see Appendix B for an example).

A simple explanation to this fact would be given by an agglomeration of colloids; the use of freshly prepared, very diluted suspensions (i.e., 1:100), although reducing the overall signal, would diminish the probability of agglomeration of the colloids and the occurrence of this effect on the samples. Since this effect appears related to preparation conditions more than being an intrinsic property of the samples, it is considered to be an artifact in the measurements and having no physical relation to true resonances of the crescent nanoparticles⁴.

3.1.2 Metal thickness (t)

It has been observed previously that the metal thickness does not seem to play a fundamental role in this system, in terms of new resonances [Rochholz 2005] but it rather contributes as a tailoring factor in terms of spectral occurrence of the main modes. Thicker structures have been observed to give rise to more blue shifted resonances in other systems [Willems and Van Duyne 2007]; a similar effect has also been observed for the crescent shaped nanoparticles [Rochholz 2005; Rochholz et al. 2007].

3.1.3 Colloidal size (d_{coll})

The overall size of the crescent shaped nanoparticles can be controlled by changing the size of the colloids used as a mask. A thorough size-dependent study, for other constant geometrical parameters ($\varphi = 0$, $\theta = 30^\circ$, 1 deposition, Au, 40 nm thickness) has been carried out previously [Rochholz 2005]: The data has been reproduced here for clearer understanding, see Figure 3-10. As an empirical trend, a linear dependence of the peak wavelength on crescent diameter is observed [Rochholz 2005]⁵, the data appear to lie close to lines that intersect for decreasing crescent

⁴ A similar contrast was observed for structures prepared with two metal depositions, and no rotation in between steps ([Rochholz, H., N. Bocchio, et al. 2007] Rochholz, H., N. Bocchio, et al. (2007). "Tuning resonances on crescent shaped noble metal nanoparticles " *New Journal of Physics* **9**(53)., compared to structures prepared with one metal deposition. In that case, no specific correlation with the colloid concentration of the mask was studied, and the samples were prepared in separate batches, so an effect of the thickness, colloid aggregation or contamination in between metal deposition steps cannot be directly ruled out from the measurements.

⁵ The colloid size (d_{coll}) presented in these measurements corresponds to the nominal size provided by the manufacturer (Polyscience). This data should only be used as a general indication of size, since significative deviations can occur in reality (see Appendix C).

diameters approximately at the particle plasmon wavelength (530 nm). In this case it is not possible to collapse the resonance frequencies as obtained from crescents with varying diameter on the same dispersion curve. This can be understood since upon increasing d_{coll} , both the contour length l_c and the width w of the crescent are increased while variations in ϕ only change l_c while keeping a constant crescent width. Normalization by the contour length Figure 3-10 c) suggests a decrease in the wavelength of guided modes with increasing width w of the structures.

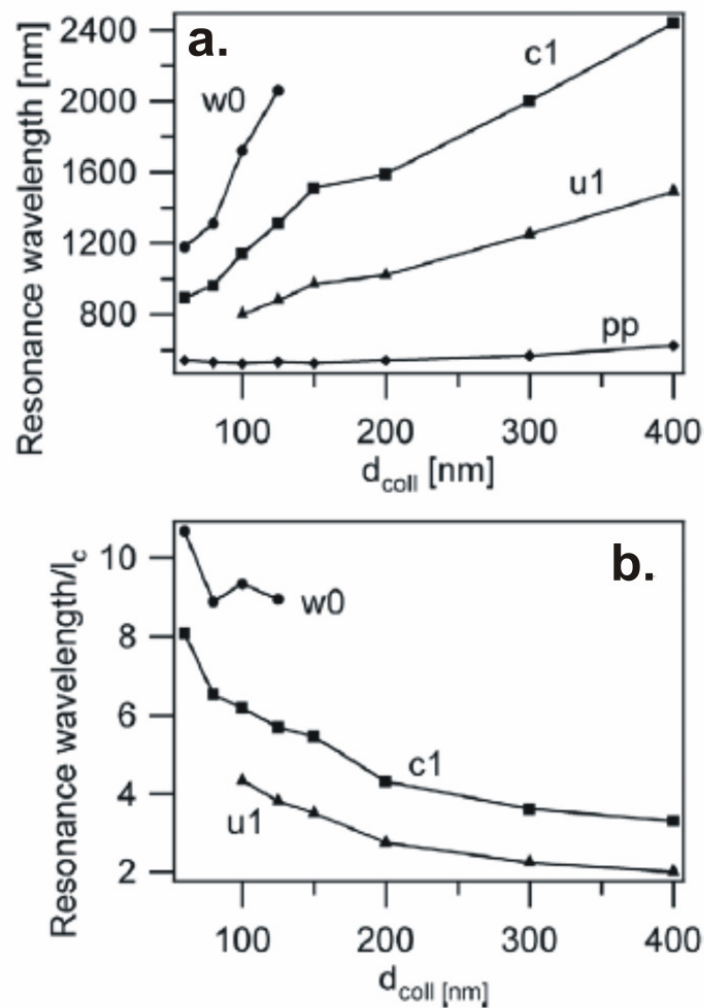


Figure 3-10: (a) Peak positions as a function of colloid diameter. (b) Peak wavelength normalised by l_c [Rochholz et al. 2007].

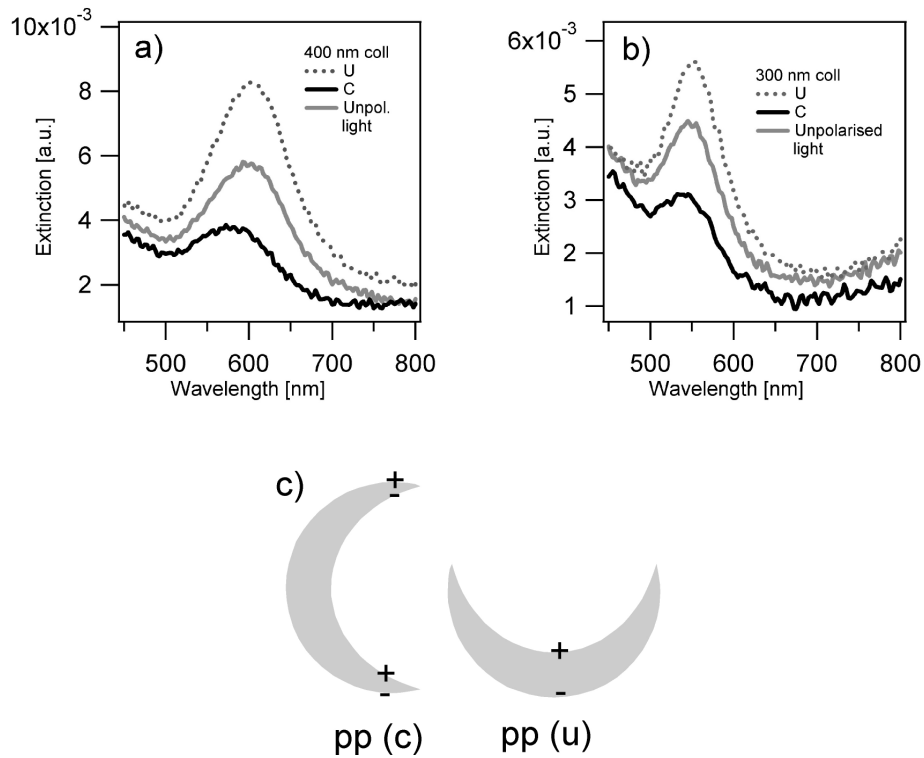


Figure 3-11: a), b) pp resonance for $d_{\text{coll}} = 400$ nm and $d_{\text{coll}} = 300$ nm (c) Sketch of the polarization of a resonance which is perpendicular to the rod for the two fundamental polarizations [Rochholz et al. 2007].

Furthermore, an apparent shift of the **pp** resonance to longer wavelengths is noted for increasing crescents' diameters in the size range explored, the shift being more pronounced for **u** than for **c** polarization. This is most clearly seen for the largest masks ($d_{\text{coll}} = 300$ nm, $d_{\text{coll}} = 400$ nm); the corresponding extinction curves are displayed in Figure 3-11. This observation points towards an interpretation for these maxima.

Locally, the crescents behave similar to a rod that supports, in addition to the standing waves along its long axis, resonances along its short axis. Such resonances are excited on the crescents for **u** and **c** polarizations predominantly at the positions indicated in Figure 3-11 c). As a consequence, **u** light excitation corresponds to resonances on a broader rod than **c**-light excitation, explaining the observed red shift (compare to [Schider et al. 2001]). Upon excitation with **c** polarized light only a weak maximum is present in agreement with the observation that in this case the $\varphi = 0^\circ$ crescent does not exhibit much portions where transverse resonances can be excited. A reinvestigation of the effect of a variable φ shows that the strength of **pp** in **c**-polarized extinction increases for increasing φ . This is intuitively clear since for a

more closed structure a longer portion can be described as a rod oriented perpendicular to the exciting electrical field in **c** – polarization.⁶

3.1.4 Metal deposition angle (θ_i)

In order to study the influence θ_i in the optical properties of the nanocrescents, standard crescent shaped nanoparticles were prepared with 3 different deposition angles, $\theta_i = 20^\circ$, 30° and 40° . The deposition angle should influence the width of the particles (see Chapter 2) considerably. According to the formula presented in Chapter 2 to estimate w (width of the particles), the widths should increase in a 1.4 and 1.8 factor for $\theta_i = 30^\circ$ and 40° , taking the $\theta_i = 20^\circ$ as a reference, which should in principle affect the u_1 resonance. Figure 3-12 presents the results for samples with $\theta_i = 20^\circ$, 30° and 40° .

No clear trend in peak position or width of the resonances is evident for this range of θ explored. All samples were prepared on the same batch, reason for which the influence of thickness variations in peak position/width is considered to be minimum.

Further atomic force (AFM) characterization⁷ (see Figure 3-13) of these structures shows no major geometrical differences among the structures, which explains the similarity of the spectra.

These measurements indicate then that the geometrical model for the estimation of the maximum width (w) does not fully describe the final shape of the structures, and should only be taken as an estimation. A possible explanation for the deviation from the model could be, i.e. extra sputtering from the etching step. This effect can be of considerable magnitude and has already been used by other authors to produce nanorings [Aizpurua, Hanarp, Sutherland, Käll, Bryant and Garcia de Abajo 2003].

For practical purposes then, and for this size range of the structures, a variation of θ_i does not play a fundamental role in the crescent's shape, and as a consequence, neither on the resonances' position or width. Further studies are necessary for larger masks and wider θ ranges.

⁶General remark - all data concerning size of the colloids bought from Polyscience corresponds to the nominal diameter provided by the manufacturer. These values should be taken only as a rough reference; since SEM images have shown deviations from these values (see Appendix C for further details).

⁷ AFM measurements can have a lateral resolution in the 5 – 10 nm range, which, though low, should be enough to detect differences of the order of 80% in 70 nm structures.

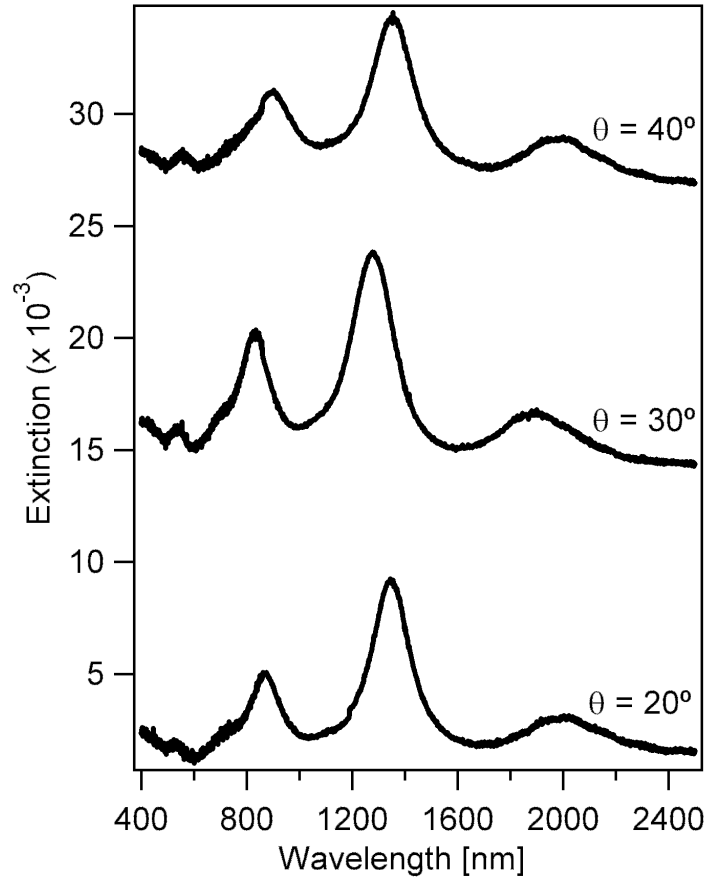


Figure 3-12: extinction spectra of *standard* crescent shaped nanoparticles prepared with $\theta_i = 20^\circ$, 30° and 40° . The curves have been displaced vertically for clarity.

	Resonance					
	C_2		U_1		C_1	
	λ_p [nm]	Width [nm]	λ_p [nm]	Width [nm]	λ_p [nm]	Width [nm]
$\theta=20^\circ$	714.4	60.6	868.8	71	1345	92
$\theta=30^\circ$	692	78	830	67	1280	104
$\theta=40^\circ$	755	83.3	900	86.2	1353.7	101

Table 3-2: peak position and width of the main resonances, as determined from lorentzian fits to the measurements

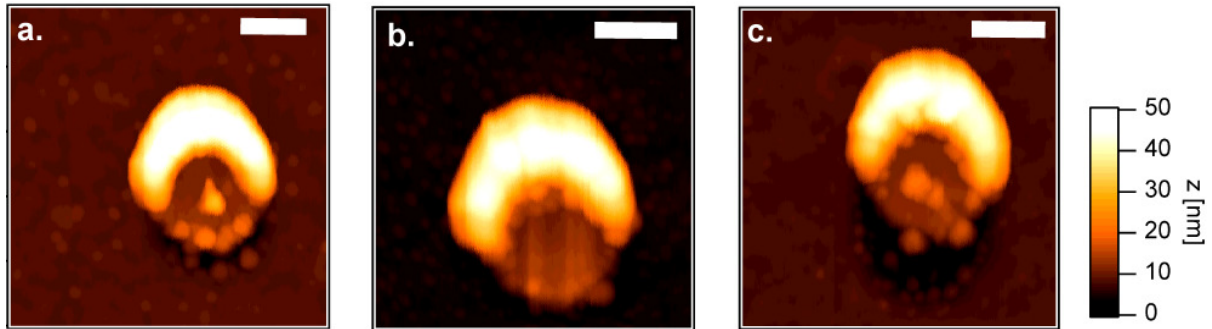


Figure 3-13: atomic force measurements, height AFM measurements of samples prepared with $\theta = 20^\circ$ (a.), 30° (b.) and 40° (c.). The scale bar represents 100 nm.

3.1.5 Etching angle (ϵ)

The etching was done perpendicularly to the surfaces in all cases presented here. The use of a $\epsilon \neq 0$ influences the final width of the structures since the colloids act as a mask protecting the metal behind them, if $\epsilon > 0$ [Rochholz 2005]. Since all studies were mostly focused on varying the contour length of the particles, this parameter was not further explored.

3.1.6 Materials

All nanostructures presented so far were produced using gold. In order to study the influence of a different material in the optical properties of the structures, *standard* crescent shaped nanoparticles were prepared using silver as metal⁸. Figure 3-14 presents the extinction spectra of particles prepared with gold (a.) and silver (b.).

In general, both spectra look very similar at first sight; all main resonances appear in similar spectral ranges.

Table 3-3 summarizes the information extracted from the extinction measurements for both Ag and Au structures, namely, peak position and width of the main resonances.

⁸ It has been discussed that for large particles, the main parameters to tailor resonances are size and shape [Murray, W. A. and W. L. Barnes 2007] Murray, W. A. and W. L. Barnes (2007). "Plasmonic Materials." *Adv. Mater.* **19**: 3771–3782.. The use of Ag is presented as an alternative to Au and the limiting size tailoring to blue shift the resonances of the crescents.

For the Ag nanostructures, peak positions for all resonances are blue-shifted with respect to the Au structures (some 60 to 90 nm, depending on the resonance). The width of the peaks does not follow the same trend, appearing in some cases broader as for Au. This could be related to different factors, i.e. surface roughness, oxide formation, etc.

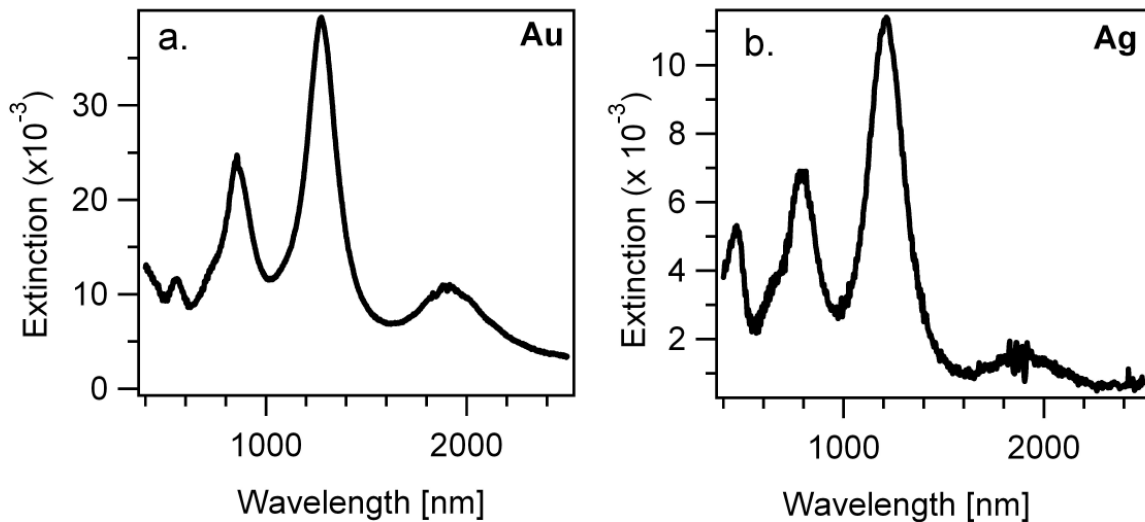


Figure 3-14: *standard* crescent shaped nanoparticles prepared using gold (a.) and silver (b.)

	Resonance					
	C ₂		U ₁		C ₁	
	λ_p [nm]	Width [nm]	λ_p [nm]	Width [nm]	λ_p [nm]	Width [nm]
Au	721	56	859	74	1278	91
Ag	636	52	791	104	1210	113

Table 3-3: peak position and width of the main resonances for standard crescent shaped nanoparticles produced using gold and silver.

The main drawback about the use of silver is that it is prone to be corroded and requires extra care in handling and storage, reason for which its use has been somewhat limited. Further studies should include the fabrication of nanocrescents with multiple deposition, to study the influence of the oxide formation in the fabrication process and the effect on the optical properties, a issue that remains an open question [Rochholz 2005].

3.2 Close-packed crescent shaped nanostructures

Metal nanostructures with small separation distances can show different optical properties than the isolated particles, some of which have proven most interesting for distance-sensing approaches [Sönnichsen et al. 2005; Jain et al. 2007]. From a practical point of view, substrates covered with a high density of particles on their surfaces can provide a fundamental technical advantage for applications, since, i.e. higher absolute absorption/scattering could be achieved or chip strategies for sensing platforms could be implemented. The same considerations hold when thinking of arrangements of nanocrescents as basic building blocks for negative refractive index / metamaterial applications.

All investigations presented so far on nanocrescents are based on particles well separated from each other (some hundred nanometers in between them). No systematic experimental data is available so far on coupled nanocrescents, save the earlier work of Enkrich et al. [Enkrich et al. 2005], producing arrangements of nanosplit resonators via e-beam lithography. In this section, a model structure consisting of close-packed arrangements of nanocrescents is compared to an isolated particle case, in terms of their optical properties. General considerations about the geometry of the particles, the fabrication method and the measurements are introduced, along with a qualitative comparison to other coupled-particle cases reported in the literature.

3.2.1 Experimental

In order to investigate the effect of small inter particle distances in crescent shaped nanoparticles, close-packed arrangements of crescent shaped nanostructures were prepared according to the method introduced in Chapter 2. A monolayer of 180 nm polystyrene (PS) nanoparticles was built on a glass substrate, etched to a final diameter of approximately 150 nm, and used as a mask for the crescents' fabrication. A second sample consisting of isolated particles was prepared using well-dispersed 145 nm PS colloids. All glass surface treatments (cleaning, silanization) and all geometrical characteristics (one metal deposition, $\phi = 0^\circ$, $\theta = 30^\circ$, 1 nm Cr, 40 nm

Au, $\epsilon = 0$) were set equal for both experiments (see Chapter 2 for further details on the fabrication process of these samples).

The samples were characterized via scanning electron microscopy (SEM) and UV-Vis/NIR extinction spectroscopy.

3.2.2 Results and discussion

Figure 3-15 (a.) and (b.) present scanning electron micrographs of the isolated (a.) and close-packed (b.) nanocrescent samples; figures (c.) and (d.) present the corresponding extinction spectra, measured in transmission mode. In (a.) particles appear scattered on the surface, with a mean interparticle distance of some tens of nanometers, while in (b.), the close packed arrangement of crescents imposes a tip-to-tip distance in the order of 10 nm. A surface coverage with metal nanoparticles in the 30%-40% range can be estimated from the SEM images.

The corresponding spectrum for the isolated particles (c.) shows all characteristic resonances described in the previous chapters. For the second case (d.), the resonances are still easily recognizable, though they are considerably wider than in the isolated particle case.

Table 3-4 summarizes the information extracted from the extinction spectra, by fitting Lorentzian curves to the measurements in Figure 3-15 (c.) and (d.). The data shows clearly the widening of the resonance, particularly c_1 , when the particles are arranged close together.

An important effect expected for a coupled-particle system is the red-shifting of their resonances [Reinhard et al. 2005; Sönnichsen et al. 2005; Jain et al. 2007]. This effect is not directly evident from these experiments, at least not for all resonances (see Table 3-4). Size and shape of the crescents can affect considerably the spectral occurrence of the resonances [Rochholz et al. 2007]. In the case presented here, both structures are comparable, but not exactly equal, a fact that might contribute to these differences; i.e. the isolated crescents show considerably sharper tips than the ones in the arrangements. Since the tips give rise to important field confinement in

these structures, their shape modification could give rise to important displacements in the spectra.

When analysing other relevant geometrical parameters, i.e. size, it is possible to notice that the width of the resonances for isolated particles is not so strongly affected by small size differences when compared to previous data [Rochholz et al. 2007]; the clear widening observed here for the **u1** and **c1**⁹ resonances should be then related to a true physical effect, i.e. coupling of the resonances, or to the slight shape differences.

It is very important to note, also, that the arrangement of crescents is not perfect (in the 10 – 20 μm^2) scale, in the sense that the samples are composed of several domains with different orientations (see sketch in Figure 3-16), a result of the colloidal monolayer fabrication procedure. Assuming an effective coupling between the structures, this factor could also play a significant role in the resonances' position and width, since different orientations would determine different geometrical coupling points (see Figure 3-16), which should in principle affect the way these particles would couple.

Since the measurements presented here correspond to the contribution of a large area covered with particles (some square millimeters), it is to be expected that this area is full with domains having different orientations. With this type of measurement, it is not possible to separate the different contributions. An in-situ approach could improve this matter, along with theoretical simulations for a coupled nanocrescent system.

⁹ The effect for the c2 resonance is somewhat arguable, considering that it is essentially weaker than the other two and the simultaneous fitting procedures can lead to significative errors in this case.

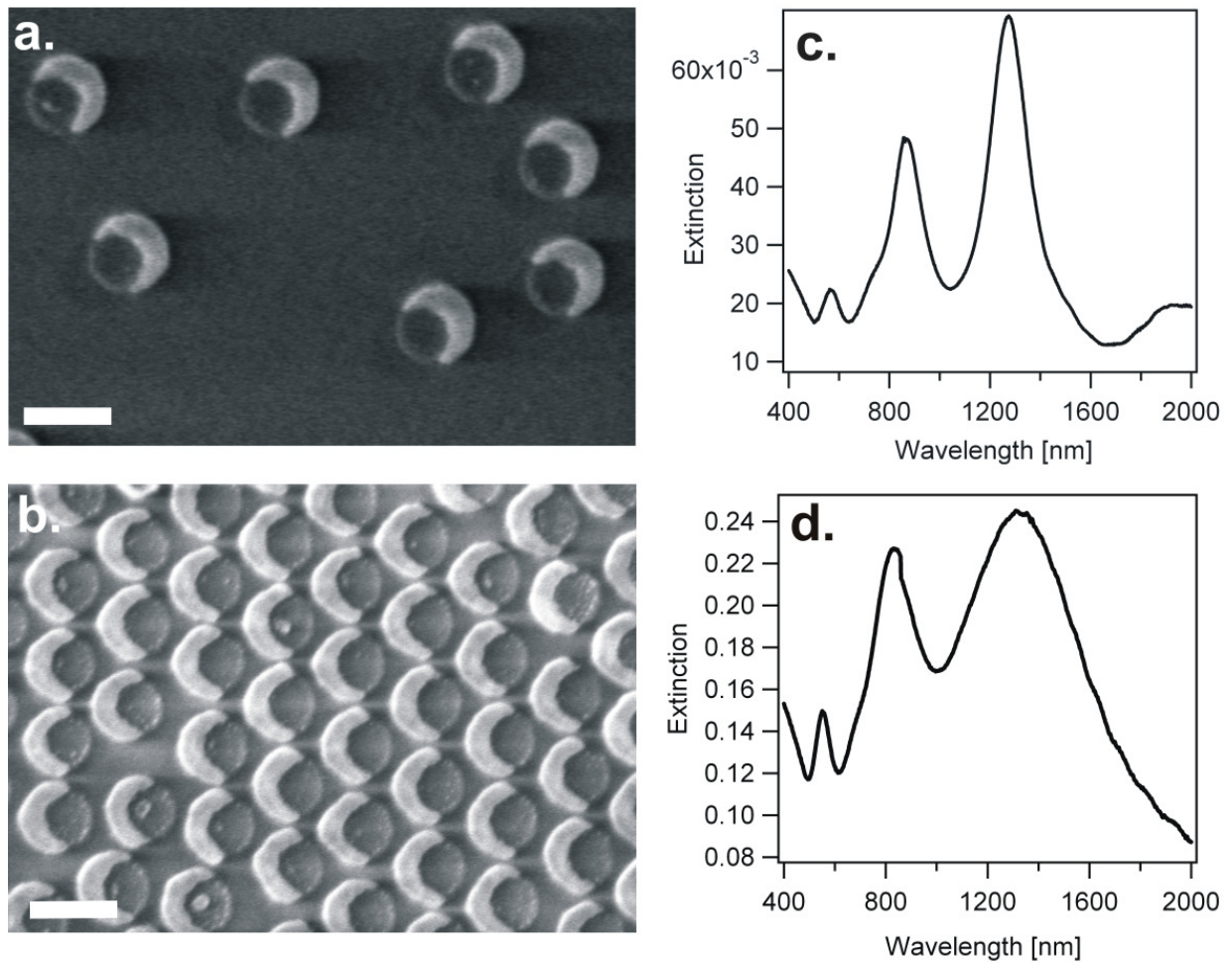


Figure 3-15: scanning electron micrographs for the isolated (a.) and close packed (b.) cases; (c.) and (d.) present their corresponding transmission spectra. The jump observed at 860 nm in the spectrum (d.) related to the spectrometer and has no physical meaning for the experiments. The scale bar represents 200 nm.

	Peak position (λ_p) [nm]			Width [nm]		
	c2	u1	c1	c2	u1	c1
Isolated	720.7	870.5	1274.9	66.8	86.5	102.9
Close packed	678	825.8	1316	30	125	358

Table 3-4: resonance position (λ_p) and width for the three main resonances (c2,u1 and c1) for isolated and close-packed structures, as obtained from fitting Lorentzian curves to the non-polarized light measurements (Rochholz, Bocchio et al. 2007).

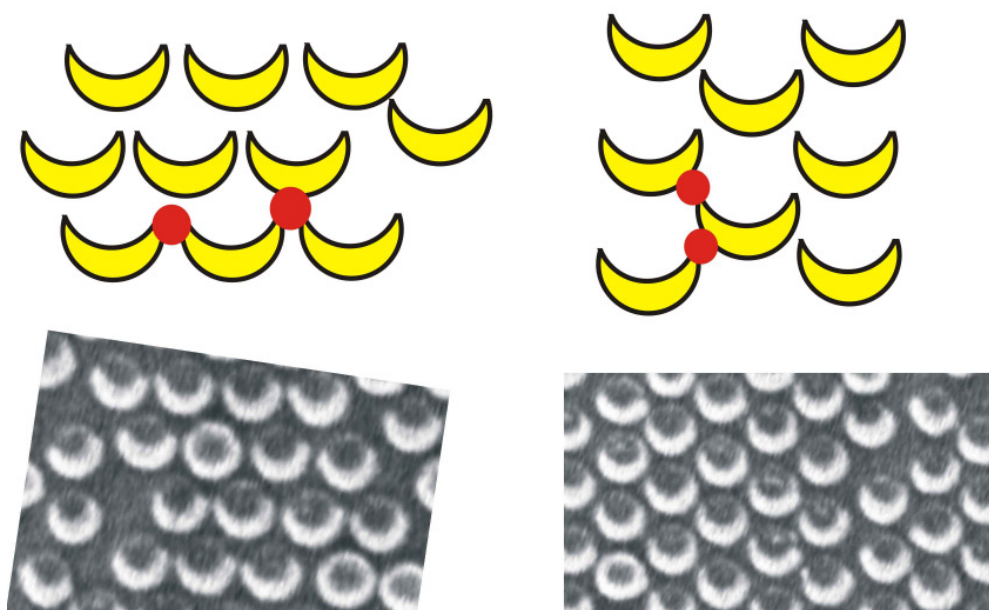


Figure 3-16: simplified sketch showing two domains with crescent arranged in different patterns and corresponding SEM images of two different areas on a same sample. The red dots in the sketch indicate possible different interaction points for the structures.

3.3 Summary and conclusions

Isolated nanoparticles

The influence of geometrical parameters on the optical properties of nanocrescents was explored systematically for Au nanostructures. Significant shifts in resonance position are observed when the size or the opening angle of the structures is varied, allowing for a fine tuning of specific resonances to a desired wavelength range. For the most prominent resonances, the response to a change in the crescents' contour length can be roughly described in terms of standing waves along the structure formed by the fundamental and higher-order modes in a metal stripe as long as interaction between the tips of the structure can be neglected. Fundamentally different responses are seen for crescents that have clearly separated tips, tips separated by only a small gap and overlapping tips. One additional peak in the visible range is identified as the transverse resonance of a rod while two more weak resonances are visible which are not fully understood and are highly sensitive to

preparation conditions. The main resonances change upon variations in metal layer thickness and diameter of the masking colloid in a way that is in qualitative agreement with this interpretation.

Close packed arrangements of nanocrescents

The arrangement of crescents studied shows resonances that match spectrally those of a comparable isolated nanoparticle system, with no detection of new modes. No clear tendency for changes in the peak position of the main resonances is identified from the measurements. The explanation for this could rely on several geometrical factors like shape, thickness or relative arrangement of the structures.

A significant broadening for the u_1 and c_1 resonances was detected. Previous data on isolated structures for different geometries; thicknesses or sizes do not explain this effect. The widening is correlated to a possible coupling mechanism among the resonances, a phenomenon that has been observed previously by other authors.

Further studies are necessary to fully describe the role of the relative orientations of the particle domains, boundaries, etc. in the resonances' position and width. Since the production single domain colloidal monolayers (that would simplify greatly the analysis of the experimental results) is not necessarily a trivial issue, the measurements should probably be accompanied by calculations that help understanding the coupling mechanism of the different resonances, as well as the role of orientation, crescents' shape and inter-particle distance.

4 Sensing with crescent shaped nanoparticles

4.1 Introduction

Several sensing techniques make use of the detuning of optical resonances in systems containing noble metal films or particles, via the attachment of a layer of a material with a refractive index that differs from the one of the subphase. The most common approach is based on propagating surface plasmons on plane metal surfaces, where a fraction of a monolayer is easily detectable. [J.G. Gordon 1977; Knoll 1998; Homola 2006]

Similarly, the shift in the resonance wavelength of metallic nano particles in response to changes in the environment can be used for sensing [Haes, Zou et al. 2004], [Englebienne 1998; Frederix et al. 2003] (see Figure 4-1 for a simplified scheme). The conceptual advantage of this approach relies in the highly localized sensing volume which allows for ultimately small amounts of analyte to be detected [Adam D. McFarland 2003]. While the sensitivity of spherical particles to deposition of a thin dielectric layer is limited, several more complex structures such as hollow spheres [Raschke et al. 2003], triangular pyramids [Haes and Van Duyne 2002; Haes, Stuart et al. 2004; Haes, Zou et al. 2004; Haes, Zou et al. 2004] and rings [Larsson et al. 2007] have shown to be more sensitive.

Particle sensing until now has been limited mostly to geometries that support only one resonance, while structures that support several resonances are known [J. R. Krenn 2000; Shumaker-Parry et al. 2005]. A system with multiple resonances would allow for the simultaneous determination of more than one material-parameter in only one experiment; i.e., thickness and refractive index in conventional thin layer sensing approaches [Knoll 1998]. These applications might be extended to study in a simple experiment, and in a highly localized manner, more complex systems like the optical properties of thin hydrogel films at different penetration depths [Beines et al. 2007], the collapse of biological brushes [Lim et al. 2007] or bio-recognition events [Yonzon et al. 2004; Kim et al. 2006; Larsson et al. 2007].

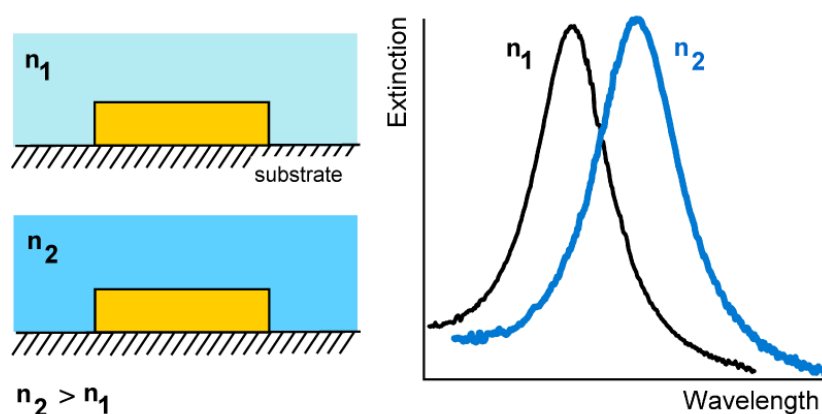


Figure 4-1: simplified scheme of a metal nanoparticle supported on a substrate, surrounded by two different refractive index materials, and their spectra.

When studying the sensing capabilities of metal nanoparticle it is possible to find 3 main approaches, based on the same basic concept of changing their local environment. These approaches consist mainly in (a.) changing the nanoparticles' environment in a bulk experiment, by covering the particles with a material that has a given refractive index (see sketch in Figure 4-1) [Rochholz 2005; Larsson et al. 2007; Rindzevicius et al. 2007; Ueno et al. 2007], (b.) adding thin layers of organic materials or oxides [Haes and Van Duyne 2004; Murray et al. 2006] and (c.) testing of bio-recognition events [Frederix et al. 2003; Haes and Van Duyne 2004]. Comparing the results obtained in these three approaches is not usually straightforward, since these three cases, although relying on the same physical phenomenon, are very different in practical terms (see Figure 4-2 for a simplified scheme of these three cases).

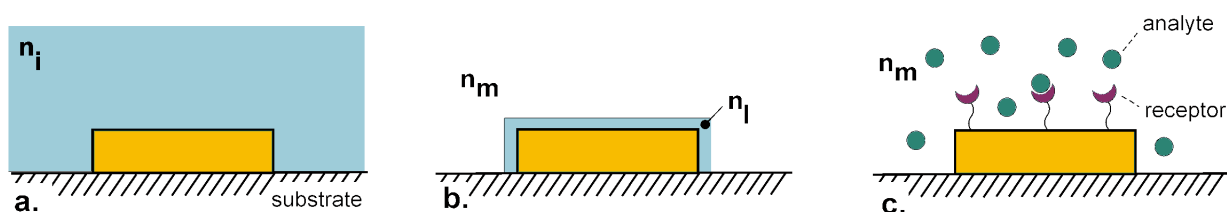


Figure 4-2: metal nanoparticles supported on a substrate, for three different sensing approaches: (a.) immersed in a medium with a bulk refractive index n_i , (b.) covered with a thin layer of a material with a refractive index n_i , immersed in a second medium of n_m , (c.) immersed in a given medium (n_m), and functionalized with a receptor for the analyte of interest.

In the particular case of the crescent shaped nanoparticles, some previous work introduces the response of these particles to different refractive index environments, in a bulk approach [Rochholz 2005]. In the following, the sensing capabilities of these particles are explored in the two main remaining contexts: Section 4.2 deals with the response to thin layers of polyelectrolytes and Section 4.3., with streptavidin-biotin recognition events for a simple bio-sensing approach.

4.2 Thin layer sensing with multipolar resonances

In order to test the sensitivity of the nanocrescents to thin films, standard crescent shaped Au nanoparticles were prepared on clean glass substrates and thin polymeric films composed of polyelectrolyte multilayers [Decher and Schmitt 1992] were deposited on them. The extinction spectrum of each sample was measured before and after the treatment, and compared. The general procedures involved in the sample preparation and characterization for these experiments correspond to those introduced in Chapter 2, and will only be briefly mentioned in the following.

4.2.1 Sample preparation

The samples were functionalized with 3-mercaptopropionic acid, a thiol compound that is expected to attach preferentially to gold and provide a site for electrostatic attachment of polyelectrolyte layers. After rinsing with ultra pure water, alternating layers of poly(allylamine) and poly(styrene sulfonate) were deposited on the samples by immersion for 20 minutes in the corresponding polyelectrolyte solutions, starting with polyallylamine [Decher and Schmitt 1992; Decher 1997; Vasilev 2004]. The samples were rinsed thoroughly with ultra pure water after each immersion step, dried under a stream of nitrogen, and stored for further measurement.

4.2.2 Characterization

The thickness of the added layers was determined for the first 3 bilayers using atomic force microscopy (AFM, Nanoscope IIIa, Veeco). The measurements were done by comparing the height of the structures before and after the attachment of the bilayers, taking the clean glass surface as zero height. This method works properly in the 1 to 3 bilayers regime; where still no full surface coverage takes place (for further details on this subject see Chapter 2). A contribution of approximately 4 nm per bilayer was determined in this regime. A thickness of 8.4 nm per bilayer was

estimated from optical methods for a larger number of bilayers [Vasilev et al. 2004], where the topology of the surface hinders a proper thickness determination by AFM measurements. The irregular thickness profile for the multilayers is a phenomenon known for the polyelectrolytes growth [Buron et al. 2007] and has been taken into account in the present work via a simplified two-step growth model (for further details on this subject see Appendix B). A sketch showing some typical dimensions of a cross section of a polymer coated crescent is shown in Figure 4-3. Here, $w \approx 65$ nm and $h \approx 40$ nm, where h represents the height and w the width of the crescent at the cross-section. The layer thickness as a function of deposited bilayers that was used in this work is presented in Figure 4-3 c.

The optical properties were studied with UV-Vis/NIR transmission spectroscopy. Non-polarized light spectra were recorded with an UV-Vis-NIR spectrometer (*Perkin-Elmer, Lambda 900*) operating in transmission mode, before and after the addition of polyelectrolyte bilayers, sampling an area of the substrates of approximately 50 mm^2 .

Peak position and width of the resonances were estimated using a multipeak fitting routine (*Igor Pro version 5.02*), adjusting Lorentzian curves in a 500 – 2500 nm range [Rochholz et al. 2007]. Peak positions were determined for each sample before and after polyelectrolyte deposition; yielding a displacement as their difference. The occurrence of an increasing absorption background upon the addition of polymers was taken into account in the fitting procedures by adding an extra Lorentzian-like decay in the 400 – 800 nm range.

4.2.3 Results and discussion

Figure 4-4 presents non-polarized extinction spectra of the samples studied in these experiment, before (black) and after (gray) the addition of the PE bilayers. The jump observed in some of the measurements (i.e. the 18 bilayers sample) at around 860 nm corresponds to switching between detectors in the spectrometer and is not related to the samples.

Figure 4-5 displays the peak position and width of the resonances as extracted from Lorentzian fits to the measurements, summarizing the information extracted from Figure 4-4. The data shows that, upon the addition of the dielectric coating, all resonances progressively red shift. The displacements of the spectra are different for each resonance. In addition to this, an increasing background in the 400 – 800 nm range sets in upon the addition of polymer, which cannot be assigned to a resonance of the crescents. Also, a clear widening is also detectable in the case of c1, but this tendency is not so pronounced in the case of u1 and c2 (see Appendix B for further information).

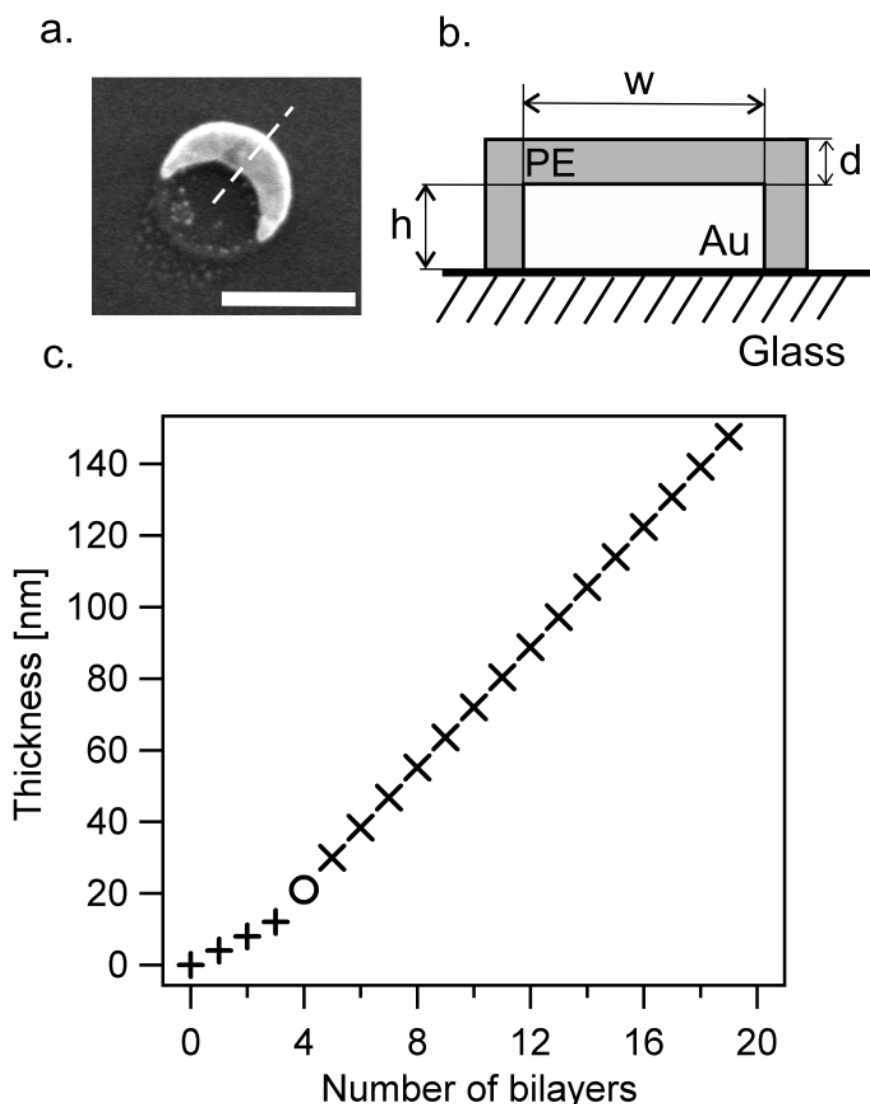


Figure 4-3:(a) scanning electron micrograph of a crescent-shaped particle; the scale bar represents 200 nm (b) sketch of a cross section of a crescent covered with polyelectrolytes along the dashed line in (a); d stands for the thickness of the film, h and w for the height and width of the structure respectively, and PE for the polyelectrolyte film. (c) Film thickness as a function of the number of bilayers. The vertical crosses (+) represent the AFM measurements, the tilted ones (x) the literature values. The circle represents an estimated intermediate value between these two regimes.

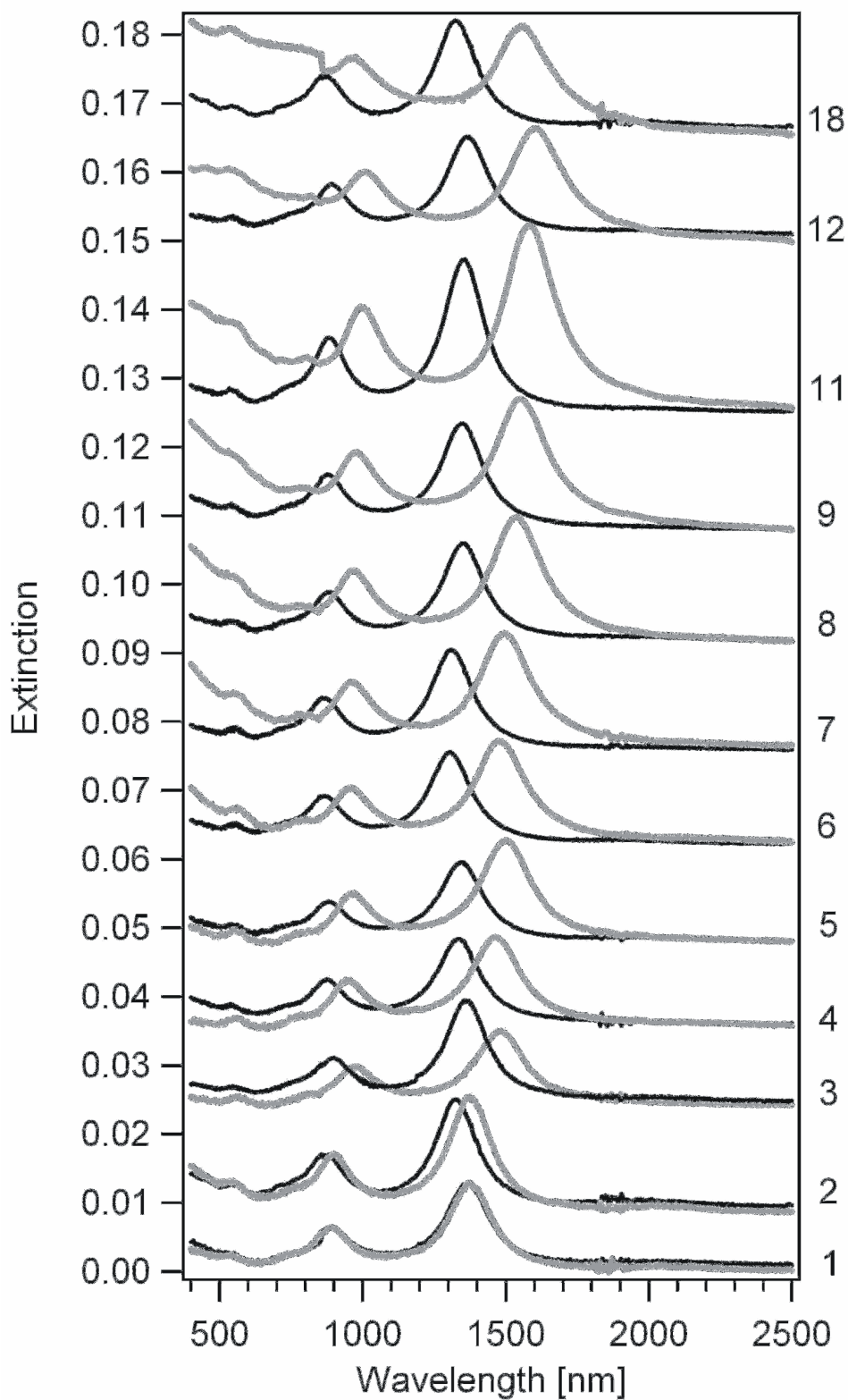


Figure 4-4 : extinction spectra of the samples before (black) and after (grey) the addition of polyelectrolyte bilayers. The corresponding number of bilayers is displayed on the right side of the graph.

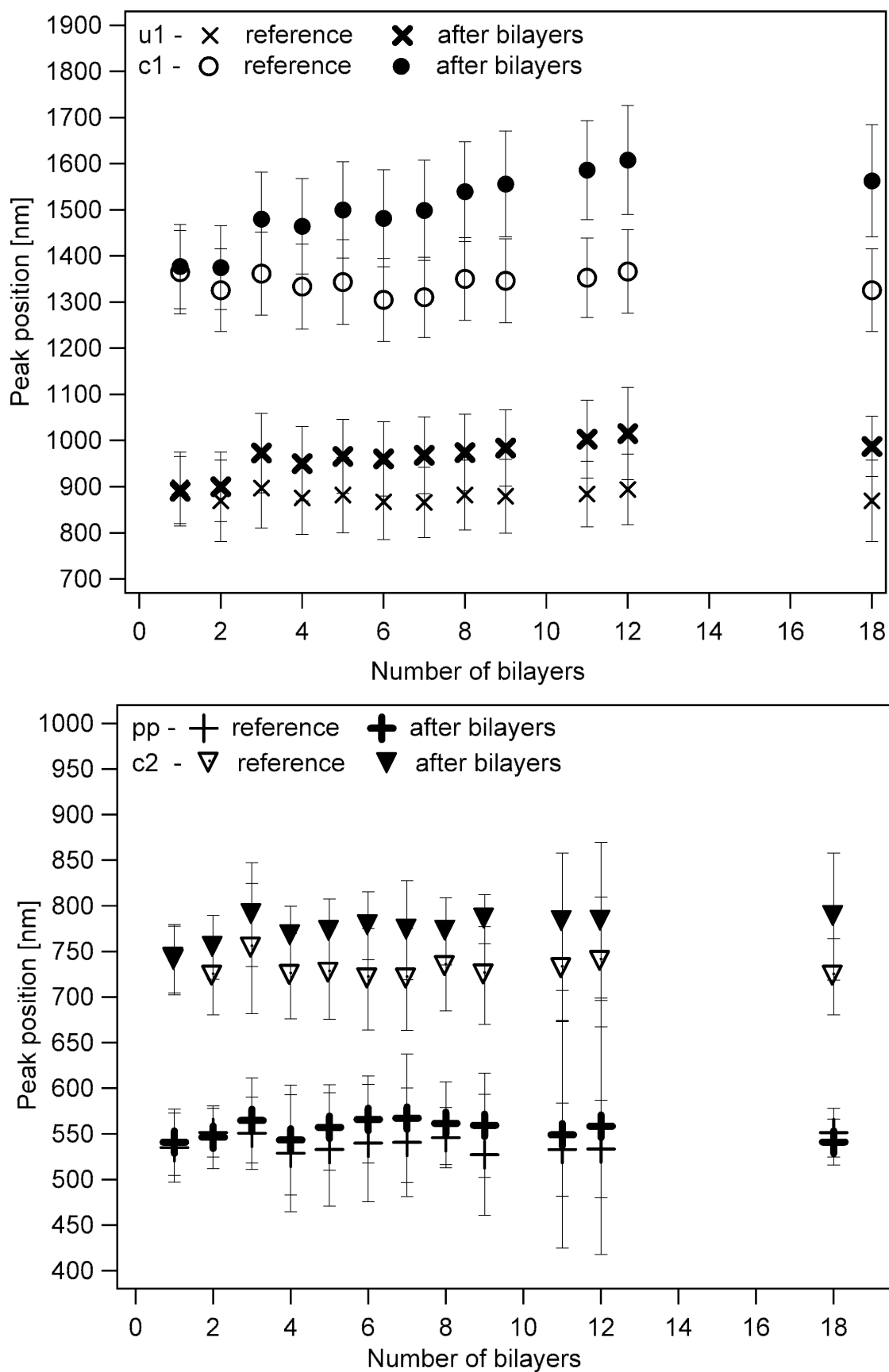


Figure 4-5: peak position of the 4 main peaks (c1, u1, c2 and pp) before and after the addition of the bilayers. The error bars represent the width (HWHM: half width at half maximum) of the resonances, as determined from the fitting procedures

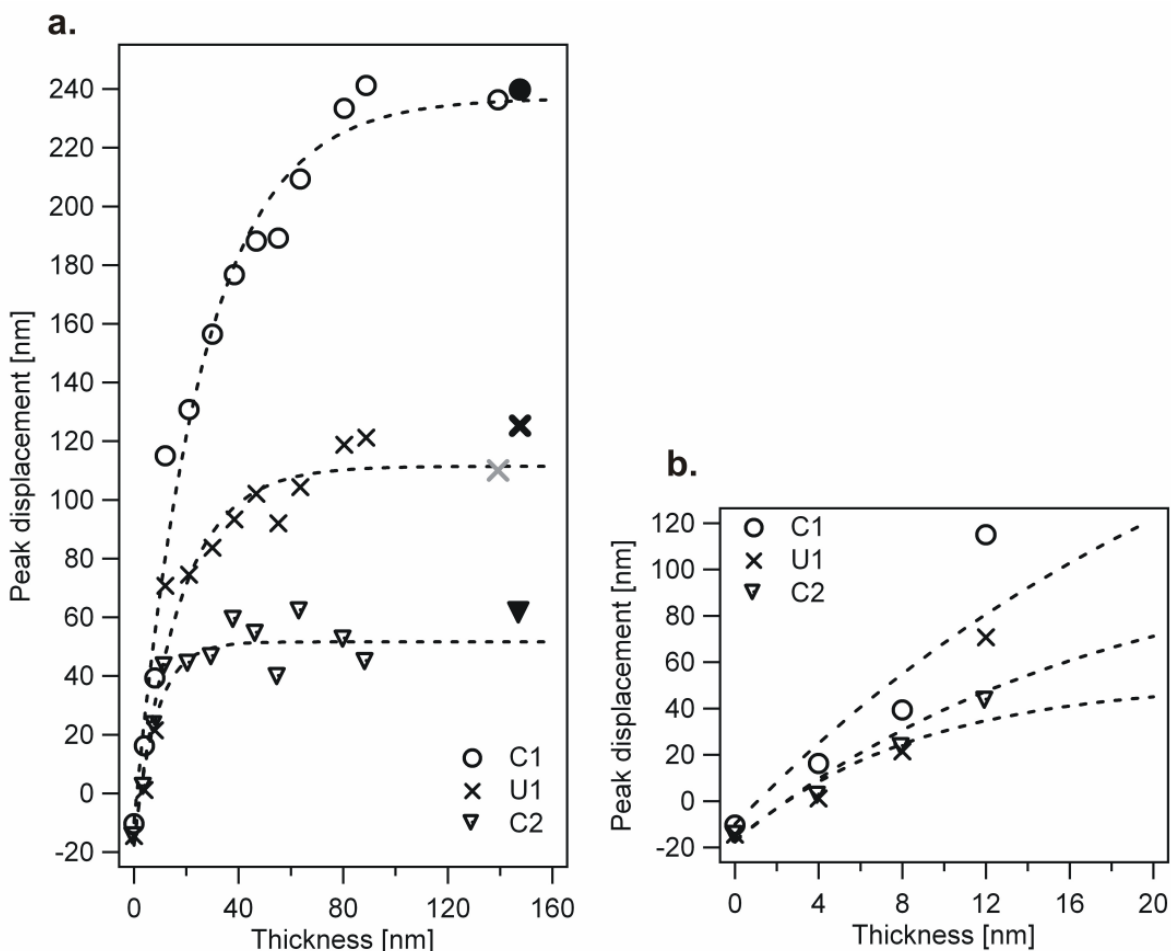


Figure 4-6: peak displacement of the main resonances in the full (a.) and first layers (b.) regimes. Resonance assignments are given in the graph. The dashed lines represent an exponential fit to the data. The extra dark markers added to (a.) correspond to the displacement obtained when immersing the samples in a $n = 1.524$ oil [Rochholz 2005]. For a thickness of roughly 140 nm (18 bilayers), only the displacement corresponding to c1 can be determined unequivocally, and is included in the overall fitting. The gray marker gives an indication for the displacement of u1 for thick coatings, but this value is not included in further calculations.

Figure 4-6 displays the peak displacement as determined from the fitting for the c1, u1 and c2 resonances as function of the coating thickness in the many- (a) and few- (b) layers regime. Each set of data points associated to a defined number of bilayers corresponds to one independent sample, except for 1, 2 and 3 bilayers. For 1 and 3 bilayers, 2 independent samples were measured; for 2 bilayers the data is based on 3 samples. The data corresponding to $d = 0$ nm correspond to functionalization with 3-MPA only (see Appendix B - Supporting information for further details). The pp mode was disregarded, since its displacement saturates rapidly – in the 5 to 10 nm range. Added to this, the increasing amount of layers gives rise to an increasingly growing background, which in turns makes also the precise fitting of pp difficult.

The shifts increase rapidly in the first layers (1 to 5) regime; and saturate for further increasing thickness. The shift at saturation can be compared to the shifts observed when the crescents are surrounded by an infinitely thick medium with homogenous refractive index; in analogy to an infinitely thick coating. Since deposition of infinitely many multilayers is experimentally impossible and deposition of thick films leads to additional interference effects [Murray et al. 2006; Rindzevicius et al. 2007] that complicate the analysis, this comparison is to be made with the crescents response when immersed in a liquid with a refractive index that equals the one of the polyelectrolytes. The latter has been determined [Vasilev 2004; Vasilev et al. 2004] to be $n = 1.54$ at $\lambda = 633$ nm. Considering normal dispersion, a refractive index of $n = 1.5$ can be used as an approximate value at the longer wavelengths where the crescents resonances occur. As a simple reference, a measurement with an $n = 1.524$ index oil [Rochholz 2005] is taken (see Figure 4-6 a.). This oil gives rise to resonance displacements that are in reasonable agreement with the values obtained for an approximately 150 nm thick layer, indicating that, for this bilayer thickness, the saturation of the shifts is reached for all resonances. It is important to note that, given the increasing background and broadening of the resonances upon the addition of polymer, only the position of the c1 resonance was determined in a reliable manner for such thick coating, and only that value was used in further analysis. An indication of the behavior of u1 is included in Figure 4-6, but was not considered in further fitting procedures.

The peak displacement, for each resonant mode ($\Delta\lambda_i$) can be quantified by fitting an exponential function of the form:

$$\Delta\lambda_i(d) = \Delta\lambda_{m,i} + (\Delta\lambda_{0,i} - \Delta\lambda_{m,i})e^{-d/d_{l,i}}$$

where $\Delta\lambda_{m,i}$ represents the resonance-specific (i) saturation limit, d the thickness of the layers, $\Delta\lambda_{0,i}$ the peak displacement at $d = 0$, and $d_{l,i}$ a typical decay length. The index “ i ” denotes the 3 main resonances (c1, u1 and c2). The results of this procedure are summarized in Figure 4-1. An apparent negative displacement for the ‘zero layer’ ($\Delta\lambda_{0,i}$) resonances is observed. This effect could be both related to a physical phenomenon like structure annealing or thiol binding [Duval Malinsky et al.

2001], or simply be the result of the scatter in the measurements, which is of the order of the observed displacements.

Fitted parameters				
	$\Delta\lambda_{m,i}$ [nm]	$\Delta\lambda_{0,i}$ [nm]	$d_{i,i}$ [nm]	$\left. \frac{d(\Delta\lambda_i)}{d(d)} \right _{d=0}$
C₁	236.9	-9.95	26.2	9.4
U₁	111.4	-17	17.2	7.4
C₂	51.6	-17.7	8.5	8.1

Table 4-1: Fitted parameters, according to Equation(1), for the three main resonances

It must be stressed here that the choice of an exponential function is not based on a physical model but represents an arbitrary and rather simple parameterization of a typical decay length. Since the exponentials describe the data quite accurately given the experimental scatter, the decay lengths as obtained from the fits can be used as a basis for the comparison with theoretical models.

Both the displacements at saturation ($\Delta\lambda_{m,i}$) and the decay lengths ($d_{i,i}$) are resonance-specific, as can be observed in Table 1. Higher order resonances (c2, u1) show much more confined near fields than the fundamental mode (c1), which leads to smaller decay lengths d_i . The first 20 nm regime is most useful for sensing, since there the relative displacements of the resonances upon the addition of layers of polymer are most pronounced. If we consider the derivative $d(\Delta\lambda_i)/d(d)$ at $d=0$ from the fitting (see Table 4-1) as an estimate to the sensitivity of the modes upon the addition of the layers, we observe that c1 is the most sensitive, followed by c2 and u1. It should be noted, though, that all values are within the same order of magnitude, meaning that all resonances are comparable. A clear advantage of c1 is its large extinction cross-section and spectral separation from the rest, which simplifies the simultaneous multippeak fitting.

A second approach to a sensitivity measurement would consist in calculating the figure of merit (FOM) of these resonances [Sherry et al. 2005].

$$FOM = \frac{dE/dn}{FWHM}$$

Where E represents the peak position (in eV), n , the refractive index of the medium, and the FWHM the full width at half maximum of the resonance (also in eV).

This approach has been mostly used to compare particles in different (bulk) index media, while the work presented here focuses on the response to thin layers.

The study of the crescent shaped nanoparticles in different index media has already been undertaken by Rochholz [Rochholz 2005], rendering FOM values in the same order of magnitude than other particles presented in the literature (FOM: 3...5) [Sherry et al. 2005; Larsson et al. 2007].

Penetration depths

Considering the results presented in Table 4-1 it is important to point out that, due to their different penetration depths, the modes give independent information about the surrounding environment. This is particularly important when considering that the simultaneous use of n resonances allows for the determination of n parameters that describe the film; for example with two resonances one may determine thickness and refractive index simultaneously; a third resonance would allow in addition the determination of another parameter like a refractive index gradient in the film. This approach is much like the strategies that are used commonly in conventional sensing with dielectric wave guide modes [Van Os et al. 1999] but here, the modal volume is far below that determined by the order of magnitude of the wavelength of light, and the modes are spatially confined.

When the resonances on the crescents are interpreted as being composed of standing waves which are formed by the superposition of a forward and a backward propagating wave along the crescents' contour, an intimate connection between the shift of the modes and their near field is directly evident.

A full numerical description of the system under study would require extensive numerical calculations, but good physical insight in the effect of different penetration depths can be gained by considering two simple model systems where analytical solutions for the field distributions of the eigenmodes are known; these models are the plane interface and the cylindrical rod in vacuum [Buckman 1995; Unger 2008].

We consider a guided electromagnetic mode with known field distribution. A change of the refractive index (Δn) within the volume where the electric field (\mathbf{E}) is not vanishing will lead to a change Δk in the propagation constant k of this mode. This change is in first approximation obtained by mode coupling theory [Buckman 1995]

$$\Delta k \propto \int dV |E|^2 \Delta n^2$$

where the integral is to be taken over the entire space. If, as it is the case here, a material with a fixed refractive index is added so that it occupies some volume in the nearby area, and we furthermore realize that for a resonator with a given length (l) a change in k will directly lead to a change in resonance wavelength, then

$$\Delta \lambda \propto \Delta n^2 \int_{V_{oc}} dV |E|^2$$

Where the integral is to be taken over the volume (V_{oc}) that is occupied with the high refractive index material. It should be stressed that this theory is only strictly valid for real dielectrics or perfect metals, which is not the case for gold in the visible range. Furthermore it is assumed that the perturbing change in the refractive index only leads to infinitesimal changes of the field, which is only true for small dielectric contrasts Δn . Despite these limitations, we use this theory for an approximate description of the observed shifts.

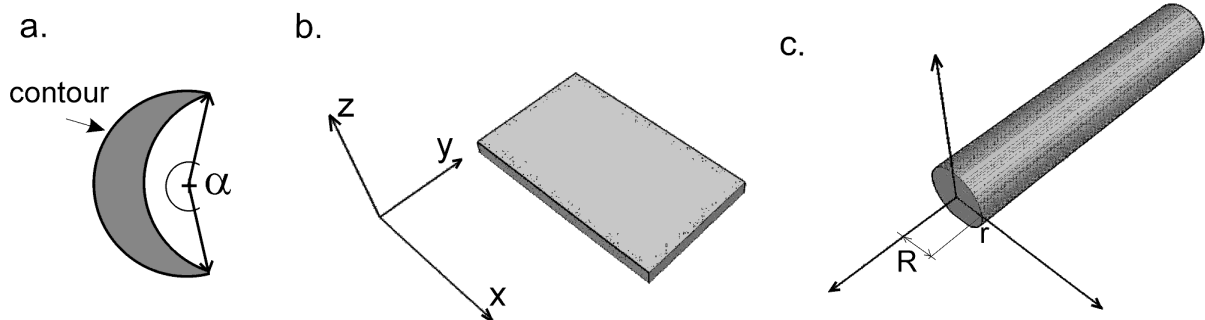


Figure 4-7: simplified sketches of a crescent (a.), a plane interface (b.) and a rod (c.)

One may compare the guided modes on the crescent with the ones on a plane interface (see Figure 4-7 for a simplified sketch), as a first rough approximation. In this case, the z-dependence of the electrical field is given as

$$E \propto e^{-\text{Im}(k_z)z}$$

where k_z is purely imaginary and is obtained for guided modes from

$$k_z^2 + k_x^2 = k_0^2$$

with k_x and k_0 being the wave vector in the propagation direction and the modulus of the wave vector of plane light waves, respectively. It is possible to estimate k_x as follows:

$$k_x = \frac{2\pi}{\lambda_{mode}} = \frac{m\pi}{l_{contour}}$$

m being the order of the resonance and $l_{contour}$ being the contour length of the crescent, which is in turn identified with the size of the resonator. In order to estimate $l_{contour}$ we chose, from geometrical considerations [Rochholz et al. 2007]

$$l_{contour} = \frac{1}{2} d_{coll} \alpha$$

where α represents the angle expressed in radians, corresponding to an arc of longitude $l_{contour}$ and d_{coll} the diameter of the colloids used to produce the crescents (see Figure 4-7). For an ideal geometry α is 1.17π . In this model, the peak position displacement as a function of the thickness (d), $\Delta\lambda_i(d)$, is obtained up to a prefactor, allowing to calculate its value normalized to the displacement for an infinitely thick coating, $\Delta\lambda_m$.

$$\frac{\Delta\lambda(d)}{\Delta\lambda_m} = 1 - e^{-2\text{Im}\{k_z\}d}$$

Which directly yields the decay depth $d_{l,PI}$,

$$d_{l,PI} = \frac{1}{2\text{Im}\{k_z\}}$$

where the subscript PI denotes the plane interface model.

Another model where field distributions are readily calculated analytically are cylindrical rods. In this case, the radial electrical \mathbf{E}_r field outside the rod is given by

$$E_r \propto H_1^{(1)}(k_z r)$$

where $H_1^{(1)}$ is a Hankel function of the first kind, and r the distance measured from the center of the rod. The E_r component of the electrical field is the normal component and dominant in the near field. This leads to

$$\Delta\lambda(d) \propto \int_R^{R+d} r [H_1^{(1)}(k_z r)]^2 dr$$

with R being the radius of the rod and d the thickness of the layer. We chose to model the crescent as a rod with a $R = 20$ nm corresponding to half the height of the crescents. The resulting normalized $\Delta\lambda_i(d)$ curves are displayed in Figure 4-8. A typical decay length ($d_{l,rod}$) was obtained in this approximation by solving the equation $\Delta\lambda(d_{l,rod}) = (1 - e^{-1})\Delta\lambda_{max}$, $\Delta\lambda_{max}$ being the shift for an infinitely thick coating.

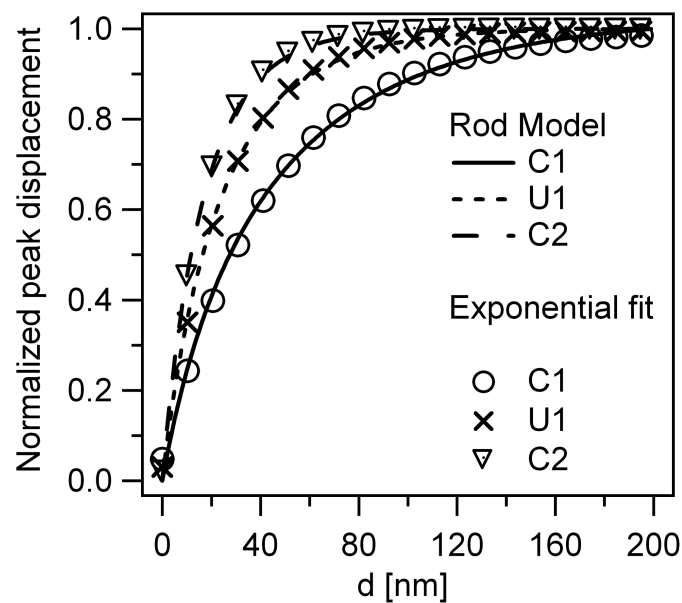


Figure 4-8: Normalized peak shift, as calculated from the rod model, as a function of the distance to the rod's surface.

Table 4-2 summarizes the results for the plane interface model, the rod model and the experiments.

Resonance	c_1	u_1	c_2
Wavelength [nm]	1364	897	742
k_x [nm ⁻¹]	0.00855	0.0171	0.02565
k_z [nm ⁻¹]	0.0072	0.0156	0.0242
$d_{i,exp}$ [nm]	26.2	17.2	8.5
$d_{i,PI}$ [nm]	70	32	20.6
$d_{i,rod}$ [nm]	44.5	25.5	17.6

Table 4-2 : Decay lengths for the different modes according to the measurements ($d_{i,exp}$) and the different models ($d_{i,PI}$, $d_{i,rod}$)

These very simple geometrical models reproduce qualitatively the experimentally observed trend of a shrinking modal volume with increasing mode number. In particular, the direct connection to a simple analytical field distribution allows for an intuitive understanding of the observed effects. The expected field extensions d_i for c_2 and u_1 are comparable for the two models, but higher than the experimental results; the rod model appears as particularly suitable to describe the response of the crescent structures. Several mechanisms may account for the quantitative difference between the models and the experiments. Firstly, the geometrical simplifications made when describing the crescents as rods/plane layers are significant, in particular, at the corners of the crescents, where a high localisation of the field occurs which is not reflected in the models and can lead to a reduced d_i . Secondly, the mode coupling theory itself is only an approximation. Finally, imperfections of the structures and the coating may also play a role, particularly for the first layers.

4.3 Testing the sensing capabilities of the nanocrescents for bio-recognition events

In order to study a more realistic case for a biosensor application, that is, that of a platform sensing a few binding events on its surface, a simple bio-recognition scheme (biotin – streptavidin) was tested on both Ag and Au standard nanocrescents. Streptavidin (Sav) is a protein with a very high affinity [Spinke et al. 1993] to biotin ($K_a \sim 10^{13} \text{ M}^{-1}$), the reason for which it is the system of preference for reference and comparative studies.

Figure 4-9 (a) and (b) display the structures of streptavidin and biotin.

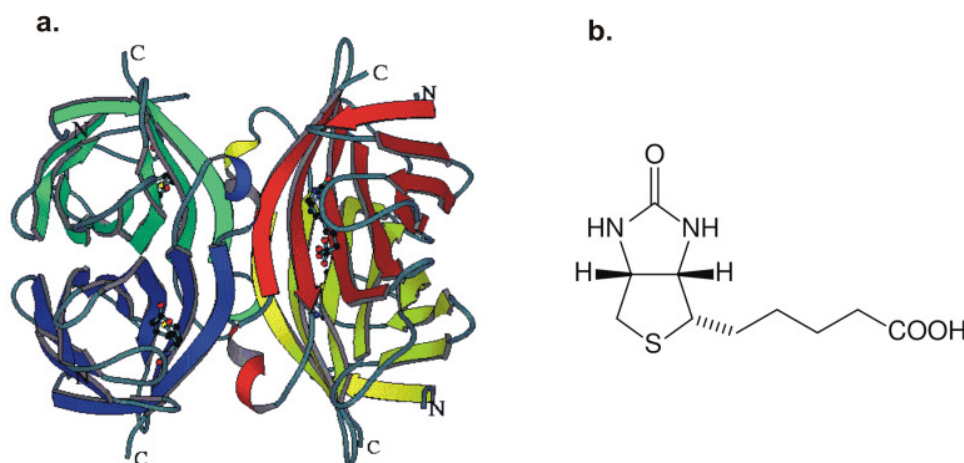


Figure 4-9: a. streptavidin [Freitag; Sato 2006] and b. biotin

A second approach to study the sensitivity of these particles to a few recognition events in their close environment was based on the use of SAV-modified Au-nanoparticles (Sav Au-NPs). Previous work on enhancement of conventional SPR sensitivity [Fang et al. 2006; Wark et al. 2007] have shown that the use of marked gold colloids allows for ultimately small amounts of analyte to be detected. It is of interest, then, to explore whether the same effect can be used in a sensing scheme based on the metallic nanocrescents.

Figure 4-10 shows a scheme of the different approaches tested in this section.

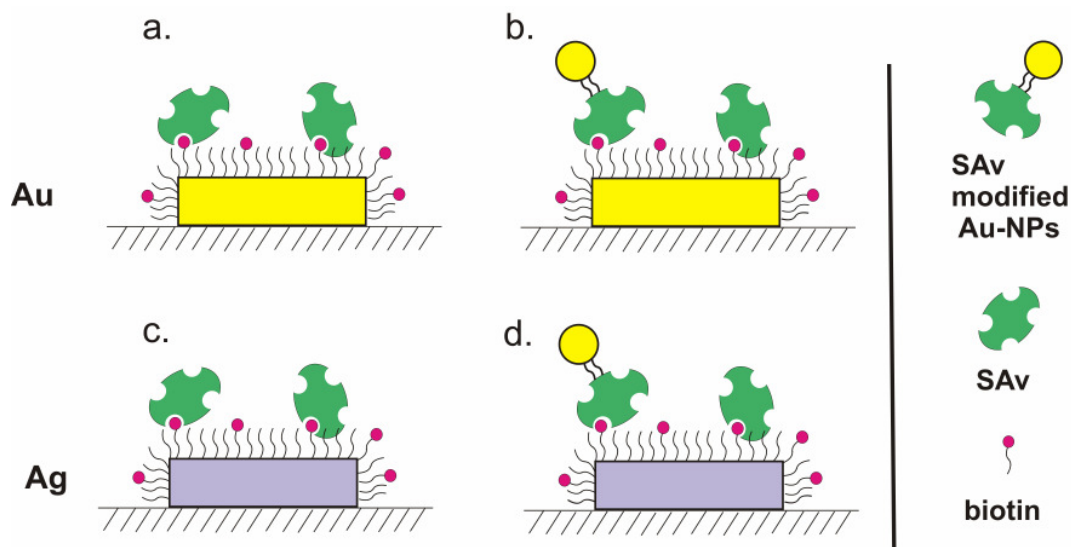


Figure 4-10: scheme of the two sensing approaches tested on Au (a. and b.) and on Ag (c. and d.) crescents

4.3.1 Sample preparation

Standard gold and silver crescent shaped nanoparticles were prepared on glass substrates following the general procedure described Chapter 2. The PS colloids had 200 nm in diameter; in both cases $\varphi = 0^\circ$ (1 deposition process), $\theta = 30^\circ$, and $\varepsilon = 0^\circ$. The metal thickness was set to 40 nm, both for Ag and Au. A 1 nm Cr layer was used as an adhesion layer to glass in the case of the Ag crescents to minimize annealing effects (see Appendix B for further details on this issue).

In order to functionalize the surface of the nanoparticles, all samples were first exposed to a thiol mixture containing biotin-terminated and hydroxy-terminated thiols. After this step, the samples were exposed either to SAv or SAv-AuNPs, for their attachment to the surface.

All of these steps were done following the procedures introduced in Chapter 2 (Section 2.4.), where all products and processes are thoroughly described.

4.3.2 Characterization

The samples were characterized by UV-Vis/NIR extinction spectroscopy. The measurements were done in transmission mode, before and after each of the surface chemical treatments, sampling an area of approximately 50 mm², in a non in-situ approach.

4.3.3 Results and discussion

Figure 4-11 and Figure 4-12 show the extinction spectra of 4 independent samples, namely, their reference spectra (as prepared), and after biotinylation and bioconjugation (with either SAV or SAV marked AuNPs). The measurements correspond to Au and Ag nanocrescents. As a general remark, it is important to point out that for all experiments neither new resonances nor strong spectral changes are detected, apart from a red shifting and widening, as if it was the case for the addition of a higher refractive index material on their surface.

The information extracted from these experiments is summarized in Figure 4-13. The peak displacements presented there are calculated as the displacements taking the biotinylation step as the reference.

Au nanocrescents

Figure 4-11 shows all the spectra before and after treatment for Au nanocrescents, All these measurements look very similar at first sight; a closer insight to the main resonance peak shows a small displacement both for the SAV and SAV-AuNPs.

For these nanostructures, none of the 2 approaches gives rise to significant displacements in the spectra (see Figure 4-13). The shifts measured - 4 to 12 nm - are in the same order of magnitude than the normal dispersion found within different positions in a sample, or among different samples (see Appendix B for further details). Since the samples were measured in a non in-situ approach, these values are then not considered to be significative.

Assuming that the binding reactions proceeded optimally in both cases and that the structures are covered by several (some hundred)¹⁰ protein molecules attached on their surface, the measured peak displacements are still very small. If a simple layer model was assumed, where all this conjugations events at the surface could be modelled as thin (~ 5 nm thick) polymeric layer of $n = 1.5$, then, a shift of about 15 to 20 nm would be expected for such a layer (see Figure 4-6). This is only an approximation, since no full surface coverage is to be expected. Still, this value lies very close to the intrinsic dispersion within a single sample, or among a group of them (see Appendix B), which agrees with the results of the experiments.

¹⁰ Estimated comparing the particle's surface to a full coverage with ~5 nm spheres

Ag nanocrescents

Figure 4-12 presents the results for the Ag nanocrescents. In this case, both for the SAV and for the SAV-AuNPs recognition, clear displacements of the spectra are easily recognizable.

The conjugation of Sav on the surface of Ag nanocrescents gives rise to spectral shifts in the 10 – 35 nm range, for the different resonances (see Figure 4-13 for details). Moreover, the use of SAV-modified Au-NPs amplifies the response considerably, since displacements in a 25 – 50 nm range are detected.

Assuming that the binding of the species on the particles' surface proceeded the same way as in the case of Au, the use of Ag would represent a factor 3 in signal amplification for SAV binding, and 3 – 5 for Sav-AuNPs. If the dispersion in resonance position within one sample is assumed to be comparable to that of the Au nanocrescents, then, these results become very significant (see Appendix B).

A statement on the relative higher sensitivity of the Ag crescents compared to the Au structures would be based on the hypothesis that all steps (biotinylation, Sav attachment or SAV-AuNPs attachment) are acting with equal efficiency for both cases; that is, that the number/distribution of these on the surface of the particles is comparable, and that no side reactions, i.e. oxidation of the metal is taking place on the particles' surface. This possibility remains an open issue that is also to be cleared out with further reference experiments, i.e. annealing of the structures in solutions containing all salts, BSA, PBS, etc. as available in the commercial products, without the addition of the agents of interest (Sav and Sav-AuNPs).

Another important consideration for both approaches (Ag and Au nanocrescents) is to be made. In this analysis, it is assumed that the BSA¹¹ (bovine serum albumin) present in the streptavidin solution does not attach to the functionalized surfaces [van Oss et al. 2003], so that the peak displacements are associated mainly to the linker

¹¹ BSA has a lower isoelectric point than the PH claimed by the producer of the solution (Aldrich), reason for which it is considered that the sticking to the surfaces should be minimum. Reference measurements are most important, since added salts can alter this significantly, and any material added to the particles / in their close proximity can produce a displacement of the resonances, hindering the phenomenon of interest.

molecules (biotin-terminated thiol) and the to the SA_v or Sav-AuNPs, respectively. The actual amount / distribution of species attached to the surface remain also an open question of fundamental importance, both for the Au and Ag nanocrescents. The spectroscopic studies presented in this work are just a (necessary) first approach to the problem; but further SEM / AFM characterization should be conducted to validate these results and obtain significative numbers to estimate the sensitivity of these particles to a few recognition events. An ultimative approach to determine the sensitivity of these structures experimentally would consist of pushing this experiment to a single particle level (i.e. combining confocal and atomic force microscopies for such purpose; correlating spectra and material distribution on the particles).

Since these first results presented here appear most interesting, these very same approaches were tested on other silver particles of different shape and size, obtaining qualitatively comparable results, which will be thoroughly described in Chapter 7.

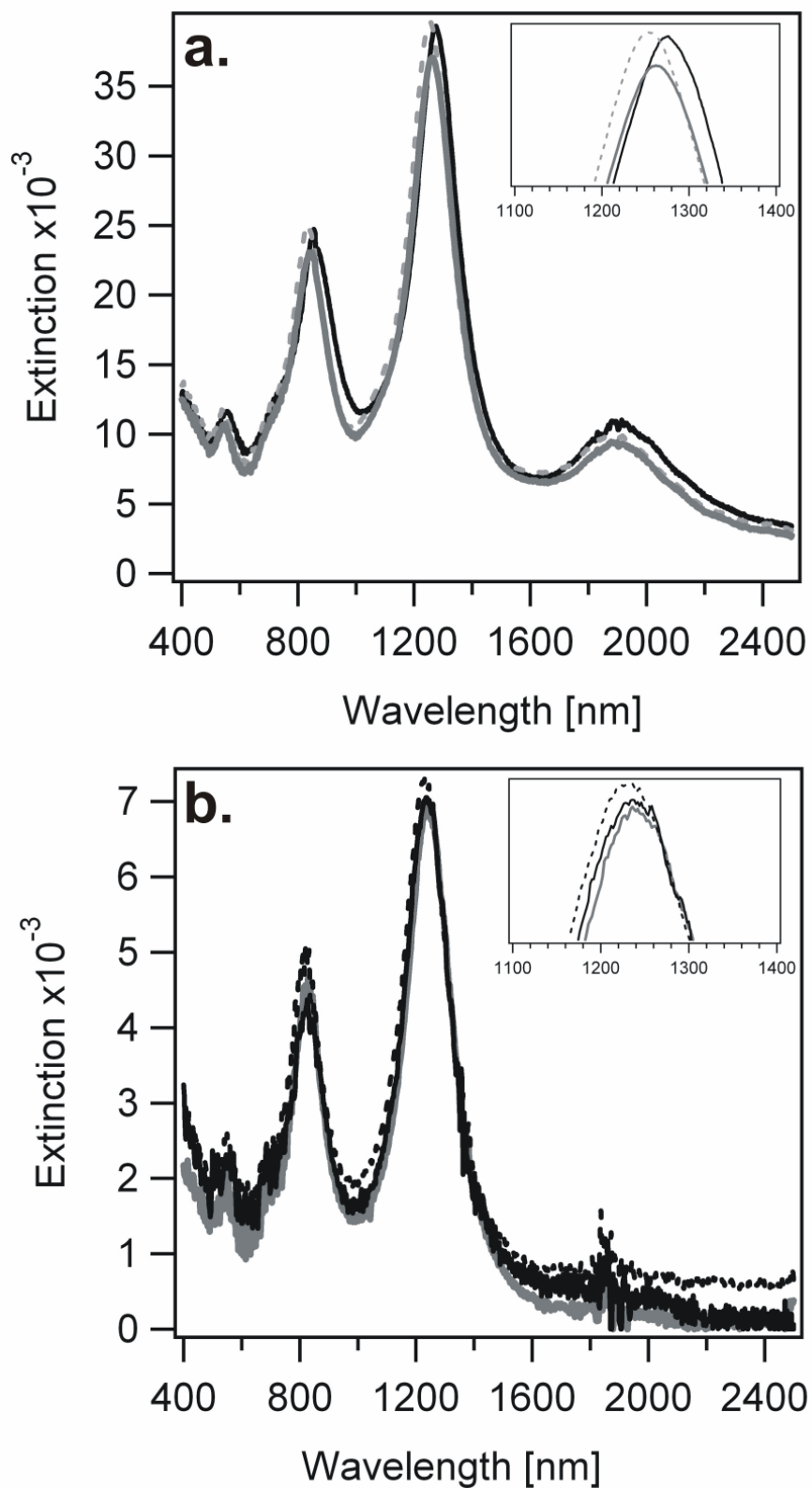


Figure 4-11: Extinction spectra of Au crescents after biotinylation and streptavidin attachment (a.) and biotinylation and streptavidin modified Au NPs bioconjugation (b.). Reference (black solid line), biotinylation step (dashed line), and bioconjugation (gray). The inset corresponds to the strongest resonance at 1300 nm (c1).

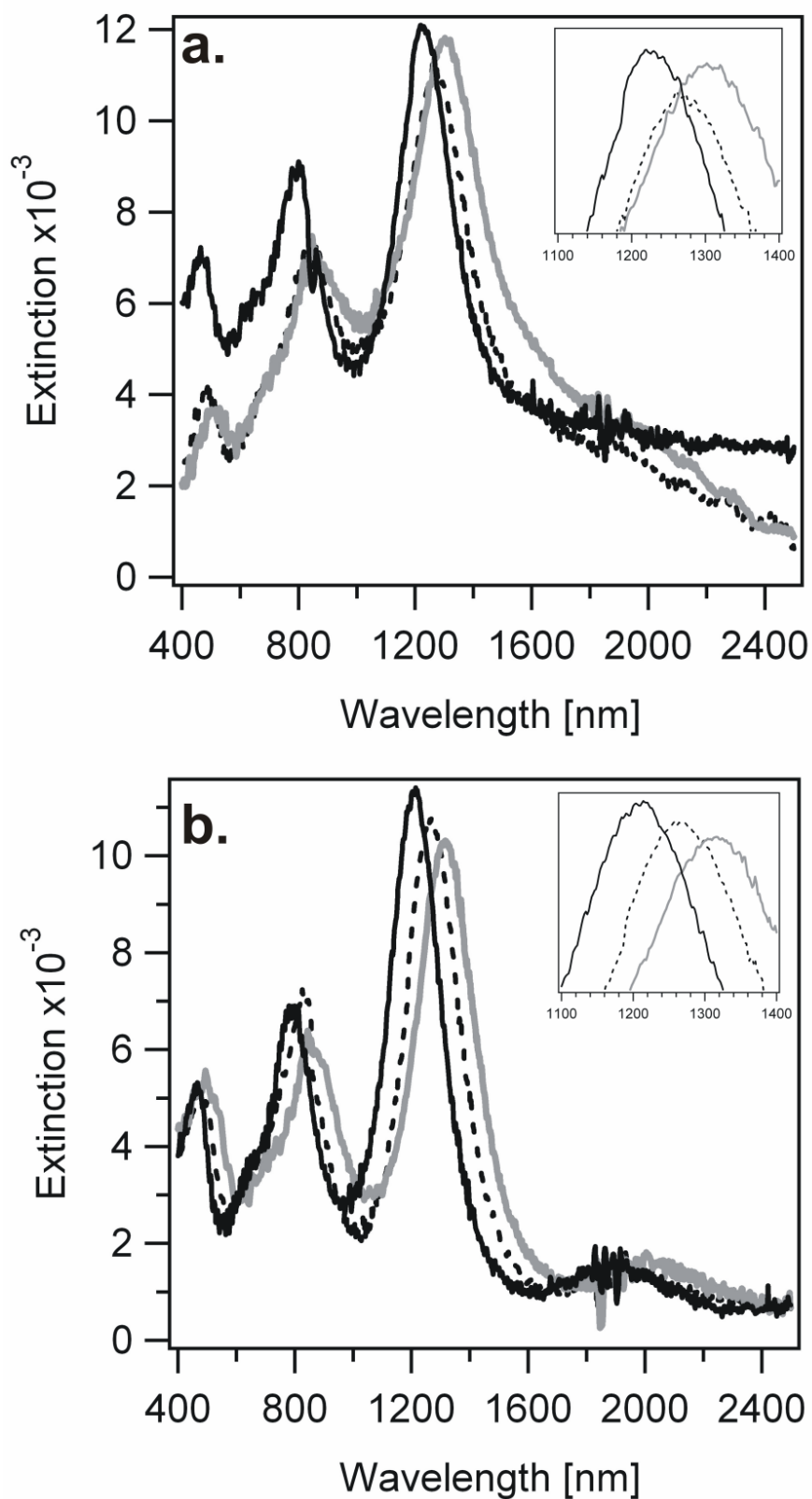


Figure 4-12: Extinction spectra of Ag crescents after biotinylation and streptavidin attachment (a.), and biotinylation and streptavidin modified Au NPs bioconjugation (b.). Reference (black solid line), biotinylation (dashed line), and after bioconjugation(gray solid line). The inset corresponds to the strongest resonance at 1300 nm (c1).

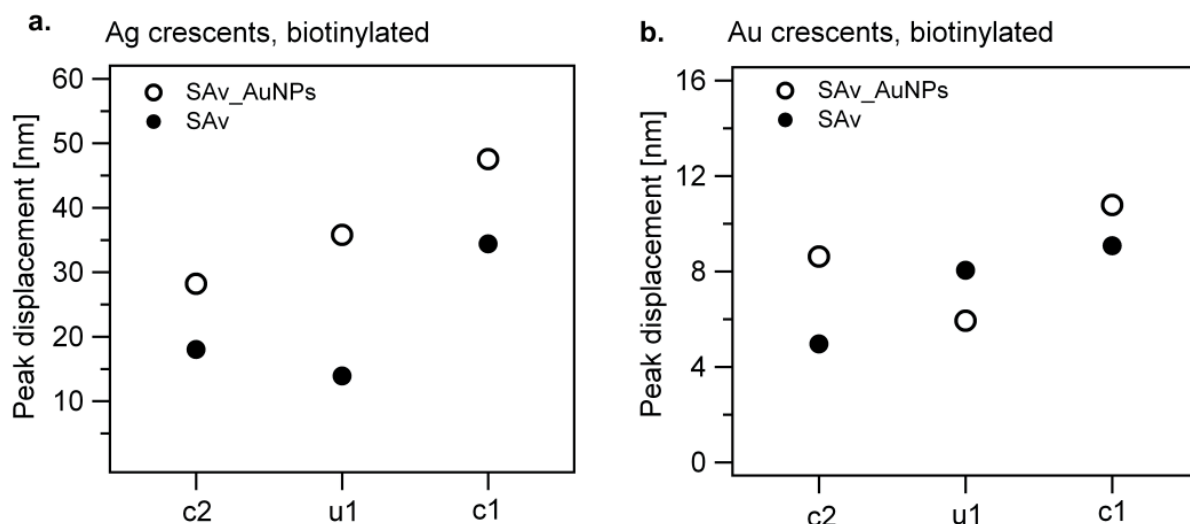


Figure 4-13: peak displacement of the 3 main resonances upon the addition of Sav and Sav-modified Au NPs for Ag (a.) and Au (b.) crescents.

4.4 Conclusions

Thin layer sensing

A measurement of the optical response of crescent shaped nanoparticles to the successive attachment of thin polymer layers was presented. These experiments resulted in a clear mode-dependent red shift of the multiple crescents' resonances upon layer growth.

Typical decay lengths were extracted from exponential fits and used as estimate for the near field confinement. In terms of sensitivity, the response of all modes was found to be comparable. The introduction of two simple physical models – the plane interface and the rod - gave estimations to the field confinements comparable to the experiments. Since it is possible to monitor several resonances in one single experiment, simultaneous determination of multiple material parameters should be possible in ultimately small modal volumes, which would represent a major advantage for sensing applications.

Sensing of bio-recognition events

The results show that the use of Au crescent shaped nanoparticles is very limited when it comes to the sensing of a few recognition events on their surface. The use of SAV-functionalized Au-NPs does not lead to significant improvements.

Since the peak displacements can not be considered significant due to the experimental approach itself, a simple solution to extract more accurate information from this type of experiment would consist in changing the approach to an in-situ one, which would eliminate the dispersion in the measurement of the peak positions. A second approach to solve this problem would consist in producing samples with narrower dispersions (improving the fabrication process). These considerations hold both for the Au as for the Ag crescents.

Silver crescents show greater peak displacements (at least a 3 x factor) upon the same chemical treatments than the Au crescents. The exposure to Sav-modified Au-NPs amplifies the measured peak displacement and could be considered for a simple approach to improve the quality of the measurements. Further tests, i.e. controlled exposure to all chemical agents save the binding species, AFM and SEM imaging are necessary to validate these first results.

In order to validate any statement about the relative higher sensitivity of the Ag nanocrescents with respect to the Au ones, it would necessary to do the thin film sensing experiments also on the Ag nanoparticles. It is important to note, though, that the thin films cannot be built using exactly the same procedure as introduced in Chapter 2, because the particles would be corroded in the acid solutions. The polyelectrolyte solutions should be properly tailored not to damage the nanocrescents, and to give rise to homogeneous thin films. All determinations of film thickness (via AFM and optical methods), refractive index, etc. should be repeated in this case. Only then a quantitative comparison on sensitivity would be meaningful. This last issue remains an open area for further studies on the sensitivity of the particles.

5 . Fluorophores close to crescent shaped nanoparticles

Tailored nanometric antennas can be used to match the absorption or emission spectrum of molecules [Novotny and Hecht 2006; Chen et al. 2007; Gerber et al. 2007; Rogobete et al. 2007], atoms [Gerber et al. 2007] or quantum dots [Farahani et al. 2005]. Changes in the electromagnetic environment the molecules sense can alter properties like their spectrum [Le Ru et al. 2007; Ringler et al. 2008], lifetime [Anger et al. 2006; Kühn et al. 2006] or even emission direction [Mertens et al. 2006; Taminiau et al. 2008].

In this chapter, gold nanocrescents were studied in their role as nanoantennas, modifying the emission of fluorescent species in their local environment. This type of study has usually been focused in the role of plasmon modes (through the near fields associated to them) modifying the emission/absorption of dyes (or other emitting species) in a one-photon approach. Non-linear processes (i.e., two-photon processes), as such, are particularly sensitive to field enhancements [Bouhelier et al. 2003; Imura et al. 2004; Ueno, Juodkazis, Mizeikis et al. 2008; Ueno, Juodkazis, Shibuya et al. 2008]; meeting plasmon resonances in a nanoparticle should then be provide ideal conditions for this type of phenomena to take place.

The nanocrescents explored in this work exhibit resonances in the near infrared part of the spectrum [Rochholz et al. 2007], which should affect the emission/absorption of i.e., dyes emitting/absorbing also in the near infrared. Fluorescence studies in this wavelength range imply several technical drawbacks, which could be easily overcome when working in the visible part of the spectrum.

When compared to the latter, two photon processes present several advantages; i.e. they are more sensitive to field enhancements and would allow for the study of plasmon-mediated enhancement using the nanocrescents as platform, but working in the visible range.

In the following, a brief introduction to two-photon processes is presented, along with a detailed description of the experimental approach to fluorescence enhancement studies, and the corresponding results.

5.1 Two-photon excitation

Two-photon processes rely on the simultaneous absorption of two photons of lower energy than the necessary to produce a transition from a ground to an excited state [Goeppert-Mayer 1930; Valeur 2002]. This is only possible in presence of a high photon flux, so that the probability of a two photon absorption process becomes significant [Goeppert-Mayer 1930; So et al. 2000; Valeur 2002].

When a single light source is used for excitation, the two photons have the same wavelength. When two different light sources are used (λ_2 and λ_3), then the wavelength corresponding to the excited transition (λ_1) can be estimated as $\frac{1}{\lambda_1} = \frac{1}{\lambda_2} + \frac{1}{\lambda_3}$. The first process (2 photons of equal energy) is usually termed simply as a two-photon process, while the second is usually referred to as a two-colour one [Valeur 2002] (see Figure 5-1 for a simplified scheme).

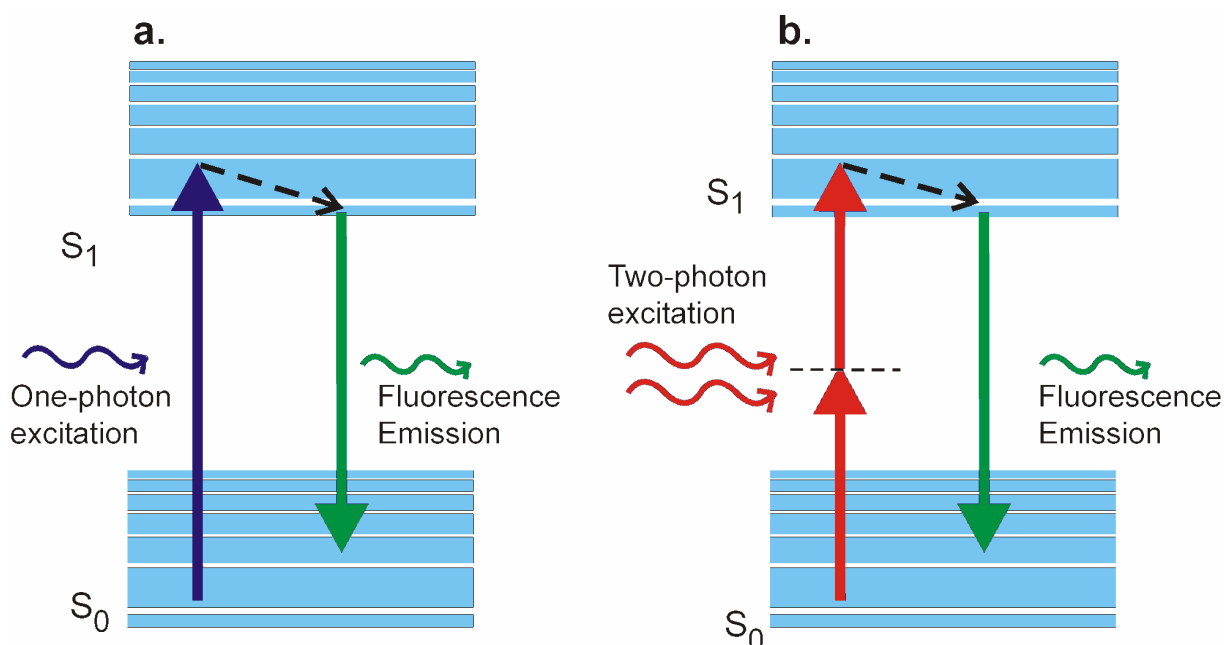


Figure 5-1: scheme of a simplified two level system, comparing one- and two-photon excitation.

In this work, first studies on the fluorescence of a green emitting dye (*Alexa 488*, *Invitrogen*) placed close to the crescent structures are presented. The crescents

have interesting resonances in the near infrared domain, which makes them ideal candidates to study resonance-mediated fluorescence phenomena in a two-photon approach.

Several factors can trigger changes in the emission of dyes; the environment they sense plays the key role [Valeur 2002; Novotny and Hecht 2006]; i.e. the distance to which the fluorophores are placed from the structures is fundamental [Kühn et al. 2006; Novotny and Hecht 2006; Gerber et al. 2007]. The emission of dyes placed too close to metal (some nanometers) could be easily quenched [Knoll 1998], while placing them too far away from the structures could hinder any near field mediated interaction with the fluorescent species.

In the following experiments, green fluorescent dyes were placed at controlled distances to the nanocrescents using polyelectrolyte bilayers. The bilayers can be attached to the particles in a controlled and easy manner (see Chapter 2 – Fabrication), and provide simultaneously a spacer and an anchor for the dyes. Like this, distance-dependent fluorescence studies on the dye-structure interaction, can be easily carried out.

5.2 Experimental

5.2.1 Sample preparation

Standard crescent shaped nanoparticles were prepared on thin glass coverslips (*Menzel Gläser #1*), to obtain mostly single, isolated structures in a square micrometer area, which allows for single particle identification when imaging in a confocal microscope. The samples were treated with 3-aminopropyltriethoxysilane (*3-APTES, Aldrich*) in gas phase, in an oven at 150 °C, for three hours (all details for this treatment can be found in Chapter 2 – *Fabrication*). After proper rinsing and drying, the samples were submerged alternately in polyelectrolyte solutions (polyallylamine, “PAH” and polystyrene sulfonate, “PSS”) in order to build 1, 3 and 5 bilayers, respectively. This procedure gives rise to substrates covered homogeneously by the bilayers (see Chapter 2). One extra sample was kept as a reference after the exposure to 3-APTES to investigate the fluorescence emission of the structures without spacers.

Fluorophores (*Alexa 488, succinimidyl ester, Invitrogen Inc.*) were diluted in dimethylsulfoxide (DMSO) to an approximately 1 μM concentration. A drop of the dye was dropped on the amine-terminated polyelectrolyte layer, and left for approximately 1 min. After this, the sample was rinsed with DMSO and blown-dried with nitrogen. Figure 5-2 presents the structure and fluorescence spectrum of this dye, and a simplified sketch of a sample, indicating the particle, the polyelectrolyte spacers and the fluorophores. The latter were attached covalently to the surface via the amino-terminated chains of PAH. The attachment of the dye proceeded just before the measurements for the samples with 3 and 5 bilayers, while the measurements for the 1 bilayer case corresponds to a sample prepared 2 weeks in advance and stored. It is assumed that, after the preparation, a comparable amount of fluorophores attaches to each sample.

5.2.2 Characterization

UV-Vis transmission spectroscopy

Non-polarized transmission spectra of the samples before and after the polyelectrolytes' attachment were measured in a conventional spectrometer (*Lambda 900, Perkin Elmer*) in order to follow the resonances' position upon the addition of polymer¹².

Confocal Microscopy

A commercial confocal laser scanning (or "CLS") microscope (*Carl Zeiss, Jena, Germany*) consisting of the module LSM 510 and an inverted microscope model Axiovert 200 was used in these experiments. A water-immersion objective was used (C-Apochromat 40x/1.2 W Corr with numerical aperture (NA) of 1.2, (*Carl Zeiss, Jena, Germany*). One-photon CLS imaging of the sample was done via excitation with an Ar laser at 488 nm. The two photon excitation was achieved using a titanium:sapphire laser (Ti:Sa) (*Mai Tai, Spectra Physics Inc., USA*) coupled to the confocal microscope. The Mai Tai laser is tunable in the range 780-920 nm and provides ~100 fs pulses at a repetition rate of 80 MHz. For the two-photon excitation, all images were recorded in a 512 x 512 pixel definition, at 8-bits/pixel resolution, integrating

¹² The complete data set can be found in Appendix B

either $1.6\mu\text{s}/\text{pixel}$ or $2.51\mu\text{s}/\text{pixel}$. The data extracted from the microscope's software (*Zeiss*) is presented in a gray scale and does not correspond to real photon counts, but to normalized data. The exact extraction of photon counts from these measurements is not a straightforward matters, but the information provided by the company (*Zeiss*) indicates a proportionality to real photon counts from the gray scale data. The fluorescence images were recorded using two polarization conditions at excitation (either c or u, see Chapter 3). The two-excitation conditions were achieved rotating the sample mechanically. The intensity of the excitation beam was measured for different wavelengths at the objective's position, without the objective being placed in the beam path. An approximate ¹³ calibration curve was built for these experiments and can be found in Appendix B. All other relevant parameter settings were left constant throughout these experiments (detector gain, pinholes, etc.).

n

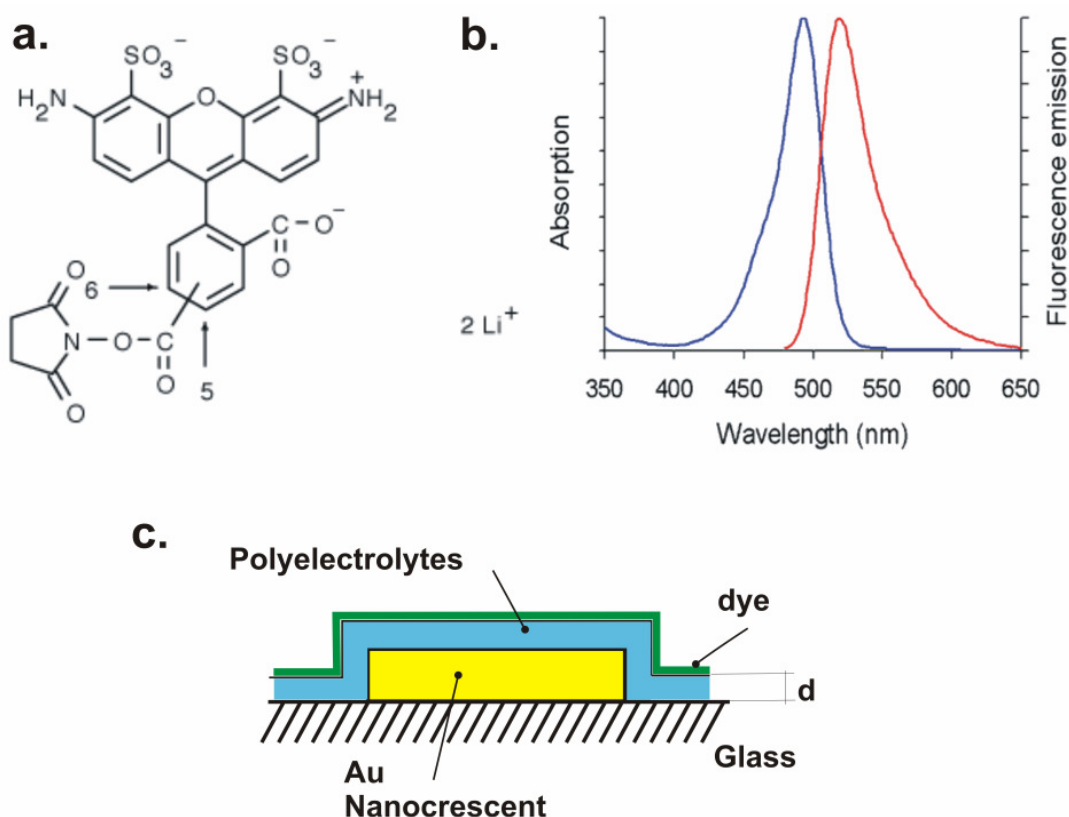


Figure 5-2: (a) structure of Alexa Fluor 488 carboxylic acid, succinimidyl ester ($\text{C}_{25}\text{H}_{15}\text{Li}_2\text{N}_3\text{O}_{13}\text{S}_2$); (b.) fluorescence spectrum of Alexa Fluor 488 dye-labeled oligonucleotide/ H_2O [Invitrogen] (c.) sketch of a cross section of typical sample (d: thickness of the polyelectrolyte bilayers).

¹³ The software provided by Zeiss to run the confocal microscope expresses intensities as procentual values, with no indication of real power being irradiated on the sample – Calibration curve to be found Appendix B

5.3 Results and discussion

Samples with nanocrescents, polyelectrolytes and no dyes

Rough metal films and nanoparticles are known to give rise to strong photoluminescence [Mooradian 1969; Boyd et al. 1986; Beverslius et al. 2003; Bouhelier et al. 2003; Imura et al. 2004; Bouhelier et al. 2005]. In order to collect reference measurements of the polymer-coated samples and quantify the possible contribution of both particles and polyelectrolytes, fluorescence images were recorded using the Ti:Sa laser as excitation before the addition of the fluorophores. Figure 5-3 (a.) and (b.) present fluorescence measurements on samples covered with crescents and only with polyelectrolytes (PE), no dyes added. The first image corresponds to a sample covered with 3 bilayers (app. 12 nm of polymer) and shows a homogeneous, relatively low background contribution. The second image corresponds to a 5 bilayer sample, also with no dyes added. There, single spots are easily recognizable, along with a homogeneous background, comparable to that of the 3 bilayer case. The spots reach a contrast of approximately 50 – 70, while the background stays in a level below 20. This effect could be related both to fluorescent contamination in the polymers, or to emission from the particles. As will be shown later, this spots can be identified with the positions where a particle sits.

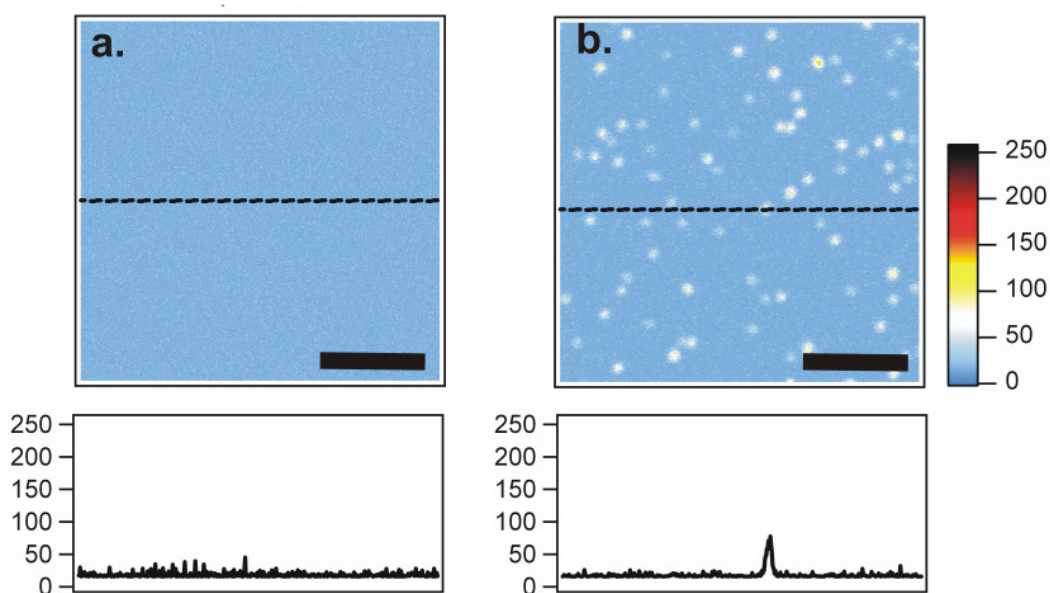


Figure 5-3: fluorescence image, excitation: 920 nm, samples before the addition of fluorophores (a.) 3 bilayers, (b.) 5 bilayers. Intensity = 5 %. The dotted line represents the line profile depicted below each measurement.

Figure 5-4 presents a fluorescence image recorded using 850 nm ($i = 1,1 \%$) as excitation of a sample covered with standard Au nanocrescents, and treated with 3-APTES (see Chapter 2 for details on fabrication procedures).

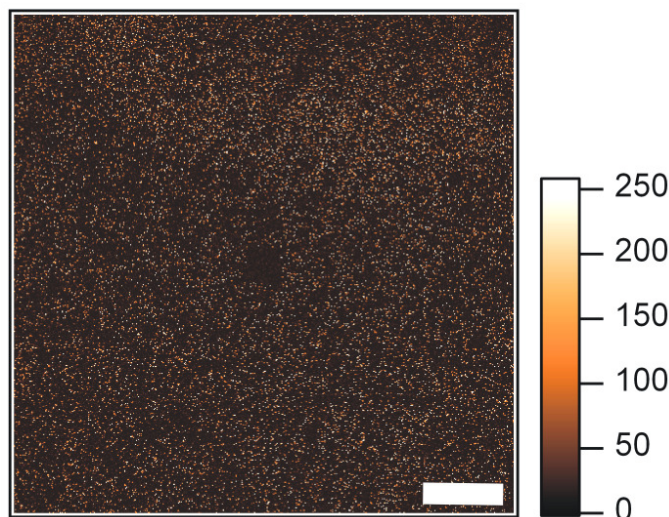


Figure 5-4: fluorescence image recorded on a Au nanocrescents sample treated with 3-APTES. Excitation: 850 nm, $i = 1,1 \%$. The scale bar represents 50 μm .

This image shows a large area of a sample covered with nanocrescents with no further treatment but a silanization. It is interesting to note that the bright spots, identified with the nanoparticles, show considerable emission, which can also be bleached (or the particles, destroyed). This is opposite to i.e. the sample presented in Figure 5-3 (a.), where the particles are covered with polyelectrolyte layers and a very low contrast is detectable. It is important to point out that these samples were prepared in different batches, although following the same fabrication procedures, which calls for further reference measurements of untreated and treated samples to quantify the emission from the bare crescents and the effect of the chemical treatments on them.

The references for the next experiments (crescents, spacers and dyes under two-photon excitation) are linked to Figure 5-3, since they were measured on the same samples, under the same conditions, but before the addition of any fluorophores.

Samples with nanocrescents, polyelectrolytes and Alexa 488

After exposing the samples to the solution of the green fluorophore, fluorescence images were recorded exciting the sample at 488 nm (one-photon process) and at

920 nm (pulsed excitation with Ti:Sa laser). The results are summarized in Figure 5-5 (a.) and (b.).

A bright, homogeneous background with dark spots can be seen in (a.), and precisely the opposite situation can be identified in (b.). The background in (a.) can be associated to the dyes excited at 488 nm (one photon process); being the dark spots identified with the positions of the nanoparticles. From this image it is possible to observe, also, the homogeneity of the dye coverage on the sample surface.

The bright spots in (b.) can be associated with the positions where particles sit. Since the sample is completely and homogeneously covered by the green emitting dye, the brighter spots identified in (b.) can be associated to enhancement events occurring for dyes close to the crescents (Figure 5-3 shows that the background counts are lower than those corresponding to Figure 5-5 (b.)).

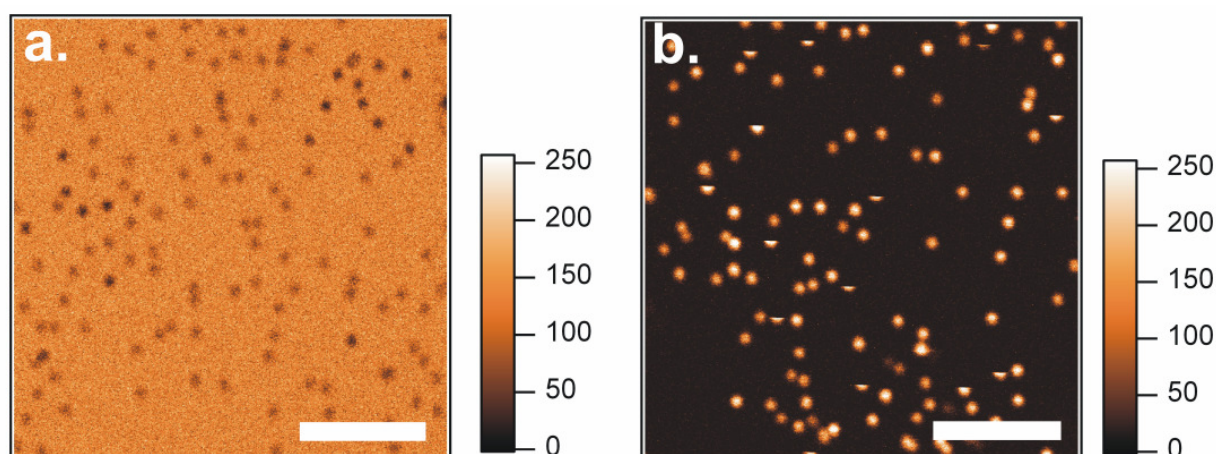


Figure 5-5: CLS image of a sample covered with PE and Alexa 488. (a.) Excitation: 488nm (b.) excitation at 920 nm. The scale bar represents 5 μ m.

These enhancement events can be associated to a two-photon process taking place in the close proximity of the nanocrescents, and are the main subject of this study.

This last figure (b.) also shows partially darkened spots. This phenomenon could be explained by melting particles or simply photobleaching. Further electron microscope imaging or single particle scattering measurements would be necessary to validate this hypothesis.

Further reference measurements (i.e. bleaching tests) were also carried out in order to test the response of the samples to intense / prolonged exposure to illumination. Figure 5-6 presents two images of such tests; the first one (a.) at 488 nm (intensity = “i” = 7 %, one photon excitation) and the second one (b.) at 920 nm (pulsed excitation).

The first image (a.) can be directly explained by bleaching of the fluorophores attached to the polymers; the second one (b., pulsed excitation), where the high contrast spots (associated to the position of the nanocrescents) disappear after scanning, could be both related to bleaching or partial destruction (i.e. melting) of the nanoparticles. The information presented in Figure 5-6 (b.) is not concluding in this respect, but it is useful to set a threshold for the maximum excitation intensities for further measurements.

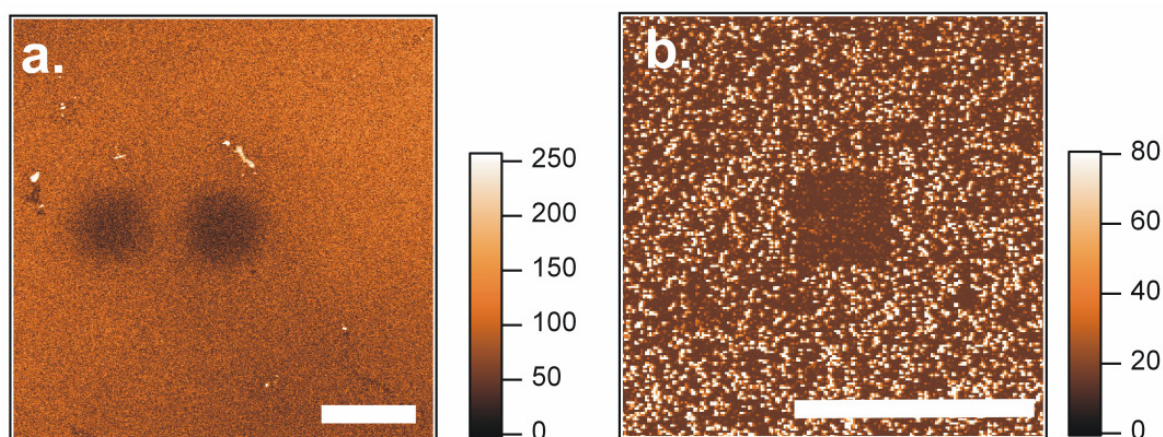


Figure 5-6: fluorescence images showing bleached spots. In (a.) the spots (and measurement) were done using a 488nm laser; in (b.), 920 nm. In both cases, the integration time/pixel is 1.6 μ s, the pinhole has 72 μ m. The scale bar represents 50 μ m.

Nanocrescents with controlled thickness spacers, and dyes: two photon excitation experiments

In the following experiments, green fluorescent dyes were placed at controlled distances to the nanocrescents using polyelectrolyte bilayers. The fluorescence emission of the crescents with polyelectrolytes and dyes is investigated when exciting the samples with a pulsed laser emitting in the near infrared.

Figure 5-7 b. through d. present schemes of the different geometrical combinations explored of sample and spacing (1, 3 and 5 bilayers), along with the extinction spectra of the samples analysed, with the fitted contributions of the **c** and **u** modes; Figure 5-7 (a.) depicts the significance of these particular spacings: there, a typical

peak displacement vs. bilayer thickness curve is displaced for the c_2 and u_1 resonances. From this type of curve it is possible to estimate decay lengths associated to each mode, which in turn play a fundamental role in the excitation of the fluorophores placed close to the nanocrescents. A saturating displacement curve for a given spacer thickness and resonance is an indication for, i.e. a negligible contribution of the near fields to the excitation of the fluorophores. In this experiments, three main conditions are explored: (1.) fluorophores very close to the structures (app. 4 nm), well embedded in these near fields; (2.) fluorophores placed with an intermediate spacing (app. 12 nm), and (3.) fluorophores placed at a thickness where the contribution of one of the modes is expected to be negligible (c_2).

Figure 5-8 through

Figure 5-10 present the results on fluorescence measurements of *standard* gold nanocrescents, covered with 1, 3 and 5 polyelectrolyte bilayers and decorated with Alexa 488, respectively. The measurements were done at mainly two different wavelengths (800 or 850 nm, and 920 nm), and at two different polarization combinations for the excitation (u and c , achieved via mechanical rotation of the sample holder). Combining different polarizations and wavelengths it is expected to meet different resonances of the nanocrescents, which should affect the emission of the fluorophores placed in their local environment. The corresponding extinction measurements of each sample, as well as the fitted contributions for each resonance of interest (c_2 and u_1) are to be found in Figure 5-7.

In the following, a description of the results for each given spacer thickness is presented.

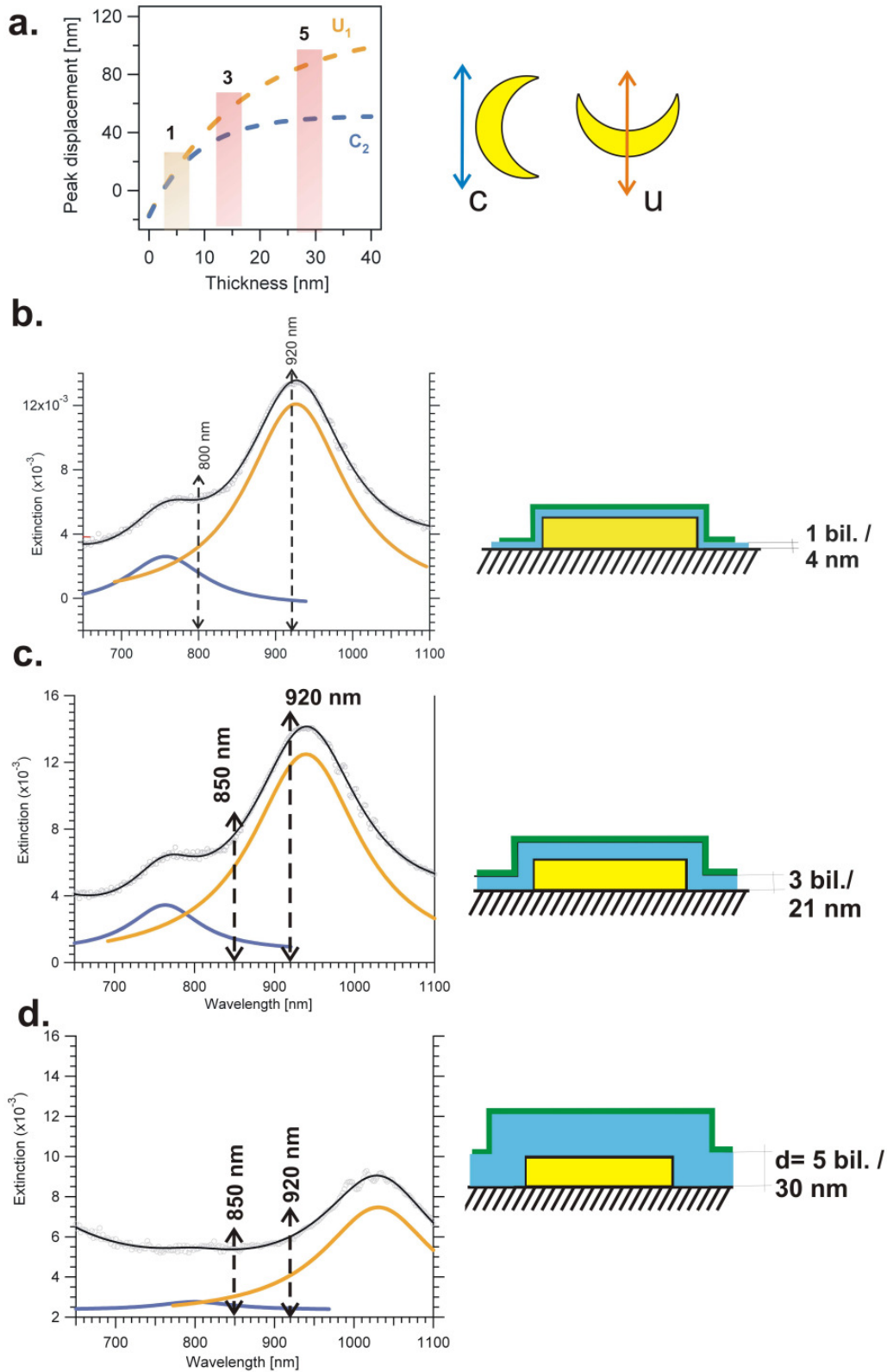


Figure 5-7: (a.) peak displacement as a function of the overlayer thickness (see Chapter 4), exemplifying the penetration depths of the u_1 and c_2 modes, and the positions of the different sample configurations used in these experiments (1, 3 and 5 bilayers); (b., c. and d.) transmission spectra of the samples used in the experiments, along with the fitted contributions of each mode (c_2 , blue, u_1 , orange) and a sketch of the final geometry of the samples.

Crescents, 1 bilayer and fluorophores

Figure 5-8 presents fluorescence measurements of a standard Au nanocrescents sample covered with 1 polyelectrolyte bilayer and green emitting fluorophores. The bilayer was approximately 4 nm thick and should help (at least partially) preventing the complete quenching of fluorescence by the metallic structure, while also helping to place the fluorophores close enough to them so that they sit within the typical decay lengths of the near fields (approximately 10 and 20 nm for the \mathbf{c}_2 and \mathbf{u}_1 resonances, respectively).

This set of images was recorded at two different wavelengths (800 and 920 nm) and two main polarization conditions (obtained by mechanical rotation of the sample). A simple division of measurements is made then for these cases; in (a.) the 800 nm measurements are presented, while (b.) introduces the 920 nm ones. The polarization at excitation is presented in two different rows, as \mathbf{c} and \mathbf{u} . The different excitation intensities¹⁴ used for the experiments are signaled in each image. Each image is usually presented accompanied by a line profile to make clearer the results expressed in the color code and make more straightforward comparisons. The color scale next to the images indicates a quantity that should be proportional to the real counts collected/pixel.

When exciting at 800 nm (section (a.) Figure 5-8) and considering any polarization / intensity combination, it is possible to observe that scanned area is covered by spots with significantly higher counts (at least a 2x factor difference for the \mathbf{u} polarization, but significantly higher for \mathbf{c}) than the fairly even background (which lies for all cases in the 20 counts range). When exciting with \mathbf{c} polarization, a high contrast in the spots is detected with relatively low excitation intensities ($i = 2\%$). The rotation of the sample to a \mathbf{u} configuration gives rise to essentially weaker spots, even for higher excitation intensities, which would correlate to a polarization (mode) dependent enhancement.

¹⁴ These are referred to as percentage, as obtained from the driving software of the microscope. A corresponding calibration curve is present in Appendix B.

When exciting at 920 nm (section b.), the contrasts for the different polarizations are even stronger. For **c**-polarized excitation, $i = 2\%$ already gives rise to a contrast of fairly 200.

Bleaching, as a drawback for this type of experiment, is already observable for, i.e. the 920 nm, **c**, $i = 2\%$ combination, where on the right side of the image weaker spots are imaged after a previous scan with the laser. This issue is of fundamental importance, since bleaching of the fluorophores hinders any real quantification of the enhancement processes behind these experiments.

For **u** excitation, almost no signal is detected for $i = 2\%$. When $i = 5\%$, a weak increase is detected.

From these set of 7 measurements, a clear point is to be observed, that is, a strong polarization character of the fluorescence intensities measured in these spots, both for the measurements at 800 and 920 nm.

If a correlation is made to the information presented in Figure 5-7 about the resonances (extinction spectra of the corresponding sample, presented in Figure 5-7 (b.)), the assignation of the strongest resonances and the enhancement events is inverted; i.e. at 920 nm the **u** component is the strongest, while the fluorescence images show the weakest spots.

A similar situation is observed for the 800 nm measurement, but the contrast is not so dramatic as for $\lambda = 920$ nm.

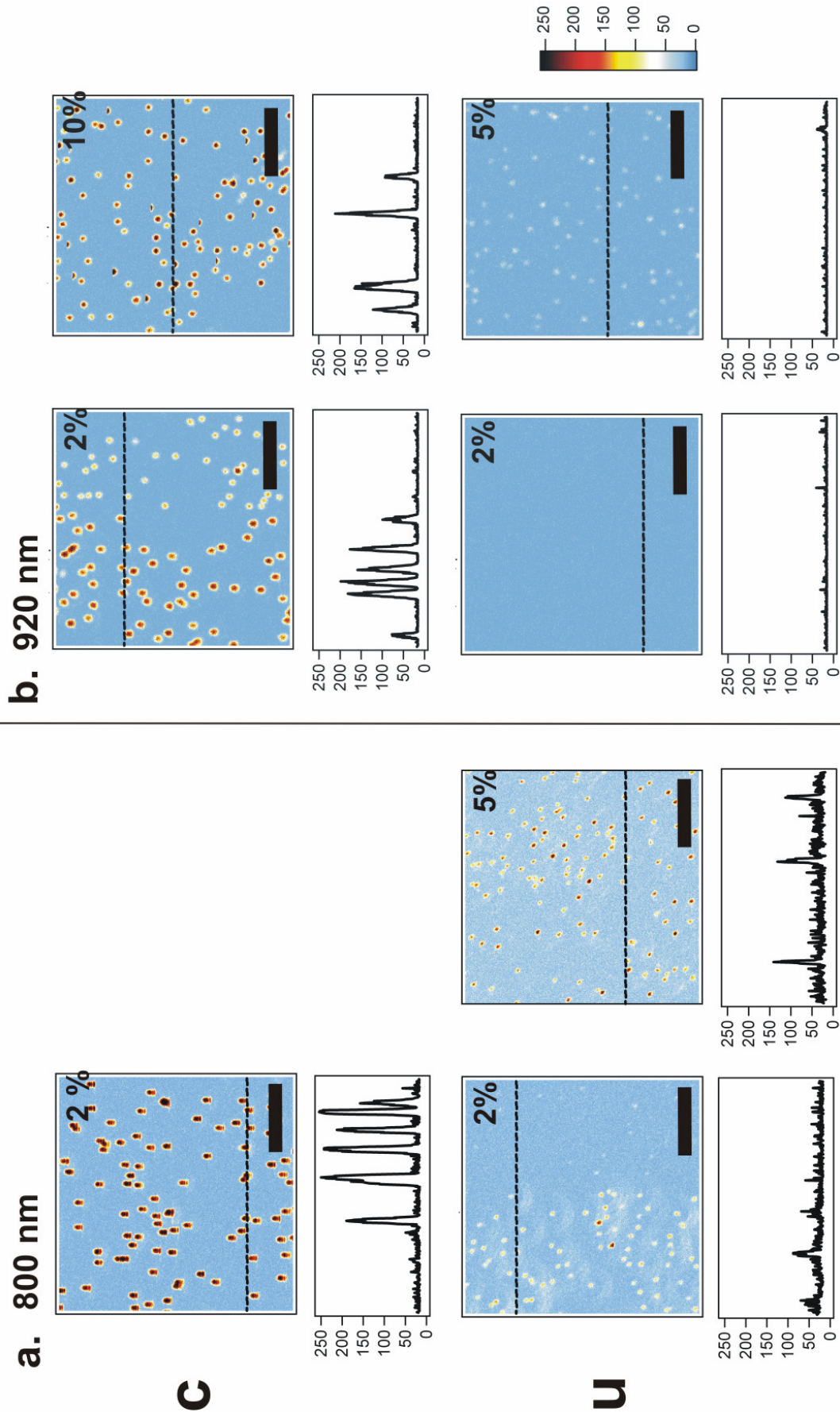


Figure 5-8: fluorescence for pulsed excitation at 800 and 920 nm, for a sample covered with 1 bilayer and Alexa 488. The scale bar represents 5 μm.

Crescents, 3 bilayers and green fluorophores

Figure 5-9 presents fluorescence measurements, of a sample covered with a thicker spacing (approximately 20 nm). Within this thickness range, the c_2 component is expected to be saturated, while the u_1 still presents a non-negligible component to the near field (see Figure 5-7 a., case “2”).

Figure 5-9 (a.) presents measurements for the 850 nm at excitation. For the c polarization, a clear contrast is detected upon increasing the intensity from 1 to 2 %, evolving from an almost homogeneous background (app. 20 counts) with no spots, to a condition where bright spots (at app. 100 – 150 in the scale) are clearly detectable.

For the u polarization, partially saturated spots are already detected even at so low intensities as 1 % at excitation. This effect correlates to a stronger u component in the spectrum (see Figure 5-7 for details) at that wavelength, indicating possibly an increased excitation condition.

When exciting with $\lambda = 920$ nm (Figure 5-9 (b.)) and c polarization, a weak increase (less than a factor 2) of the contrast with respect to the background at some spots is detectable for $i = 2\%$. The increase to 5% on the intensity gives rise to, in some cases, a 3 – 4 factor increase on the spots compared to the background.

For the same wavelength, and u polarization, a comparable effect is seen, but the 3 – 4 factor increase is correlated to a change of only 1% to 2 % in the excitation (compared to a 1 to 5 % for the c case). At this wavelength, the u polarization should play a significant role in the excitation process see Figure 5-7 (c.) for details), since the near field associated with it should not be saturated in this case, and the orientation of the sample should be optimum for a plasmon-mediated phenomenon.

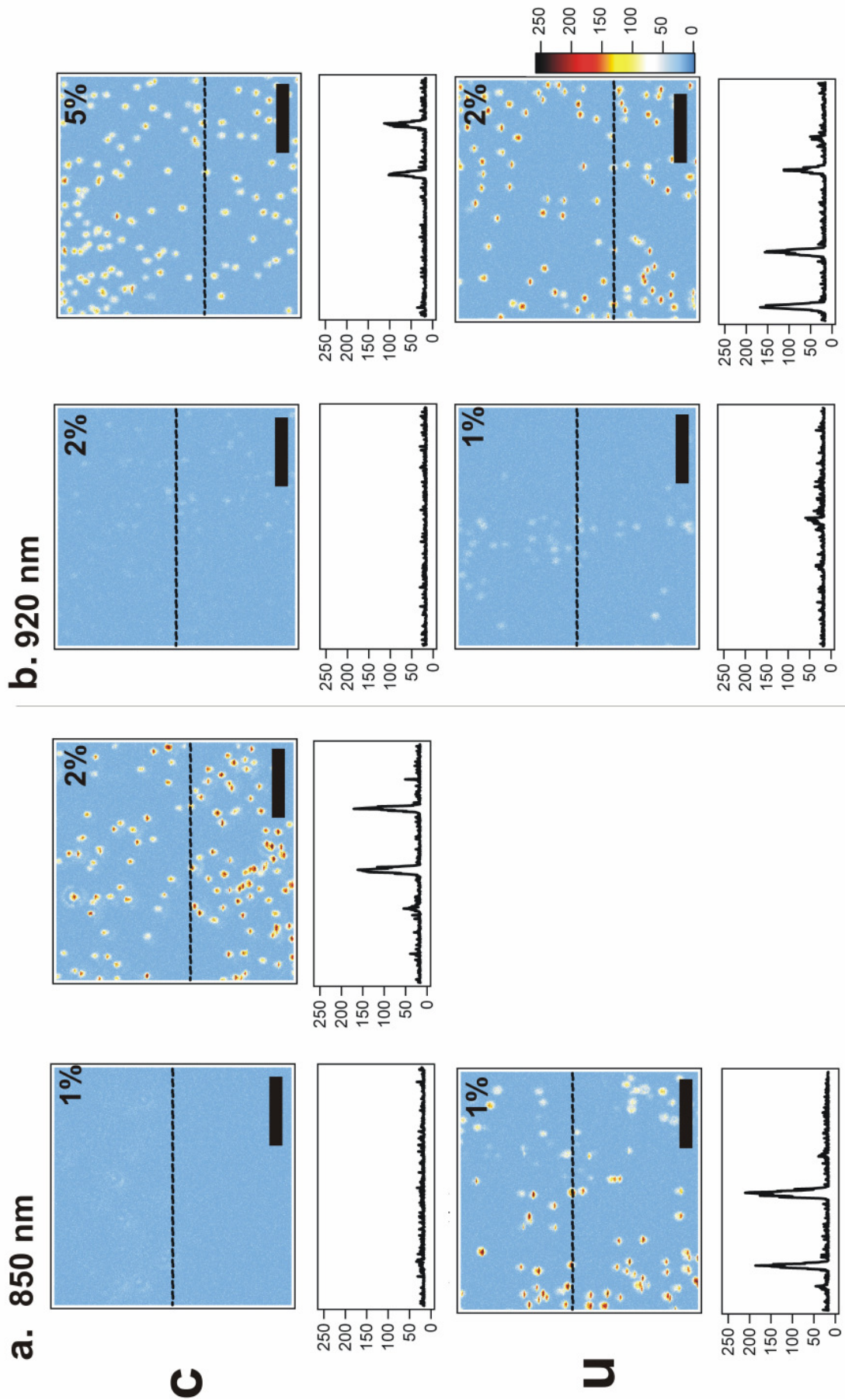


Figure 5-9: fluorescence measurements, 2-photon excitation at 850 and 920 nm, for a sample covered with 3 bilayers and Alexa 488. The scale bar represents 5 μm .

Crescents, 5 bilayers and fluorophores

Figure 5-10 presents the results for a standard nanocrescent sample covered with 5 polyelectrolyte bilayers and fluorophores. All experimental parameters are equal to the previous (3 bilayers) experiment.

The first point to notice in these measurements (for both 850 and 920 nm, that is Figure **5-10** (a.) and (b.)) is that the overall contrast of the bright spots (when detectable) is in all cases significantly smaller than in the previous 2 experiments. For the 850 nm excitation and *c* polarization, some weak bright spots are detectable for $i = 2\%$ (compare to the results on Figure 5-9). When increasing the excitation to 5%, the contrast increases in an almost $\times 3 - 4$ factor (see Figure **5-10** for details). The bleaching effects are also present in these measurements, one of the reasons for which only a qualitative description of the phenomenon can be made.

For the *u* polarization, some weak (50 – 100 in the color scale) spots are detectable at $i = 2\%$ (compare to the same measurement, but on Figure 5-9, where for $i = 1\%$ and same conditions, an average doubled contrast is evident).

When $\lambda = 920$ nm (section (b.)) and *c* polarization, only weakly enhanced spots are present for $i = 5\%$ (compare for the experiments with 3 bilayers in Figure 5-9, where almost twice as intense spots are detectable for similar excitations). The contrast for the *u* polarization at this wavelength is significantly stronger than that for *c*, but still comparable to the results of the 3-bilayer experiment (see Figure 5-9).

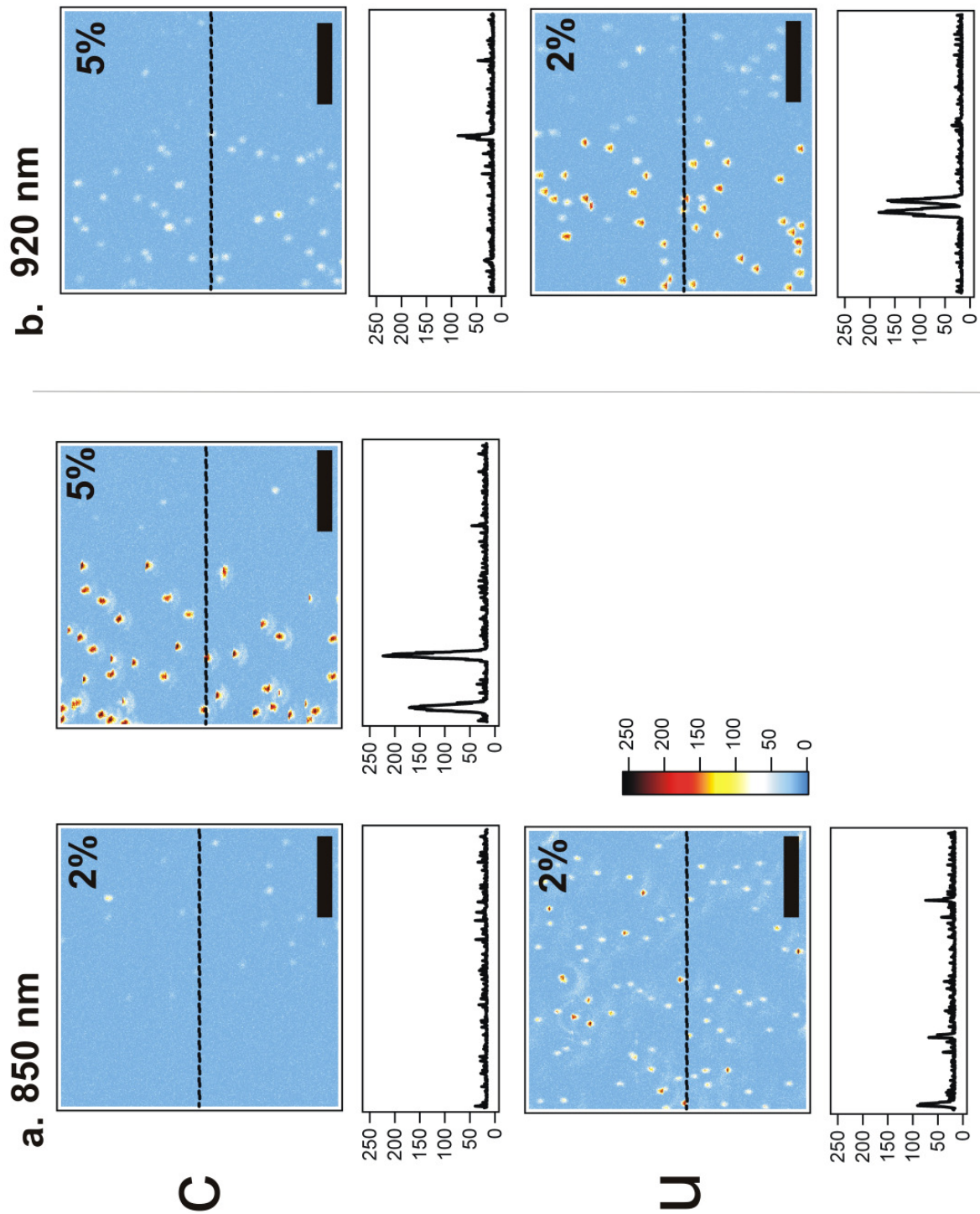


Figure 5-10: fluorescence measurements, 2-photon excitation at 850 and 920 nm, for a sample covered with 5 bilayers and Alexa 488. The scale bar represents 5 μm .

5.4 Summary and conclusions

Standard nanocrescents with resonances in the near infrared were prepared on glass and decorated with different amounts of polyelectrolyte layers (spacers), and fluorophores emitting in the green part of the spectrum. The samples were investigated using confocal fluorescence microscopy, to a single particle level, when excited with a Ti:Sa laser working in the 780-920 nm range. The combination of excitation and fluorophores should favour a two-photon process.

Several questions were addressed in these experiments, but namely the focus was set on role of the resonances on the particles – tested via polarization changes -, the role of the excitation intensity, and the effect of placing fluorophores at significantly different distances to the particles (and prove the interaction of the near field of each mode with the fluorophores). Assuming that, i.e. the amount of fluorophores is comparable in all samples, etc. the measurements would show that, upon greater spacer thicknesses, the enhancement events are drastically reduced, as expected for decaying near fields.

The polarization effect (meeting the **u** or **c** resonances, respectively) is also present, obtaining usually stronger contrast when meeting one resonance in wavelength and polarization conditions. This is observable for both the 3 and 5 bilayer cases, though not so clear in the 1 bilayer case (for fluorophores placed to a 4 nm distance to the crescents).

In order to do a real estimation for the enhancement events, it is of fundamental important to access the actual counts from the fluorescence measurements, as well as establishing a proper calibration for the excitation intensity. Without this information, all comparison made holds a qualitative character.

An important point to solve also in this respect is that of the strong bleaching (which is present and easily noticeable during the measurements), and of the possible destruction of the nanocrescents at high excitation powers. The measurements presented in this work, though suggestive, should be considered only as proof of principle and first approach to the problem; further experiments under controlled conditions are necessary to build a fully quantitative view of the phenomenon.

Part II

**Model system: ellipsoid-like noble-metal
Nanoparticles**

6 . Fabrication of discs and ellipsoid-like noble metal nanoparticles

6.1 *Introduction and motivation*

Nanosphere (or “natural”) lithography, as introduced in Chapter 2, has proven to be a powerful technique to fabricate with great ease a wide range of structures using colloids as a masks, i.e. from simple disc-like structures [Hanarp 2003], to more complex nanotriangles [Willems and Van Duyne 2007], nanorings [Aizpurua, Hanarp, Sutherland, Käll, Bryant and Garcia de Abajo 2003] or nanocrescents [Shumaker-Parry et al. 2005].

In general, all of these structures can be tuned spectrally by changing their size, material, or modifying slightly their shape [Willems and Van Duyne 2007]. For the nanocrescents, in particular, this is done with relative ease in the near infrared part of the spectrum, as has been presented throughout Chapters 3 and 4. Shifting the main resonances to higher energies requires the fabrication of essentially smaller nanocrescents. From a technical point of view, this process is limited to some 60 – 80 nm particles [Rochholz 2005]. These (gold) particles have resonances that lie, at most, in the 700 nm range [Rochholz 2005].

From technical considerations, it is most desirable to be able to work in the visible part of the spectrum, since there a wide range of commercial products (detectors, spectrometers, etc.) are readily available. Based on all the information collected so far for the nanocrescents, an intrinsic barrier is present in the near infrared.

It is of interest, then, to explore new shapes and materials to mimic the polarization-dependent nature of the resonances of the crescents, and to push the spectra into the visible.

In this chapter, nanosphere lithography is applied to produce silver and gold ellipsoid-like, flat nanoparticles. Previous work on gold flat ellipsoidal nanoparticles produced with conventional electron beam lithography has shown that these structures possess a wide spectral tuneability and a polarization-dependent response [Grand et al. 2006]. While the fabrication of metallic nanodiscs using nanosphere

lithography is already known from the literature [Hanarp 2003; Hanarp, Käll et al. 2003; Hanarp, Sutherland et al. 2003]; the technique can be easily extended to produce nanoellipsoids. For this purpose, a slight modification to the general approach for producing nanodiscs is introduced.

Section 6.2 deals with the fabrication procedures for both nanodiscs and nanoellipsoids, using nanosphere lithography. The optical properties of both discs and ellipsoids are explored in Section 6.3, where a wide range of sizes and shapes (ellipticities) were explored in order to study the spectral tuneability of these systems.

6.2 Fabrication

6.2.1 General methodology

The basic fabrication procedure for the nanoellipse/nanodiscs consists of dispersing the colloidal mask on a thin metal layer previously deposited on a flat substrate, and etching the material not protected by the colloidal mask with an ion beam. When the etching proceeds perpendicularly to the substrate, the resulting structures are nanodiscs; otherwise, the projection of the mask describes an ellipse on the substrate, with a given ellipticity determined by the etching angle (ϵ). After the etching procedure is finished, the mask is removed mechanically using a tape, leaving metallic shadows behind, which are finally the nanostructures of interest.

Figure 6-1 depicts schematically the fabrication process. The simplest structures occur for $\epsilon = 0$, resulting in nanodiscs. For $\epsilon > 0$, the resulting structures are expected to be flat ellipsoids. The long axis of the ellipses can be estimated to be $d_{\text{coll}}/\cos(\epsilon)$, being ϵ the angle of the beam relative to the surface normal. The short axis can be roughly estimated as d_{coll} .

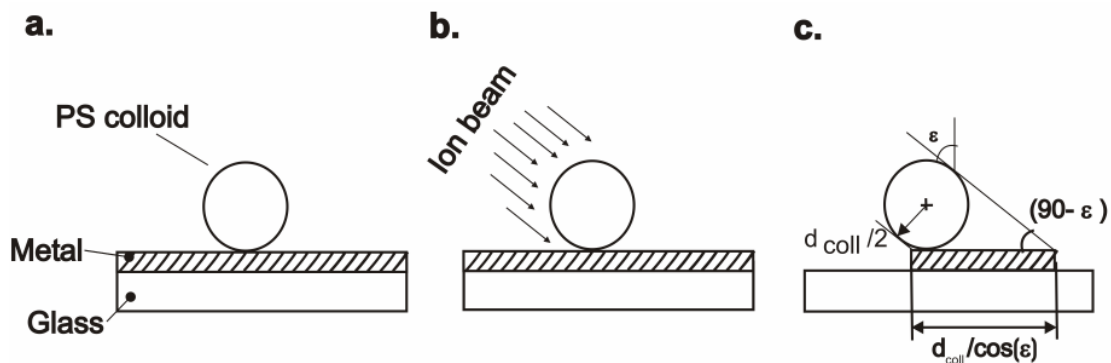


Figure 6-1. simplified scheme of the fabrication procedure for the nanoellipsoids - a) colloid dispersion on the surface of a metal-covered glass substrate b). ion etching c). (ideal) geometrical description of the particles according to its fabrication: the minor axis of the ellipse correspond to the colloids' diameter; the long axis can be estimated as $d_{\text{coll}}/\cos(\epsilon)$.

The main variables, then, to tailor the geometry of the particles are reduced in this case when compared to the nanocrescents (see Chapter 2); here, in principle, only the size of the colloidal mask (d_{coll}) and the etching angle (ϵ) plays a significant role.

Figure 6-2 presents a sketch of the geometries expected for an ideal process, using different etching angles ($\epsilon = 0^\circ, 30^\circ, 45^\circ$ and 65°).

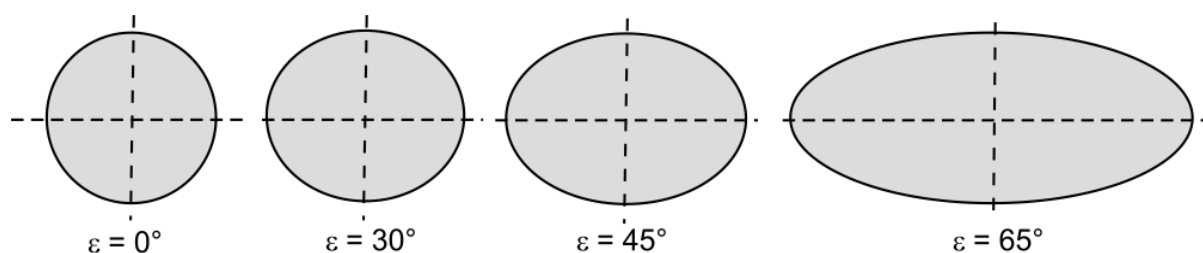


Figure 6-2: sketch of the different geometries expected for different etching angles ($\epsilon = 0^\circ, 30^\circ, 45^\circ$ and 65°)

For this picture to be valid, it is assumed that the ion beam is homogeneous and non-divergent, and that the colloids remain unetched or non-deformed. The last two factors are, at best, an approximation; but this still represents fairly well the shape of the resulting structures, as will be shown in the following.

Any drastic deviation from this model should lead to important distortions in the final shape of the particles, particularly, the ellipsoids.

When compared to the procedures to fabricate nanocrescents (see Chapter 2), it is possible to observe that this methodology is essentially simpler than to produce nanocrescents. Still, and as it will be shown in this and the following chapters, the particles produced by this method are very versatile plasmonic structures that can be used for sensing and enhanced spectroscopies.

6.2.2 Sample preparation

Ag and Au nanoellipse

A 40 nm thick silver (or gold) film was evaporated (*Auto 306, Edwards, Sussex UK*) on detergent (*Hellmanex, Hellma GmbH*) cleaned glass substrates (*Objektträger Glas, Menzel Gläser, Germany*). Polystyrene “PS” nanospheres (*Polystyrene*

Nanobead: NIST, Polysciences, Warrington USA) of different nominal diameters were randomly dispersed on top of the films, on a submonolayer coverage level. The samples were then exposed to an argon ion beam (*RR-I SQ76, Roth & Rau, Wüstenbrand, Germany*) incident on the surface at different angles (ϵ), and etched. The colloids, acting as protecting mask, prevented the removal of the material behind them. After the etching process, the colloidal mask was removed mechanically by means of an adhesive tape (*Scotch Magic Tape 810: 19mm × 33m, 3M France*). The remaining metallic objects (“shadows” of the colloidal masks) constitute the metallic nanoparticles.

6.3. Characterization

The samples were characterized using conventional UV-VIS-NIR transmission spectroscopy (*Perkin-Elmer, Lambda 900*). The device was equipped with polarization optics.

Scanning electron micrographs of representative samples were recorded with a scanning electron microscope (*LEO Gemini 1530*).

The photographs of the samples presented in this work were made with a conventional digital camera (*Fuji*).

6.3 Results and discussion

6.3.1 Nanodiscs ($\epsilon = 0^\circ$)

Ag nanodiscs

Figure 6-3 shows pictures of a some square centimetres sample covered with 100 nm Ag discs (a.) and (b.), and its corresponding scanning electron micrograph (c.). The sample shown in Figure 6-3 is very colourful, “reflecting” (scattering) green light and “transmitting” the red. This can be related to a plasmonic resonance occurring in the visible part of the spectrum; the fact of being so easily detectable with the eye is also related to the high surface coverage¹⁵ (several particles per μm^2 - see Figure 6-3 c. for a SEM image of the same sample, where the metallic discs on the substrate are easily recognizable).

¹⁵ Samples prepared with more diluted masks (less than 1 particle / μm^2) appear transparent to the naked eye.

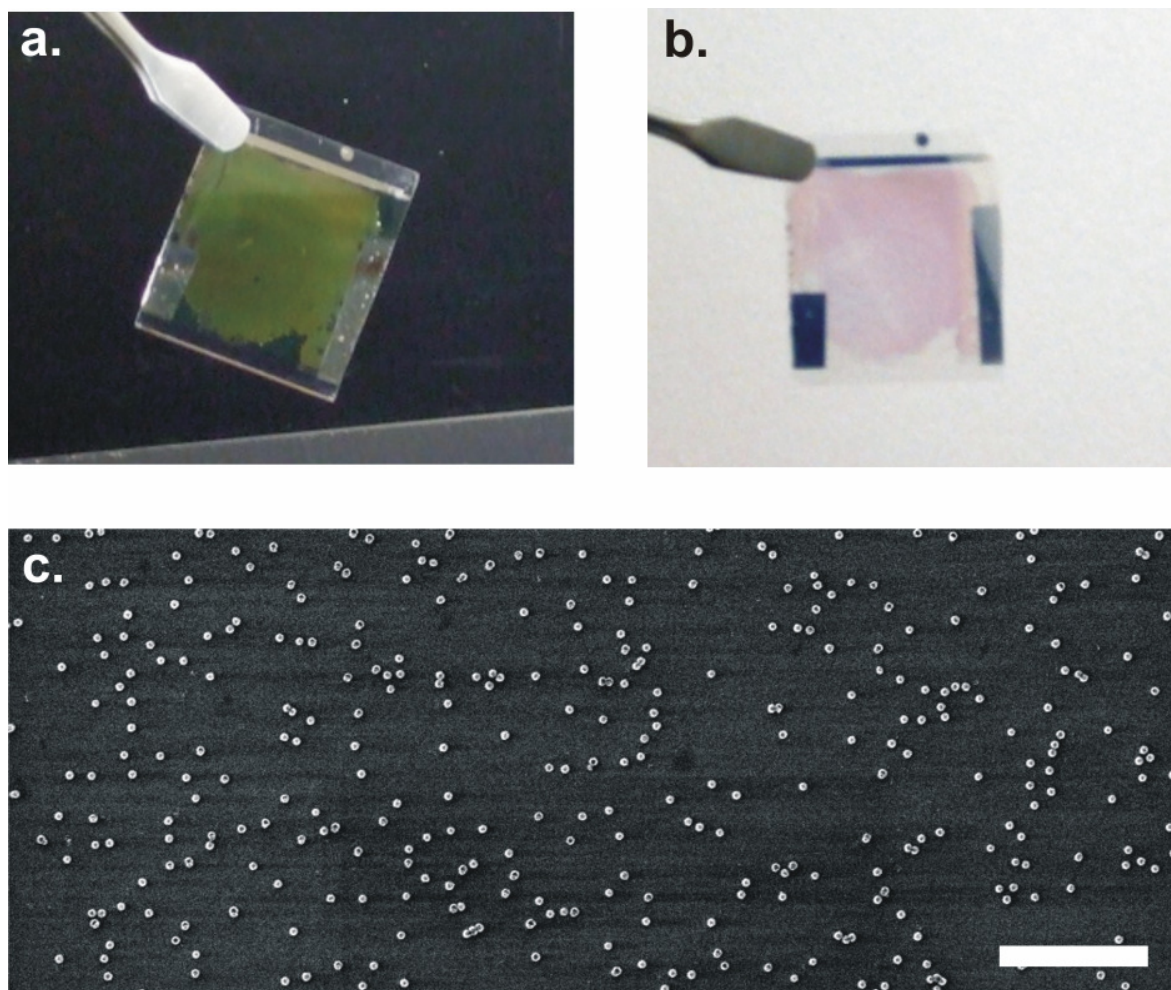


Figure 6-3: 100 nm Ag discs. White light illumination, (a.) dark background (“reflected light”) and (b.) white background (“transmitted light”); (c.) SEM micrograph of the same sample (100 nm Ag discs). The scale bars represents 2 μm .

Figure 6-4 (a) presents the spectra corresponding to silver discs of different nominal diameters (80, 100, 125, 150 and 300 nm)¹⁶. The spectra, recorded in a wavelength range from 350 to 2000 nm, show the evolution of one strong peak as from 500 nm into the near infrared. As expected, this resonance becomes also significantly broader for larger particles. Both the peak position and width of this main resonance are extracted from the measurements by fitting lorentzian curves to the data¹⁷. The results are presented in Figure 6-4 (b.) and (c.). The evolution of the peak position is fairly a linear relationship to the size of the colloids (slope: 3.2), as it also

¹⁶ These sizes correspond to the nominal diameters provided by the manufacturer (Polyscience), and should only be taken as a reference, since deviations are found (see Appendix C for the data available). In particular, the greatest deviation is found for the 150 nm colloids, with a 200 nm diameter.

¹⁷ A comparison on the results for Lorentzian, Gaussian and Voigt curves can be found in Appendix C.

is that of the width (slope: 2). The smallest particles produced (80 nm discs) do not seem to follow this tendency; further measurements on smaller discs would be necessary to determine whether there is an intrinsic limit for this size range.

Apart from the main resonance considered so far, weaker peaks are detectable at longer wavelengths for almost all samples. The latter are considered to be an artifact resulting from colloid agglomeration during fabrication and will be discussed later in detail. For the largest discs produced in this work ($d_{\text{coll}} > 200$ nm) a second peak is also detectable at higher energies than that of the main resonance, approximately at 400 nm. This resonance is not considered to be an artifact; a possible interpretation for these measurements could be related to a higher order resonance of the particles.

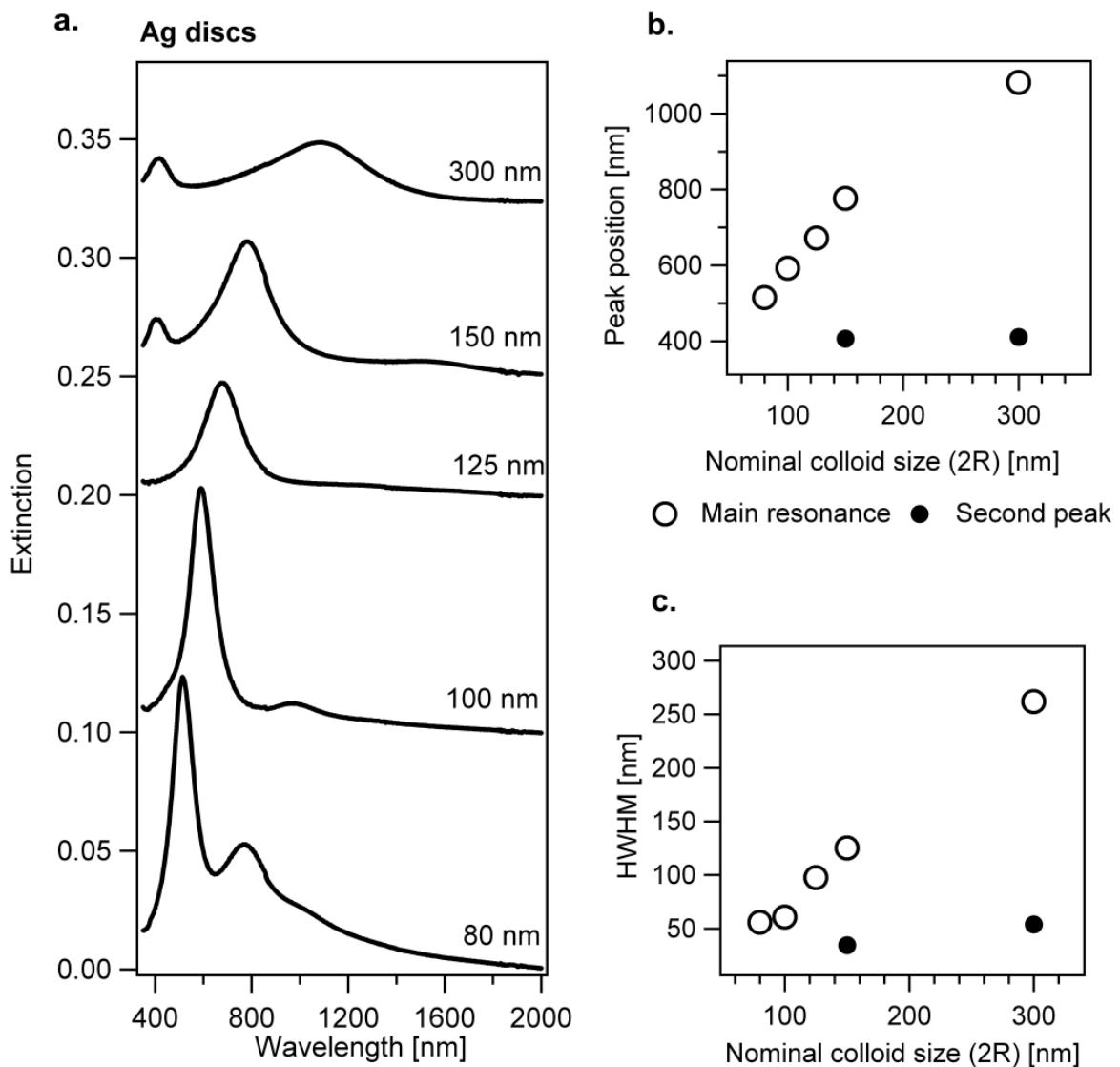


Figure 6-4: (a.) Extinction spectra of Ag nanodiscs, (b.) and (c.) Peak positions and width, as determined from fitting Lorentzian functions to the extinction measurements.

A general consideration is to be made related to the intensity of the peaks measured for the different samples (both for Ag and Au). The absolute values not to be compared, since no normalization procedure was carried out for these measurements. An approximation to the intrinsic cross-sections of these particles would require, in principle, a good approximation to the surface density on the samples. This information is not available for all samples, reason for which no normalization procedures were carried out in these spectra.

Gold nanodiscs

Figure 6-5 presents photographs of 100 nm Au discs sample; in this case the “reflected” (scattered) (a.) light is in the red part of the visible spectrum, appearing blue when faced to a white background (“transmitted” light).

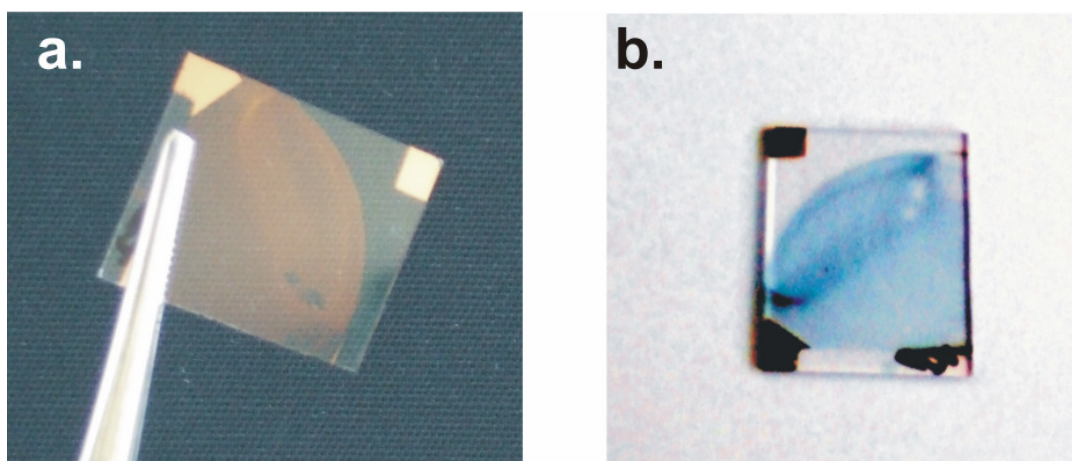


Figure 6-5: 100 nm Au discs. White light illumination, (a.) dark background (“reflected light”) and (b.) white background (“transmitted light”)

Figure 6-6 (a.) shows the spectra of gold nanodiscs (including those in the previous Figure), produced using different mask sizes (60, 100, 125 and 150* nm)¹⁸. In this case, as for the Ag nanodiscs, a strong, main resonance peak is easily recognizable from the spectra, evolving from app. 570 nm for the 60 nm discs into the red for increasing sizes. Lower energy resonances are also detectable in most samples; but these are most likely related to an artifact of the production process.

¹⁸ For these samples, an extra 1 nm Cr layer was used as adhesion promoter to the glass substrate

A rather broad extinction peak appears for the larger discs at roughly 400 nm, but this effect is not so evident as it is for the Ag nanodiscs (see Figure 6-4).

Figure 6-6 (b.) and (c.) display a summary of the results for the peak position and width of the resonances as obtained from fitting Lorentzian curves to the measurements¹⁹.

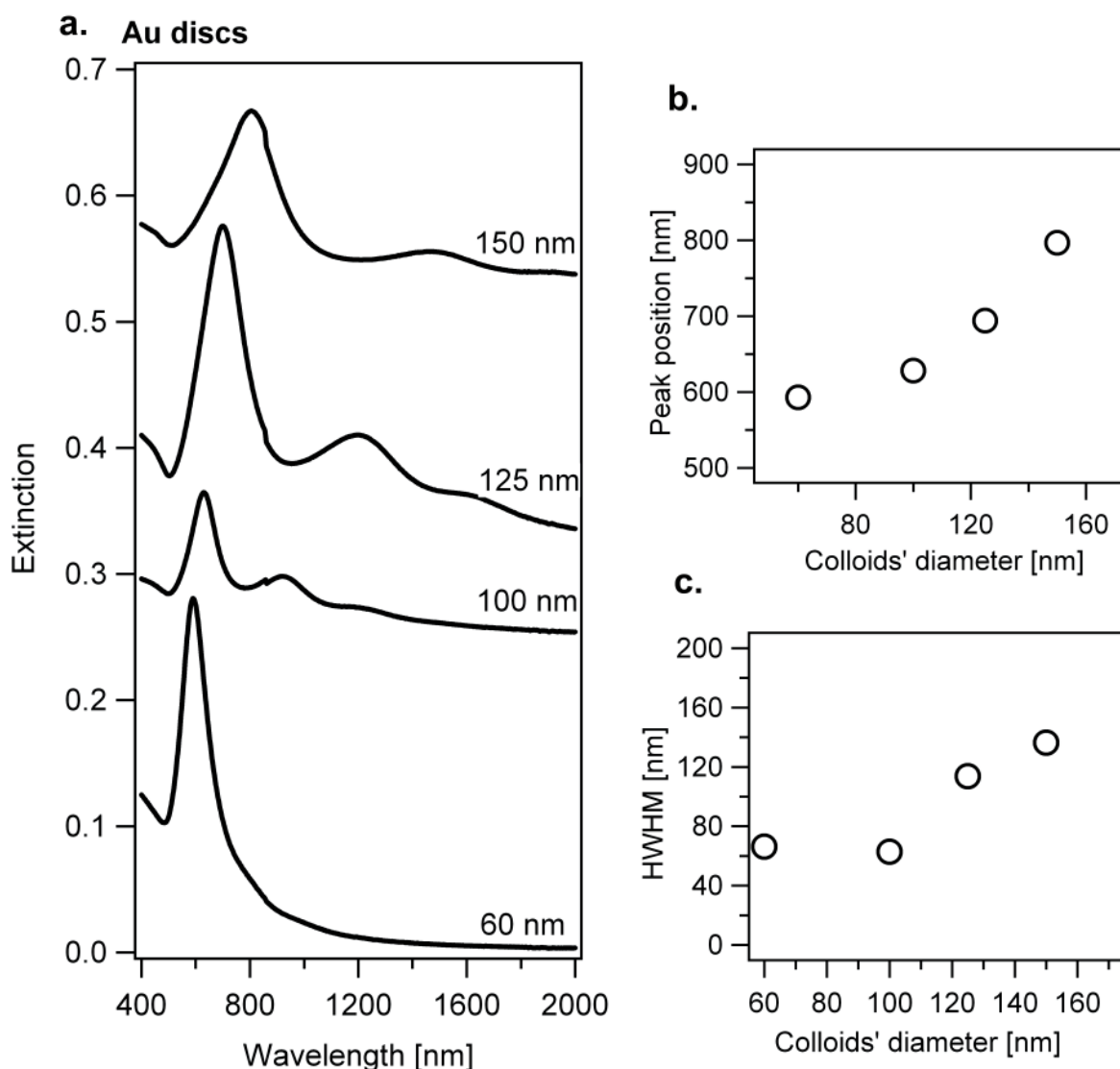


Figure 6-6: (a.) Extinction spectra of 60, 100, 125, and 150 nm gold nanodiscs. All curves have been displaced vertically for clarity. Peak position (b) and widths (c.) of the resonances, as obtained from fitting Lorentzian functions to the spectra. No data normalization has been carried out.

¹⁹ A comparison of different curves to fit the data is presented in Appendix C.

The resonances evolve into the infrared with increasing size, as expected, and so do their widths (see Figure 6-6). Both quantities evolve linearly as from 100 nm on. The data obtained for the smaller discs (60 nm in diameter) appears as if a plateau in this size range had been reached. A similar consideration has already been made for the Ag nanodiscs, also for structures of comparable size.

Interpretation

The main peak in the extinction spectra can be associated to a dipole-like response, the simplest resonant mode that a structure could support [Kreibig et al. 1987; Aizpurua, Hanarp, Sutherland, Käll, Bryant and Garcia de Abajo 2003; Hanarp 2003].

Lower energy resonances

Longer wavelength resonances could be interpreted as an artifact of the fabrication process. In order to support this hypothesis, Figure 6-7 displays the results obtained for 200 nm Au discs produced with two different colloidal mask concentrations. The measurement indicated as (A) corresponds to a sample produced using a colloidal mask with a concentration 5 times higher as for (B). The increasing amount of colloids on the surface leads most likely to the formation of aggregates that, once being the sample etched, would contribute to the overall extinction at longer wavelengths.

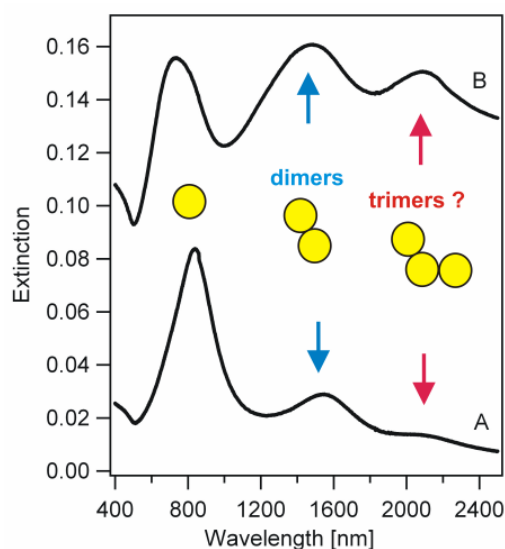


Figure 6-7: 200 nm Au discs, prepared from a Cr: 1.5 nm, Au: 25 nm film, using two different concentrations of the colloids' suspension (A: 1:100, B: 1:20)²⁰

²⁰ The measurements also show that an adequate tailoring of the process can lead to almost artifact-free samples. Surface functionalization can lead to comparable results (see Hanarp et.al.). In this

Higher energy resonances

The detection of a higher energy resonance than the dipole-like for large ($d_{\text{coll}} > 200$ nm) silver discs (see Figure 6-8), could in principle be related to a higher order mode resonance. Such possibility has already been investigated by Kreibig et. al. [Kreibig and Vollmer; Kreibig et al. 1987] for metallic spheres, for the same size ranges and materials.

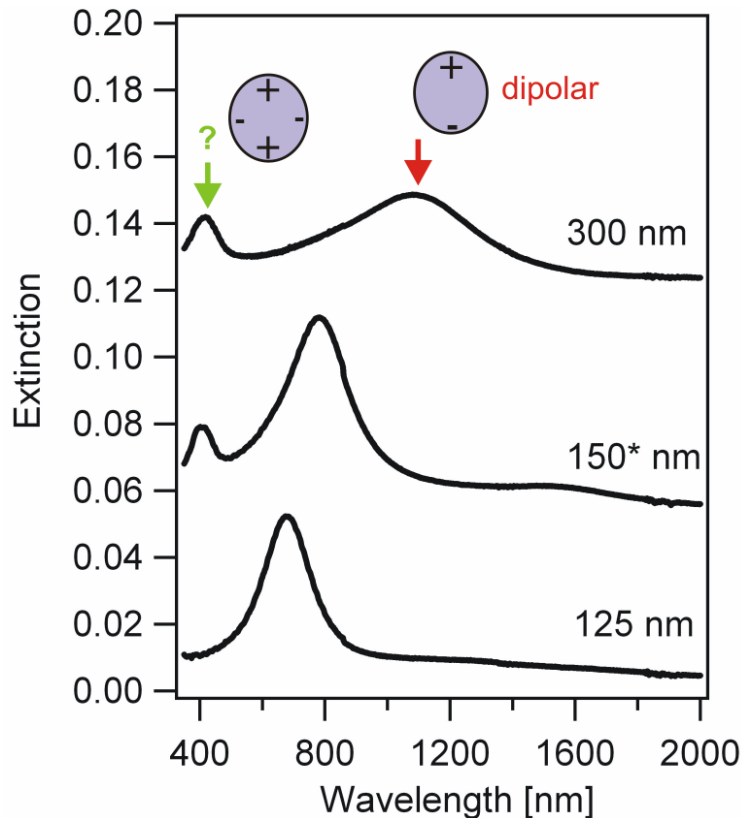


Figure 6-8: 125, 150* and 300 nm Ag discs on glass.

In this case, though not dealing with spheres, these should be a qualitatively representative approximation to the discs.

No extensive studies have been found, though, for metallic nanodiscs of large (> 200 nm in diameter) size to compare further the results presented here, which should be confirmed by further full numerical calculations or measurements (i.e. near field scattering [Keilmann and Hillenbrand 2004]).

work, no chemical treatments were applied to the metal surfaces before the spreading of the mask on them.

6.3.2 Ellipsoids ($\epsilon > 0$)

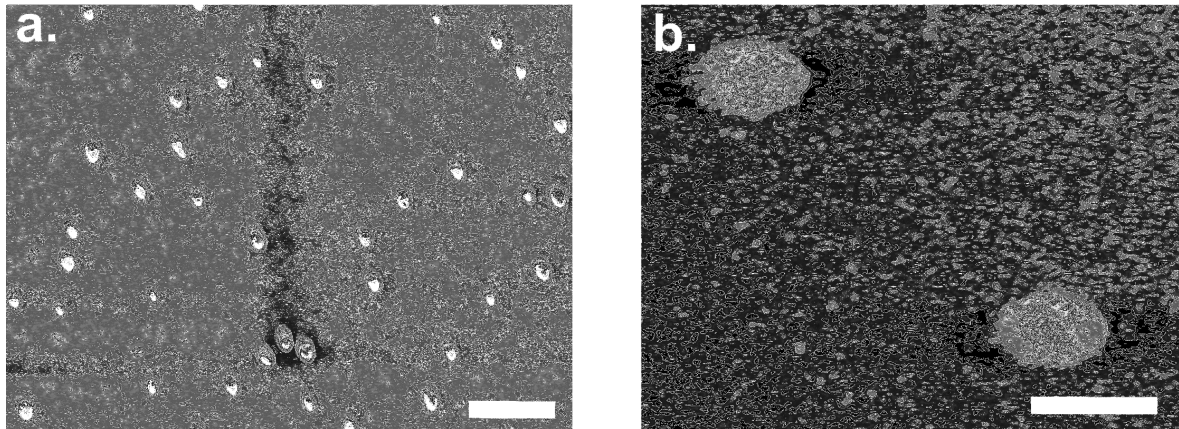


Figure 6-9: SEM micrographs of (a.) Au ellipsoids produced using 80 nm PS colloids. The size dispersion of the particles on this sample can be related to the quality of the colloidal mask used for these samples (see Appendix C for details) (b.) Ag ellipsoids, produced using 1 μm PS colloids. The scale bars represent 400 nm (a.) and 2 μm (b.).

Figure 6-9 presents scanning electron micrographs of samples prepared with 80 nm (a.) and 1 μm (b.) colloids, and etched at $\epsilon = 65^\circ$. The micrographs show the ellipsoidal shape of the particles produced when the samples are etched not perpendicularly to the surface. The smaller particles Figure 6-9 (a.) show strong deviations from the ideal morphology; still, the general ellipsoidal shapes are easily recognizable. Figure 6-9 (b.) shows a micrograph of comparatively larger structures (in the micrometer range) that look, though not perfect, much better defined than in the case presented in (a.). The etching/deformation of the colloids when exposed to the ion beam is probably much smaller for these big PS particles as for the 80 nm ones.

Silver ellipsoids

Figure 6-10 presents the spectra of ellipsoids produced namely 80 and 100 nm colloids, measured with light polarized along their major and minor axis of symmetry. The samples were prepared using different etching angles ($\epsilon = 30^\circ, 45^\circ$ and 65°) (see also Figure 6-2 for a sketch of the different geometries). The resonances for the two main polarizations clearly separate for larger ϵ , as expected from the final symmetry of the particles, remaining that of the short axis of symmetry in fairly the same position, while the second peak red-shifts for larger ϵ - as would be expected for larger structures.

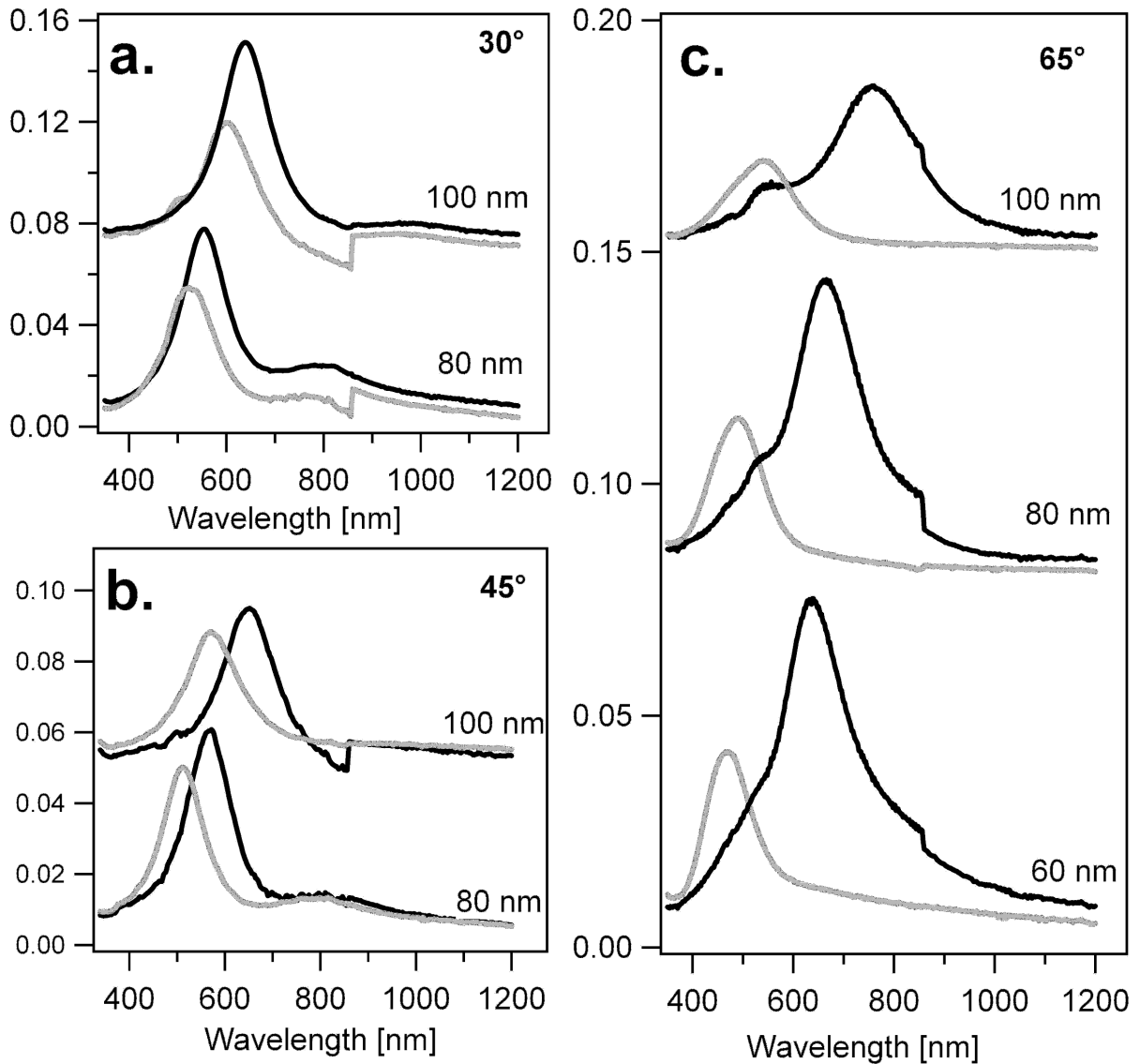


Figure 6-10: extinction spectra of Ag ellipse-like particles measured with light polarized along their minor (gray) and major (black) axis of symmetry. The structures were produced with $\epsilon = 30^\circ$ (a.), 45° (b.) and 65° (c.). The jump in the spectra at 860 nm is related to the spectrometer and has no physical meaning for the particles. Some of the spectra have been displaced vertically for clarity.

Figure 6-11 summarizes the information extracted from these measurements (peak position and width), by fitting Lorentzian curves to the data, for all combinations of etching angles and sizes, both along the short and long axis of symmetry.

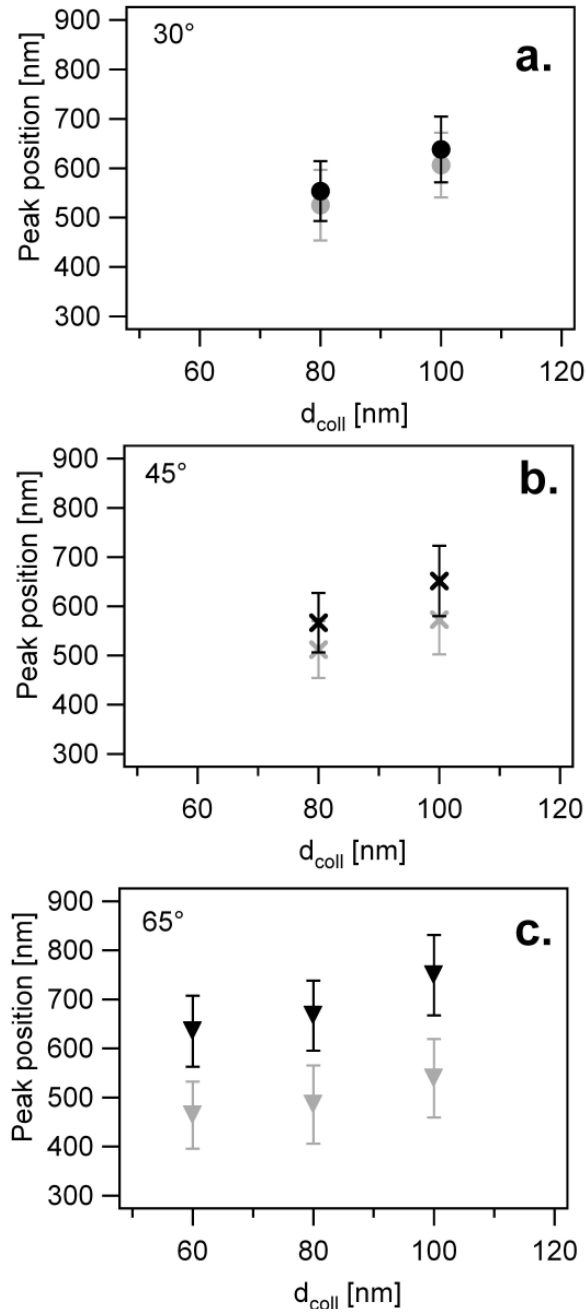


Figure 6-11: peak position and width (error bars) of the resonances for structures etched at 30° (a.), 45° (b.) and 65° (c.). The gray markers correspond to measurements along the short axis of symmetry, while black markers correspond to the long one.

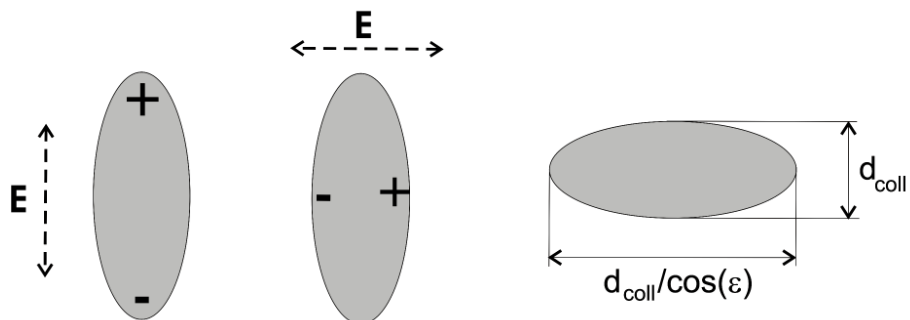


Figure 6-12: sketch of an ellipsoidal structure and the different polarizations.

It is important to note that geometrical deviations from this simplified model can occur. A non-homogeneous etching beam or a deforming/etching colloid can lead to significant distortions, i.e. egg-like shape (see Figure 3-10 (a.)). The measurements show that in all cases studied the polarization dependent resonances are still easily identifiable.

Gold ellipsoids

Figure 6-13 displays the spectra measured for particles produced using 80 and 100 nm colloids and etched at 65°. The measurements were done with the use of polarization optics, along the major and minor axis of symmetry of the ellipsoids.

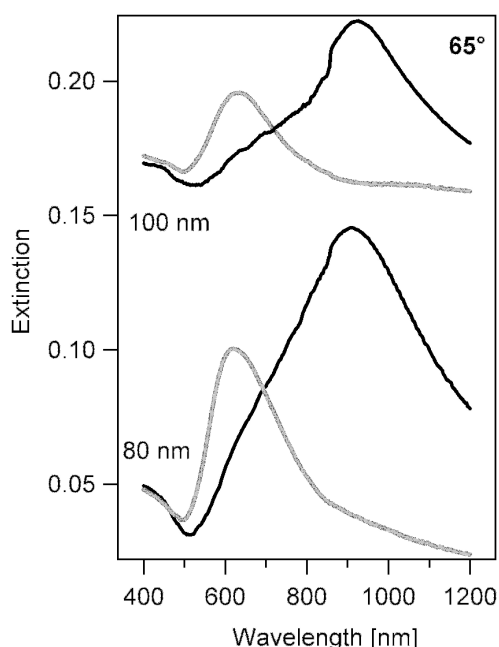


Figure 6-13: Au ellipsoids produced using 80 and 100 nm colloids. The samples were etched at 65°. The spectra measured with light polarized along the short axis of symmetry appear in gray; for the long axis, in black.

As in the case of the Ag ellipses, the two main resonances are easy to detect and separate by means of polarization optics. The resonance corresponding to the short axis polarization resembles that of the discs of similar size (compare with Figure 6-6). The longer axis resonance broadens considerably and shifts into the red. The broadening and slight shape distortion is most likely a combination of an intrinsic property of the resonance, and possible misalignments during fabrication / measurement. If the data for peak positions presented in Figure 6-6 is extrapolated to

the 1000 nm regime, the resonances for the major axis of the particles presented in Figure 6-13 are comparable to discs in the 200 – 300 nm range, and in turn, to the simple approximation of $d_{\text{coll}}/\cos(65^\circ)$ corresponding to the length of the major axis of the ellipsoids.

6.4 Conclusions

Flat metallic nanodiscs and nanoellipses of different sizes and materials were produced by means of nanosphere lithography, expanding the available range of structures fabricated with this method. The fabrication of metallic nanoellipses was achieved by a very simple extension of the procedure for the nanodiscs, giving rise to structures with multiple, polarization-dependent resonances in the visible and near infrared regions of the spectrum. The introduction of particles with multiple resonances can be particularly interesting for sensing applications, as for the nanocrescents, where more information can in principle be extracted from the independent modes in one single, simple experiment. These systems are also interesting from a technical point of view for studying plasmon mediated phenomena, i.e. fluorescence, since they are highly tunable in the visible range, allowing for the use of all standard optical elements and commercially available dyes.

From the fabrication point of view, the easy tunability of the sizes of the nanostructures is intrinsic to the process itself. Structures ranging from 60 nm up to 1 μm were produced in a simple manner, in a large scale and in a parallel way, which is not easily achievable neither with chemical nor conventional lithographic methods.

The exploration of a broader size range for the nanodiscs has proven most important in the case of the silver particles, where a second resonance appearing at shorter wavelengths has been detected. A hypothesis based on previous calculations on spherical particles suggest that this could be a higher order mode [Kreibig and Vollmer; Kreibig et al. 1987]. Further measurements, i.e. of the same particles in different refractive index media, and full numerical modeling of the structures are necessary to validate this last point.

This effect is not evident from the measurements for the Au nanodiscs in the size range explored.

7 . Sensing with metallic nanodiscs

The ellipsoid-like nanoparticles produced by means of nanosphere (or natural) lithography are probably, along with the holes in metallic films [Deckman and Dunsmuir 1982; Rindzevicius et al. 2005], the simplest structures that can be produced by this method. Both the holes in films and the metallic nanodiscs have been studied previously in terms of their sensing capabilities, namely their response to different dielectric environments, in biosensing schemes [Rindzevicius et al. 2005] and, more recently, even as platforms for recognition of structural/electronic changes upon gas absorption [Langhammer et al. 2007].

Limited experimental information is available, though, on their sensitivity to single recognition events, to thin films, or on other relevant parameters, i.e. field decay lengths around these structures.

In this work, the sensitivity of metallic nanodiscs to thin polymeric layers was studied with a simple approach based on the sequential deposition of polyelectrolyte layers and the optical characterization of the resulting capped nanoparticles. This methodology, already introduced in Chapter 4 to study the response of different resonant modes on crescent shaped nanoparticles, was extended here for the metallic nanodiscs. This method proved to be a powerful tool to estimate not only sensitivities, but also typical decay lengths of the field around these structures. Both these quantities are of fundamental importance, since they give a rough indication for the feasibility of building a sensor based on local changes to their environment, and the sensing ranges they are confined to.

Section 7.1 deals with the optical response of discs to thin films on their surface. Since these nanoparticles are very versatile and particularly simple to fabricate, it is of interest to study their sensing capabilities to a few bio recognition events on their surface. Section 7.2 is focused on testing the potential of the nanodiscs for biosensing, using a conventional biotin-streptavidin recognition approach. As in the case of the nanocrescents, the use of a species marked with Au nanoparticles is also explored as an approach for signal amplification.

7.1 Thin film sensing with Au nanodiscs

As introduced, the study of the optical properties of nanoparticles covered with thin layers of a dielectric material, i.e. resonance displacements upon layer attachment, can render valuable information like sensitivity and field extension around the nanoparticles.

In order to test the response of the metallic nanodiscs to thin polymeric films, polyelectrolyte multilayers [Decher and Schmitt 1992; Decher 1997] were deposited on the surface of the particles. This approach is particularly interesting because of its simplicity and ease of thickness control with a nanometer precision.

The extinction spectra of the samples were measured first as bare particles, and then after a definite number of bilayers. The peak displacements extracted from the reference and final spectra were in turn linked to the thickness of the material added on the surface of the particles. As introduced previously in Chapter 4 for the nanocrescents, this simple approach allows for a good estimation of the sensitivity of these particles to the thin films and the determination of an effective distance working range for these nanosensors.

The experimental details in this section will be described briefly, since they are almost identical to those introduced in Chapter 6 for the fabrication of the nanodiscs, and to those in Chapter 2 for the polymer films on the metallic nanostructures. General concepts on sensing with metallic nanoparticles and an example for the data analysis used in this section can be found in Chapter 4.

7.1.1 Experimental

Gold nanodiscs were prepared on conventional borosilicate glass substrates, following the procedure introduced in Chapter 6. All materials, machines and methods correspond to the ones presented there. A 1nm Cr and a 40 nm Au films were used for producing the discs in these experiments. Three different sizes for the colloidal masks were used, namely 60, 125 and 150²¹ nm colloids.

After the fabrication of the discs, polyallylamine (PA) and polystyrene sulfonate (PSS) layers were deposited alternatively on the samples, in order to build up thin bilayers on top of the structures. A 'bilayer' is constituted by a layer of PA and one of

²¹ Nominal diameters, as given by the producer (Polyscience). The 150 nm colloids correspond to a 200 nm in diameter (see Appendix C).

PSS; the average bilayer thickness is estimated to be 4 nm, in the 1 to 3 bilayers regime, and 8,4 nm further on (see Chapter 4 for further details on this subject).

7.1.2 Characterization

The samples were characterized by means of UV-VIS/NIR transmission measurements. In these experiments, and differing from the approach used for the crescents in Chapter 4, only one sample of each disc size is sequentially measured and treated with polyelectrolytes, meaning that each measurement is related to only one reference measurement (bare particles).

7.1.3 Results and discussion

Figure 7-1 presents transmission spectra²² for (a.) 60 nm, (b.) 125 nm and (c.) 150²³ nm discs, upon the addition of polyelectrolyte bilayers. It is possible to observe in this figure that all spectra progressively red-shift upon the deposition of polymer on the samples; a significant widening of the resonances is also evident from the measurements. For the largest discs (200 nm in diameter) a double peak structure is recognizable from the measurements. This distortion becomes more evident with increasing amount of polymer on the sample. This effect is not so clear for the other nanoparticles; a more comprehensive comment about this effect will be presented at the end of this section.

Peak position and width (HWHM: half width at half maximum) of the resonances were extracted from the extinction measurements by fitting Lorentzian curves (see Appendix A) to the data sets. All data treatment was done using Igor Pro v. 5.0. The information extracted from the fitting procedures is summarized in Figure 7-2, where the peak displacements for each disc size are presented. In all three cases, the displacements upon increasing polymer thickness evolve in an exponential-like saturating form. This saturation is clear in the case of the 60 and 125 nm discs, but does not seem to be fully reached for the 200 nm discs. This information, as in the case of the crescents, is approximated by a function of the form:

²² The jump in the spectra at approximately 860 nm corresponds to a feature of the spectrometer and does not have a physical meaning.

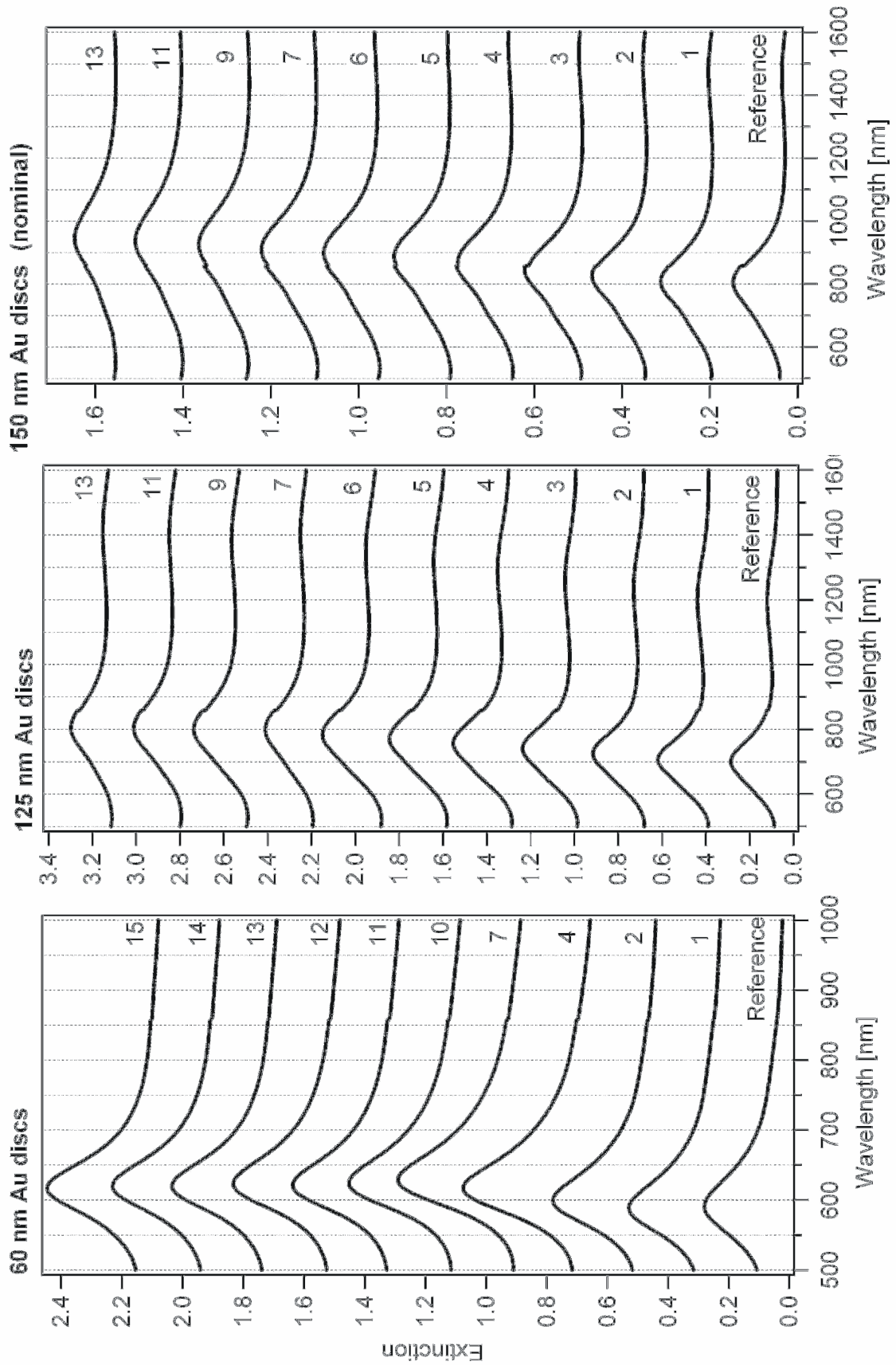


Figure 7-1: extinction spectra of Au nanodiscs of 60 (a.), 125 (b.) and 150 nm (nominal) (c.) upon the attachment of an increasing number of polyelectrolyte bilayers.

$$\Delta\lambda_i(d) = \Delta\lambda_{m,i} + (\Delta\lambda_{0,i} - \Delta\lambda_{m,i})e^{-d/d_{l,i}}$$

where $\Delta\lambda_{m,i}$ represents the saturation limit, d the thickness of the layers, $\Delta\lambda_{0,i}$ the peak displacement at $d = 0$, and $d_{l,i}$ a typical decay length. The index “ i ” refers to each type of sample (disc size) used in the experiments.

A simple estimation of the sensitivity of the particles to the addition of the bilayers is represented by $\left. \frac{d(\Delta\lambda)}{d(d)} \right|_{d=0}$.

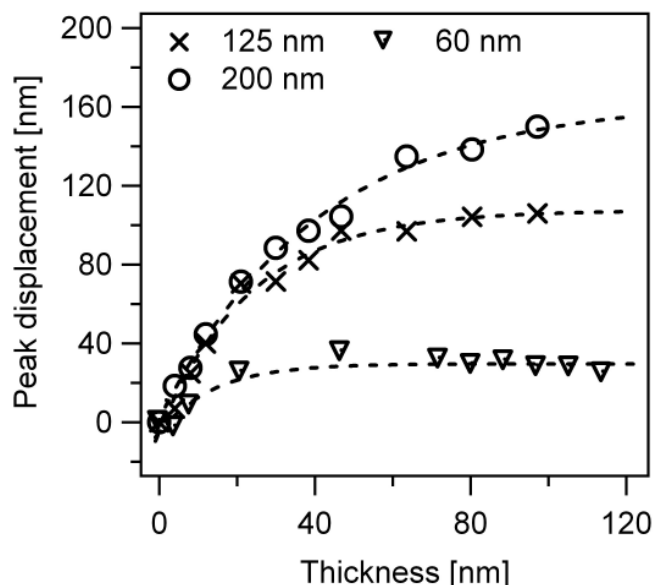


Figure 7-2: Peak displacements as a function of the amount of added polymer, for the three sample sizes explored in this work. The dashed lines represent exponential fits to the data.

All parameters extracted from the exponential fits, including the typical decay lengths

(d) and sensitivities ($\left. \frac{d(\Delta\lambda)}{d(d)} \right|_{d=0}$) are summarized in Table 7-1.

	$\Delta\lambda_m$ [nm]	d_l [nm]	$\Delta\lambda_0$ [nm]	$\left. \frac{d(\Delta\lambda)}{d(d)} \right _{d=0}$
60 nm particles	29.6	14	-5	2.46
125 nm particles	107.5	23.6	-4.6	4.7
200 nm particles	163.3	40.8	1.7	4

Table 7-1: results from fitting exponential saturating functions to the calculated peak displacements in the bilayer experiment, for the three different sizes explored (corresponding to curves A, B and C in Figure 2.a.)

The data presented in Table 7-1 shows that the decay lengths scale with the size of the discs (a linear fit on d_1 versus diameter gives a slope of 0.19).

The slope of the exponential fits for $d = 0$ show that, for thin film sensing, larger particles are more sensitive than smaller ones (almost a factor 2 to 1, for the 60 and 125 nm discs). The sensitivities for the 125 and 150* nm discs appear, despite the size differences, somewhat comparable. Further measurements for other particle sizes should be carried out to validate these results and analyse size/sensitivity relationships.

Comparing these results on nanodiscs to those for the nanocrescents in Chapter 4, it is evident that, for similar sizes, the crescents possess higher sensitivities (on average, a factor 2) and more confined near fields than the discs. This comparison should only be taken as an indication, since the shapes and near field distributions expected for these particles are very different. A better approach to compare the sensitivities should probably be done analyzing the form of merit (FOM) of these structures [Sherry et al. 2005] versus the ones of the nanocrescents [Rochholz 2005] (see also Chapter 4).

Shape distortion of the extinction spectra

Rindzevicius et. al. [Rindzevicius et al. 2007] have recently tested the sensing capabilities of nanodiscs with an approach comparable to the one presented in this section. The authors present results on Langmuir-Blodgett multilayers of 22-tricosenoic acid built on nanodiscs, but extend the analysis to greater overlayer thicknesses. Their result on peak displacement versus overlayer thickness presents an oscillatory character (red and blue shifting of the resonances upon increasing layer thickness), which is explained with an image-dipole model. This oscillatory behavior has not been observed in the measurements presented in this section; a reason for this may lie on the narrower thickness ranges explored here. A second feature observed by these authors is an anomalous broadening of the spectra upon the addition of the multilayers. This distortion could probably also be explained by the model proposed by Rindzevicius et. al., but it remains an open question, since it is not clearly observable for the other particle sizes.

7.2 Sensing of bio-recognition events with nanodiscs

Metallic nanodiscs/ellipsoids are an interesting approach for a sensing platform based on nanoparticles. They are particularly simple to produce and measure; and present a sensitive response to thin polymeric films. In this section, the sensing capabilities of metallic nanodiscs to a few recognition events on their surface are tested via a conventional biotin-streptavidin recognition system. As in the case of the nanocrescents (see Chapter 4), the possibility of signal amplification by using SAV-marked Au nanoparticles is also explored and quantified, both for Au and Ag discs.

7.2.1 Experimental

Sample preparation

Metallic (Ag and Au) nanodiscs were prepared following the procedures introduced in Chapter 6. A 40 nm thick film (either Ag or Au) was evaporated on the substrates to prepare the nanodiscs. For the Ag samples, an extra 0.8 nm Cr film was used as an adhesion promoter. All procedures, products and equipment used for these experiments correspond to those introduced in Chapters 2 and 6.

In order to functionalize the surface of the nanoparticles, all samples were first exposed to a thiol mixture containing biotin-terminated and hydroxy-terminated thiols. After this step, they were exposed either to SAV or SAV-AuNPs, for their attachment to the surface. All of these steps were done following the procedures introduced in Chapter 2 (Section 2.4.), where all products and processes are thoroughly described.

Characterization

The samples were characterized using conventional UV-Vis/NIR transmission spectroscopy, before and after the chemical treatments.

7.2.2 Results and discussion

Au nanodiscs

Figure 7-3 (a.) and (b.) present the extinction spectra of discs as bare particles, after biotinylation and after either SAV (a., c.) or SAV-AuNPs attachment (b.). It is important

to note that these samples present a great amount of aggregates, which can be noticed in the intensity of the peak appearing at roughly 750 nm, an artifact of the fabrication. This effect is related to the quality of the colloidal mask used for the experiments.

A higher quality (low agglomeration, see Appendix C) colloidal suspension of 125 nm PS spheres was applied in (c.), which was used to check the quality and reproducibility of these measurements. The results correspond to SAV recognition events in 125 nm Au discs. In these samples, no agglomeration effects are detected.

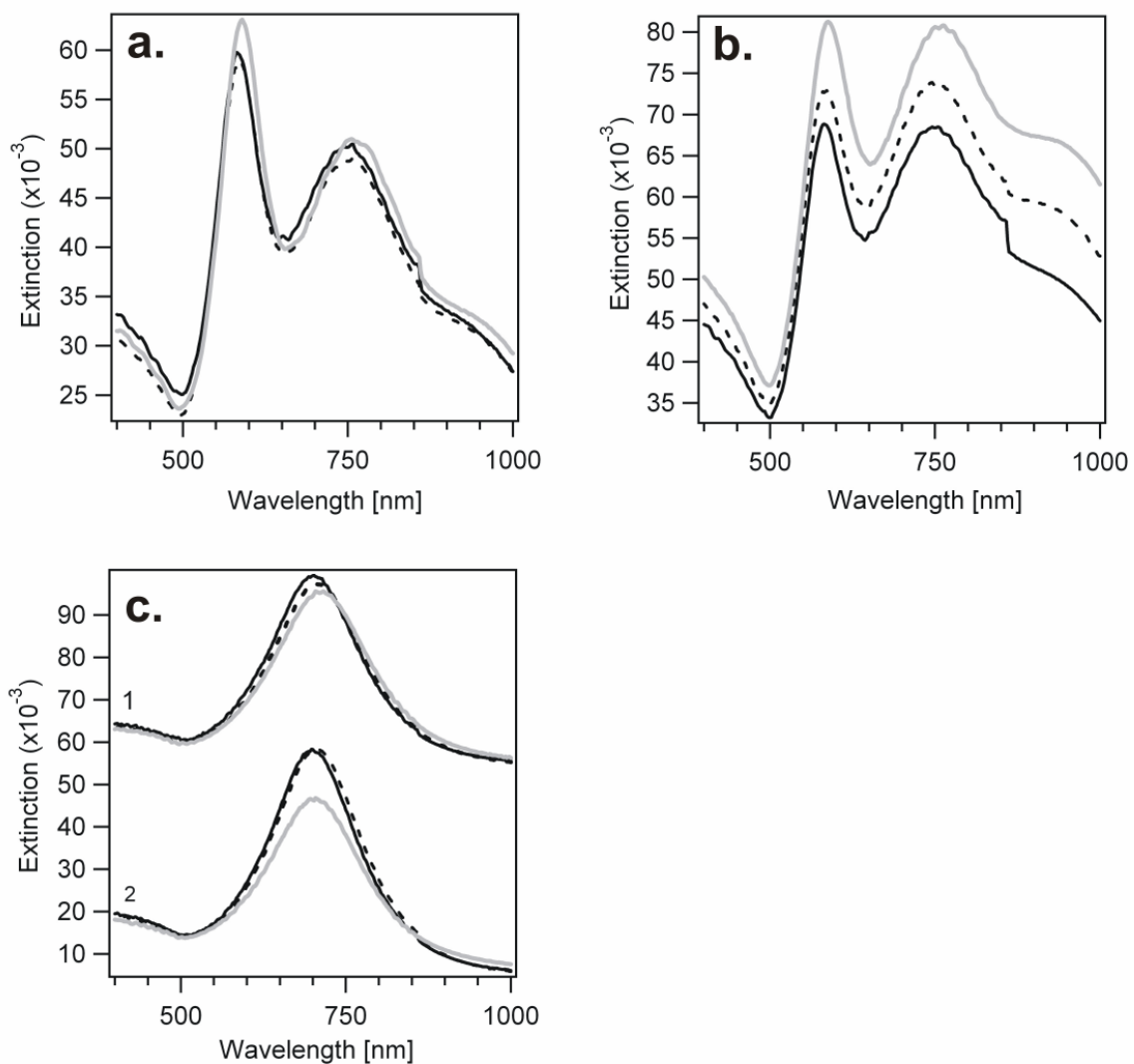


Figure 7-3: 80 nm Au nanodiscs after the attachment of Sav (a.) and Sav-AuNPs (b.); 125 nm Au nanodiscs after the attachment of Sav (c.). The solid, black line corresponds to the reference measurements, the dashed line, to biotinylation and the grey one, after either Sav or Sav-AuNPs attachment.

		Bare particles	Biotin	Biotin + SAV	Biotin+ SAV-AuNPs	$\Delta\lambda_p$ [nm]
80 nm Au discs	λ_p [nm]	578.7	579.3		590.8	12.1
	Width [nm]	40.7	44.3		45.5	
80 nm Au discs	λ_p [nm]	582.1	582	587		4.9
	Width[nm]	38.1	47.4	46.3		
125 nm Au discs (1)	λ_p [nm]	700.9	705.7	712		11.1
	Width[nm]	94.2	98.3	101.2		
125 nm Au discs (2)	λ_p [nm]	699.8	705.7	703		3.2
	Width[nm]	91.4	94.3	98		

Table 7-2: peak position (λ_p) and width (HWHM: half width at half maximum) for the Au nanodiscs samples, before and after the functionalization and Sav/Sav-AuNPs attachment. All peak displacements are calculated taking the peak position after biotinylation as a reference.

Both for the 80 and 125 nm Au nanodiscs, no major peak displacements upon biotinylation or SAV/SAV-AuNPs attachment are evident from the measurements.

Peak position and width of the main resonance were extracted by fitting multiple – when necessary – lorentzian curves to the extinction spectra.

The information extracted from the fitting procedures in Figure 7-3 is summarized in Table 7-2:. The data presented in

Table 7-2: shows that the displacements measured for the 80 nm discs are approximately 5 nm for the SAV case, and 12 nm for the SAV-AuNPs one. The measurements on Sav binding detected on two samples of 125 nm discs show displacements of 3 and 11 nm, respectively. Considering the dispersion detected for the 125 nm discs (3 and 11 nm displacements), it is clear that further tests are necessary to carry out proper statistics and validate these results.

Ag nanodiscs

Ag nanodiscs, 80 nm in diameter, were biotinylated and decorated with SAV and SAV-AuNPs, as in the case of the gold discs. Figure 6-4 summarizes the extinction spectra after each of these experiments. In both cases, all spectra displace upon each chemical treatment (biotinylation, bio-recognition). In the case of Sav, a small,

negative displacement is detected after biotinylation. For the Sav-AuNPs functionalized nanodiscs, the main resonance displaces considerably after after bio-recognition (see Figure 6-4 (b.)). No new resonances or significant spectral distortions are detected in any of the experiments, save a red-shifting and widening of the peaks.

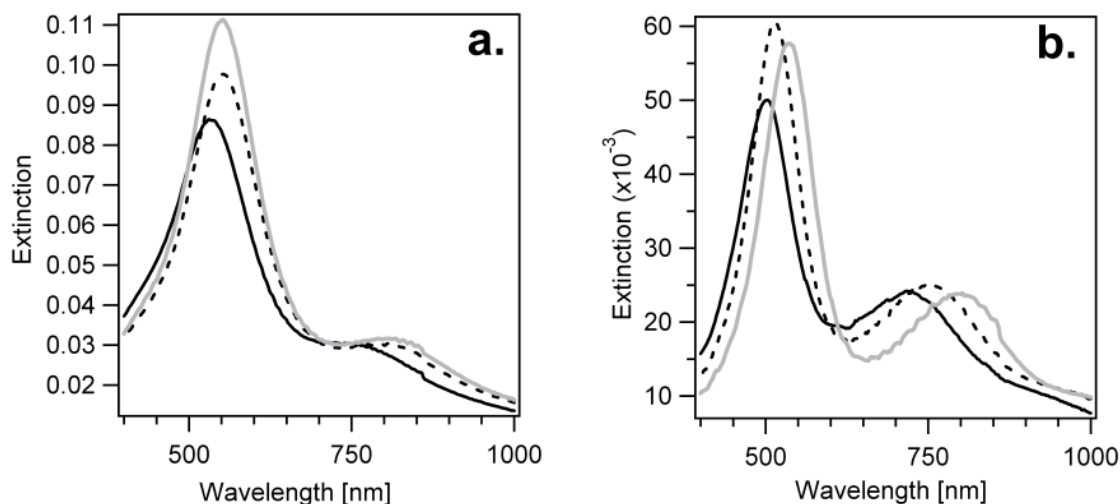


Figure 7-4: 80 nm Ag nanodiscs after the attachment of Sav (a.) and Sav-AuNPs (b.). The solid, black line corresponds to the reference measurement, the dashed line – after biotinylation and the grey line, after either Sav (a.) or Sav-AuNPs (overnight) (b.). All peak displacements are calculated taking the peak position after biotinylation as a reference.

Table 7-3 summarizes the data extracted from fitting Lorentzian curves to the measurements presented in Table 7-3. The relative peak displacements are calculated, in all cases, taking the measurements after biotinylation as reference.

In the case of the Ag nanodiscs, the sensitivity to SAV attachment appears misleading; a relative negative shift is detected (-1 nm) after the exposure to SAV. For the SAV-AuNPs case, an approximately 6 nm shift is detected after 5 hs of treatment, and some 20 nm after an overnight exposure.

The interpretation of the results of these experiments is not a trivial task. On the one hand, Au nanodiscs show limited response to all surface treatments. If the species attached to the surface of the nanoparticles could be modelled as a thin layer (~5nm) of a material with $n = 1.5$, then, a peak displacement of roughly 10 nm could be expected (see Figure 7-2), which falls in the dispersion associated to these samples.

It is important to point out, also, that this result is comparable in that respect to the behaviour of the Au nanocrescents (see Chapter 4). On the other hand, gold structures are less affected by solvent-annealing (see Appendix B for further details), an effect that could certainly hinder the detection of the attachment of a few species

on the surface of the nanoparticles, i.e. a blue shift caused by solvent annealing, combined with the detection of species on the surface of the particles could lead to a non-significative net displacement of the resonances.

		Bare particles	+ Biotin	Biotin + SA _v	Biotin + Sav-AuNPs		$\Delta\lambda_p$ [nm]
					5 hs exposure	Overnight exposure	
80 nm Ag discs	λ_p [nm]	498.9	513.3		519.2	534	5 hs: 5.9 Overnight: 20.7
	Width [nm]	57	50.2		49.1	55.1	
80 nm Ag discs	λ_p [nm]	534.4	552.9	551.9			-1
	Width [nm]	79.8	73.3	69			

Table 7-3 peak position (λ_p) and width (HWHM: half width at half maximum) for 2 Ag-nanodiscs samples, before and after the functionalization and Sav-AuNPs/SA_v attachment, correspondingly. All peak displacements are calculated taking the peak position after biotinylation as a reference.

The Ag nanodiscs present a very limited response to the attachment of SA_v (after biotinylation), and a time-dependent response for the exposure to SA_v-AuNPs (see Table 7-3). The latter lead to a 6 nm shift after 5 hs of treatment, and to a 20 nm one after an overnight exposure. These results are comparable to the values obtained for the Ag nanocrescents (see Chapter 4).

A number of experimental details have to be considered for any of these experiments, which can hinder a proper interpretation of the results. First, as in the case of the nanocrescents, if a non-in-situ approach for the measurements is applied, a proper statistical evaluation of the dispersion of peak position / widths of the resonances for one sample, and for different batches of samples, is of extreme importance to validate the results of any of the measurements.

Second, and in particular for Ag nanostructures, annealing effects on the nanoparticles when exposed to solutions can be of considerable magnitude [Willets and Van Duyne 2007] and make the detection of any effect produced by the binding of a species on the surface a difficult task (see Appendix B for details on annealing control tests). A Cr layer (approximately 1 nm thick) was added as an adhesion agent for the nanoparticles to the glass substrates, a method commonly used for metal

films on flat surfaces. Still, the effectivity / reproducibility of this approach for nanoparticles is somewhat arguable, since no thorough quantification is available. This means that slightly different Cr layers could lead to different peak displacements upon solvent-annealing, making the effective detection of any event on the surface of the discs a very difficult task²⁴.

Third, all considerations about a relative higher sensitivity of the Ag nanodiscs when compared to similar Au structures are based on the assumption that all surface binding mechanisms / functionalization procedures work in the same way for Au as for Ag, which can be, at best a good approximation.

A final consideration has to be made for all of the chemical treatments applied to the structures. These procedures might lead to side reactions on the surface of the silver particles. The results on Ag discs for the SAV-AuNPs treatment are particularly suggestive in this regard, since the measured peak displacements increase considerably when comparing a 5 hs exposure to an overnight one. One explanation for this could be related to further attachment of material on the surface or close enough to the nanoparticles (i.e. not only SAV-AuNPs, but also BSA, etc., see AFM images of a treated surface in Appendix C); a second view to the effect could suggest that unwanted reactions may have taken place (i.e. oxidation of the surface of the nanoparticles). A thorough, stepwise AFM characterization and a controlled exposure to all chemicals involved in these procedures should help clarifying these issues and validating the results of these first experiments, as it was the case for the nanocrescents presented in Chapter 4.

7.3 Conclusions

Thin layer sensing

The main resonance of these particles shifts upon the addition of polyelectrolyte bilayers. The measured displacements, represented as a function of the bilayers thickness, can be approximated via an exponentially saturating function. From this approximation, information like typical decay lengths and sensitivity can be easily

²⁴ It is important to note that the use of Cr alters the shape of the resonances producing a slight red-shift and widening of the main peak (see Figure 7-4 or Appendix B for an example).

extracted. The extension of the near field for the 60, 125 and 150* nm discs was estimated to be 14, 23 and 41 nm. The sensitivity of the 150* nm metallic nanodiscs is, as expected, essentially smaller than that of the crescents of the same nominal size (roughly a x2 factor).

Even when the multipolar nature and the interesting sensitivity of the nanocrescents is lost for these small discs, the advantage for their use relies on the fact of an even simpler and faster fabrication method, and also on the relative ease to tailor these structures into the visible range, which makes measurements more simple and accessible, using standard spectrometers and conventional optics.

Bio-recognition events

The experiments have shown that the Au nanodiscs give rise to negligible resonance displacements upon biotinylation and attachment of either SAV or SAV-AuNPs. Ag nanodiscs, on the other side, present significative displacements when functionalized and exposed to SAV-AuNPs, but a rather misleading effect when exposed only to SAV. Both solvent annealing effects and possible chemical side reactions on the surface of the Ag nanodiscs may be playing a significant role, hindering a proper quantification of the sensitivity of the nanodiscs to a few recognition events on their surface. The results on the use of SAV-AuNPs as a to amplify the measured peak displacements are a first, necessary step for the study on the potential use of the nanodiscs as sensors, but further reference studies on the effect of the different chemicals and surface characterization, along with a thorough statistical analysis are of fundamental importance to validate the significance of these first results.

As introduced in Chapter 4, a real comparison on the sensitivity of Ag and Au structures should be made, i.e. repeating the thin film experiments for the Ag structures, but tailoring the polyelectrolyte solutions not to corrode the nanoparticles, and giving rise to films of comparable characteristics. This point remains an open question for further comparative studies.

8 . Tailoring plasmon resonances – blue shifting

8.1 Introduction

Plasmon resonances in metallic nanoparticles can be red-shifted with relative ease and control when increasing the refractive index of the surrounding environment. Given a certain local environment, blue shifting implies, in many cases, changing intrinsic characteristics of the particle, like the size, or the shape (i.e. annealing effects [Haes and Van Duyne 2004; Willets and Van Duyne 2007])

In the case of metallic sols, it has been observed that electrochemical processes occurring at the particles' surface can alter their plasmonic properties. In particular, the addition of a second metal on the surface, even on a sub-monolayer coverage level, can have this effect [Mulvaney 1996]. In the case of small (2 – 10 nm colloids), and depending on the metals involved, blue shifting of the resonances have already been observed [Mulvaney 1996]. More recently, this has been seen for other particles that the addition of a second metal, i.e. silver on gold nanorods, can lead to both a blue-shift and narrowing of the resonances, a phenomenon that has been termed by the authors as “plasmonic focusing” [Becker et al. 2008].

In the following, an approach exploiting controlled metal deposition via electrochemistry is applied to substrate-supported Au nanodiscs. This approach is based on a technique known as Under Potential Deposition (UPD), which has been applied now for some decades to deposit certain metals on given substrates, in a controlled manner, and in a sub-monolayer coverage level.

Under Potential Deposition (UPD)

Metal adatoms and other adsorbates on a submonolayer coverage level are believed to have different electronic properties than those of the bulk material, and could alter those of the substrate material itself [Herrero et al. 2001].

The electrochemical deposition of a metal A on an electrode B in the sub-monolayer regime occurs at more positive potentials as compared to the Nernst potential if the interaction of A with B is thermodynamically more advantageous than that of A with A.

This phenomenon allows for controlled surface coverage, and therefore, the study of coverage dependent properties [Herrero et al. 2001].

In the following set of experiments, 200 nm Au nanodiscs prepared on indium-tin oxide (ITO) covered glass substrates are subject to UPD of Ag on them, and the optical properties of the system are studied before and after such treatment.

8.2 Experimental

8.2.1 Sample preparation

Gold nano discs were prepared on a detergent-cleaned, ITO-covered glass substrates (*Fern Universität Hagen*) using a nano-sphere lithography approach [Hanarp 2003; Hanarp, Käll et al. 2003]. Thin chromium (1.2 nm) and gold (40 nm) films were deposited on the substrates (in that order), and subsequently 200 nm and 100 nm polystyrene (PS) colloids were dispersed on their surface (on different substrates). An Ar-ion etching procedure was applied perpendicularly to the surface, removing the metal not protected by the colloids. Finally, the colloids were removed mechanically with an adhesive tape. The remaining metal below the colloids are the nano discs, of approximately 200 and 100 nm in diameter, in each case. All procedures, products, machines, etc. are identical to those introduced in Chapter 6, save the use of an ITO-sputtered glass substrate instead of glass.

Under potential deposition (UPD) of Ag on Au nanostructures

The hybrid Ag/Au surface was voltammetrically prepared by Ag-UPD on the Au nanostructures supported on ITO from $5 \cdot 10^{-4}$ Ag_2SO_4 + 1M H_2SO_4 . The electrode was polarized during a few seconds (nearly 5 s) at 0.3 V (vs. Ag^+/Ag) and then rinsed with ultrapure (*Milli-Q*) water. Voltammetric runs were made in a glass-made electrochemical cell containing three electrodes. A large graphite electrode was used as a counterelectrode and an Ag wire was used as reference electrode for Ag UPD experiments.

Control test

The nanostructures supported on ITO were exposed to a $5 \cdot 10^{-4}$ Na₂SO₄ + 1M H₂SO₄ solution. The electrode was polarized during a few seconds (nearly 5 s.) at 0.3 V (vs. Ag⁺/Ag) and then rinsed with ultra pure water. All other details are equal to those applied for the Ag-UPD treated samples.

Voltammetric runs on flat metal surfaces versus discs on ITO

Figure 8-1 presents voltammetric measurements performed on a flat gold film deposited on glass (a.) and on an ITO sample presenting Au nanodiscs on its surface (b.). The curves in (a.) present mainly three peaks. These peaks show the deposition/dissolution of the Ag adatoms from the surface. Consequently, cathodic (negative) and anodic (positive) currents represent the deposition and dissolution of Ag adatoms, respectively. The shape of the voltammetric response differs from the well-known Ag UPD peaks observed on single crystalline Au(111) surfaces due to the polycrystalline nature of our substrates, including the Au nanodiscs. Moreover, Figure 8-1 also shows significant changes in the double layer capacitance when the voltammetric response of evaporated flat gold and Au nanodiscs-covered ITO electrodes are compared. This can be attributed to the differences in conductivities displayed by both substrates (ITO and Au).

From these measurements, and previous experiments on flat single-crystalline surfaces [Herrero et al. 2001] 0.3 V is the chosen potential for the controlled deposition of Ag on the Au nanodiscs.

8.2.2 Characterization

UV-Vis/NIR extinction spectra were recorded in a conventional spectrometer (*Lambda 900, Perkin Elmer*), operating in transmission mode, in a 400 nm – 1200 nm range. An ITO covered glass substrate was used as reference to subtract the background contribution. Complementary measurements for ITO can be found as supporting information in Appendix B.

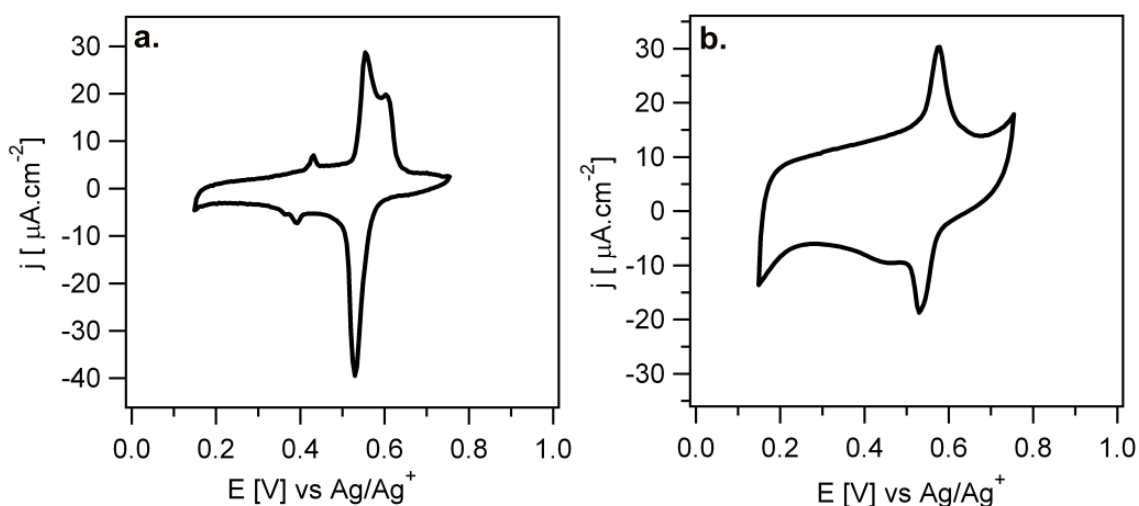


Figure 8-1: a. reference measurement on a gold electrode, using a Ag_2SO_4 solution; b. Au discs on ITO

8.3 Results and discussion

Figure 8-2 presents the transmission spectra of a control sample (a.) and a sample with Ag deposition (b.) The peak centered at approximately 900 nm corresponds to the resonance of the Au nanodiscs. The absorbing background measured on both samples corresponds to ITO²⁵, which strongly absorbs in the visible (see Appendix B for further details).

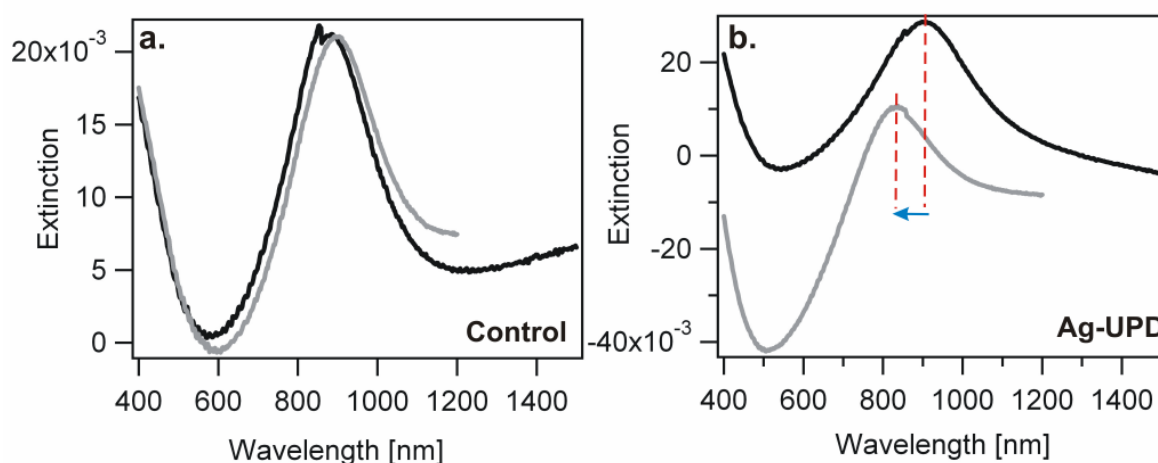


Figure 8-2: Control treatment (a.) and after Ag –UPD (b.) for 200 nm discs. Reference curves are displayed in black, and the resulting extinctions after treatment in gray, in both cases.

²⁵ The use of ITO on the glass substrate also alters the spectral position of the resonances slightly, with respect to glass. Further details on this can be found in Appendix B.

	Before treatment [nm]		After treatment [nm]	
	$\lambda_{m,0}$ [nm]	Width[nm]	$\lambda_{m,i}$ [nm]	Width[nm]
Control test	868.5	155.9	887.9	170.8
Ag-UPD	904.3	191.08	811	187.2

Table 8-1: peak position and width of the discs' resonance for a control test and Ag-UPD deposition, before and after the electrochemical treatment. The width corresponds to the half width at half maximum (HWHM) of the peak.

The control experiment was carried out in a solution of same ionic concentrations as the one for the Ag-UPD deposition, but exchanging Ag^+ by Na^+ ions. This has been done to avoid the Ag deposition and check any possible solvent annealing effects [Willets and Van Duyne 2007] (see also Appendix B). The result of the control experiment shows no major changes in the resonance position or width of the discs; as an indication of no major surface- or morphological changes in the nanodiscs. In the case of the Ag-UPD modified samples (Figure 8-2 (b.)), a considerable blue shift (app. 90 nm) is detected. Precise determination of the width of the resonance can be a non-trivial task, given the strong absorptive contribution of the ITO sputtered substrates.

The information extracted from the measurements, for both control and actual sample, are summarized in

Table 8-1. The data shows a significant blue shift (~ 90 nm) of the main resonance after the Ag-UPD treatment. The changes in the resonance's width are, though, not so pronounced and are not considered to be significant.

The same experiment was carried out using Au nanodiscs which were 100 nm in diameter, thus obtaining a blue shift of 70 nm.

Figure 8-3 presents the results of this experiment; the information extracted from the measurements is summarized in

Table 8-2. The narrowing of the resonance in this case is also negligible as in the case of the 200 nm discs, though the blue shift of the main peak is very clear.

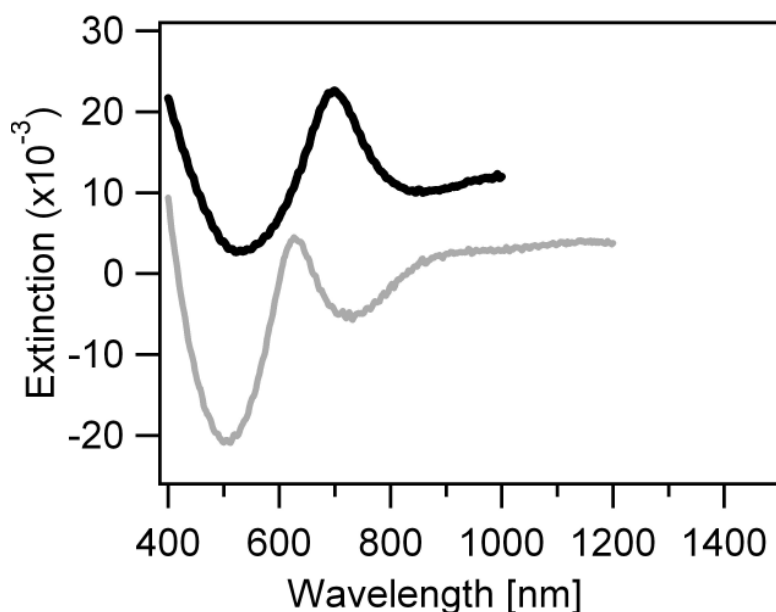


Figure 8-3: 100 nm Au discs on ITO before (black) and after (gray) Ag-UPD

	Reference	After Ag-UPD treatment
λ_p [nm]	692	622
Width [nm]	66	64

Table 8-2: the data extracted from the measurements on the 100 nm Au nanodiscs before and after the Ag-UPD treatment.

The surface coverage with Ag is estimated for flat substrates to be approximately 30 - 50 %, on an atomic monolayer level [Herrero et al. 2001]. This estimation is used as a first guess for the Ag coverage in the Au nanodiscs.

8.4 Conclusions

This very simple electrochemical approach appears as a powerful method to blue shift plasmon resonances, without necessarily introducing major changes in materials, size or form of the particles. The blue shift of the plasmon resonance should have a direct impact on the figure of merit (as a measure of the sensitivity) of the particles.

This processes can be, in principle, applied to a variety of metallic nanoparticles, considering the vast range of UPD metal pairs combining different substrates and

metal adsorbates [Herrero et al. 2001]. The case of Au and Ag is just an example and, in principle, it could be also extended to other metals, i.e. Cu.

The simplicity of these experiments should also open a clear way to study fundamental material properties of metal particles with adsorbed species on their surface in the nanoscale regime, or even surface alloying processes [Mulvaney 1996; Herrero et al. 2001] on metallic nanoparticles, via conventional spectroscopy, in a very simple and straightforward manner.

9 . Summary and outlook

9.1 Crescent shaped nanoparticles

In this work, crescent shaped nanoparticles were studied in terms of their optical properties, and their potential application in sensing and enhanced spectroscopy schemes. The general preparation procedures introduced early in 2005 by Shumaker-Parry et al. were extended to give rise to more complex (isolated) structures. The optical properties of such structures were studied with transmission spectroscopy and a simple multipole model for their response was proposed.

The introduction of evenly spaced monolayers of colloids as masks allowed for the fabrication of large arrays ($\sim\text{cm}^2$) of crescents. This represents a major technical advance for its simplicity, and large output. The procedure could be easily extended to other structures, i.e. discs, to produce arrays of nanoparticles for plasmonic applications. These first experiments also show that the ordered crescents present all the same resonances as the isolated particles; no new extinction peaks were identified from the measurements. The main difference observed in the optical response of isolated and ordered particles relies in the width of the peaks, which is for all resonances significantly higher than that of the isolated particles. Further studies in this field would include a thorough investigation of the distance-dependent coupling phenomenon, the exploration of new geometries and the investigation of the potential applications of this platform for building multilayered structures.

The fabrication methods presented in this work were extended not only to new shapes or arrangements of particles, but included also a targeted surface tailoring of the substrates and the structures, using different thiol and silane compounds as linkers for further attachment of polyelectrolyte layers. These procedures allow for a controlled tailoring of the nanoenvironment of the crescents, and set the experimental frame for further tests, i.e. for thin layer sensing or distance-controlled attachment of fluorophores. The same techniques should also be applicable when attempting a targeted surface decoration using i.e., proteins, antibodies/antigens, etc. which would be most relevant for bio-sensing applications.

When exploring the application of the crescents for sensing, two main approaches were tested, namely thin film sensing, and the binding of a few recognition events on the surface of the particles. In the case of the thin polymeric films, it was found that the crescents present an interesting mode-dependent sensitivity and spatial extension. Parallel to this, the penetrations depths were modelled with two simplified schemes, that of a plane interface and of a rod, obtaining good agreement in spite of the simplifications. The multiple modes of the particles with their characteristic decay lengths and sensitivities open the possibility for determining multiple parameters (refractive index, thickness) by making simultaneous use of the resonances.

The bio-recognition experiments show, on the contrary, that the use of the crescents in the scheme presented here is rather limited, since the measured peak displacements are in the same order of magnitude than the typical uncertainties associated to a sample, or a group of them. The use of an in-situ approach, or even single particle measurements could improve this and allow for the extraction of useful information from the experiments. A similar effect is observed for the detection of streptavidin-functionalized Au nanoparticles.

It is important to note, though, that the use of Ag nanocrescents, in particular for the sensing of colloidal Au-marked species, has given rise to greater peak displacements than any of the previous approaches. Further experiments are needed in this sense to validate the use of Ag nanocrescents as effective bio-sensors, and to make reasonable comparisons of their sensing capabilities, i.e. thin film sensing and AFM studies that allow quantifying the actual amount of material on their surface.

As introduced, these particles were also studied in terms of their capabilities to alter the emission properties of fluorophores placed close to them. In this work, green emitting fluorophores were placed close to the structures, using polyelectrolyte bilayers as a controlled spacer, fluorescence images of the samples were recorded on a confocal microscope, using a pulsed laser emitting in the NIR as excitation source. These first results show clear fluorescence enhancement events on the positions where the nanoparticles are located. Since the structures were tailored to match the excitation source spectrally in terms of resonances, it is expected that

strong near fields are found close to them, which would favor any plasmon-mediated phenomenon, i.e. fluorescence enhancement.

This approach for studying plasmon-mediated fluorescence enhancement is particularly interesting, because it allows to perform experiments in the visible range and, i.e. exploit these capabilities for sensing of fluorescently labeled species. Further experiments (i.e. intensity dependence, spectral and lifetime modifications) are needed to study the process in detail and quantify the real enhancement factors, but the first results presented in this work support the feasibility of the use of these structures as antennas for fluorophores emitting in the visible. Further applications could include sensing of fluorescently-labeled bio-species down to very confined excitation volumes, and applications in fluorescence correlation spectroscopy.

9.2 Ellipsoid-like nanoparticles

An even simpler and faster approach to produce plasmonic structures than that for the crescents was tested. Metallic nanodiscs were produced by means of nanosphere lithography following a procedure introduced earlier in the literature. The major advantage of these particles is that, though simpler, for sizes comparable to or below 100 nm, their main resonance lies in the visible range, both for Ag and Au. This represents an important advantage from a technical point of view, since most of the commonly available optical instruments are designed to work in this range.

The standard fabrication process for these particles was extended to different materials and sizes, allowing for collecting first evidence on higher order resonances on disk-like structures. Also, from the fabrication approach, tailoring geometrical parameters in the process allowed for the production of ellipsoid-like nanoparticles, which, just like the crescents, show a polarization-dependent character.

The main advantage of the ellipsoids relies, as in the case of the discs, on the ease of fabrication and on the resonances being in the visible part of the spectrum. The resonances of the silver nanoellipsoids are particularly simple to tailor and can be tuned with ease across the spectrum.

Since this approach offers some advantages compared to the crescents, it was interesting to investigate if it can offer as many interesting optical properties as the

latter do. The sensing capabilities of the metallic nanodiscs were explored in the same manner as for the nanocrescents. Their response to thin layers and to a few recognition events on their surface was studied. The sensitivity of these particles to thin films proved to be lower than that of the crescents, but in the same order of magnitude (roughly a 2 factor as a difference). Experimental information about the near field extension for the Au nanodiscs of different sizes was also extracted from these measurements.

The smaller nanodiscs (diameters below 100 nm) showing a narrower resonance in the visible range, lack of a multipolar character that could allow for the determination of multiple material parameters (refractive index, thickness, etc.) in one single experiment. Still, the discs are particularly simple to make, measure and analyse. A second resonance could be introduced in the system by switching to the ellipsoids, and still work in the visible range.

When it comes to the sensitivity of these particles to a few recognition events on their surface, the results are not 100 % conclusive in any of the cases tested. For the Au nanodiscs, rather small displacements were measured upon the attachment of either streptavidin or streptavidin-modified Au nanoparticles. These results could only be considered significant with either further statistics, or an in-situ approach for the measurements. For the Ag nanodiscs, although significant peak displacements were detected for both streptavidin and streptavidin-modified Au nanoparticles attachment to the surface, further reference tests are necessary to quantify annealing effects, possible chemical side reactions or uncontrolled attachment of other species on the surface, and validate these results.

A third issue explored using nanodiscs was the tailoring of the plasmonic resonances using under potential deposition of Ag on ITO-supported Au nanodiscs. With this very simple technique, it is possible in principle to deposit a metal on a second one (for given pairs of materials) in a controlled manner, to a submonolayer coverage level. The process of depositing Ag on Au nanodiscs lead to peak displacements of several tens of nanometers, making this technique a very interesting approach to tailor resonances, without necessarily change the core material of the particles or their size/shape. This procedure should then be, in

principle, applicable to Au nanocrescents to, i.e. push their resonances into the visible. This technique is not only interesting for this purpose, but also because it would allow to study more fundamental questions regarding the effect of surface modifications on metals, and how this affects, i.e. their dielectric constants, etc.

A number of interesting questions remain open about the use of nanodiscs/nanoellipses for studying plasmon-mediated fluorescence processes or other enhanced spectroscopies. These structures, as shown throughout Chapters 6 and 7, show resonances in the visible range, which makes them ideal from a technical point of view. Also, more information on typical field decay lengths (in turn, effective interaction lengths) are now available. The combination of all these factors and the fabrication strategies presented (surface modification, passivation, controlled polyelectrolyte attachment) provide an ideal basis for carrying out fundamental work like distance-dependence fluorescence enhancement / quenching, distance-dependent two photon excitation of dyes mediated by the structures, field confinement effects, and others.

LIST OF FIGURES

FIGURE 1-1: SKETCH OF A SPHERE IN A GIVEN ELECTRIC FIELD (E_0). THE METAL AND THE SURROUNDING MEDIUM ARE REPRESENTED THROUGH ϵ_1 AND ϵ_2	14
FIGURE 2-1: A. COLLOIDS' DEPOSITION ON A CLEAN, FLAT (SI OR GLASS) SURFACE, B. OBLIQUE (θ_i) METAL DEPOSITION – THIS STEP CAN BE DONE MULTIPLE TIMES, COMBINING DIFFERENT DEPOSITION ANGLES (I.E. θ_i, θ_j), ROTATION OF THE SAMPLE BETWEEN DEPOSITIONS (ϕ) AND DIFFERENT METAL THICKNESSES (T); C. ION ETCHING OF THE SURFACE (AT A GIVEN ANGLE, ϵ), D. MECHANICAL REMOVAL OF THE COLLOIDS. STRUCTURES PRODUCED USING 150 NM PS COLLOIDS	24
FIGURE 2-2: SKETCH OF THE PARTICLE GEOMETRY INDICATING THE ROTATION ANGLE ϕ FOR DOUBLE EVAPORATION, THE DIAMETER D_{COLL} OF THE MASKING COLLOID AND A COORDINATE SYSTEM TO BE REFERRED TO. THE ANGLE α DEFINES THE CIRCULAR SEGMENT IDEALLY COVERED BY THE GOLD FILM IN A SINGLE EVAPORATION STEP.	25
FIGURE 2-3: SKETCH OF A COLLOIDAL MONOLAYER (A.) BEFORE AND AFTER (B.) THE PLASMA ETCHING. THE ETCHED MONOLAYER IS THE BASIC TEMPLATE FOR THE CRESCENT FABRICATION (C.), FOLLOWING THE CONVENTIONAL METAL DEPOSITION AND AR ION ETCHING OF THE SURFACE.....	27
FIGURE 2-4: 180 NM PS NANOPARTICLE MONOLAYER BEFORE (A.) AND AFTER (B., C.) PLASMA ETCHING. THE SCALE BARS REPRESENT 200 NM.	30
FIGURE 2-5: A. PHOTO AND B. SCANNING ELECTRON MICROGRAPHS OF ONE SAMPLE PREPARED BY THIS METHOD. THE SCALE BAR IN (B.) REPRESENTS 1 μM	30
FIGURE 2-6 (A.) SCHEMATIC DRAWING SHOWING THE ATTACHMENT OF SILANE AND THIOL MONOLAYERS ON THE GLASS AND GOLD SURFACES (B) STRUCTURES OF PAH AND PSS	33
FIGURE 2-7 TAPPING MODE AFM TOPOGRAPHY (A) AND PHASE (B) IMAGES OF GOLD CRESCENT SHAPED NANOPARTICLES ON GLASS. A HEIGHT PROFILE OF THE NANOPARTICLE AND SUBSTRATE (ALONG THE INDICATED VERTICAL LINE) IS PRESENTED IN THE INSET.	35
FIGURE 2-8 AFM TOPOGRAPHY AND PHASE OF SAMPLES WITH NANOCRESCENT STRUCTURES TREATED WITH 3-MPA, AS A FUNCTION OF THE NUMBER OF TIMES DIPPED IN POLYELECTROLYTE SOLUTIONS (PAH+PSS): A) 0 BILAYER; B) 1 BILAYER; C) 3 BILAYERS; D) 7 BILAYERS; E) 9 BILAYERS. THE VERTICAL SCALE IS 50 NM IN ALL CASES. THE INSETS PRESENT THE PHASE IMAGE OF THE SELECTED AREA FROM THE TOPOGRAPHIC IMAGE.	36
FIGURE 2-9 TAPPING MODE AFM PHASE IMAGES (TOP) AND SECTION PROFILES (BOTTOM) FOR SAMPLES TREATED WITH APTE AND WITH 0 (A), 2 (B) AND 4 (C) BILAYERS OF POLYELECTROLYTES. ALL THE IMAGES HAVE THE SAME Z-SCALE. THEIR CORRESPONDING TOPOGRAPHIC IMAGES ARE PRESENTED IN THE INSETS.	37
FIGURE 2-10: EXTINCTION SPECTRA BEFORE (BLACK) AND AFTER (GREY) THE ATTACHMENT OF 3-MPA (A.) AND OF 3-APTES (B.) AND 3 POLYELECTROLYTE BILAYERS.....	37
FIGURE 3-1: SKETCH OF THE “U” AND “C” POLARIZATIONS; THE DASHED ARROW REPRESENTS THE ELECTRIC FIELD.....	43
FIGURE 3-2: EXTINCTION SPECTRA FOR VARYING CRESCENT OPENING, PRODUCED BY DOUBLE EVAPORATION (ϕ) AS INDICATED IN FIG. 1. THE DIAMETER OF THE MASKING COLLOID AND THE FILM THICKNESS WERE HELD CONSTANT AT $D_{\text{COLL}}=200$ NM AND $D_{\text{Au}}=2 \times 20$ NM RESPECTIVELY. A), B) AND C) SHOW EXTINCTION SPECTRA RECORDED WITH U-POLARIZED, C-POLARIZED AND NON-POLARIZED LIGHT, RESPECTIVELY....	45
FIGURE 3-3: CRESCENT SHAPED NANOPARTICLES PRODUCED BY MULTIPLE METAL DEPOSITIONS, WITH DIFFERENT ϕ_j , WITH EXCEPTION OF THE FIRST ($\phi = 0, 1$ DEPOSITION). THE SCALE BAR REPRESENTS 200 NM.....	46

FIGURE 3-4: REPRESENTATIVE SCANNING ELECTRON MICROGRAPHS OF CRESCENTS PREPARED WITH $\phi: 140^\circ$. ($D_{\text{COLL}}: 200 \text{ NM}$, $T_{\text{AU}}: 20\text{NM}+20\text{NM}$). THE SCALE BAR REPRESENTS 500 NM.	46
FIGURE 3-5: A) UV-VIS EXTINCTION FOR NON-POLARIZED, C POLARIZED AND U POLARIZED LIGHT OF A STRUCTURE THAT WAS OBTAINED BY A TRIPLE EVAPORATION ROUTINE WITH ($\phi: 0^\circ, 120^\circ, 240^\circ$, $T_{\text{AU}}=3 \times 20 \text{ NM}$, $D_{\text{COLL}}=150 \text{ NM}$ COLLOIDS); (B.) CORRESPONDING SCANNING ELECTRON MICROGRAPH (C) SKETCH OF THE STRUCTURE AS PRODUCED AND OF THE PROPOSED OSCILLATING CHARGE DISTRIBUTION OF THE RESONANCE.....	48
FIGURE 3-6: INFLUENCE OF CRESCENT CONTOUR LENGTH ON THE OPTICAL RESONANCES. A) RESONANCE WAVELENGTHS FOR A RANGE OF ROTATION ANGLES ϕ AS INDICATED IN THE GRAPH. B) RESONANCE WAVELENGTHS (λ_{RES}) NORMALIZED BY THE CONTOUR LENGTH (L_c) OF THE CRESCENT; SEE TEXT FOR DETAILS.	48
FIGURE 3-7: SKETCH OF CHARGE DISTRIBUTION FOR THE RESONANCE ON A CLOSED RING AND THE THREE STRONGEST RESONANCES OF OPEN CRESCENTS.	51
FIGURE 3-8 : DISPERSION PLOT $\omega(k)$ FOR FIVE RESONANCES. THE DOTTED LINE INDICATES THE LIMITING FREQUENCY FOR SURFACE PLASMONS ON PLANE SUBSTRATES.....	51
FIGURE 3-9 : EXTINCTION SPECTRA OF TWO INDEPENDENT SAMPLES, PREPARED ON THE SAME MANNER, BUT USING TWO DIFFERENT CONCENTRATIONS OF COLLOIDS FOR THE MASK	52
FIGURE 3-10: (A) PEAK POSITIONS AS A FUNCTION OF COLLOID DIAMETER. (B) PEAK WAVELENGTH NORMALISED BY L_c [ROCHHOLZ ET AL. 2007].	54
FIGURE 3-11: A), B) PP RESONANCE FOR $D_{\text{COLL}} = 400 \text{ NM}$ AND $D_{\text{COLL}} = 300 \text{ NM}$ (C) SKETCH OF THE POLARIZATION OF A RESONANCE WHICH IS PERPENDICULAR TO THE ROD FOR THE TWO FUNDAMENTAL POLARIZATIONS [ROCHHOLZ ET AL. 2007].....	55
FIGURE 3-12: EXTINCTION SPECTRA OF <i>STANDARD</i> CRESCENT SHAPED NANOPARTICLES PREPARED WITH $\theta_i = 20^\circ, 30^\circ$ AND 40° . THE CURVES HAVE BEEN DISPLACED VERTICALLY FOR CLARITY.	57
FIGURE 3-13: ATOMIC FORCE MEASUREMENTS, HEIGHT AFM MEASUREMENTS OF SAMPLES PREPARED WITH $\theta = 20^\circ$ (A.), 30° (B.) AND 40° (C.). THE SCALE BAR REPRESENTS 100 NM.....	58
FIGURE 3-14: <i>STANDARD</i> CRESCENT SHAPED NANOPARTICLES PREPARED USING GOLD (A.) AND SILVER (B.).	59
FIGURE 3-15: SCANNING ELECTRON MICROGRAPHS FOR THE ISOLATED (A.) AND CLOSE PACKED (B.) CASES; (C.) AND (D.) PRESENT THEIR CORRESPONDING TRANSMISSION SPECTRA. THE JUMP OBSERVED AT 860 NM IN THE SPECTRUM (D.) RELATED TO THE SPECTROMETER AND HAS NO PHYSICAL MEANING FOR THE EXPERIMENTS. THE SCALE BAR REPRESENTS 200 NM.....	63
FIGURE 3-16: SIMPLIFIED SKETCH SHOWING TWO DOMAINS WITH CRESCENT ARRANGED IN DIFFERENT PATTERNS AND CORRESPONDING SEM IMAGES OF TWO DIFFERENT AREAS ON A SAME SAMPLE. THE RED DOTS IN THE SKETCH INDICATE POSSIBLE DIFFERENT INTERACTION POINTS FOR THE STRUCTURES.	64
FIGURE 4-1: SIMPLIFIED SCHEME OF A METAL NANOPARTICLE SUPPORTED ON A SUBSTRATE, SURROUNDED BY TWO DIFFERENT REFRACTIVE INDEX MATERIALS, AND THEIR SPECTRA.	67
FIGURE 4-2: METAL NANOPARTICLES SUPPORTED ON A SUBSTRATE, FOR THREE DIFFERENT SENSING APPROACHES: (A.) IMMERSSED IN A MEDIUM WITH A BULK REFRACTIVE INDEX N_i , (B.) COVERED WITH A THIN LAYER OF A MATERIAL WITH A REFRACTIVE INDEX N_L , IMMERSSED IN A SECOND MEDIUM OF N_{M_1} , (C.) IMMERSSED IN A GIVEN MEDIUM (N_M), AND FUNCTIONALIZED WITH A RECEPTOR FOR THE ANALYTE OF INTEREST.....	67
FIGURE 4-3:(A) SCANNING ELECTRON MICROGRAPH OF A CRESCENT-SHAPED PARTICLE; THE SCALE BAR REPRESENTS 200 NM (B) SKETCH OF A CROSS SECTION OF A CRESCENT COVERED WITH	

POLYELECTROLYTES ALONG THE DASHED LINE IN (A); D STANDS FOR THE THICKNESS OF THE FILM, H AND W FOR THE HEIGHT AND WIDTH OF THE STRUCTURE RESPECTIVELY, AND PE FOR THE POLYELECTROLYTE FILM. (C) FILM THICKNESS AS A FUNCTION OF THE NUMBER OF BILAYERS. THE VERTICAL CROSSES (+) REPRESENT THE AFM MEASUREMENTS, THE TILTED ONES (x) THE LITERATURE VALUES. THE CIRCLE REPRESENTS AN ESTIMATED INTERMEDIATE VALUE BETWEEN THESE TWO REGIMES. 70

FIGURE 4-4 : EXTINCTION SPECTRA OF THE SAMPLES BEFORE (BLACK) AND AFTER (GREY) THE ADDITION OF POLYELECTROLYTE BILAYERS. THE CORRESPONDING NUMBER OF BILAYERS IS DISPLAYED ON THE RIGHT SIDE OF THE GRAPH..... 71

FIGURE 4-5: PEAK POSITION OF THE 4 MAIN PEAKS (C1, U1, C2 AND PP) BEFORE AND AFTER THE ADDITION OF THE BILAYERS. THE ERROR BARS REPRESENT THE WIDTH (HWHM: HALF WIDTH AT HALF MAXIMUM) OF THE RESONANCES, AS DETERMINED FROM THE FITTING PROCEDURES 72

FIGURE 4-6: PEAK DISPLACEMENT OF THE MAIN RESONANCES IN THE FULL (A.) AND FIRST LAYERS (B.) REGIMES. RESONANCE ASSIGNMENTS ARE GIVEN IN THE GRAPH. THE DASHED LINES REPRESENT AN EXPONENTIAL FIT TO THE DATA. THE EXTRA DARK MARKERS ADDED TO (A.) CORRESPOND TO THE DISPLACEMENT OBTAINED WHEN IMMERSING THE SAMPLES IN A $n = 1.524$ OIL [ROCHHOLZ 2005]. FOR A THICKNESS OF ROUGHLY 140 NM (18 BILAYERS), ONLY THE DISPLACEMENT CORRESPONDING TO C1 CAN BE DETERMINED UNEQUIVOCALLY, AND IS INCLUDED IN THE OVERALL FITTING. THE GRAY MARKER GIVES AN INDICATION FOR THE DISPLACEMENT OF U1 FOR THICK COATINGS, BUT THIS VALUE IS NOT INCLUDED IN FURTHER CALCULATIONS..... 73

FIGURE 4-7: SIMPLIFIED SKETCHES OF A CRESCENT (A.), A PLANE INTERFACE (B.) AND A ROD (C.)..... 77

FIGURE 4-8: NORMALIZED PEAK SHIFT, AS CALCULATED FROM THE ROD MODEL, AS A FUNCTION OF THE DISTANCE TO THE ROD'S SURFACE. 79

FIGURE 4-9: A. STREPTAVIDIN [FREITAG; SATO 2006] AND B. BIOTIN..... 81

FIGURE 4-10: SCHEME OF THE TWO SENSING APPROACHES TESTED ON AU (A. AND B.) AND ON AG (C. AND D.) CRESCENTS 82

FIGURE 4-11: EXTINCTION SPECTRA OF AU CRESCENTS AFTER BIOTINYLATION AND STREPTAVIDIN ATTACHMENT (A.) AND BIOTINYLATION AND STREPTAVIDIN MODIFIED AU NPs BIOCONJUGATION (B.). REFERENCE (BLACK SOLID LINE), BIOTINYLATION STEP (DASHED LINE), AND BIOCONJUGATION (GRAY). THE INSET CORRESPONDS TO THE STRONGEST RESONANCE AT 1300 NM (C1)..... 86

FIGURE 4-12: EXTINCTION SPECTRA OF AG CRESCENTS AFTER BIOTINYLATION AND STREPTAVIDIN ATTACHMENT (A.), AND BIOTINYLATION AND STREPTAVIDIN MODIFIED AU NPs BIOCONJUGATION (B.). REFERENCE (BLACK SOLID LINE), BIOTINYLATION (DASHED LINE), AND AFTER BIOCONJUGATION (GRAY SOLID LINE). THE INSET CORRESPONDS TO THE STRONGEST RESONANCE AT 1300 NM (C1)..... 87

FIGURE 4-13: PEAK DISPLACEMENT OF THE 3 MAIN RESONANCES UPON THE ADDITION OF SAV AND SAV-MODIFIED AU NPs FOR AG (A.) AND AU (B.) CRESCENTS. 88

FIGURE 5-1: SCHEME OF A SIMPLIFIED TWO LEVEL SYSTEM, COMPARING ONE- AND TWO-PHOTON EXCITATION. 91

FIGURE 5-2: (A) STRUCTURE OF ALEXA FLUOR 488 CARBOXYLIC ACID, SUCCINIMIDYL ESTER ($C_{25}H_{15}Li_2N_3O_{13}S_2$); (B.) FLUORESCENCE SPECTRUM OF ALEXA FLUOR 488 DYE-LABELED OLIGONUCLEOTIDE/ H_2O [INVITROGEN] (C.) SKETCH OF A CROSS SECTION OF TYPICAL SAMPLE (D: THICKNESS OF THE POLYELECTROLYTE BILAYERS). 94

FIGURE 5-3: FLUORESCENCE IMAGE, EXCITATION: 920 NM, SAMPLES BEFORE THE ADDITION OF FLUOROPHORES (A.) 3 BILAYERS, (B.) 5 BILAYERS. INTENSITY = 5 %. THE DOTTED LINE REPRESENTS THE LINE PROFILE DEPICTED BELOW EACH MEASUREMENT..... 95

FIGURE 5-4: FLUORESCENCE IMAGE RECORDED ON A AU NANOCRESCENTS SAMPLE TREATED WITH 3-APTES. EXCITATION: 850 NM, I= 1,1 %.. THE SCALE BAR REPRESENTS 50 μM.....	96
FIGURE 5-5: CLS IMAGE OF A SAMPLE COVERED WITH PE AND ALEXA 488. (A.) EXCITATION: 488NM (B.) EXCITATION AT 920 NM. THE SCALE BAR REPRESENTS 5 μM.	97
FIGURE 5-6: FLUORESCENCE IMAGES SHOWING BLEACHED SPOTS. IN (A.) THE SPOTS (AND MEASUREMENT) WERE DONE USING A 488NM LASER; IN (B.), 920 NM. IN BOTH CASES, THE INTEGRATION TIME/PIXEL IS 1.6 μS, THE PINHOLE HAS 72 μM. THE SCALE BAR REPRESENTS 50 μM.	98
FIGURE 5-7: (A.) PEAK DISPLACEMENT AS A FUNCTION OF THE OVERLAYER THICKNESS (SEE CHAPTER 4), EXEMPLIFYING THE PENETRATION DEPTHS OF THE U1 AND C2 MODES, AND THE POSITIONS OF THE DIFFERENT SAMPLE CONFIGURATIONS USED IN THESE EXPERIMENTS (1, 3 AND 5 BILAYERS); (B., C. AND D.) TRANSMISSION SPECTRA OF THE SAMPLES USED IN THE EXPERIMENTS, ALONG WITH THE FITTED CONTRIBUTIONS OF EACH MODE (C2, BLUE, U1, ORANGE) AND A SKETCH OF THE FINAL GEOMETRY OF THE SAMPLES.....	100
FIGURE 5-8: FLUORESCENCE FOR PULSED EXCITATION AT 800 AND 920 NM, FOR A SAMPLE COVERED WITH 1 BILAYER AND ALEXA 488. THE SCALE BAR REPRESENTS 5 μM.....	103
FIGURE 5-9: FLUORESCENCE MEASUREMENTS, 2-PHOTON EXCITATION AT 850 AND 920 NM, FOR A SAMPLE COVERED WITH 3 BILAYERS AND ALEXA 488. THE SCALE BAR REPRESENTS 5 μM.....	105
FIGURE 5-10: FLUORESCENCE MEASUREMENTS, 2-PHOTON EXCITATION AT 850 AND 920 NM, FOR A SAMPLE COVERED WITH 5 BILAYERS AND ALEXA 488. THE SCALE BAR REPRESENTS 5 μM.....	107
FIGURE 6-1. SIMPLIFIED SCHEME OF THE FABRICATION PROCEDURE FOR THE NANOELLIPSOIDS - A) COLLOID DISPERSION ON THE SURFACE OF A METAL-COVERED GLASS SUBSTRATE B). ION ETCHING C). (IDEAL) GEOMETRICAL DESCRIPTION OF THE PARTICLES ACCORDING TO ITS FABRICATION: THE MINOR AXIS OF THE ELLIPSE CORRESPOND TO THE COLLOIDS' DIAMETER; THE LONG AXIS CAN BE ESTIMATED AS $D_{COLL}/\cos(\epsilon)$	112
FIGURE 6-2: SKETCH OF THE DIFFERENT GEOMETRIES EXPECTED FOR DIFFERENT ETCHING ANGLES ($\epsilon = 0^\circ$; 30° , 45° AND 65°).....	113
FIGURE 6-3: 100 NM AG DISCS. WHITE LIGHT ILLUMINATION, (A.) DARK BACKGROUND ("REFLECTED LIGHT") AND (B.) WHITE BACKGROUND ("TRANSMITTED LIGHT"); (C.) SEM MICROGRAPH OF THE SAME SAMPLE (100 NM AG DISCS). THE SCALE BARS REPRESENTS 2 μM.....	115
FIGURE 6-4: (A.) EXTINCTION SPECTRA OF AG NANODISCS, (B.) AND (C.) PEAK POSITIONS AND WIDTH, AS DETERMINED FROM FITTING LORENTZIAN FUNCTIONS TO THE EXTINCTION MEASUREMENTS.	116
FIGURE 6-5: 100 NM AU DISCS. WHITE LIGHT ILLUMINATION, (A.) DARK BACKGROUND ("REFLECTED LIGHT") AND (B.) WHITE BACKGROUND ("TRANSMITTED LIGHT").....	117
FIGURE 6-6: (A.) EXTINCTION SPECTRA OF 60, 100, 125, AND 150 NM GOLD NANODISCS. ALL CURVES HAVE BEEN DISPLACED VERTICALLY FOR CLARITY. PEAK POSITION (B) AND WIDTHS (C.) OF THE RESONANCES, AS OBTAINED FROM FITTING LORENTZIAN FUNCTIONS TO THE SPECTRA. NO DATA NORMALIZATION HAS BEEN CARRIED OUT.	118
FIGURE 6-7: 200 NM AU DISCS, PREPARED FROM A CR: 1.5 NM, AU: 25 NM FILM, USING TWO DIFFERENT CONCENTRATIONS OF THE COLLOIDS' SUSPENSION (A: 1:100, B: 1:20).....	119
FIGURE 6-8: 125, 150* AND 300 NM AG DISCS ON GLASS.	120
FIGURE 6-9: SEM MICROGRAPHS OF (A.) AU ELLIPSOIDS PRODUCED USED 80 NM PS COLLOIDS. THE SIZE DISPERSION OF THE PARTICLES ON THIS SAMPLE CAN BE RELATED TO THE QUALITY OF THE COLLOIDAL	

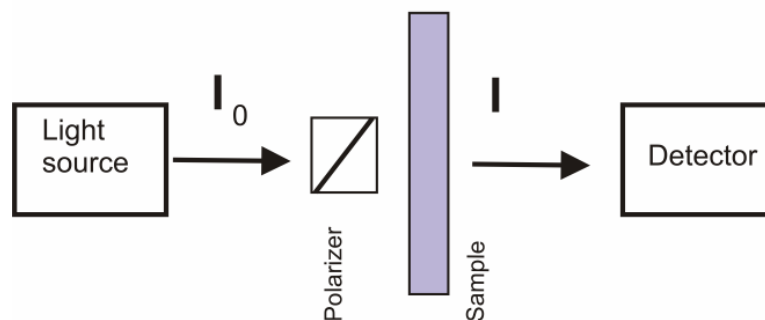
MASK USED FOR THESE SAMPLES (SEE APPENDIX C FOR DETAILS) (B.) AG ELLIPSOIDS, PRODUCED USING 1 μ M PS COLLOIDS. THE SCALE BARS REPRESENT 400 NM (A.) AND 2 μ M (B.).	121
FIGURE 6-10: EXTINCTION SPECTRA OF AG ELLIPSE-LIKE PARTICLES MEASURED WITH LIGHT POLARIZED ALONG THEIR MINOR (GRAY) AND MAJOR (BLACK) AXIS OF SYMMETRY. THE STRUCTURES WERE PRODUCED WITH $\epsilon = 30^\circ$ (A.), 45° (B.) AND 65° (C.). THE JUMP IN THE SPECTRA AT 860 NM IS RELATED TO THE SPECTROMETER AND HAS NO PHYSICAL MEANING FOR THE PARTICLES. SOME OF THE SPECTRA HAVE BEEN DISPLACED VERTICALLY FOR CLARITY.	122
FIGURE 6-11: PEAK POSITION AND WIDTH (ERROR BARS) OF THE RESONANCES FOR STRUCTURES ETCHED AT 30° (A.), 45° (B.) AND 65° (C.). THE GRAY MARKERS CORRESPOND TO MEASUREMENTS ALONG THE SHORT AXIS OF SYMMETRY, WHILE BLACK MARKERS CORRESPOND TO THE LONG ONE.	123
FIGURE 6-12: SKETCH OF AN ELLIPSOIDAL STRUCTURE AND THE DIFFERENT POLARIZATIONS.	123
FIGURE 6-13: AU ELLIPSOIDS PRODUCED USING 80 AND 100 NM COLLOIDS. THE SAMPLES WERE ETCHED AT 65° . THE SPECTRA MEASURED WITH LIGHT POLARIZED ALONG THE SHORT AXIS OF SYMMETRY APPEAR IN GRAY; FOR THE LONG AXIS, IN BLACK.	124
FIGURE 7-1: EXTINCTION SPECTRA OF AU NANODISCS OF 60 (A.), 125 (B.) AND 150 NM (NOMINAL) (C.) UPON THE ATTACHMENT OF AN INCREASING NUMBER OF POLYELECTROLYTE BILAYERS.	129
FIGURE 7-2: PEAK DISPLACEMENTS AS A FUNCTION OF THE AMOUNT OF ADDED POLYMER, FOR THE THREE SAMPLE SIZES EXPLORED IN THIS WORK. THE DASHED LINES REPRESENT EXPONENTIAL FITS TO THE DATA.	130
FIGURE 7-3: 80 NM AU NANODISCS AFTER THE ATTACHMENT OF SAV (A.) AND SAV-AUNPs (B.); 125 NM AU NANODISCS AFTER THE ATTACHMENT OF SAV (C.). THE SOLID, BLACK LINE CORRESPONDS TO THE REFERENCE MEASUREMENTS, THE DASHED LINE, TO BIOTINYLATION AND THE GREY ONE, AFTER EITHER SAV OR SAV-AUNPs ATTACHMENT.	133
FIGURE 7-4: 80 NM AG NANODISCS AFTER THE ATTACHMENT OF SAV (A.) AND SAV-AUNPs (B.). THE SOLID, BLACK LINE CORRESPONDS TO THE REFERENCE MEASUREMENT, THE DASHED LINE – AFTER BIOTINYLATION AND THE GREY LINE, AFTER EITHER SAV (A.) OR SAV-AUNPs (OVERNIGHT) (B.). ALL PEAK DISPLACEMENTS ARE CALCULATED TAKING THE PEAK POSITION AFTER BIOTINYLATION AS A REFERENCE.	135
FIGURE 8-1: A. REFERENCE MEASUREMENT ON A GOLD ELECTRODE, USING A Ag_2SO_4 SOLUTION; B. AU DISCS ON ITO	142
FIGURE 8-2: CONTROL TREATMENT (A.) AND AFTER AG –UPD (B.) FOR 200 NM DISCS. REFERENCE CURVES ARE DISPLAYED IN BLACK, AND THE RESULTING EXTINCTIONS AFTER TREATMENT IN GRAY, IN BOTH CASES.	142
FIGURE 8-3: 100 NM AU DISCS ON ITO BEFORE (BLACK) AND AFTER (GRAY) AG-UPD.	144

Appendix A

Materials and Methods

UV-Vis/NIR transmission spectroscopy

Polarized and non-polarized light spectra of particles produced on glass substrates were recorded in a conventional UV-Vis-NIR spectrometer equipped with polarization optics (*Perkin-Elmer, Lambda 900*) operating in transmission mode.



Appendix A 1: schematic representation of the spectrometer used for these experiments

$$\text{Transmission} = T = \frac{I}{I_0} \times 100\%$$

$$\text{Absorbance} = A = -\log\left(\frac{I}{I_0}\right)$$

The term “absorbance” can also be found commonly as extinction, with the same definition (extinction = scattering + absorption).

Scanning electron microscopy (SEM)

The scanning electron microscope (SEM) is a type of electron microscope that images the sample surface by scanning it with a high-energy beam of electrons in a raster scan pattern. As a result of this interaction, electrons (secondary and backscattered) can be collected, as well as X-rays, and an image of counts and positions can be built.

The device used in the experiments presented in this work is a *Leo Gemini* electron microscope model 1530, with acceleration voltages between 0.4 and 3 kV.

Confocal microscopy

Confocal microscopy is an optical imaging technique used to increase micrograph contrast and/or to reconstruct three-dimensional images by using a pinhole to eliminate out-of-focus light or flare in specimens that are thicker than the focal plane (Confocal)

Marvin Minsky introduced the confocal principle in 1957. In a conventional fluorescence microscope, the entire specimen is illuminated. In contrast, a confocal microscope uses point illumination and a pinhole in an optically conjugate plane in front of the detector to eliminate out-of-focus information. Only the light within the focal plane can be detected, so the image quality is much better than that of wide-field images.

In the recent past years this technique, particularly when combined with spectroscopy and photon-counting devices - has been used quite frequently to do single particle investigations (scattering and fluorescence – see i.e. (Stefani 2004; Novotny and Hecht 2006)).

Confocal microscopy is applied in this work to do particle-fluorophore interaction studies on a single particle level, for two photon processes.

A commercial confocal laser scanning (or “CLS”) microscope (*Carl Zeiss, Jena, Germany*) consisting of the module LSM 510 and an inverted microscope model Axiovert 200 was used in these experiments, with a water-immersion objective (C-Apochromat 40x/1.2 W Corr with numerical aperture (NA) of 1.2, (*Carl Zeiss, Jena, Germany*)). The two photon excitation was achieved using a titanium: sapphire laser (Ti:Sa) (*Mai Tai, Spectra Physics Inc., USA*) coupled to the confocal microscope setup. The Mai Tai laser is tunable in the range 780-920 nm and provides ~100 fs pulses at a repetition rate of 80 MHz.

Atomic Force Microscopy (AFM)

The AFM consists of a cantilever with a sharp tip (probe) at its end that is used to scan a specimen's surface. When the tip is brought into proximity of a sample surface, forces between the tip and the sample lead to a deflection of the cantilever. Typically, the deflection is measured using a laser spot reflected from the top of the cantilever into an array of photodiodes. It allows for imaging the topography of a sample with nanometer precision.

For this work (namely, nanocrescents' characterization), a commercial AFM (*Nanoscope IIIa, Veeco*) was used, working in tapping mode. Silicon cantilevers (*Olympus*) 160 μm long, 50 μm wide and 4.6 μm thick, with an integrated tip of a nominal spring constant of 42 N/m and a resonance frequency of 300 kHz were used. The tip was typically scanned on the samples at rates around 0.4 Hz for scan sizes of ~ 2 microns, and minimal applied forces were used when imaging.

Data analysis

Lorentzian function

A Lorentzian function is a function of the form (when normalized):

$$y(x) = \frac{1}{\pi} \frac{\frac{1}{2}\Gamma}{(x-x_0)^2 + \left(\frac{1}{2}\Gamma\right)^2}$$

where x_0 is the center position, and Γ represents its full width at half maximum (FWHM). It is commonly used in spectroscopy, and also because it represents the solution to the equations of a forced oscillator.

Gaussian function

A Gaussian function is a function of the form:

$$f(x) = \frac{1}{\sigma\sqrt{2\pi}} e^{-\frac{(x-\mu)^2}{2\sigma^2}}$$

being μ the center value and σ the dispersion.

Voigt function

The Voigt function is a convolution of a Lorentz profile and a Gaussian one.

$$V(x, \sigma, \gamma) = \int_{-\infty}^{\infty} G(x', \sigma) L(x - x', \gamma) dx'$$

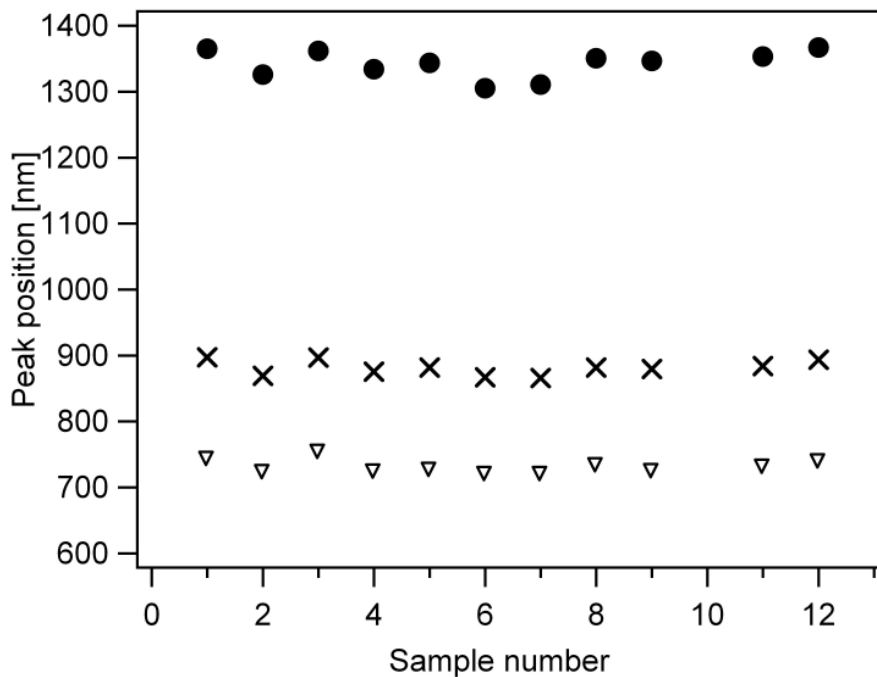
Appendix B

Au crescents

Peak position of the different resonances – dispersion among different samples

200 nm collids, 40 nm thick Au, 1 deposition ($\varphi = 0^\circ$), $\theta = 30^\circ$

Peak position for the c1, u1 and c2 resonances, as determined for lorentzian fits from 11 samples –

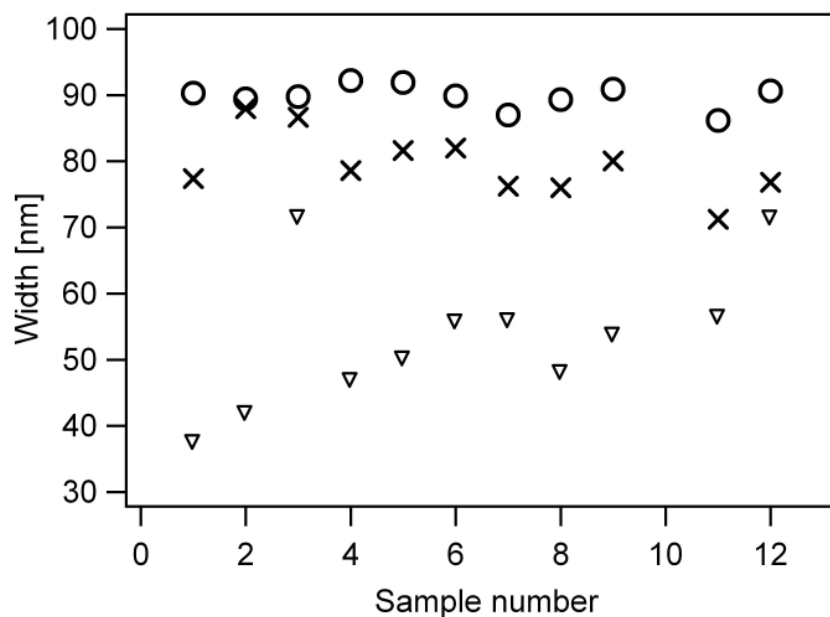


Appendix B 1: peak position for the c2 (triangles), u1 (crosses) and c1 (black dots) resonances, for 11 independent samples

Resonance	Average peak position [nm]	Std. Deviation [nm]
C1	1342	21
U1	881.1	11.3
C2	730	10.8

Appendix B 2: average peak position and standard deviation for the c1, u1 and c2 resonances

150 nm in *nominal* diameter, as provided by Polyscience

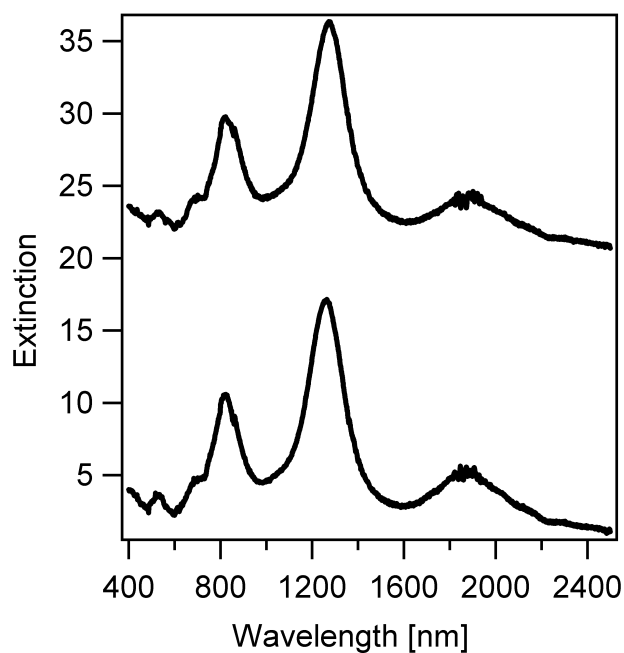


Appendix B 3: peak position for the c2 (triangles), u1 (crosses) and c1 (black dots) resonances, for 11 independent samples. The width corresponds to the half width at half maximum (HWHM) of the peaks.

Resonance	Average width [nm]	Std. Deviation [nm]
C1	89.7	1.8
U1	79.5	4.9
C2	53.5	10.7

Appendix B 4: average width and standard deviation for the c1, u1 and c2 resonances

Peak position of the different resonances – dispersion within one sample, measured at different positions



Appendix B 5: extinction spectra of one Au crescent sample, measured in two different spots

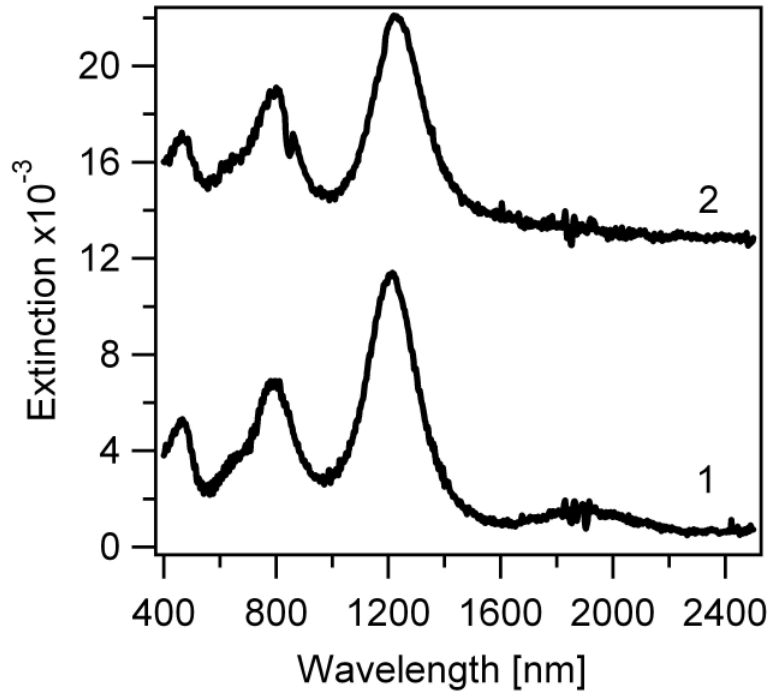
Resonance	C1		U1		C2	
	λ_p [nm]	W [nm]	λ_p [nm]	W [nm]	λ_p [nm]	W [nm]
Sample 1	1261	100.3	823	69	676.2	40.2
Sample 2	1273.7	97	830	47	677	24

Appendix B 6: peak position and width (HWHM) for measurements on a same Au nanocrescents' sample

Ag crescents

Peak position of the different resonances – dispersion between different samples

200 nm collids, 40 nm thick Ag, 1 deposition ($\varphi = 0^\circ$, $\theta = 30^\circ$)



Appendix B 7: extinction spectra of two independent Ag nanocrescent samples

Resonance	C1		U1		C2	
	λ_p [nm]	W [nm]	λ_p [nm]	W [nm]	λ_p [nm]	W [nm]
Sample 1	1211.8	119.2	790.9	101.6	637.5	53.2
Sample 2	1231	113.2	787.5	109.2	631.9	70.6

Appendix B 8: peak position and width for the main resonances for two independent Ag nanocrescent samples

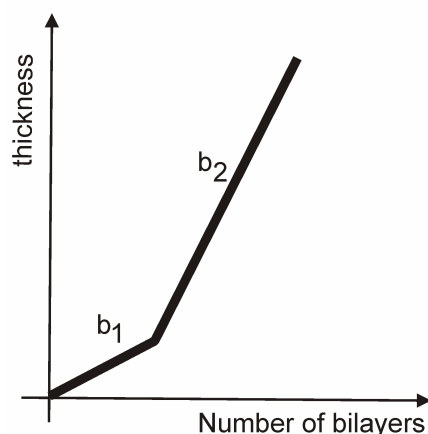
Thin layer sensing experiments - Supporting information

Thickness profiles, influence on the decay lengths

The correct determination of the thickness profile used for the thin film sensing experiments with nanocrescents (Chapter 4) or nanodiscs (Chapter 7) is of fundamental importance, since it determines, in turn, the quality of the method.

The results presented in Chapter 4 correspond to the thicknesses determined via atomic force microscopy images (AFM) of the samples, for a few polyelectrolyte layers, and optical (light scattering and SPR) for larger thicknesses (Vasilev K 2004; Vasilev K 2004). The determination of the thickness in of the first layers is a crucial issue, since the estimations on sensitivity and decay lengths are linked directly to these values.

Here, a chart summarizing different (fictitious) scenarios for polymer thicknesses is presented, and their influence on the decay lengths estimated from them, analysed.



Appendix C 1: scheme of the thickness profile for the film sensing experiments in Chapter 4.

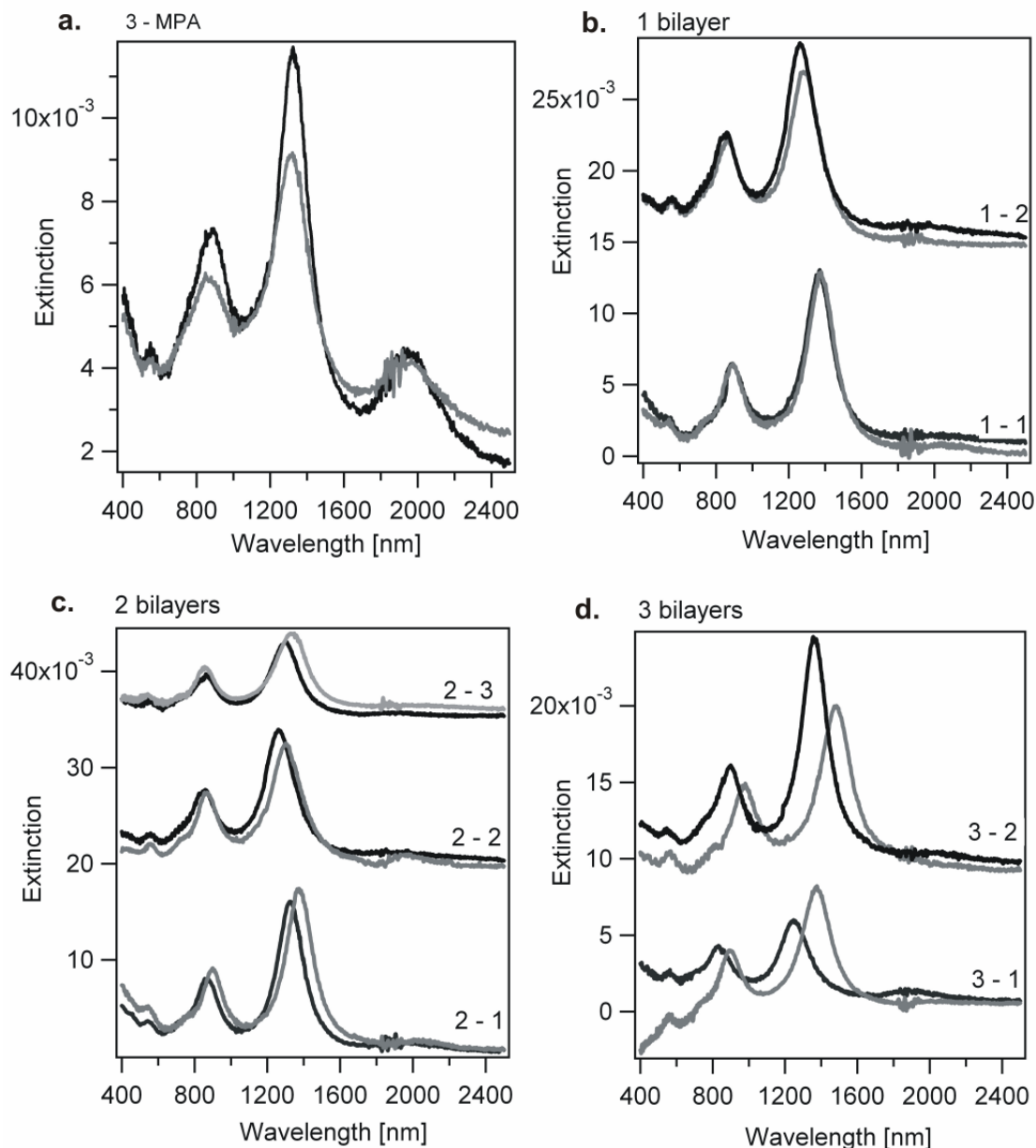
	Estimated decay lengths [nm]		
	C1	U1	C2
B1 =4, b2 = 8	20.3	11.4	5.8
B1 =4.5, b2 = 7.5	26.5	16.6	6
B1 = 3, b2 = 8.5	17.2	8	8

Appendix C 2: estimation of different scenarios for the decay lengths based on different film thicknesses

The c2 resonance appears as the one less affected for the different (fictitious) thickness profiles tested; the variations lie in a 2 nm range. Thinner first layers influence strongly the decays estimated for u1 and c1. Still, for all cases, the decay lengths would remain roughly in a 20 – 30 nm range for c1, 10 – 20 for u1, and in a 5 to 10 nm for c2.

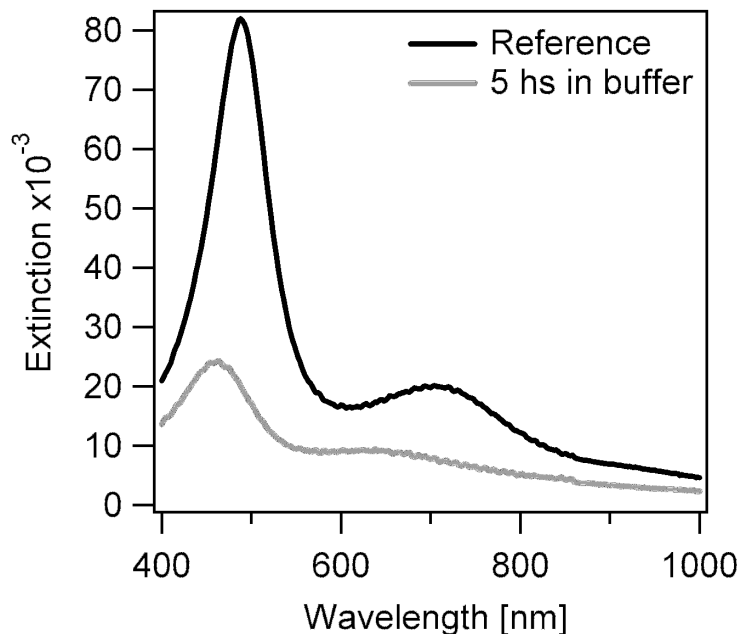
First layers

Spectra for the first layers deposited on the crescents



Appendix C 3: extinction spectra of several independent standard Au nanocrescents (Ch. 4) after functionalization with 3-MPA (a.), and the attachment of 1,2 and 3 bilayers (b., c., and d.).

Annealing of Ag nanoparticles exposed to PBS buffer solutions

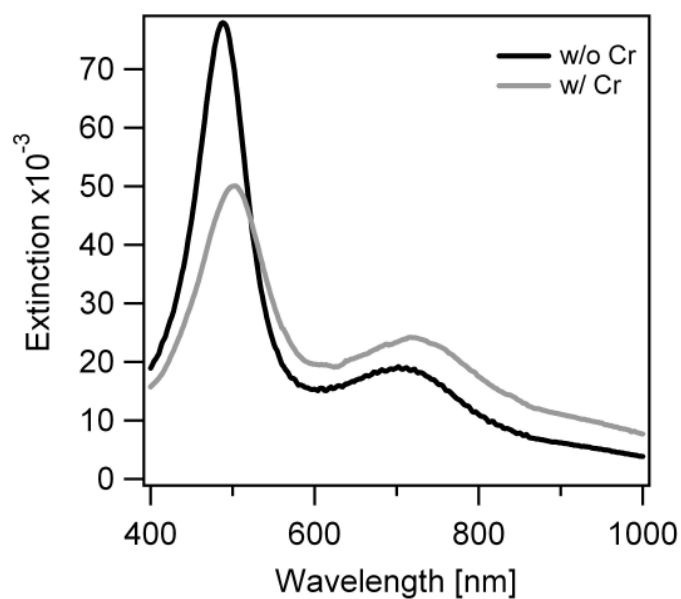


Appendix B 9: 80 nm Ag nanodiscs (without Cr as adhesive layer to glass) before (black) and after (gray) 5 hs of immersion in a PBS buffer

	Reference	After annealing
λ_p [nm]	485.5	457.2
Width [nm]	40.7	54

Appendix B 10: Peak position and width of the main resonance, before and after solution annealing

Ag particles are very sensitive to solvent annealing (Duval Malinsky, Lance Kelly et al. 2001). Leaving samples immersed in conventional PBS buffer can lead to a blue shift of the resonance of the order of 30 nm, which then convolutes with the displacements associated to the attachment on the surface of species to be detected. In order to solve this, a 1 nm Cr adhesion layer is added between the Ag film and the glass, which should prevent the particles from changing shape/deattaching from the surface. The addition of this Cr layer induces minimum changes to the spectra (namely, a red shift and a slight widening of the main peak), as can be observed in Appendix B 11.



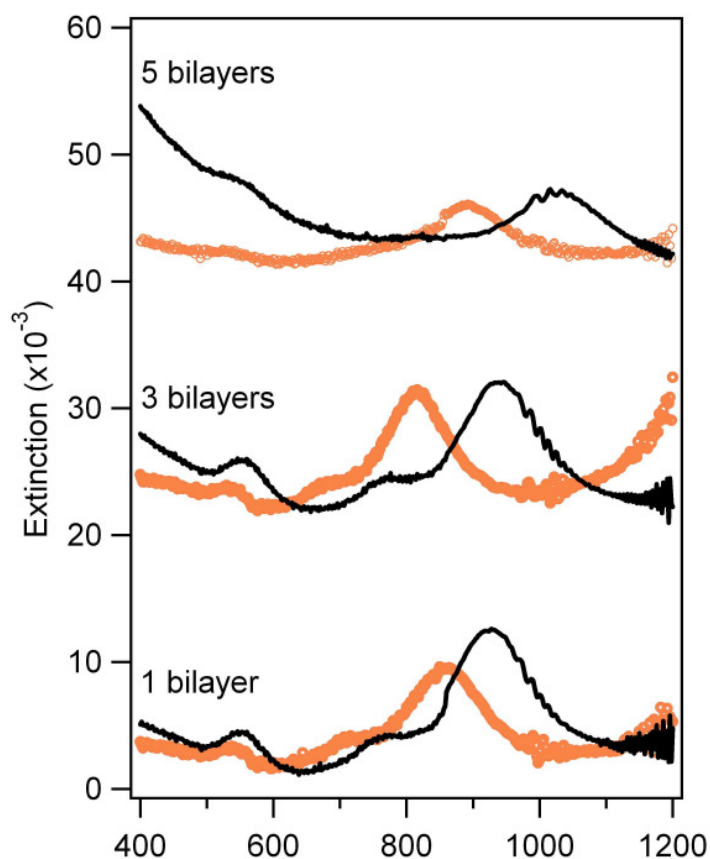
Appendix B 11 : 80 nm Ag discs, with (gray) and without (black) a ~1nm Cr adhesion layer

	W/o Cr	W/Cr
λ_p [nm]	485.8	498.4
Width [nm]	38.8	49.5

Appendix B 12: peak position and width of the main resonance of 80 nm Ag discs, prepared with and without Cr as adhesion layer

Two photon experiments - Supporting Data

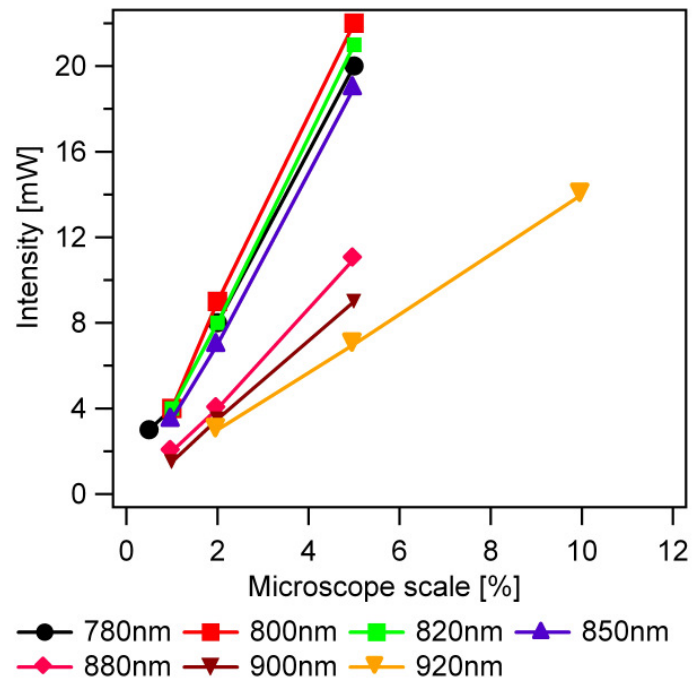
Spectra of all samples before and after the polyelectrolyte attachment



Appendix B 13: transmission spectra of the nanocrescents before (orange) and after (black) the deposition of 1, 3 and 5 bilayers

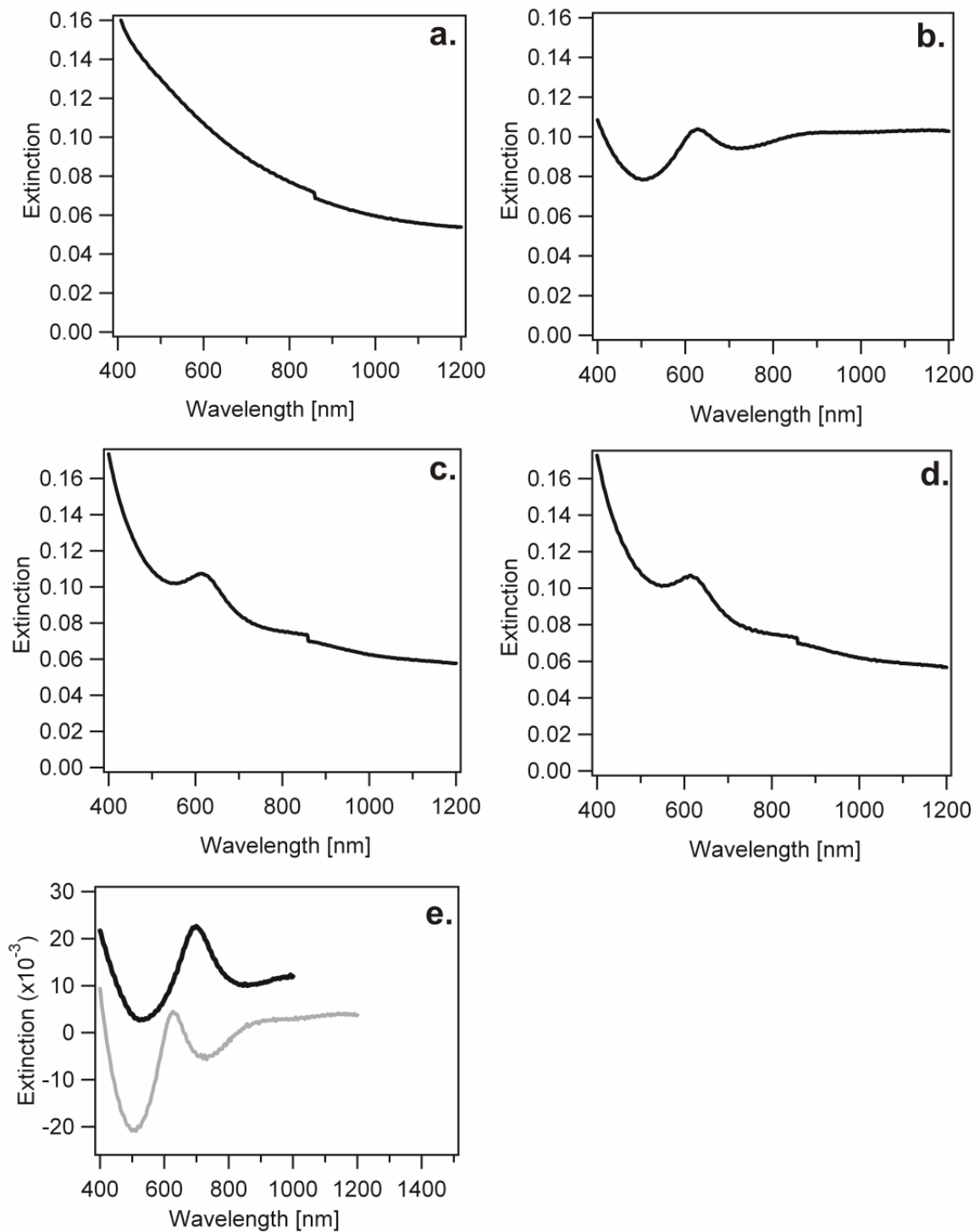
Intensity calibration

Appendix B 14 presents an intensity calibration curve for the Mai Tai laser coupled to the confocal microscope (LSM 510, Zeiss). The intensities are measured at the objective's position, without the objective (meaning, the real excitation power on the sample is still modified by the presence of the objective, though this effect is supposedly minimized by the use of highly corrected optics, as it is the case here). These values are, therefore, only a rough indication of the power irradiated on the sample.



Appendix B 14: Intensity calibration for the LSM 510 (Zeiss). Intensity measured at the objective's position, without the objective in place.

Ag-UPD experiments - Complementary experiment on 100 nm Au discs



Appendix B 15: (a.) ITO on glass vs air (base: air); (b.) treated Au discs on ITO, vs. ITO (base: air), (c.) treated discs on ITO vs. air (base: air), (d.) addition of (a.) and (b.), (e.) sample before (black) and after (gray) the Ag-UPD deposition (100 nm Au discs)

Appendix C

Colloidal masks

Products from Polyscience -

Polyscience – PS nanobeads			Observed from SEM images (no statistics)
Nominal diameter	Size	SD	
80	75	1.9	35 – 75 nm
100	104	4.1	80 – 105 nm
125	130	2.6	80 – 125 nm
150	155	1.5	140 – 220 nm
200	205.6 ± 2.6	6.3	180 – 195 nm
300	285.6 ± 3.6	19.5	230 – 260 nm
500	491.3 ± 6.2	14.4	465 – 525 nm

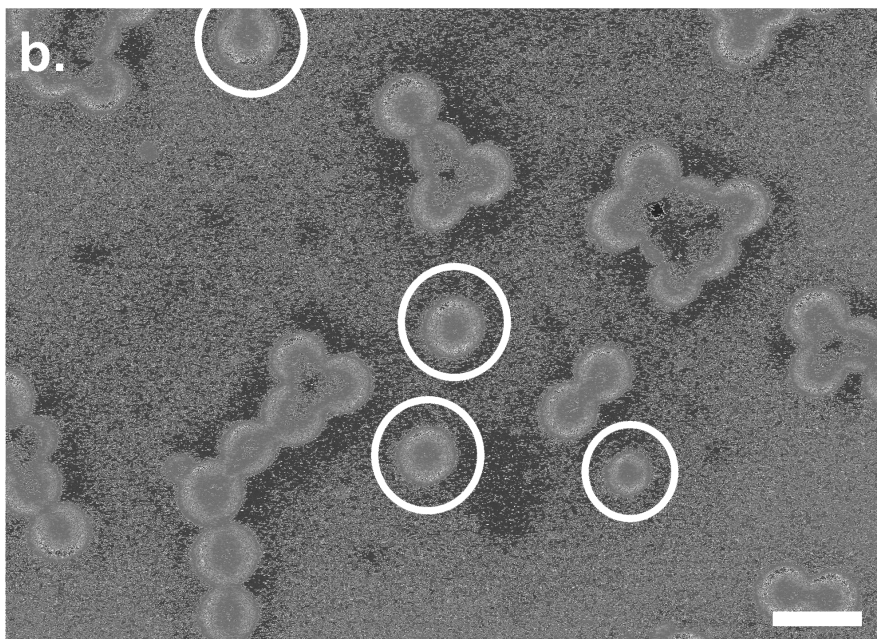
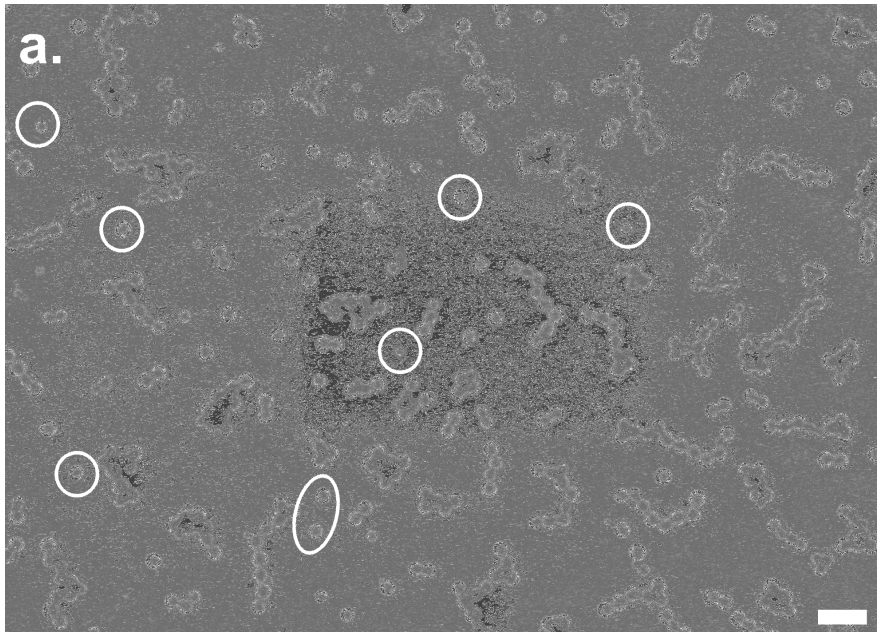
Appendix C 4: summary of the product information provided by the company and size estimation with SEM measurements

A drop of each colloidal suspension (as bought) was spread on a clean silicon substrate and studied by SEM. The images show that the sizes of the particles differ considerably to the information given by the company. Some particles were measured to gain a rough idea of the range of sizes for each case; a thorough statistical study is to be carried out to determine a real mean value and the corresponding dispersion in sizes for these colloids.

The quality of the colloidal mask is of fundamental importance, since it determines that of the crescents / discs / ellipses produced with this material.

In the following, a brief collection of SEM images of the masks is presented to support the information presented in Appendix C 4, particularly, of the most disperse material (80 nm colloids). The products most affected in terms of size dispersion were the smallest colloids (80, 100, 125 nm). This dispersion in the masks call for new tests on crescents, discs and ellipses produced with low dispersion materials, and for comparison with calculated spectra.

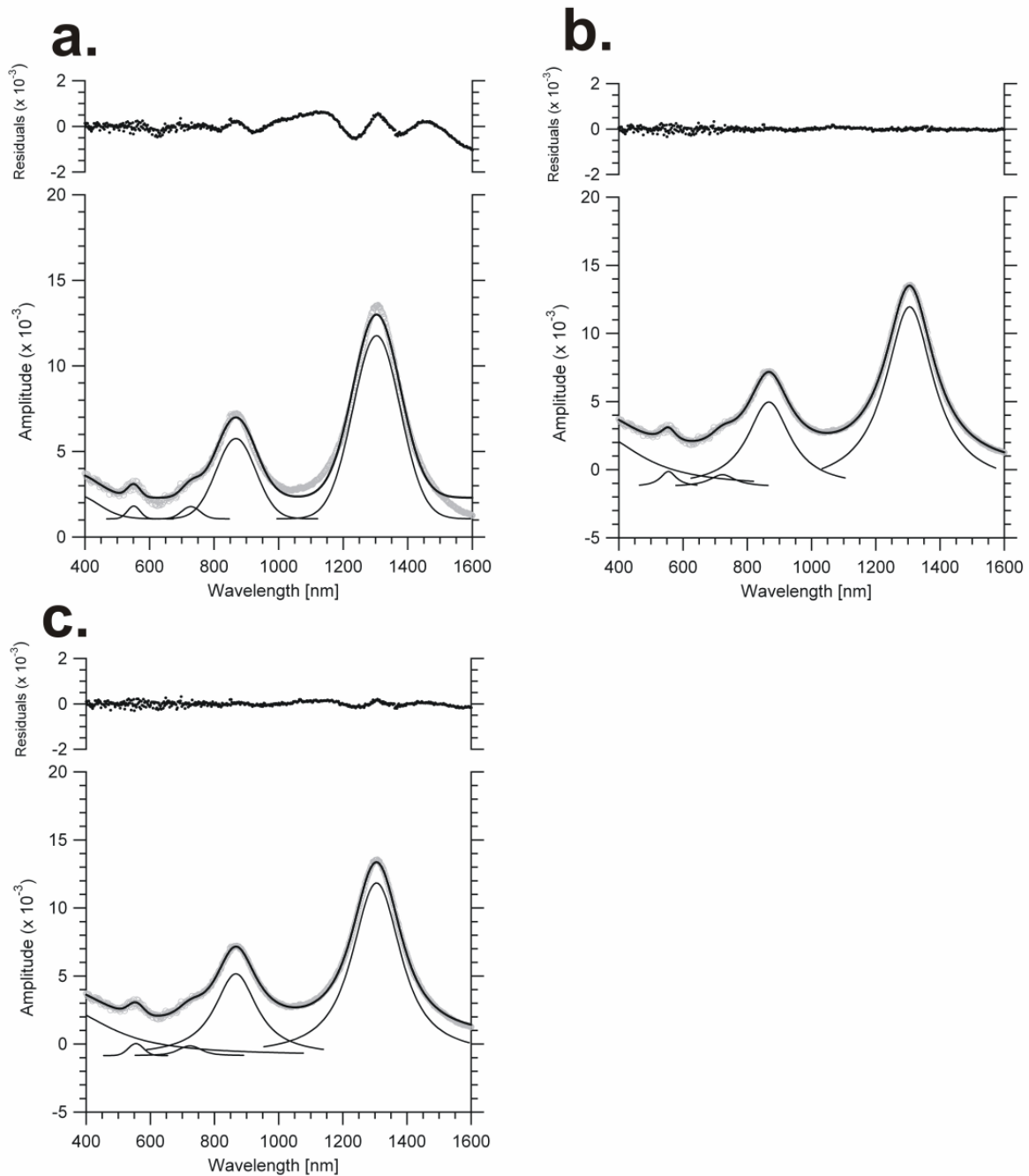
80 nm colloids



Appendix C 5: 80 nm colloids, as bought from Polyscience. Scales: (a.) 200 nm, (b.) 100 nm

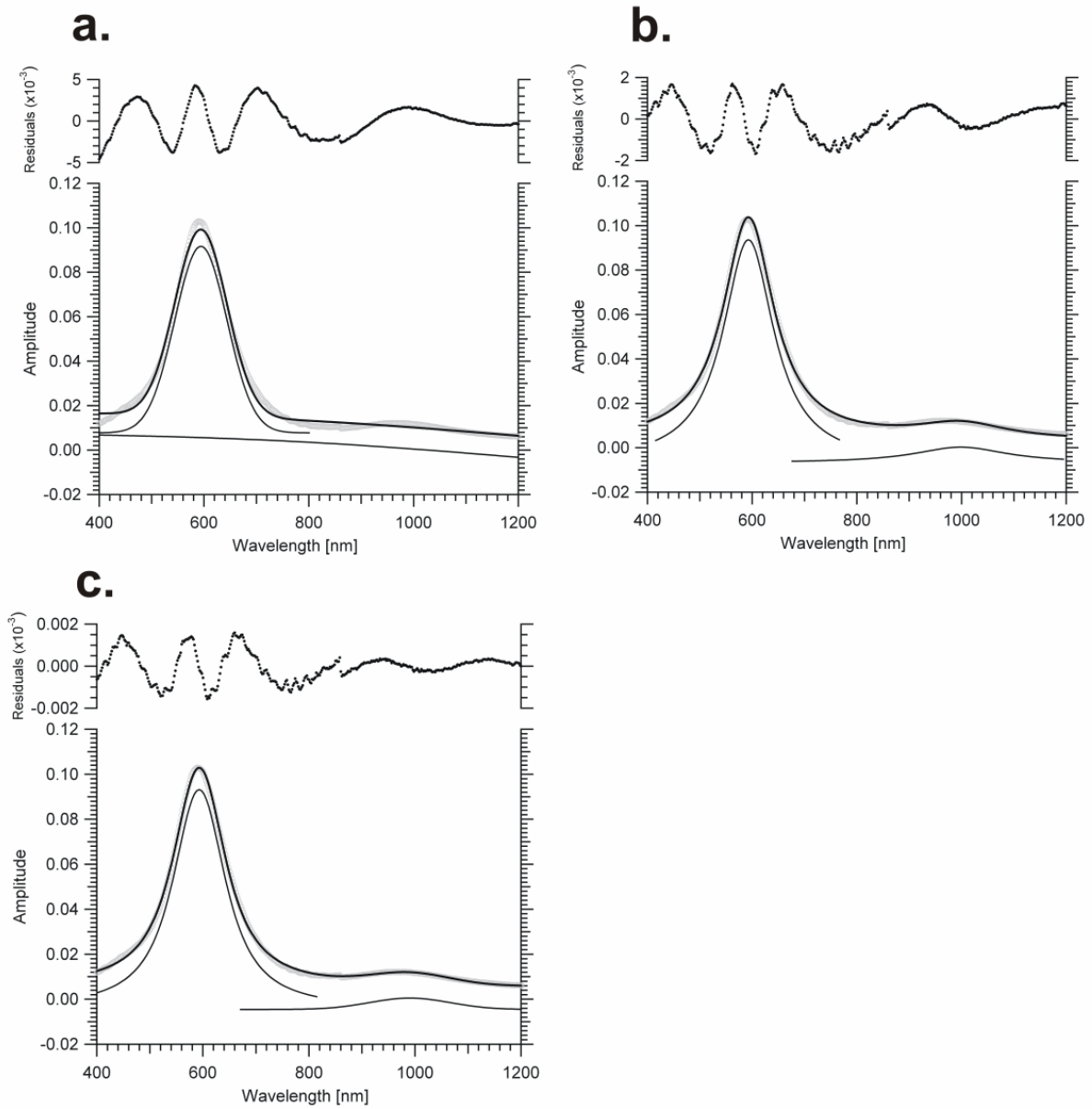
Fitting Lorentzian, Gaussian and Voigt curves

Crescents



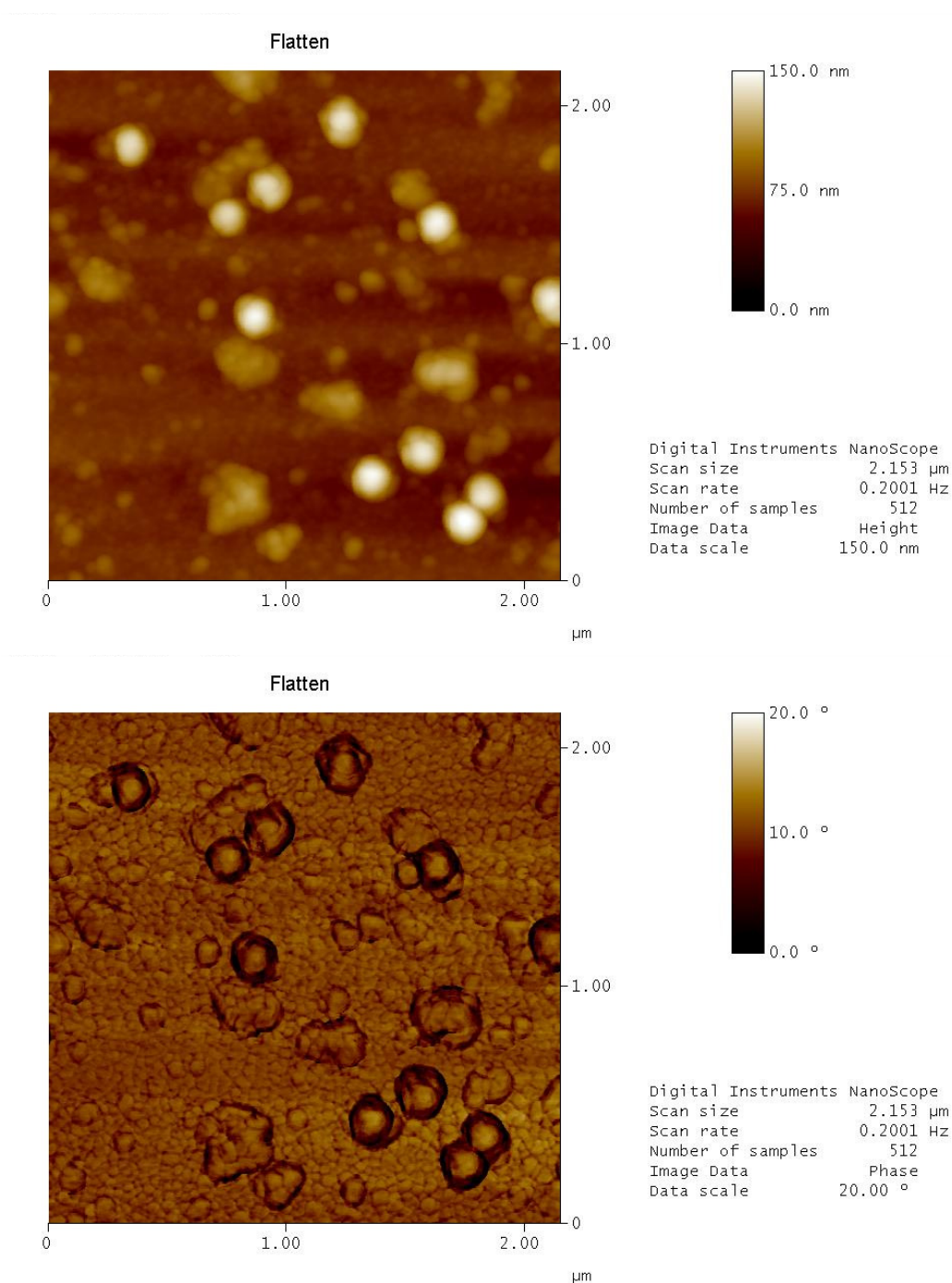
Appendix C 6: Simultaneous peak fitting (thin black lines) of a extinction spectrum (gray) of a *standard* crescent shaped nanoparticle sample using (a.) Gaussian curves and (b.) Lorentzian curves (c.) Voigt curves. Lorentzian fits (b.) give rise to the smallest residuals of all 3 options.

Discs



Appendix C 7: fitting gaussian (a.), lorentzian (b.) and Voigt curves (c.) on extinction spectra of metallic nanodiscs on glass.

Ag nanodiscs and SAV-AuNPs – AFM imaging



Height and phase measurements on a sample prepared with Ag nanodiscs and SAV-AuNPs. The surface appears rough, covered with several agglomerations, most likely due to the attachment of BSA and SAV-Au NPs to the glass substrate. The height measurements also reveal the presence of colloids from the mask that haven't been thoroughly removed from the surface by stripping. Proper surface analysis of material attaching only to the discs should be done most likely using previous surface passivation of the glass.

References

[Adam D. McFarland, R. P. V. D. 2003]

Adam D. McFarland, R. P. V. D. (2003). "Single Silver Nanoparticles as Real-Time Optical Sensors with Zeptomole Sensitivity." Nanoletters **3**(8): 1057-1062.

[Aizpurua, J., P. Hanarp, et al. 2003]

Aizpurua, J., P. Hanarp, et al. (2003). "Optical properties of gold nanorings." Phys. Rev. Lett. **90**(5): 057401.

[Anger, P., P. Bharadwaj, et al. 2006]

Anger, P., P. Bharadwaj, et al. (2006). "Enhancement and quenching of single-molecule fluorescence." Physical Review Letters **96**.

[Ashcroft, N. W. and T. Mermin 1976]

Ashcroft, N. W. and T. Mermin (1976). Solid State Physics Cengage Learning Services.

[Barnes, W. L. 1998]

Barnes, W. L. (1998). "Fluorescence near interfaces: the role of photonic mode density." J. Modern Optics **45**(4): 661-699.

[Becker, J., I. J. Zins, et al. 2008]

Becker, J., I. J. Zins, et al. (2008). "Plasmonic Focusing Reduces Ensemble Linewidth of Silver-Coated Gold Nanorods." Nano Letters.

[Beines, P. W., I. Klosterkamp, et al. 2007]

Beines, P. W., I. Klosterkamp, et al. (2007). "Responsive thin hydrogel layers from photo-crosslinkable poly(n-isopropylacrylamide) terpolymers." Langmuir **23**(4): 2231-2238.

[Bertrand, P., A. Jonas, et al. 2000]

Bertrand, P., A. Jonas, et al. (2000). "Ultrathin polymer coatings by complexation of polyelectrolytes at interfaces: suitable materials, structure and properties." Macromolecular Rapid Communications **21**(7): 319-348.

[Beverliius, M. R., A. Bouhelier, et al. 2003]

Beverliius, M. R., A. Bouhelier, et al. (2003). "Continuum generation from single gold nanostructures through near-field mediated intraband transitions." Physical Review B **68**.

[Biteen, J. S., N. S. Lewis, et al. 2006]

Biteen, J. S., N. S. Lewis, et al. (2006). "Spectral tuning of plasmon-enhanced silicon quantum dot luminescence." Applied Physics Letters **88**.

[Bohren, C. F. and D. R. Huffman 1983]

Bohren, C. F. and D. R. Huffman (1983). Absorption and scattering of light by small particles, John Wiley & Sons.

[Boleininger, J., A. Kurz, et al. 2006]

Boleininger, J., A. Kurz, et al. (2006). "Microfluidic continuous flow synthesis of rod-shaped gold and silver nanocrystals." Physical Chemistry Chemical Physics **8**(3824).

[Bouhelier, A., R. Bachelot, et al. 2005]

Bouhelier, A., R. Bachelot, et al. (2005). "Surface plasmon characteristics of tunable photoluminescence in single gold nanorods."

[Bouhelier, A., M. R. Beverslius, et al. 2003]

Bouhelier, A., M. R. Beverslius, et al. (2003). "Characterization of nanoplasmonic structures by locally excited photoluminescence." Applied Physics Letters **83**(24).

[Boyd, G. T., Z. H. Yu, et al. 1986]

Boyd, G. T., Z. H. Yu, et al. (1986). "Photoinduced luminescence from the noble metals and its enhancement on roughened surfaces." Physical Review B **33**(12).

[Buckman, B. A. 1995]

Buckman, B. A. (1995). Guided wave Photonics, Saunders College/ Harcourt Brace Publishing

[Buron, C. C., C. Filiâtre, et al. 2007]

Buron, C. C., C. Filiâtre, et al. (2007). "Early steps in layer-by-layer construction of polyelectrolyte films: The transition from surface/polymer to polymer/polymer determining interactions." Journal of Colloid and Interface Science **314**: 358-366.

[Chen, Y., K. Munechika, et al. 2007]

Chen, Y., K. Munechika, et al. (2007). "Dependence of Fluorescence Intensity on the Spectral Overlap between Fluorophores and Plasmon Resonant Single Silver Nanoparticles." Nano Letters **7**(3): 690-696.

[Clark, A. W., A. K. Sheridan, et al. 2007]

Clark, A. W., A. K. Sheridan, et al. (2007). "Tuneable visible resonances in crescent shaped nano-split-ring-resonators." APPLIED PHYSICS LETTERS **91**: 093109.

[Decher, G. 1997]

Decher, G. (1997). "Fuzzy nanoassemblies: Toward layered polymeric multicomposites." Science **277**(5330): 1232-1237.

[Decher, G., J. D. Hong, et al. 1992]

Decher, G., J. D. Hong, et al. (1992). "Buildup of Ultrathin Multilayer Films by a Self-Assembly Process .3. Consecutively Alternating Adsorption of Anionic and Cationic Polyelectrolytes on Charged Surfaces." Thin Solid Films **210**(1-2): 831-835.

[Decher, G. and J. Schmitt 1992]

Decher, G. and J. Schmitt (1992). "Fine tuning of the film thickness of ultrathin multilayer film composed of consecutively alternating layers of anionic and cationic polyelectrolytes." Colloid and Polymer Science **89**: 160-164.

[Deckman, H. W. and J. H. Dunsmuir 1982]

Deckman, H. W. and J. H. Dunsmuir (1982). "Natural Lithography." Applied Physics Letters **41**(4): 377-379.

[Duval Malinsky, M., K. Lance Kelly, et al. 2001]

Duval Malinsky, M., K. Lance Kelly, et al. (2001). "Chain Length Dependence and Sensing Capabilities of the Localized Surface Plasmon Resonance of Silver Nanoparticles Chemically Modified with Alkanethiol Self-Assembled Monolayers." J. Am. Chem. Soc. **123**: 1471-1482.

[Englebienne, P. 1998]

Englebienne, P. (1998). "Use of colloidal gold surface plasmon resonance peak shift to infer affinity constants from the interactions between protein antigens and antibodies specific for single or multiple epitopes." Analyst **123**(7): 1599-1603.

[Enkrich, C., F. Pérez-Willard, et al. 2005]

Enkrich, C., F. Pérez-Willard, et al. (2005). "Focused-Ion-Beam Nanofabrication of Near-Infrared Magnetic Metamaterials." Adv. Mater. **17**: 2547–2549.

[Fang, S., H. J. Lee, et al. 2006] Fang, S., H. J. Lee, et al. (2006). "Attomole Microarray Detection of MicroRNAs by Nanoparticle-Amplified SPR Imaging Measurements of Surface Polyadenylation Reactions." J. Am. Chem. Soc. **128**: 14044-14046.

[Faraday, M. 1857] Faraday, M. (1857). Philos. Trans. R. Soc. London **147**.

[Farahani, J. N., D. W. Pohl, et al. 2005]

Farahani, J. N., D. W. Pohl, et al. (2005). "Single Quantum Dot Coupled to a Scanning Optical Antenna: ATunable Superemitter." Physical Review Letters **95**.

[Fischer, U. and H. P. Zingsheim 1981]

Fischer, U. and H. P. Zingsheim (1981). "Submicroscopic Pattern replication with visible light." J. Vac. Sci. Technol. **19**(4).

[Frederix, F., J. M. Friedt, et al. 2003]

Frederix, F., J. M. Friedt, et al. (2003). "Biosensing Based on Light Absorption of Nanoscaled Gold and Silver Particles." Anal.Chem. **75**: 6894-6900.

[Freitag, S.]

<http://faculty.washington.edu/stenkamp/stefanieweb/abstratct.html>

[Gerber, S., F. Reil, et al. 2007]

Gerber, S., F. Reil, et al. (2007). "Tailoring light emission properties of fluorophores by coupling to resonance-tuned metallic nanostructures." Physical Review B **75**.

[Girard, C., O. J. F. Martin, et al. 1995]

Girard, C., O. J. F. Martin, et al. (1995). "Molecular Lifetime Changes Induced By Nanometer-Scale Optical-Fields." Physical Review Letters **75**(17): 3098-3101.

[Goeppert-Mayer, M. 1930] Goeppert-Mayer, M. (1930). Ueber Elementarakte mit zwei Quantensprungen. Goettingen, Goettingen. **PhD**.

[Grand, J., P.-M. Adam, et al. 2006] Grand, J., P.-M. Adam, et al. (2006). "Optical Extinction Spectroscopy of Oblate, Prolate and Ellipsoid Shaped Gold Nanoparticles : Experiments and Theory." Plasmonics **1**: 135-140.

[Haes, A. and R. P. Van Duyne 2004] Haes, A. and R. P. Van Duyne (2004). "A unified view of propagating and localized surface plasmon resonance biosensors." Anal Bioanal. Chem. **379**: 920-930.

[Haes, A. J., D. A. Stuart, et al. 2004]

Haes, A. J., D. A. Stuart, et al. (2004). "Using solution-phase nanoparticles, surface-confined nanoparticle arrays and single nanoparticles as biological sensing platforms." Journal Of Fluorescence **14**(4): 355-367.

[Haes, A. J. and R. P. Van Duyne 2002]

Haes, A. J. and R. P. Van Duyne (2002). "A nanoscale optical biosensor: Sensitivity and selectivity of an approach based on the localized surface plasmon resonance spectroscopy of triangular silver nanoparticles." Journal Of The American Chemical Society **124**(35): 10596-10604.

[Haes, A. J., S. L. Zou, et al. 2004]

Haes, A. J., S. L. Zou, et al. (2004). "Nanoscale optical biosensor: Short range distance dependence of the localized surface plasmon resonance of noble metal nanoparticles." Journal Of Physical Chemistry B **108**(22): 6961-6968.

[Haes, A. J., S. L. Zou, et al. 2004]

Haes, A. J., S. L. Zou, et al. (2004). "A nanoscale optical biosensor: The long range distance dependence of the localized surface plasmon resonance of noble metal nanoparticles." Journal Of Physical Chemistry B **108**(1): 109-116.

[Haes, A. J. Z., J. , S. Zou, et al. 2005]

Haes, A. J. Z., J. , S. Zou, et al. (2005). "Solution-Phase, Triangular Ag Nanotriangles Fabricated by Nanosphere Lithography." J. Phys.Chem. B **109**.

[Haginoya, C., M. Ishibashi, et al. 1997]

Haginoya, C., M. Ishibashi, et al. (1997). "Nanostructure array fabrication with a size-controllable natural lithography." Applied Physics Letters **71**(20): 2934-2936.

[Hanarp, P. 2003]

Hanarp, P. (2003). Optical properties of nanometer disks, holes and rings prepared by colloidal lithography. Department of Applied Physics. Göteborg, Sweden, Chalmers University of Technology and Göteborg University. **PhD**.

[Hanarp, P., M. Käll, et al. 2003]

Hanarp, P., M. Käll, et al. (2003). "Optical Properties of Short Range Ordered Arrays of Nanometer Gold Disks Prepared by Colloidal Lithography." J. Phys. Chem. B **107**: 5768-5772.

[Hanarp, P., D. S. Sutherland, et al. 2003]

Hanarp, P., D. S. Sutherland, et al. (2003). "Control of nanoparticle film structure for colloidal lithography." Colloids and Surfaces A: Physicochem. Eng. Aspects **214**: 23-36.

[Haynes, C. L. and R. P. Van Duyne 2001]

Haynes, C. L. and R. P. Van Duyne (2001). "Nanosphere Lithography: a versatile nanofabrication tool for studies of size-dependent nanoparticle optics." J. Phys. Chem. B **105**.

[Herrero, E., L. J. Buller, et al. 2001]

Herrero, E., L. J. Buller, et al. (2001). "Underpotential Deposition at Single Crystal Surfaces of Au, Pt, Ag and Other Materials." Chem. Rev. **101**: 1897-1930.

[Homola, J. 2006]

Homola, J. (2006). Surface Plasmon Resonance (Springer Series on Chemical Sensors and Biosensors), Springer.

[Imura, K., T. Nagahara, et al. 2004]

Imura, K., T. Nagahara, et al. (2004). "Plasmon mode imaging of single gold nanorods." JACS **126**: 12730-12731.

[Invitrogen]

Invitrogen - www.invitrogen.com

[J. R. Krenn, G. S., W. Rechberger, B. Lamprecht, A. Leitner, F. R. Aussenegg 2000]

J. R. Krenn, G. S., W. Rechberger, B. Lamprecht, A. Leitner, F. R. Aussenegg (2000). "Design of multipolar plasmon excitations in silver nanoparticles." Applied Physics Letters **77**(21).

[J.G. Gordon, J. D. S. 1977]

J.G. Gordon, J. D. S. (1977). "The effect of thin organic films on the surface plasma resonance on gold." Optics Communications **22**(3): 374-376.

[Jain, P. K., W. Huang, et al. 2007]

Jain, P. K., W. Huang, et al. (2007). "On the Universal Scaling Behavior of the Distance Decay of Plasmon Coupling in Metal Nanoparticle Pairs: A Plasmon Ruler Equation." Nanoletters **7**(7): 2080-2088.

[Jonas, U., et al., , 2002, 99(8), 5034-5039 2002]

Jonas, U., et al., , 2002, 99(8), 5034-5039 (2002). Proceedings of the National Academy of Sciences of the United States of America **99**(8): 5034-5039.

[Keilmann, F. and R. Hillenbrand 2004]

Keilmann, F. and R. Hillenbrand (2004). "Near-field microscopy by elastic light scattering from a tip." Phil.Trans. R. Soc. Lond. A **362**: 787-805.

[Kim, S., J.-M. Jung, et al. 2006]

Kim, S., J.-M. Jung, et al. (2006). "Patterned arrays of Au rings for localized surface plasmon resonance." Langmuir **22**: 7109-7112.

[Klitzing, R. v., J. E. Wong, et al. 2004]

Klitzing, R. v., J. E. Wong, et al. (2004). "Short range interactions in polyelectrolyte multilayers." Current Opinion in Colloid and Interface Science **9**: 158-162.

[Knoll, W. 1998]

Knoll, W. (1998). "Interfaces and thin films as seen by bound electromagnetic waves." Annual Review Of Physical Chemistry **49**: 569-638.

[Kosiorok, A., W. Kandulski, et al. 2005]

Kosiorok, A., W. Kandulski, et al. (2005). "Fabrication of nanoscale rings, dots, and rods by combining shadow nanosphere lithography and annealed polystyrene nanosphere masks." Small **1**(4): 439-444.

[Kreibig, U., B. Schmitz, et al. 1987]

Kreibig, U., B. Schmitz, et al. (1987). "Separation of plasmon-polariton modes of small metal particles." Physical Review B **36**(9).

[Kreibig, U. and M. Vollmer]

Kreibig, U. and M. Vollmer Optical properties of metal clusters. Berlin, Springer.

[Krenn, J. R., G. Schider, et al. 2000]

Krenn, J. R., G. Schider, et al. (2000). "Design of multipolar plasmon excitations in silver nanoparticles." Applied Physics Letters **77**(21): 3379-3381.

[Krenn, J. R., G. Schider, et al. 2000]

Krenn, J. R., G. Schider, et al. (2000). "Design of multipolar plasmon excitations in silver nanoparticles." Applied Physics Letters **77**(21).

[Kühn, S., U. Hakanson, et al. 2006] Kühn, S., U. Hakanson, et al. (2006). "Enhancement of single-molecule fluorescence using a gold nanoparticle as an optical nanoantenna." Physical Review Letters **97**.

[Langhammer, C., I. Zoric, et al. 2007]

Langhammer, C., I. Zoric, et al. (2007). "Hydrogen Storage in Pd Nanodisks Characterized with a Novel Nanoplasmonic Sensing Scheme." Nanoletters **7**(10): 3122-3127.

[Larsson, E. M., J. Alegret, et al. 2007]

Larsson, E. M., J. Alegret, et al. (2007). "Sensing characteristics of NIR localized surface plasmon resonances in gold nanorings for application as ultrasensitive biosensors." Nanoletters **7**(5): 1256-1263.

[Le Ru, E. C., P. G. Etchegoin, et al. 2007]

Le Ru, E. C., P. G. Etchegoin, et al. (2007). "Mechanisms of spectral profile modification in surface enhanced fluorescence." J. Phys. Chem. C **111**: 16076-16079.

[Li, K., L. Clime, et al. 2008]

Li, K., L. Clime, et al. (2008). "Surface enhanced Raman scattering on long-range ordered noble-metal nanocrescent arrays." Nanotechnology **19**: 145305.

[Lim, R. Y. H., B. Fahrenkrog, et al. 2007]

Lim, R. Y. H., B. Fahrenkrog, et al. (2007). "Nanomechanical Basis of Selective Gating by the Nuclear Pore Complex." Science **318**.

[Linden, S., C. Enkrich, et al. 2004]

Linden, S., C. Enkrich, et al. (2004). "Magnetic Response of Metamaterials at 100 Terahertz." Science **306**(19).

[Lu, Y., G. L. Liu, et al. 2005]

Lu, Y., G. L. Liu, et al. (2005). "Nanophotonic crescent moon structures with sharp edge for ultrasensitive biomolecular detection by local electromagnetic field enhancement effect." Nano Letters **5**(1): 119-124.

[LycurgusCup]

www.britishmuseum.org/explore/highlights/highlight_objects/pe_mla/t/the_lycurgus_cup.aspx.

[Mertens, H., J. S. Biteen, et al. 2006]

Mertens, H., J. S. Biteen, et al. (2006). "Polarization-Selective Plasmon-Enhanced Silicon Quantum-Dot Luminescence." Nano Letters **6**(11): 2622-2625.

[Mooradian, A. 1969]

Mooradian, A. (1969). "Photoluminescence of metals." Physical Review Letters **22**: 185-187.

[Mulvaney, P. 1996]

Mulvaney, P. (1996). "Surface Plasmon Spectroscopy of Nanosized Metal Particles." Langmuir **12**: 788-800.

[Murray, W. A. and W. L. Barnes 2007]

Murray, W. A. and W. L. Barnes (2007). "Plasmonic Materials." Adv. Mater. **19**: 3771-3782.

[Murray, W. A., J. R. Suckling, et al. 2006]

Murray, W. A., J. R. Suckling, et al. (2006). "Overlayers on Silver Nanotriangles: Field Confinement and Spectral Position of Localized Surface Plasmon Resonances." Nanoletters **6**(8).

[Novotny, L. 2007]

Novotny, L. (2007). "Effective wavelength scaling for optical antennas." Physical Review Letters **98**(26).

[Novotny, L. and B. Hecht 2006]

Novotny, L. and B. Hecht (2006). Principles of Nano-Optics, Cambridge University Press.

[Pakizeh, T., M. S. Abrishamian, et al. 2006]

Pakizeh, T., M. S. Abrishamian, et al. (2006). "Magnetic-field enhancement in gold nanosandwiches." Optics Express **4**(18).

[Pendry, J. B. 2000]

Pendry, J. B. (2000). "Negative Refraction Makes a Perfect Lens." Physical Review Letters **85**(18).

[Pendry, J. B., A. J. Holden, et al. 1999]

Pendry, J. B., A. J. Holden, et al. (1999). "Magnetism from Conductors and Enhanced Nonlinear Phenomena." IEEE TRANSACTIONS ON MICROWAVE THEORY AND TECHNIQUES **47**(11).

[Pérez-Luna, V. H. O. B., M.J.; Opperman, K.A.; Hampton, P.D.; López, G.P.; Klumb, L.A.; Stayton, P.S. 1999]

Pérez-Luna, V. H. O. B., M.J.; Opperman, K.A.; Hampton, P.D.; López, G.P.; Klumb, L.A.; Stayton, P.S. (1999). J. Am. Chem. Soc. **121**: 6469-6478.

[Puscasu, I., W. L. Schaich, et al. 2001]

Puscasu, I., W. L. Schaich, et al. (2001). "Modeling parameters for the spectral behavior of infrared frequency-selective surfaces." Applied Optics **40**(1): 118-124.

[Raschke, G., S. Kowarik, et al. 2003]

Raschke, G., S. Kowarik, et al. (2003). "Biomolecular recognition based on single gold nanoparticle light scattering." Nano Letters **3**(7): 935-938.

[Reinhard, B. M., M. Siu, et al. 2005]

Reinhard, B. M., M. Siu, et al. (2005). "Calibration of dynamic molecular rulers based on plasmon coupling between gold nanoparticles." Nano Letters **5**(11): 2246-2252.

[Retsch, M., Z. Zhou, et al. 2008]

Retsch, M., Z. Zhou, et al. (2008). Fabrication of large area, transferable colloidal monolayers utilizing self assembly at the air-water interface. Mainz.

[Rindzevicius, T., Y. Alaverdyan, et al. 2005]

Rindzevicius, T., Y. Alaverdyan, et al. (2005). "Plasmonic Sensing Characteristics of Single Nanometric Holes." Nanoletters **5**(11): 2335-2339.

- [Rindzevicius, T., Y. Alaverdyan, et al. 2007]** Rindzevicius, T., Y. Alaverdyan, et al. (2007). "Long-Range Refractive Index Sensing Using Plasmonic Nanostructures." J. Phys. Chem. C **111**: 11806-11810.
- [Ringler, M., A. Schwemer, et al. 2008]**
Ringler, M., A. Schwemer, et al. (2008). "Shaping emission spectra of fluorescent molecules with single plasmonic nanoresonators." Physical Review Letters **100**: 203002.
- [Rochholz, H. 2005]** Rochholz, H. (2005). Mainz.
- [Rochholz, H., N. Bocchio, et al. 2007]**
Rochholz, H., N. Bocchio, et al. (2007). "Tuning resonances on crescent shaped noble metal nanoparticles " New Journal of Physics **9**(53).
- [Rogobete, L., F. Kaminski, et al. 2007]**
Rogobete, L., F. Kaminski, et al. (2007). "Design of plasmonic nanoantennae for enhancing spontaneous emission." Optics Letters **32**(12).
- [Sato, A. 2006]**
Sato, A. (2006). Surface Plasmon Fluorescence Spectroscopy and Optical Waveguide Fluorescence Spectroscopy in Limit of Detection Studies. Department of Information Processing Mainz, Tokyo Institute of Technology. Masters.
- [Schider, G., J. R. Krenn, et al. 2001]**
Schider, G., J. R. Krenn, et al. (2001). "Optical properties of Ag and Au nanowire gratings." Journal Of Applied Physics **90**(8): 3825-3830.
- [Schider, G., J. R. Krenn, et al. 2003]**
Schider, G., J. R. Krenn, et al. (2003). "Plasmon dispersion relation of Au and Ag nanowires." Physical Review B **68**(15).
- [Sheridan, A. K., A. W. Clark, et al. 2007]**
Sheridan, A. K., A. W. Clark, et al. (2007). "Multiple plasmon resonances from gold nanostructures." APPLIED PHYSICS LETTERS **90**: 143105.
- [Sherry, L., S.-H. Chang, et al. 2005]**
Sherry, L., S.-H. Chang, et al. (2005). "Localized surface plasmon resonance spectroscopy of single silver nanocubes." Nanoletters **5**(10): 2034-2038.
- [Shumaker-Parry, J., H. Rochholz, et al. 2005]**
Shumaker-Parry, J., H. Rochholz, et al. (2005). "Fabrication of crescent shaped optical antennas." Advanced Materials **17**: 2131 - 2134.
- [Smith, D. R., J. B. Pendry, et al. 2004]**
Smith, D. R., J. B. Pendry, et al. (2004). "Metamaterials and Negative Refractive Index." Science **305**.
- [So, P. T. C., C. Y. Dong, et al. 2000]**

So, P. T. C., C. Y. Dong, et al. (2000). "Two photon excitation fluorescence microscopy." Annu. Rev. Biomed. Eng. **02**: 399-429.

[Sönnichsen, C., B. M. Reinhard, et al. 2005]

Sönnichsen, C., B. M. Reinhard, et al. (2005). "A molecular ruler based on plasmon coupling of single gold and silver nanoparticles." Nature Biotechnology **23**(6).

[Spinke, J., M. Liley, et al. 1993]

Spinke, J., M. Liley, et al. (1993). "Molecular Recognition at Self-Assembled Monolayers: Optimization of Surface Functionalization." J. Chem. Phys. **99**: 7012-7019.

[Taminiau, T. H., F. D. Stefani, et al. 2008]

Taminiau, T. H., F. D. Stefani, et al. (2008). "Optical antennas direct single-molecule emission." Nature Photonics **2**.

[Tamm, M. 2008]

Tamm, M. (2008). Chirale Plasmonik, Fachhochschule Wiesbaden. Dipl.-Ing.

[Tan, B. J.-Y., C.-H. Sow, et al. 2004]

Tan, B. J.-Y., C.-H. Sow, et al. (2004). "Fabrication of a two-dimensional periodic non-close-packed array of polystyrene particles." J. Phys. Chem. B **108**: 18575-18579.

[Tavlove, A. 1995]

Tavlove, A. (1995). Computational Electromagnetics. The Finite Difference Time-Domain Method, Artech House, Boston.

[Turkevich, J., P. C. Stevenson, et al. 1951]

Turkevich, J., P. C. Stevenson, et al. (1951). "A study of the nucleation and growth processes in the synthesis of colloidal gold." Disc. Far. Soc. **11**: 55.

[Ueno, K., S. Juodkazis, et al. 2007]

Ueno, K., S. Juodkazis, et al. (2007). "Spectral sensitivity of uniform arrays of gold nanorods to dielectric environment." J. Phys.Chem. C **111**: 4180-4184.

[Ueno, K., S. Juodkazis, et al. 2008]

Ueno, K., S. Juodkazis, et al. (2008). "Clusters of Closely Spaced Gold Nanoparticles as a Source of Two-Photon Photoluminescence at Visible Wavelengths." Adv. Mater.(20): 26-30.

[Ueno, K., S. Juodkazis, et al. 2008]

Ueno, K., S. Juodkazis, et al. (2008). "Nanoparticle plasmon-assisted two-photon polymerization induced by incoherent excitation source " JACS **130**: 6928-6929.

[Unger, A. 2008]

Unger, A. (2008) – Private communication.

[Valeur, B. 2002]

Valeur, B. (2002). Molecular Fluorescence. Weinheim, Wiley-VCH.

[Van Os, M. T., B. Menges, et al. 1999]

Van Os, M. T., B. Menges, et al. (1999). "Characterization of Plasma-Polymerized Allylamine Using Waveguide Mode Spectroscopy." Chem. Mater. **11**: 5.

[van Oss, C. J., R. F. Giese, et al. 2003]

van Oss, C. J., R. F. Giese, et al. (2003). "Macroscopic-scale surface properties of streptavidin and their influence on aspecific interactions between streptavidin and dissolved biopolymers." Colloids and Surfaces B: Biointerfaces **30**: 25-36.

[Vasilev, K. 2004]

Vasilev, K. (2004). Halle-Wittenberg, Martin-Luther-Universitaet

[Vasilev, K. 2004]

Vasilev, K. (2004). Fluorophores near metal interfaces. Halle, Martin-Luther-University Halle-Wittenberg.

[Vasilev, K., W. Knoll, et al. 2004]

Vasilev, K., W. Knoll, et al. (2004). "Fluorescence intensities of chromophores in front of a thin metal film " Journal of Chemical Physics **120**(7).

[Wark, A. W., H. J. Lee, et al. 2007]

Wark, A. W., H. J. Lee, et al. (2007). "Nanoparticle-Enhanced Diffraction Gratings for Ultrasensitive Surface Plasmon Biosensing." Anal. Chem. **79**: 6697-6701.

[Whitney, A. V., J. W. Elam, et al. 2005]

Whitney, A. V., J. W. Elam, et al. (2005). "Localized surface plasmon resonance nanosensor: A high-resolution distance-dependence study using atomic layer deposition." Journal Of Physical Chemistry B **109**(43): 20522-20528.

[Willets, K. A. and R. P. Van Duyne 2007]

Willets, K. A. and R. P. Van Duyne (2007). "Localized Surface Plasmon Resonance Spectroscopy and Sensing." Annu. Rev. Phys. Chem. **58**: 267-297.

[Willets, K. A. and R. P. Van Duyne 2007]

Willets, K. A. and R. P. Van Duyne (2007). "Localized surface plasmon resonance spectroscopy and sensing." Annual Review of Physical Chemistry **58**: 267-297.

[Yonzon, C. R., E. Jeoung, et al. 2004]

Yonzon, C. R., E. Jeoung, et al. (2004). "A comparative analysis of localized and propagating surface plasmon resonance sensors: The binding of concanavalin a to a monosaccharide functionalized self-assembled monolayer." Journal Of The American Chemical Society **126**(39): 12669-12676.

[Zhang, G., D. Wang, et al. 2007]

Zhang, G., D. Wang, et al. (2007). "Fabrication of Multiplex Quasi-Three-Dimensional Grids of One-Dimensional Nanostructures via Stepwise Colloidal Lithography." Nanoletters.

[Zhang, G., D. Wang, et al. 2007]

Zhang, G., D. Wang, et al. (2007). "Ordered Binary Arrays of Au Nanoparticles Derived from Colloidal Lithography." Nanoletters **7**(1): 127-132.

[Zhang, X., C. R. Yonzon, et al. 2006]

Zhang, X., C. R. Yonzon, et al. (2006). "Nanosphere lithography fabricated plasmonic materials and their applications." J.Mater.Res. **21**(5).

[Zheng, Y. B., B. K. Juluri, et al. 2008]

Zheng, Y. B., B. K. Juluri, et al. (2008). "Systematic investigation of localized surface plasmon resonance of long-range ordered Au nanodisk arrays." Journal of applied physics **103**: 014308.

Collaborations

Acknowledgements

Curriculum Vitae – Noelia Laura Bocchio

Publications

